National Technical University of Athens
School of Naval Architecture and Marine Engineering
Shipbuilding Technology Laboratory

Diploma Thesis

Study of Methods for Measuring Torque and Strains on Shafts Made of Composite Materials

Theodoros Mavrozoumis

Thesis Supervisor: Professor N. Tsouvalis

November 2022

Acknowledgements

I would like to express my deepest appreciation to my thesis supervisor, Professor Nicholas Tsouvalis for giving me the chance to conduct this thesis at the Shipbuilding Technology Laboratory (STL) of the School of Naval Architecture and Marine Engineering of the National Technical University of Athens. His constant interest, guidance and his insightful suggestions throughout the entire conduction of this thesis were determinant.

Furthermore, I am grateful to PhD Student Elias Bilalis for his contribution and enlightening comments for every aspect and difficulty that arose during both the bibliographic and experimental part of my thesis. The completion of this thesis would not have been possible without his constant encouragement and inspiration.

I would also like to thank all the personnel of the STL, especially Mr. Thanasi Markoulis and Mr. Charis Xanthos, for their contribution in the conduction of the experimental tests at the Laboratory.

Last but not least, I am grateful to my family for their constant support and encouragement throughout my entire university studies.

Abstract

Nowadays, composite materials are widely used in a variety of applications in marine and automotive industries, aerospace, aircrafts, buildings, and sport equipment. Low weight and high strength are the most predominant features of such materials which makes them a favorable option for even wider use is many structures. Composite shafts, mainly carbon fiber reinforced polymer, are a characteristic case where such materials have started to be used and research for their development is steadily increasing. Especially in the marine sector, composite driveshafts can also offer corrosion resistance, low bearing loads, reduced magnetic signature and higher fatigue resistance among other advantages.

For driveshafts torque monitoring during operation is an essential need for measuring the power transmitted to the propeller or for performance evaluation and process monitoring and control of combustion engines or electric motors. Another aspect is the strain measurement of shafts, or in general of other composite cylindrical structures (e.g. pipes, tubes), for stress analysis which is related to Structural Health Monitoring.

The main aim of this thesis, therefore, is an overview of the methods that are used for torque and strain measurements on such structures. In the context of this thesis methods that are commonly used in commercial applications or other that are still in a more preliminary - laboratory level are presented. Based on the technique and/or the sensors that are used, a first categorization was made. Strain Gauges (SG) are the most widely used system for strain measurement and many commercially available torque transducers are based on this technique. For the connection between the rotating shaft and the stationary part of the measurement system contact connection with slip rings or non-contact connection with either inductive power supply and/or signal transmission or with wireless RF telemetry can be made. On composite shafts due to their orthotropic behavior, SG are more difficult to be used and more aspects are needed to be taken into account. Fiber Optic Sensors (FOS) are also under development for both SHM and torque measurement but still in a laboratory level. Fiber Optic Rotary Joints (FORJ) and other systems which use special lenses (Graded-Index or C-lenses) can be used for non-contact signal transmission although the problem ingress/egress point of such systems on rotating driveshaft is still unsolved. Twist angle measurement is also widely used in commercial off-the-selves systems as it offers simultaneously speed measurement and can be mounted on already existing shafting systems without disassembly. Lastly, other systems which utilize Surface Acoustic Waves (SAW), Digital Image Correlation (DIC) or other techniques that are under development were also found.

A static torsional test on a CFRP shaft was conducted in the Laboratory of Testing and Materials (LTM) of the School of Applied Mathematics and Physical Science of NTUA in Athens in order to check the validity of the TorqueTrak 10k torque meter from Binsfeld which is based on the wireless RF telemetry signal transmission technique. For that reason, analytical estimation of equivalent mechanical properties of the shaft was made and a split-disk test in ring-shaped

specimens for the experimental calculation of the Young's modulus in the hoop direction. Although many problems were encountered in both experimental procedures, some useful conclusions about the applicability of this torque meter on composite shafts could be drawn after processing the results.

Finally, FEM analysis in ANSYS simulation program was conducted. Deviation between the numerical and experimental torsional stiffness was observed. This is probably attributed to the overestimation of material mechanical properties considered for the modelling of the shaft (mainly E_1) and some deviations in the geometry (thickness, exact orientation of layers). Lastly, since the maximum torque achieved during the torsional test was much lower than the critical buckling torque of the shaft obtained from FEM and analytical solutions, no safe estimation of the torsional buckling modeshape could be made.

CONTENTS

CHAPTER 1 INTRODUCTION

1.1 Composite materials and shafts made of composite materials

Composite material is considered this which consists of two or more components or phases. Each component is from different material with much different mechanical and physical properties from the others and at least 10% content by volume. The final material overall has therefore significantly different properties than those of its individual components (Tsouvalis 1998). Commonly, two components are used with one of them being the reinforcing material. Such materials can be fibers, particulates and laminates. The fiber reinforced plastics (FRP) are the most widely used composite materials. Fibers that are mainly used are glass, graphite, and silicon carbides and have high strength. The other material is called matrix, is commonly a resin (e.g. thermosetting like polyester, epoxy) and is the bonding material which holds the fibers together. In that way light and strong materials are created. FRP offers the advantage that fiber layers can be optionally placed at any orientation which gives the composite material enhanced properties at specific, desired orientations.

Composite materials are widely used in marine and automotive industries, aerospace, aircrafts, buildings, and sport equipment. Predominant advantages of FRP material, especially when compared to other conventional materials, are the low weight and therefore high specific strength and stiffness. Especially in the marine sector, applications of composite materials include commercial and navy ships, submarines, offshore energy, underwater repair of steel pipelines, superstructures, propellers, shafts, rudders, piping systems, masts, bulkheads, decks, doors, hatches etc. (Mouritz et al 2001, Graham-Jones & Summerscales 2016). At least over the last 50 years FRP are predominantly used in the recreational boating industry, in small crafts and pleasure boats and more recently in racing vessels, both power and sail (Green 1999). Some of the main advantages of composite materials are:

- Low weight, which lead to fuel consumption efficiency and thus reduction of the operational costs and the ability to carry more payload.
- Corrosion resistance which reduces the maintenance costs
- Vibration and noise dumping (a primary reason for the use of composites in pleasure boats)

On the other hand, some disadvantages are:

- The high cost for acquiring the raw material (fibers, resins) and manufacturing costs (experienced personnel and controlled environmental conditions)
- Maintenance is more difficult as the whole structure must be examined and not specific, vulnerable points as in metal structures
- Poor recyclability

Composite shafts have been highly used in automotive industry and in marine structures for around three decades, mainly as propulsion shaft (Figure 1.1). In these shafts the main fiber and resin materials used are carbon and epoxy respectively. A composite material shaft can weigh up to 75% less than traditional steel or aluminum shafts thus reducing the overall weight of the shaft system which accounts for 2% of the total ship weight (Mouritz et al. 2001). In addition, they can offer advantages such as corrosion resistance, low bearing loads, reduced magnetic signature, higher fatigue resistance, greater flexibility, excellent vibration damping and improved life-cycle cost. On the other hand, understanding the mechanical behavior and the failure mode of the composite shaft may be difficult. During design and manufacturing of the shaft, the mechanical properties of the final structure are not a priori known as they depend on the final fiber-matrix layup. Finding the best layup can be a difficult task. Empirical data was mainly used in the past, but more recently Finite Element Method and the relevant simulation programs gave a boost in the design and analysis of composite shafts (Bilalis 2016).

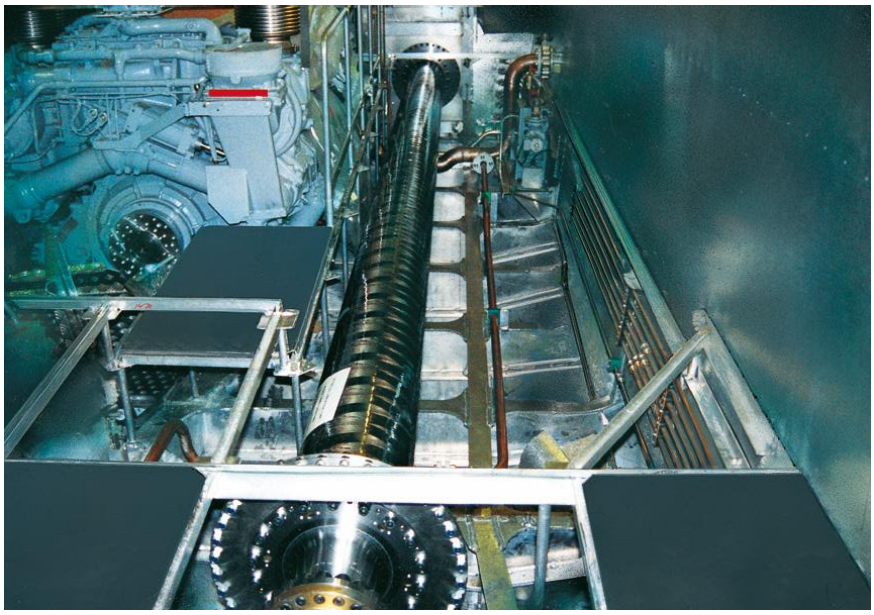

Figure 1.1 CENTADISC carbon fibre shaft in ship

Other cylindrical structures made of composite materials that are used in various industries are piping systems (oil industry, coal mine, paper mill, power production, marine piping systems). In this case, fiberglass is the most commonly used fiber material while resin material depends upon the given application. With composite pipes of large diameter handling is greatly improved and corrosion issues are managed. Furthermore, the interior surfaces of such pipes are smoother compared to pipe made of conventional materials such as steel, therefore frictional losses are eliminated. On the other hand, connection between consecutive parts can be a difficult task. FRP materials are also used in storage tanks, mainly when the materials to be stored can lead to corrosion of the conventional steel tanks (Green 1999).

Some composite shaft manufacturers for marine applications are GEISLINGER, DYNEXA, REXNORD-CENTA, VULKAN, JAURE and others. In Bilalis (2016), (2020), Vavatsikos (2020) and the respective site of each manufacturer, more detailed information can be found. The manufacturing process of composite shafts (pipes and tanks included) that is almost entirely used is filament winding (Figure 1.2). It is an automated process where the fibers, which are formed in roving, are wounded around a rotating mold tool called mandrel (either in a helical or a polar manner) after they are passed through a resin impregnation stage. The fiber delivery eye can be placed at any orientation with respect to the rotating fiber so that the desired pre-defined winding pattern is achieved. With this method, high production rates are achieved and high quality products are made.

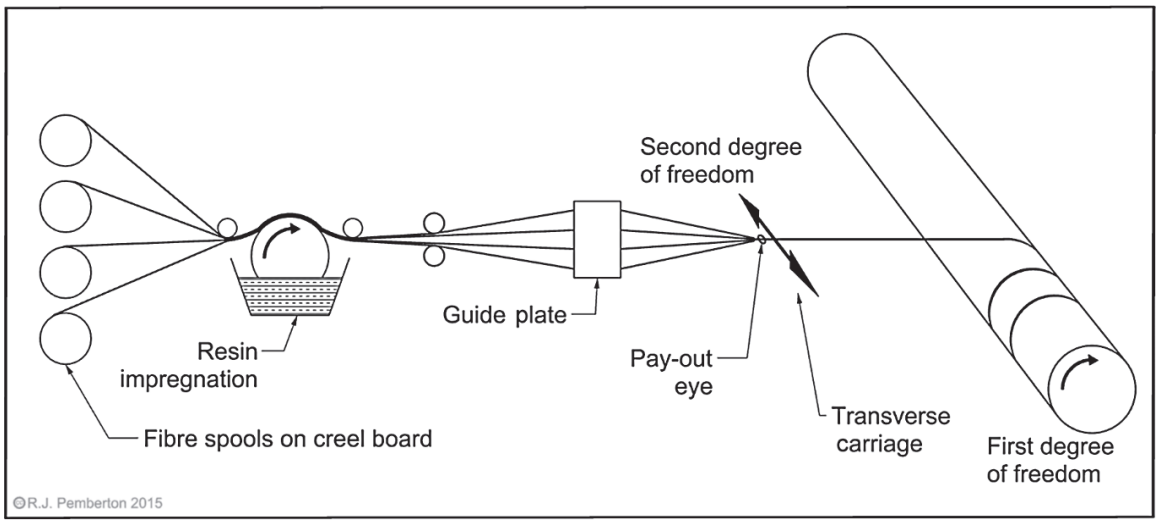

Figure 1.2 Filament winding of mast section

1.2 Scope of this thesis

Composite shafts and other composite cylindrical structures are gaining more and more ground in the marine and other industries. Crucial aspects that need to be addressed in such cases are the strain measurements, mainly for stress analysis of the structure which in turn is related to Structural Health Monitoring of the structure, and the torque measurements of driveshafts which are necessary for the power measurement that is delivered to the propeller of the ship. Strains comprise the effect of the application of torque on shafts and are practically easier to be measured than straightforward torque measurement. Thus, these two aspects overlap each other and commonly, when torque needs to be measured on shafts, strain measurements precede.

In the context of this thesis, methods for measuring strain and torque on rotating shafts, or on cylindrical structures in general, are presented. Emphasis was given on applications of rotating driveshafts made of composite materials wherever that was possible. Both conventional and novel methods that are still in laboratory level are presented. In the next sections of this chapter, some general information and definitions about SHM are given, which is one of the main fields

that strains sensors are used. Basic principles of common techniques that are used such as Strain Gauges and Optical Fibers are also presented. Specific aspects when it comes for application of such techniques in composite material structures are also discussed. In Chapter No. 2 methods that are used for strain and torque measurement on shafts are given. It is categorized based on the specific technique that is used, namely Strain Gauges, Fiber Optic sensors, Twist Angle measurement and other methods such Surface Acoustic Waves (SAW), Digital Image Correlation (DIC) and more. Great emphasis was given in the way that the measurement signal is transmitted contactless from the shafts to the stationary equipment of the measuring system. Two torque meters that are owed by the Laboratory of Marine Engineering (the T10F flange from HBM and the portable, non-contact TorqueTrak 10k (TT 10k) from Binsfeld) are also presented. In Chapter No. 3 calculation of the equivalent Young's modulus in the hoop direction of a specific carbon-epoxy shaft obtained by the Shipbuilding Technology Laboratory was made. Split-disk test was also made according to ASTM D2290 on ring-shaped specimens, which were from a previous used identical shaft, in order to get an experimental value of the Young's modulus. These values were used in the analysis of the results of the static torsional test of this shaft that was conducted and presented in Chapter No. 4. During this test TT 10k torque meter was attached on the CFRP shaft. The main aim of this test was to examine whether it is feasible to use this device on composite shaft which was done for the first time in the author's knowledge. Results from the analytical solution of a model of the shaft created in ANSYS simulation program were also obtained for comparison to the experimental results. Buckling modeshape estimation was also made for that purpose. Conclusions and recommendations for future work are finally given in Chapter No. 5.

1.3 Structural Health Monitoring

1.3.1 Definition - Introduction

According to (Staszewski et al. 2004), health is the ability to function/perform and maintain the structural integrity throughout the entire lifetime of a structure, monitoring is the process of diagnosis and prognosis, and damage is a material, structural or functional failure.

In this sense, **Structural Health Monitoring (SHM)** is defined as a load monitoring and damage detection and identification (diagnosis) technique for structures. Its primary aim is to provide a diagnosis of the state of the structure as a whole, of the different parts constituting this structure and of the materials condition. SHM is based on a comparison between two different states of the structure, one of which is assumed to represent the initial undamaged state and the second may involve damage. Damages can change the condition of the structure, the structural materials and the geometric properties either in short or long timescales and length scales. Thus early detection of damages can prevent sudden loss of the structure therefore leading to increased safety, extended operational limits and reduced maintenance costs (Ibrahim 2017). SHM also provides prognosis (prediction of the evolution of damage, the residual life, etc.) of the structure

with the aim that the state of the structure must remain in the optimal working conditions specified in the design stage, although aging, environmental conditions and accidents can normally have negative effects.

SHM can be considered as an evolution of regular Non Destructive Testing methods (ultrasonic, X-ray, thermography and eddy current methods) and an improved way to apply NDT methods. This is partially true, but SHM is much more. NDT methods only allow the off-line testing in a local manner in space. Complicated and heavy equipment plus labor-extensive and time-consuming processes especially for large-scale structures are required. In addition, the accessibility of the areas to be tested may demand that the structure itself may need to be disassembled which further increases the maintenance costs (Cai et al. 2012). On the other hand, SHM can provide with real-time and on-line damage detection from in-situ sensors combined with intelligent algorithms to interrogate the structural health condition. Therefore, SHM involves the integration of sensors, possibly smart materials, data transmission, computational power, and processing ability inside the structures (Balageas et al. 2006).

SHM is employed on structures in many industries such as aerospace, civil, naval and of course to mechanical engineering structures (Singh et al. 2022). SHM becomes necessity due to some major benefits offered to end-users. Among others, most significant is the economic motivation as it offers constant maintenance costs and reliability. This is achievable due to performance-based (or condition-based) maintenance instead of periodically scheduled maintenance inspections. This reduces the labor needed or at least the unnecessary labor, the need to dismount parts of the structure for regular inspection for hidden defect and generally the human involvement. Thus human errors are minimized which further improves safety and reliability.

According to Glisic et al. (2007) five basic components, constitute a health monitoring system in general. These are presented in sequence below:

i. *Sensors*, which convert the measured parameter into a quantity able to obtain, save and analyze like an electrical signal. In this sense, they also called *transducers*.
ii. *Cable network*, which merely transfers the signal (or signals) from the transducer to the DAQ system
iii. *Data Acquisition system (DAQ)*, which gathers the data collected from the transducer via the cables and transform them into a suitable form for us to process, usually into digital data.
iv. *Data management system*, which efficiently save the acquired data to analyze later. Databases are nowadays mainly used for long-term use.
v. *Data analysis*, where conclusion and thus decision are made based on the analysis of the collected data.

A complete SHM system is presented in Figure 1.3. What mainly interests us in this thesis is the first part of the system which is related to the monitored physical phenomenon of the

structure and thus the appropriate sensor implemented. It should be mentioned here that several sensors of the same type, constituting a network, can be multiplexed and their data merged with those from other types of sensors (Balageas et al. 2006).

As this thesis is mainly related to shafts made of composite materials, it has to be mentioned that SHM scheme when applied to rotating reciprocating machinery (Farrar et al. 2013) is called *condition monitoring*. Therefore it deals with damage identification and generally the mechanical condition of the machinery and its parts such as bearings, shaft, and gear teeth (Ibrahim 2017). Different parameters are monitored and different technologies can be applied for condition monitoring which among others are: vibration monitoring, acoustic emission (noise) monitoring, thermography (temperature monitoring), oil monitoring, monitoring of the performance and efficiency of machine, shaft displacement monitoring and strain measurement (Goyal et al. 2018, Elforjani 2010). Strains measurement in general is a way for testing the physical condition of the materials when stresses and thermal loads can lead to fracture and usually strain gauges are utilized for that purpose although they are not appropriate for long-term use.

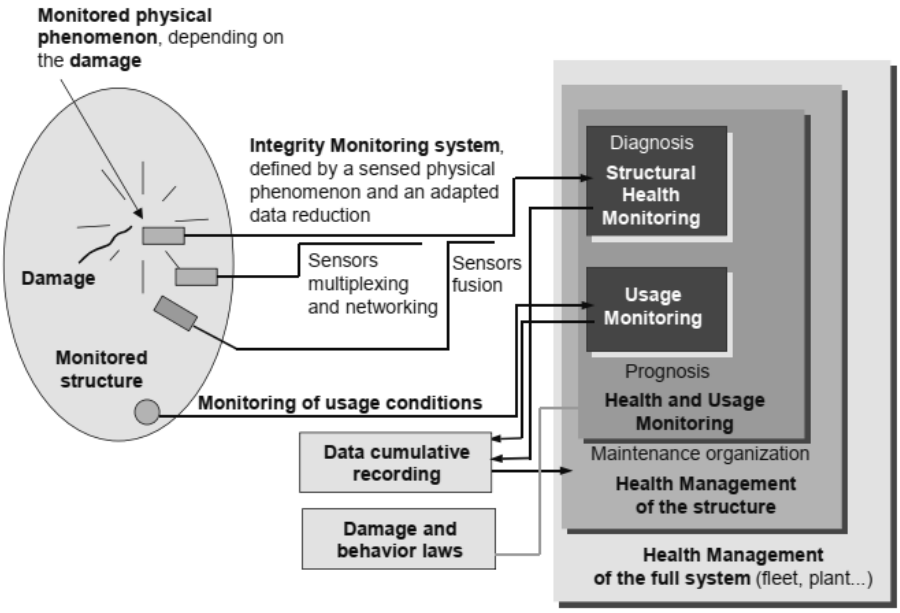

Figure 1.3 Principle and organization of SHM system (Balageas et al. 2006)

1.3.2 SHM on Composite Materials

The aforementioned also apply to structures made of Composite Materials. The demand for SHM on composite materials is mainly driven by their rising use in many industries. But due to the special properties and structure of these materials compared to other conventional materials (e.g. metal), the SHM schemes that are employed to these materials may need more and special consideration.

Common damages in composites are fiber breakage, matrix cracking, foreign object inclusions, inter-laminar voids, fiber waviness and wrinkles, fiber-matrix debonding and delamination between plies which if not detected and located in early stages may lead to severe degradation of the performance of the composite structure. Damages that commonly occur in composite material may not visible as they occur below the surface. This may not allow some traditional NDT methods to be applied (e.g. naked-eye inspections) although NDT can generally be used for these instances. But, as already mentioned before, NDT methods in general are not cost effective processes especially when examination of entire structures e.g. hull of ships, has to be made (Cai et al. 2012).

SHM can deal with these characteristics of composite materials as it gives the possibility for sensors to be integrated into the components during the manufacturing process of the composite (Balageas et al. 2006). On the one hand, this can be used to monitor the processing parameters in order to optimize the initial properties of the material in the stage of fabrication while on the other hand smart structures can be realized in this way, meaning structures designed with integrated actuators, sensors and signal processors and thus having more reliable damage monitoring system (Staszewski et al. 2004). Such structures can be fabricated to be sensitive and adaptable to environmental conditions. Smart materials have also been developed in some industries but these will not be further discussed in this thesis.

1.3.3 SHM methods categorization

SHM methods can be either *active* or *passive*. In the first case of the active SHM, structures are firstly excited by actuators appropriately attached on or embedded in the structure. The corresponding structural response, generated by the interaction of actuators and the structure, is then received by sensors in order to monitor the health state of the structure. In the other case, passive methods merely monitor the health state of the structure using appropriate sensors. Figure 1.4 vividly depicts the two ways a hypothetical experimenter can examine the structure.

SHM methods can be also divided based on other factors. As already mentioned before, timescale can be one of them. In that sense SHM can be performed either in the short term (typically up to few days), mid-term (few days to few weeks), long term (few months to few years) or during the entire lifespan of the structure (Glisic et al. 2007).

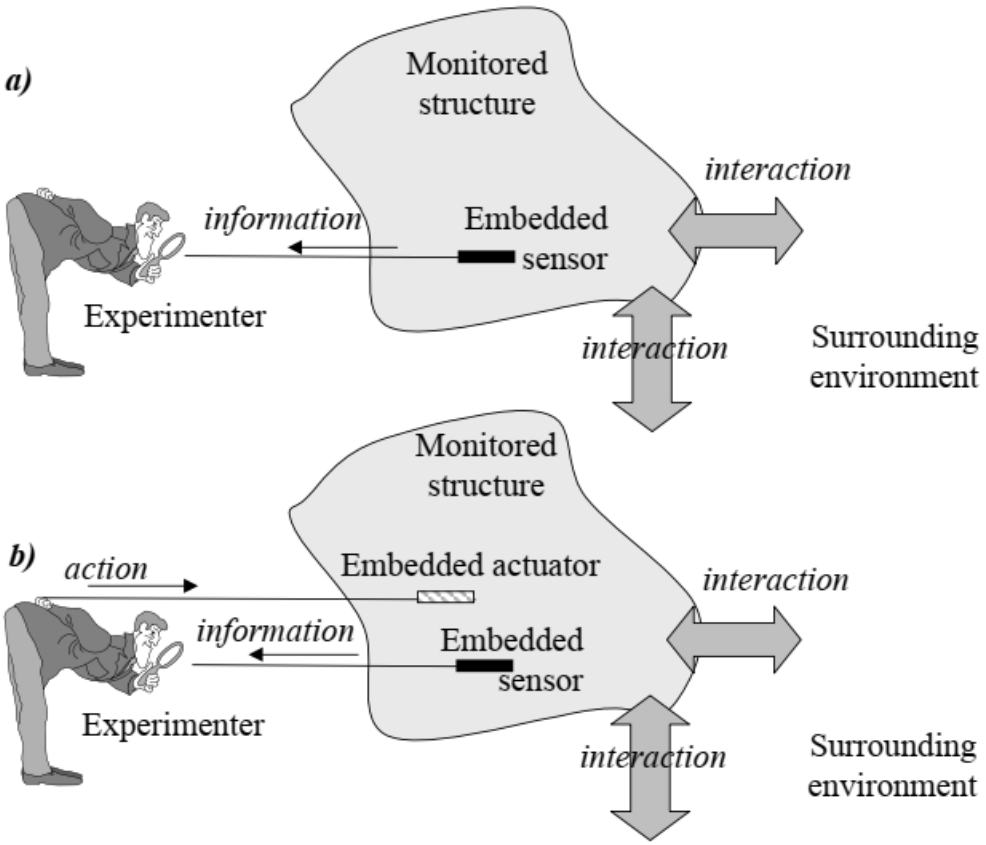

Figure 1.4 Passive (a) and active (b) ways of monitoring

Another factor is the length-scale, meaning that SHM can be applied either in a local spot, providing in this way information about the local behavior of the material, or at the whole structure. The gauge length of the sensors, meaning the distance between two measurement points of a point sensor, is critical in order to discern between local or global monitoring of the structure. Short gauge sensors are suitable for giving information about the local behavior of the construction materials at the expense of global structural behavior as they may miss anomalies and discontinuities larger than the gauge length. On the other hand, long gauge sensors fulfill this demand making them appropriate for global structural monitoring as they may cover tens of meters with micrometer resolution. Distributed sensors can also replace a chain of point sensors integrating in this way a long gauge sensor.

The most significant division between SHM methods though is related to the monitored parameters of the structure. These can be mechanical, physical or chemical. In Glisic et al. (2007) a representative table (Table 1.1) of the most frequently monitored parameters is given. Depending on which of these parameters is monitored, the appropriate sensors are deployed. Strain-based methods along with their corresponding sensors are mainly concerned in this thesis.

Table 1.1 Parameters most frequently monitored (Source: Glisic et al. 2007)

Mechanical	Strain, deformation, displacement, cracks opening, stress, load
Physical	Temperature, humidity
Chemical	Chloride penetration, sulfate penetration, pH, carbonatation penetration, rebar oxidation, steel oxidation, timber decay

In *Strain-based* methods damage detection is realized by monitoring the strains induced on the structure. This can be difficult and in occasions danger for the integrity of the structure. For example, a local crack may slowly grow up and therefore may not lead to significant changes in the strain distribution field, except the area nearby the crack, although operational and failure loads will be affected. Thus, sensors may not detect in time the growing level of the crack and fail to promptly warn about the catastrophic failure. Solution schemes are proposed in Valanduit et al. (2021) like strain mapping approaches with distributed sensors in plenty of spots around the structure accompanied by adequate pattern recognition algorithms.

In general, strain-based methods can be realized in two ways. In the first one, the strains measured on the structure in the initial undamaged condition can be used as the baseline for the future comparison with the values of strains measured during the lifetime of the structure. A-priori knowledge of the exact locations where damages will occur, before the structure is in service, is necessary in order to plan a monitoring system which takes into considerations these critical regions and thus appropriately install the sensor network. This can be accomplished with structural model, experimental tests or previous experience (Silva Munoz et al. 2008). In the other way, a theoretical structural model of the undamaged-healthy state is made and the real strains measurements are directly compared to the theoretical ones predicted from that model. This approach may not be feasible when it comes to complex structures where the creation and execution of the theoretical model can be difficult and time consuming.

As already mentioned before, it this thesis ways of measuring strains on composite structures and especially on shafts are presented with emphasis on SHM applications where that was possible. But firstly, an introduction to the most commonly strain sensors used is given. These are resistance Strain Gauges and Fiber Optic Sensors.

1.4 Strain Gauges

1.4.1 General

Strain Gauges (SG) are the most commonly used element for determining the strain developed on structures. The term SG (or metal strain gauge) has been mainly established to describe the devices that measure strains based upon the strain/resistance relationship of electrical conductors (metal alloy measuring grid), as this distinct from other type of gauge that measure strains such as semiconductor, vapor-deposited (thin-film), capacitive, piezoelectric, photoelastic, mechanical SG etc. (Hoffmann 1989). Main application domains of SG are stress analysis for structural

monitoring, with the SG acting as a sensor, and the measurement of torque in shafts for power measurement, where SG are used as the main sensing component of a transducer. The right SG can be selected based on the above categorization along with other parameters that are mentioned below, keeping in mind that there is no SG fulfilling the requirements of all possible implementations. A brief presentation of their principle and characteristics follows, mainly based on HBM publications (Hoffmann 1989) which provide complete theoretical and practical guides on SG principles and their use.

Operating Principle: In Figure 1.5 a typical schematic representation of a metal strain gauge is depicted. The connection tabs (solder tabs) are used for the connection with the electrical wires to the power supply and for the output signal. With the application of stress, the electrical resistance of an electrical conductor changes due to the deformation of the metal grid and the change of resistivity of the conductor's material which is owed to changes in microstructural level. eq. (1.1) describes this relationship:

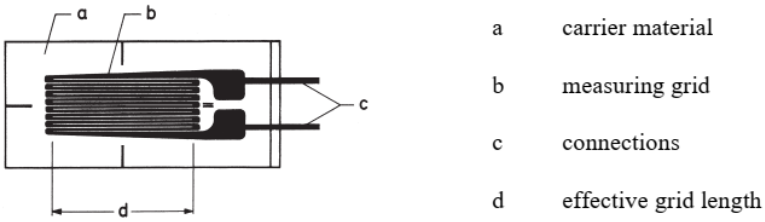

Figure 1.5 Typical schematic representation of a Strain Gauge

$$\frac{dR}{R_o} = \varepsilon(1 + 2v) + \frac{dQ}{Q} \tag{1.1}$$

where: R is the electrical resistance (Ohm), ε the strain, v the Poisson's ratio and Q the resistivity ($Ohm \cdot m$)

Alloys for which the value of the slope of their curves $S = \frac{\Delta R/R}{\varepsilon}$, in a $\frac{dR}{R_o} - \varepsilon$ diagram is equal to $2\frac{\Omega/\Omega}{m/m}$ at the elastic region, are generally preferred for the manufacture of SG. This quantity is called **Gauge Factor**, it is a characteristic of the SG which expresses the sensitivity of the SG and is symbolized with the letter ***k.*** For each SG manufactured, the nominal value plus a tolerance is specified on its package.

Measuring System: Due to the relatively small strains that a SG typically measures, the corresponding change in electrical resistance is small. Thus, for the accurate measurement of this change, SGs are commonly included in a measurement system, a representative scheme of which is shown in Figure 1.6. Briefly, the elementary components of this system are:

1. The sensor, which is the strain gauge placed on the structure and converts the mechanical strain into an electrical resistance change.

2. The measuring circuit is typically a Wheatstone bridge with the SG being an arm of it. The Wheatstone bridge principle is presented below and gives a clear view of how the strain change can be measured through the voltage output of the bridge.
3. SG and the bridge are passive components. In order to operate, energy supply is necessary which is passed with the form of electrical voltage.
4. Amplifier of the bridge voltage output is also typically used.
5. The output voltage display which can be either analog or digital. Recordings system can also be used in parallel when the strain data through time needed to be saved for future processing.

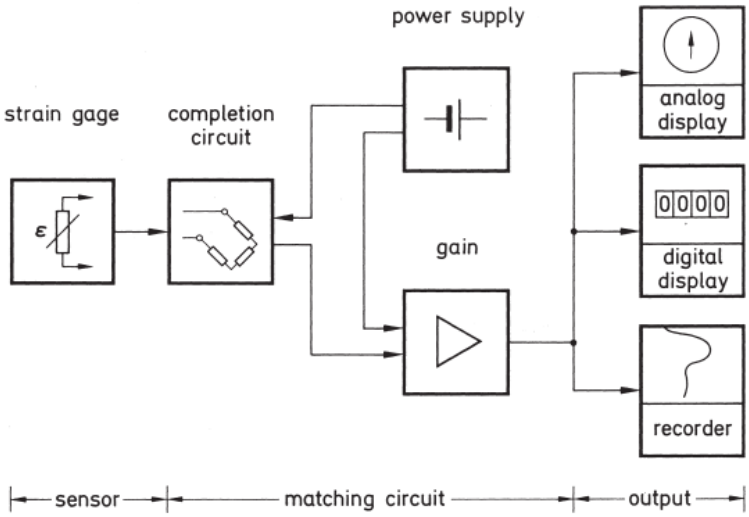

Figure 1.6 Diagram of a measuring system of a Strain Gauge

Wheatstone bridge: In general, Wheatstone bridge circuits are used to measure electrical resistance. In SG these circuits are used for the determination of the relative change of resistance. As shown in Figure 1.7, a Wheatstone bridge circuit consists of four arms (or branches), which are formed by four electrical resistances R_1 to R_4 respectively. The corner points 2 and 3 of the bridge are connected to the bridge excitation voltage V_s (power supply), which is usually a stabilized direct voltage, while corner point 1 and 4 are used for the bridge output voltage V_o, which is the measurement signal that corresponds to the change of the electrical resistance of the SG, thus to the change of strain.

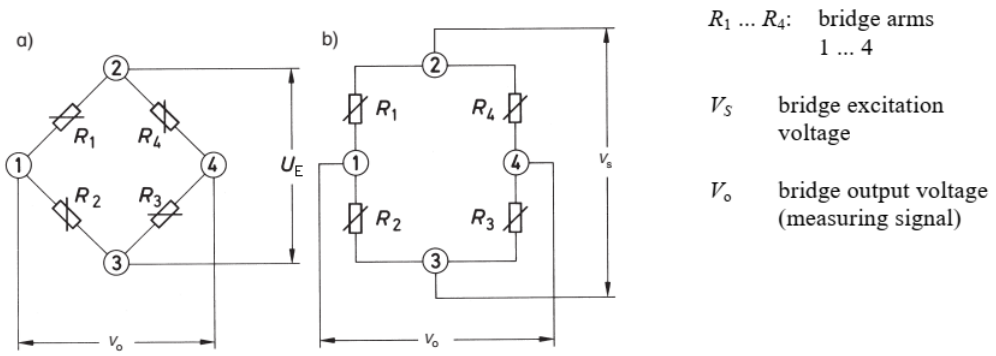

Figure 1.7 Two identical schemes of a Wheatstone bridge circuit. The first is the one widely used while the second is a simplified form

When a voltage is supplied through nodes 2 and 3, then, if the bridge is not balanced, meaning that the ratios $\frac{R_1}{R_2}$ and $\frac{R_3}{R_4}$ are not equal, then a different voltage will appear at nodes 1 and 4, which is the output voltage of the bridge. This is calculated from eq. (1.2).

$$\frac{V_o}{V_s} = \frac{R_1}{R_1 + R_2} - \frac{R_4}{R_3 + R_4} \tag{1.2}$$

In the case of a balanced bridge, i.e. when $\frac{R_1}{R_2} = \frac{R_3}{R_4}$ or $R_1 = R_2 = R_3 = R_4$, the above equation transforms to eq. (1.3):

$$\frac{V_o}{V_s} = 0 \tag{1.3}$$

In most cases where strains are measured with SG, the bridges are balanced with more or less deviation, thus eq. (1.3) is generally used. When the resistances R_1 to R_4 vary though, a voltage output different from zero appears. With the assumption that ΔR_i is relative small compared to R_i, from eq. (1.2) and after calculations (see Hoffmann 1989), the eq. (1.4) below is obtained which gives the relationship between the excitation and the output voltage.

$$\frac{V_o}{V_s} = \frac{1}{4}\left(\frac{\Delta R_1}{R_1} - \frac{\Delta R_2}{R_2} + \frac{\Delta R_3}{R_3} - \frac{\Delta R_4}{R_4}\right) \tag{1.4}$$

Taking into consideration that the $\frac{\Delta R}{R_o}$ fractions can be written as in eq. (1.5), the final form of the relationship between V_s and V_o is obtained in eq. (1.6).

$$k = \frac{\frac{\Delta R}{R_o}}{\varepsilon} \tag{1.5}$$

$$\frac{V_o}{V_s} = \frac{k}{4}(\varepsilon_1 - \varepsilon_2 + \varepsilon_3 - \varepsilon_4) \tag{1.6}$$

With the given polarity of the excitation voltage U_E, i.e. node (2) = negative and (3) = positive, the output will be:

- Positive potential (at node (1)) if $\varepsilon_1 > \varepsilon_2$ and/or $\varepsilon_3 > \varepsilon_4$
- Negative potential (at node (1)) if $\varepsilon_1 < \varepsilon_2$ and/or $\varepsilon_3 < \varepsilon_4$

where the strain values are in the algebraic sense and not the magnitudes.

In cases when stress analysis is conducted, commonly only one arm out of four will exhibit a resistance change. This arm corresponds to the active strain gauge while the others will then be formed from resistors of passive SG. On the other hand, in transducers application, where more accuracy is required, all the arms will be formed of active SG. Thus, the configuration of the bridge and the number of the active SGs depends on the specific application. In Figure 1.8, the most common arrangements are presented. These are quarter Bridge, half bridge and full bridge. Practically, all configurations have all of the four arms. The ones which do not consist of active SGs are replaced with fixed resistor. This is commonly accomplished through the other instruments of the measuring system (e.g. the amplifier).

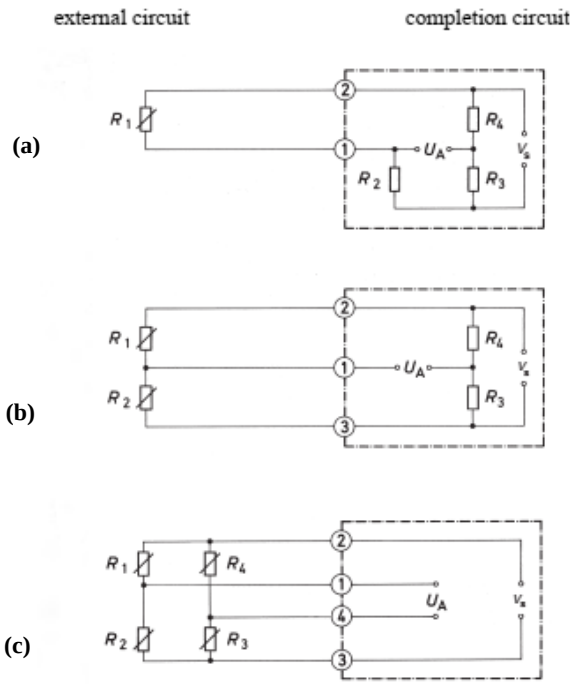

Figure 1.8 Typical arrangements of Wheatstone bridge: (a) quarter Bridge, (b) half bridge and (c) full bridge

Depending on the configuration of the bridge and the specific application, the algebraic values of strains of each SG in the eq. (1.6) can be either positive or negative depending on their relative

position. Thus, eq. (1.6) can be also written in the form of eq. (1.7), where ε_1 the strain from SG No.1 and B is called the bridge factor. For example, in the case of measurement on a twisted shaft (Figure 1.9), where four active SGs (full bridge) are placed in $\pm 45°$ angles with reference to the shaft axis due to the biaxial stress state, all the absolute strain values will be the same, thus $B = 4$.

$$\frac{V_o}{V_s} = \frac{k}{4} \cdot B \cdot \varepsilon_1 \tag{1.7}$$

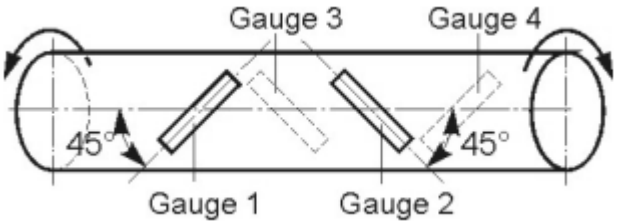

Figure 1.9 SG arrangement for measuring torsion on a shaft

Strain Gauge application: Next, some important factors are briefly mentioned which should be taken into consideration before every strain measurement task. When the user can a priori define them in order and on time, the whole process of choosing the right SG will lead to better and less expensive solutions:

1. Measurement problem (experimental stress analysis, transducer)
2. Mechanical conditions at the point of measurement (stress state, stress field topology, loading type)
3. Environmental conditions (duration of the measurement, temperature, disturbance effects like: humidity, oil, chemicals, pressure, E/M fields, external forces)
4. Electrical conditions at the point of measurement (measurement circuit, SG supply, cable)
5. Application conditions (component material, accessibility of the surface)

The bonding of the SG with the structure is also crucial so that the strains are transferred to the SG without losses. Commonly, the SGs are attached on the outer surfaces of the object to be measured. Adhesive provides the best solution for these cases and should be selected according to the manufacturer's guides. For composite material though, measurements inside the structure (through the thickness) can also be achieved, with the SG being embedded during the manufacturing process. More details on the application of SG on composite materials are provided in Chapter 2.

For the right selection of type of SG, a number of parameters must be previously known based on some basic criteria that are presented below.

Geometry - Multiple Strain Gauges:

- Linear SG, for one-direction measurements.

- T rosettes, for biaxial stress state with known principal directions and tension/compression bars.
- V-shaped SG, for torsion bars and for shear stresses occurring in shear beams around the neutral axis.
- Double linear SG, for bending beams.
- Rosettes with 3 measuring grids, for biaxial stress state with unknown principal directions.
- X rosettes with measurement grid axes at 90° to one another, for torsion bars and for shear stresses occurring in shear beams around the neutral axis.

Length: Choice of the right grid length is affiliated to the homogeneity or not of the strain field (thus the homogeneity or not of the material of the structure) and the available space on the measuring object. SG's sensitivity is not dependent on the grid's absolute length, but rather to each relative elongation. The main concern for the SG length selection is to cover the inhomogeneities of the underlying tested material (e.g. in concrete or composite materials). As the SG integrates the strains below its surface and the average strains are measured, the SG length should be large enough in order to avoid local strain concentration and peaks due to these inhomogeneities. Very small SGs should only be used where they are practically necessary e.g. if peak values are to be obtained or local strain condition (like in notches) need to be determined. A zero length grid would be appropriate for such use which of course is impossible although grid of 0.2mm length can be manufactured nowadays. In cases like this, problems of transferring the strain from the measuring object to the measuring grid arise along with other practical difficulties in attaching the SG and heat dissipation issues due to the small size of the grid. In inhomogeneous materials (like concrete and fiber-reinforced plastics) a long grid length can bridge these inhomogeneities and is proposed for transducers applications. In general, measuring grid lengths of 3 or 6 mm (0.118 or 0.236 inches) represent a good solution.

Electrical Resistance: Electrical resistance of the SG is called the difference in electrical resistances between two metal leads, solder tabs or cable ends for connecting the measuring cable. Electrical resistance can vary offering the biggest group of different types of SG. Typical values are: 120, 350, 700 and 1000 Ohms. Three factors are significantly important is the selection of electrical resistance of the SG (HBM-Strains):

- compliance to the instrumentation to which the strain gage is connected
- effects of the interconnecting wiring between the strain gage and the instrumentation
- the electrical loading that the SG can withstand

120 Ohm and 350 Ohm are the most commonly used values. The 350 Ohm SGs have an increased use in transducers as they provide less heat dissipation, due to the lower current, along with a minimum zero shift in the amplifier (when combined with high voltage supply) due to the insensitiveness to ohmic resistance in the connection lines to the amplifier. This comes in

expanse of the receiving interference that these SGs may have which can lead to the formation of antennas.

Excitation Voltage: Play an important role because of the heat dissipated by the SG. It has to be noted that the supply voltage is applied to the whole Wheatstone bridge. For that reason, in general high values must be avoided or only applied to materials with excellent heat conduction characteristics (e.g. steel). In contrast, in composite materials (e.g. fiber-reinforced) SG should be applied with smaller values of excitation voltage (or used with an impulse-like manner) due to their poor heat dissipation.

Environmental issues: External conditions affect the measuring point and the SG itself. To name a few: temperature, humidity, hydrostatic pressure, vacuum ionizing radiation, magnetic fields are some of them. It has to be mentioned that these factors should be also taken into consideration during the storage of the SGs.

1.4.2 Strain Gauges in composite materials

As in any other structure, SGs in composite material structures are mainly used for stress analysis (SHM) and for transducer applications as for torque measurement on a rotating shaft. In addition, SG have been used in a number of bench experiments for determining the material properties of standardized test samples made of composite materials. To name a few: bending tests (3-point, 4-point), tensile tests, shear tests (interlaminar), open hole/filled hole, compression after impact, compression tests, notched-bar impact-bending tests, hole-bearing tests, split-disk test etc. The last one, in which the apparent hoop tensile strength and hoop elastic modulus are determined, was conducted in this thesis and presented in Chapter 3.

The general aspects arising when SGs are applied on composites and the differentiations to the cases when metal structures are strain-measured are well known in the scientific society approximately the last three decades (see Tuttle 1984, Perry 1987, Horoschenkoff et al. 1996 and Vishay Micro Measurement 2010). According to them the mechanical, thermal and chemical properties are the principal differences, compared to metals, which strongly affect experimental stress analysis. These properties need to be taken into account so that right selection and use of SGs be made. Thus, the need for user's expertise is highly important.

The elastic modulus is the predominant property that poses problem in the SG application as far as the mechanical properties are concerned. In general composite structures have a relative lower elastic modulus compared to steel structures, especially in specific directions (e.g. transverse to a unidirectional laminate). This results in higher strain levels which lead to high demands for the SG bonding and wiring procedures. This may also have impact on the transfer of the strain to the grid which may be incomplete. In addition, Poisson's ratio can also affects the transverse sensitivity of the SG and as a result correction may need to be applied. Lastly, the temperature dependence of the mechanical properties (creep phenomena on composite materials) along with the non-linear stress/strain characteristics (particularly in shear) should be taken into consideration.

Thermal properties have also an important effect on SG on composite structures. Thermal coefficients of expansion are usually larger in unreinforced plastics compared to metal, and in unidirectional reinforced composites differ between longitudinal and transverse direction. This directionality can cause difficulties when it comes to compensation or correction for the thermal outputs of the SG measurements, especially in environments where temperature varies and/or when SG rosettes are used and the thermal output differs between grids. Thermal conductivity in composite can be 2-times lower than that in metals and thus, the heat produced by SG cannot be easily dissipated in the structure as in metals. SG size, resistance and excitation voltage are affected in that way, along with the placement of pre-attached wired SGs, which are generally preferred in cases of composite structures.

In addition, moisture on the environment can also affect SG measurements in two ways: either by dimensionally changing the composite structure (like in thermal output), which leads into a false hygroscopic expansion/contraction, or by altering the material mechanical properties. The last one calls for special consideration in the selection of the SG type, adhesive and protective coating.

The last crucial factor is the chemical properties. The main concern here is the potentiality of reaction between the composite material and the chemical that are used for cleaning (solvents), bonding (adhesives) and protection (coatings) of the SG. Moreover, abrasion of surfaces may not be permitted in surface preparation procedures, and at times, due to the chemical properties of the the bonding between SG and the composite may be difficult to achieve or maintain, composite.

After the determination of the various parameters that mainly affect the SG selection, attachment and performance, the type of SG should be selected from a variety of SG designs that are available (Tuttle 1984). The SG parameters that should be then designated (which are also presented previously) are briefly discussed below for the case of composite materials:

Gage Length: In composites, the SG length should usually exceed the fiber distance by a minimum factor of 5 (HBM proposes the 6 mm and 10 mm as the most popular solutions). Similarly, the gage width should enclose several fibers. If strain gradients due to local strain peaks are needed, SG chains can be used. In general, SG of 3 mm length or more exhibit better stability and larger strain range. The grid power density (power dissipation per unit of grid area) should be also taken into account in the length selection. A relatively big gage length may also compensate when incomplete transfer of the strain from the underlying layer to the SG occurs, for example when the SG is placed at a “weak” direction (e.g. transverse to the fiber direction in a uniaxial laminate)

Resistance: As far as the gauge resistance is concerned, it is generally admitted that, due to the low thermal conductivity of composites, a high resistance value (350 Ohm or greater) is preferred in order to minimize the heat dissipation during operation. Of course, the whole combination of gauge resistance, grid length and excitation voltage should be selected in that way so that the temperature rise is kept as low as possible and to ensure stability.

Excitation Voltage: The power from the voltage applied in the SG is getting lost in the form of heat (Figure 1.10), while a negligible fraction of the power input stays in the output of the circuit (Vishay Micro Measurement 2010). Due to the low conductivity of composite, the heating-up of the sensor and the components are inevitable and excessive high temperature can arise which can cause problems that affect the SG proper operation (loss of self-temperature-compensation, hysteresis and creep phenomena, zero load instability). Thus, in order to ensure stability on the measurement process (meaning that the heat flow is equal to the power applied and does not exceed it), excitation voltage should be kept low. Of course, as it has been mentioned before, the selection of excitation voltage should be in conjunction to the gauge resistance, grid length, backing and adhesive material, environmental temperature etc. Having that in mind, a small voltage value is preferable, with the HBM proposing a value of less than 2.5 V for poorly cooling materials, such as composites. A small heat-up phase prior to the application is also recommended.

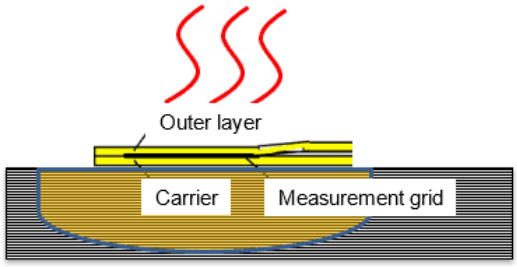

Figure 1.10 Power loss in SG in the form of heat

Backing and foil material: In general, a low modulus backing material (e.g. polyimide) is considered as the best solution as it offers several advantages such as: flexibility due to lower gage stiffness and (in the case of high-performance composites) resistance against premature failure in the event of local fiber or matrix breakages. As far as the foil material is concerned, the strain range is the predominant parameter that affects this decision. Annealed constantan is commonly used as it offers high elongation, although this is not always the case. Karma-type nickel-chromium alloy is also an option, which offers a wider temperature operation range, higher gauge resistances and better corrosion characteristics, at the expense of the creation of solder pads, which is more difficult in that case.

Another important aspect is the thermal output compensation for which various techniques have been established such as self-temperature-compensation (S-T-C) SGs (although may not be practical on composite due to directionality), dummy gauge in a half-bridge arrangement or conventional compensation when the relationship between temperature and thermal output is known from experiments (Ajovalasit 2011).

Another aspect is the pre-wired SGs which are generally preferred on composites, mainly for the reason that the creation of soldered pads (and the potential damage of the composite structure) is avoided in that way. The procedure to place these SG is in general the same as for any other material and should always be done according to the manufacturer.

The user should also pay attention at surface preparation (cleaning, roughening), bonding and protection procedures and to SG misalignment. Manufacturers' guides should be consulted for detailed information. Surface preparation includes the cleaning and roughening procedures. There are no standard cleaning solvents and procedure for composites in general as they are material dependent. Of course, the reaction of the chemicals with the composite should be avoided. Ways for surface abrasion that are common in metal (e.g. abrasive paper) are also applicable (except high-performance composite) if only contamination of the surface is prevented. As far as the bonding adhesive is concerned, cyanoacrylate adhesives are appropriate for short term applications, while conventional or special-purpose (e.g. for high operational temperatures) epoxy adhesives can also be used. Unfilled adhesive is the standard way for gage bonding while filled can also be used in occasions.

SG angular misalignment from the desired measurement direction also affects the strain results. By contrast to the isotropic materials, misalignment in the case of orthotropic may produce greater errors in the strain results for the same angular deviation due to the fact that the principal strain directions differ from the principal stress directions. Misalignment errors can also depend upon the ratio of the maximum and minimum principal strains and the misalignment angle from the intended axis, just like in isotropic materials (Tuttle 1984). The above observations mainly apply for the case of single grid SG in CM where the correct placement is usually questionable and difficult to achieve. On the other hand, angle misalignment in SG rosettes does not play such important role, but the exact position should be known for data-reduction processes afterwards or for estimating the strains along the principal axis of each lamina of the composite (Ajovalasit 2011).

Another aspect is the transverse sensitivity, which refers to the undesirable responding of the SG to strains perpendicular to each major measurement axis. Grid geometry, gauge alloy material, gauge backing and other manufacturing properties affects this phenomenon. Due to the nature of orthotropic materials, errors in strain data due to transverse sensitivity are greater than from isotropic materials, and under certain circumstances can even completely dominate the strain output results (Tuttle 1984).

1.4.3 Strain Gauges embedded in laminated composites

Integration of SG inside laminated composite materials had been initially proposed during 60s. Since then, many researchers have investigated this subject and great developments have been done. The main aim of SG integration in CM is the determination of the internal strain field for structural monitoring. With this technique, interlaminar strains can be measured, which is important in order to monitor the performance of each component in the composite and thus predict and prevent critical events (e.g. types of internal failure such as delamination and fiber breakage) that may occur, during in-service conditions (Belhouideg & Lagache 2017, Aloisi et al. 1998). Residual stresses can also be specified in that way. Here, some general aspects encountered during application of this technique are briefly discussed, such as the integration

procedure, its feasibility and reliability, along with the interaction of the SG with the composite and the effects this may have on the integrity and mechanical strength of the structure.

Typical SGs that are commonly employed for integration are shown in Figure 1.11. The feature that distinguishes them from standard SG is the vertical pins which are used for the external connection with the leads. These pins have to be insulated in order to avoid interaction with electrically conductive carbon fibers and to overcome the mechanical and thermal stresses at the interference of the adjacent laminae. For the external connection with the leading wire, it is recommended that the insulation layer should be removed. This can be done by mechanically shaving it off with a cable stripper (Horoschenkoff et al.1996). In Schnack et al. (2004), it has been demonstrated that in the case of carbon fibers/epoxy laminated, the whole gauge itself should be insulated and not only the pins. 'Kapton' foils are proposed which slightly increase the thickness locally though. In the same paper, a polyamide carrier (backing), on which the SG is glued, is used. In that case only the one side of the SG could be insulated. Other special characteristic of this SG is that pins are placed at a distance from the grid, as can be seen in Figure 2.2. This is done so as the fibers of the adjacent laminae that are displaced from the pins, do not affect the strain distribution and thus homogeneous strain field is produced around the grids. Furthermore, strain relief areas exist, with which the stresses acting on the pins are prevented to be transmitted to the grid.

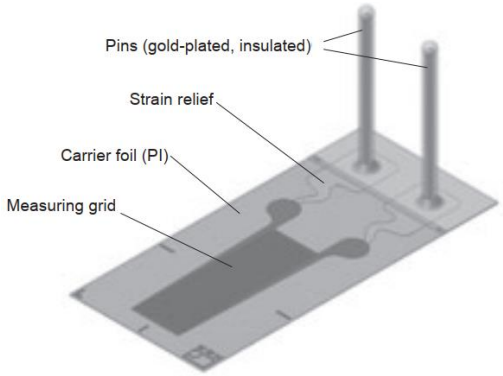

Figure 1.11 Typical SG for integration (Horoschenkoff 1996)

Pre-wired SGs, with their leading wires lying in-plane with the laminae, should better not be used for integration into composite, mainly due to the potential effects on the structural integrity and the mechanical properties of the laminate (leading wires are "treated" as defects, especially in multiple SG arrangement), although this has been proven that is not always true (see Kim et al. 1992). Furthermore, the effects on the measured strains may also be disrupted (structural deformation will pass to the leading wires and change their resistance which will affect the measured strains). SG with vertical pins, in contrast, offers some competitive advantages (Horoschenkoff et al. 1996). To name a few, it does not damage the fibers as they pierce the adjacent laminae, holds the SG firmly attached to each position due to the pins piercing and make easier the handling due to the absence of leading wires.

When it comes to positioning the SG, alignment is crucial, as for every SG in composites. In that case though, alignment marks cannot be drawn as in the case of surface-mounted SG. Other techniques can be used in the production process such as: conventional measuring tool (angle gauge and ruler), preparing an installation template and inserted it in the molding tool, stretching threads along the structure or use laser projects. Similarly, the SG must be also held in place when the dry fibers are placed. This can be down in two possible ways (Horoschenkoff et al. 1996): either with binder powder at the SG areas, which is a thermoplastic material that must be first melted and then cooled, or with special spray adhesives (the so-called tack sprays). Lastly, after the installation, the best way to connect the pins to the leading wires is soldering as schematically depicted in Figure 1.12. Appropriate protection of the connection point should be also provided.

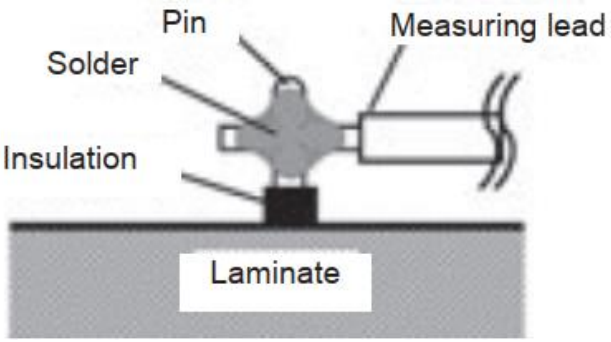

Figure 1.12 Soldering the vertical pins

Another crucial issue is the potential mechanical degradation of the composite structure due to the presence of the integrated SGs (and the leading wires that in some cases may travel through the composite laminae). Delamination is a potential side effect that the embedment of the SGs can provoke. For that reason, the effects of the integration of SGs inside composites on their mechanical properties have been investigated in literature. An important factor that can be detrimental is the relative larger size of the embedded sensors to the typical scale of the composite layers (Schaaf et al. 2005). In almost all cases encountered though, the embedment of SGs did not result in significant defects. For bending tests, it was also observed an increase of the flexural stiffness and strength which was attributed to the local increase of the thickness of the composite specimen due to the presence of the SG (Belhouideg & Lagache 2008). As far as the reliability and the accuracy of the strain measurements of embedded SGs, again no predominant deviation from measurements of surface attached SGs has been observed in general

Lastly, it is mentioned that an embedded SG between two laminae is subject not only to longitudinal and transverse stresses (relative to its principal axis) but also to perpendicular to its plane, just like if hydrostatic pressure was applied to an externally bonded SG. The measurement error that induced in that way though, is normally small (around 0.2% according to

Horoschenkoff et al. 1996). In Ajovalasit (2005) is also reported that transverse sensitivity and pressure (perpendicular) sensitivity are coupled.

1.5 Fiber Optic Sensors

1.5.1 General

Initially, optical fibers were commonly used in telecommunication for data transmission from the 1970s. Nowadays, more industries have taken advantage of optical fiber such as communications in general, including Internet and military needs for data transmission, power delivery for laser cutting, welding, drilling, and lighting in automotive industry and for health application. In the last decades though, sensing applications of optical fiber have faced a huge rise up, making Fiber Optic Sensors (FOS) an equivalent, and in some case a predominate competitor along other traditional sensors like SG. The better resolution and the absence of a huge network consisting of wires etc. have provided big advantages over SGs (Arena & Viscardi 2020). Their small compact size along with their embedding capabilities makes them an important candidate for the goals of a monitoring system, composite materials structures included. FOS main application areas, especially on CM, are strain and/or temperature measurements, curing of composite structures and vibration, humidity, delamination and cracking monitoring (Ramakrishnan et al. 2016). The have also found widespread application in civil structures like building, bridges, dams, pipelines, tunnels, heritage structures and aviation and aerospace structures for continuous monitoring. For detailed description for each of the above application areas reader should refer to the literature cited (Glisic et al. 2007, Kotsidis 2012)

Optical fibers and their working principle are a complicated issue involving electromagnetic theory. In addition, different models can be used to explain the procedures taking place during operation of an optical fiber and light transmission (Balageas et al. 2006). In general though, their working principle can be easily explained through the basic laws of optics. Optical fiber is a cylindrical waveguide where light can travel. Commonly used material is silica while plastic optical fibers also available in market. The silica core is cladded by another material (may also be from silica) which has a slightly lower refractive index than the core's one (around 1.46). Light beam traveling inside the core can constantly reflect on the boundaries of the core and the cladding (Figure 1.13), in accordance to the Snell's law, only if the incident angle of the ray is higher than the critical angle (defined by the properties of the two adjoining materials). For environmental protection an additional external coating is used (from acrylate or polyimide) (Staszewski et al. 2004).

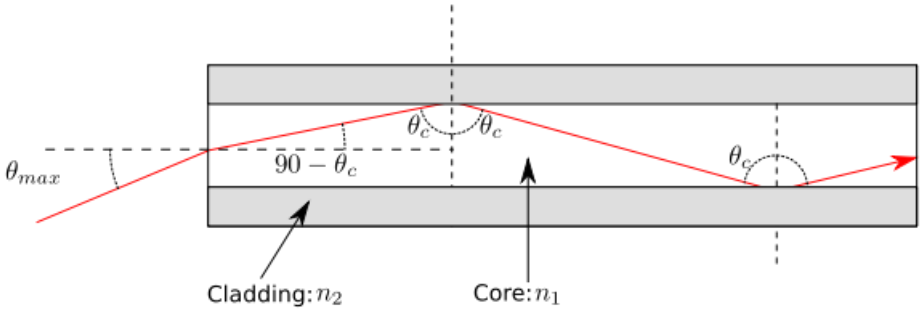

Figure 1.13 Schematic representation of the working principle of optical fiber

1.5.2 Optical Fibers types - Fiber Bragg Gratings

1.5.2.1 General categorization

Optical fibers can be categorized in groups based on a variety of criterions such as number of modes, technology etc. In that way, optical fibers are firstly divided into two groups based on the number of modes allowed to transmit:

1. *Single Mode*, which usually have small core (around 10 μm) (Balageas et al. 2006) and allow only of mode (one path) of light to travel inside their core as their name indicates. Suitable for long distances transmission of information.
2. *Multimode*, with two or more modes (usually two). They have larger cores (30 to 100μm) (Balageas et al. 2006), are better for short distances and are mainly used in sensors deploying intensity of light (see intensity-based FOS below).

Furthermore, optical fibers used in sensing applications can be either:

1. *Intrinsic*, which utilize only a small length of the fiber for sensing the desired parameter. This portion of the length of the fiber is sensitive to environmental changes which affect the measuring parameters e.g. strain.
2. *Extrinsic*, which utilize an external sensing device (head) while the fiber acts merely as the transmission path which delivers the light.

1.5.2.2 Categorization based on the technology used

The most significant categorization though, and the one mainly concerns us, is based upon the *mechanism* exploited when optical fibers are used as sensing elements, meaning which optical parameter of the light wave (phase, intensity etc.) is affected and changed by the external-environmental action monitored (e.g. strain) (Balageas et al. 2006, Staszewski et al. 2004).

***Intensity-based* sensors**: The simplest FOS and among the older ones used. Changes in the intensity of light give information about the measured property. They consist of a light source, an optical fiber and a photodetector. They can be used to measure small distances, like displacements of a shaft, and for damage and cure monitoring. Due to their working principle,

they may introduce errors to the measuring parameter due to losses or variations of the light intensity either in the optical fiber path or in the emission source.

Phase-modulated sensors (interferometers)*:* Due to the fact that no direct measurement of phase in optical wave is achievable, interference of two different waves is used. In this type of sensors a light beam is split into two distinct ones by a coupler (like when light splits in a conventional mirror). These two beams follow different paths as they travel through the fiber and consequently have different phases due to the delay of one beam to another. The one act as the reference wave and the other is sensitive to the measured property. When recombined, the interference produced will be directly related to the measured parameter. The output light intensity may even be zero if the phases of the two waves are opposite and do not match. This type of sensor can be extremely sensitive and precise e.g. for distance measurements, which consequently makes it convenient for laboratory use if any perturbation of the phases is to be detected. Well known sensors of this type are SOFO, Mach-Zender, Michelson and Fabry-Perot. The former one (Figure 1.14) which is a special design, reflection occur at the end of the optical fiber at the Fabry-Perot cavity and the two created beams travel back and interfere. These sensors can be used for strain measurement.

Polarimetric sensors: Changes in the polarization of the light travelling inside the optical fiber as a result of effect of stress, strain pressure or temperature on the fiber is received by the sensor and related the desired property to be measured. Embedment into CM structures is possible for strain/temperature measurements but not for local points as the averaged strain along the entire length of the fiber is measured.

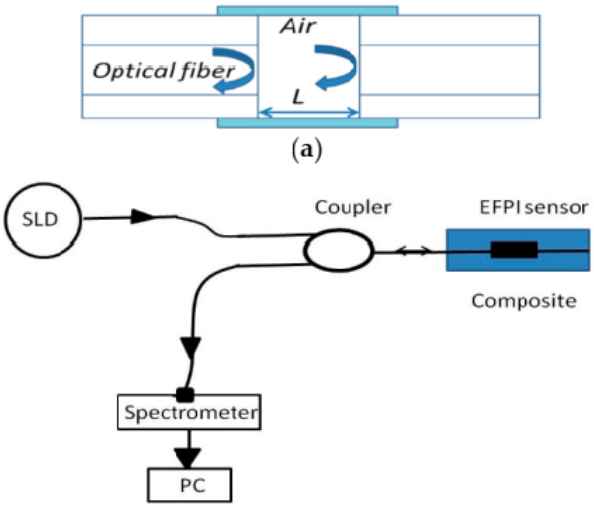

Figure 1.14 Extrinsic Fabry-Perot sensor

Back scattering sensors: This type of sensor use a technique called Optical Time Domain Reflectivity (OTDR) in which the time for a light beam to travel since it was pulsed into a fiber and a portion of it to scatter back is measured. This time gives information about the distance

between the point where the pulse began and the point where scattering occurred. In this way useful information can be obtained about fractures, good integration of the fiber and generally the condition of the structure and the fiber in specific points. These sensors are used with long length fibers but may exhibit low spatial resolution. Averaging of the signals of multiple pulses or light amplifiers may be necessary as a count-measure to compensate for the weakness of a single back-scattering light beam and to enhance the optical signal. Raman-scattering and Brillouin-scattering are well known back scattering phenomena which are exploited in such sensors for specifics parameters measurements like strain and temperature (see Glisic et al. (2007) for more).

Wavelength based sensors, or Fiber Bragg Gratings (FBG): Last but not least, wavelength based sensors are the most significant sensors used predominantly as strain sensors since their first appearance in 90's. As the name indicates, the crucial parameter is the wavelength of light wave which is analyzed to get information about the strain or other desired parameter. This is achieved by altering the refractive index of the core of the fiber at specific point along the length of the fiber and creating a short area of periodic modulation of the refractive index, something like a series of parallel reflective mirrors (gratings) printed on the fiber's core, which range from low to high refractive indexes. Light passing through the fiber and the corresponding area will coupled with the referenced gratings and reflect back only these wavelengths that are directly proportional to the spacing of the gratings.

Fiber Bragg Gratings (FBG) are well known sensors utilizing this technique. In these sensors, the central wavelength reflected from the gratings is given by the simplified form of the diffraction law in eq. (1.8), first given by Bragg (Balageas et al. 2006):

$$\lambda_B = 2\bar{n}\Lambda \tag{1.8}$$

with $\bar{n}$ being the mean refractive index and Λ the grating pitch.

Figure 1.15 schematically illustrates the way FBG works along with the pitch Λ and the reflected wavelength λ_B. In the spectrum the reflected light is observed as peak which is shifted when e.g. strain is applied and the pitch Λ is altered. On the other hand, in the transmitted light a gap is found. Through this simplified way, when the monitored structure is under load, strain in the area of the grating can be calculated (Staszewski et al. 2004). The above sensitivity to strain, through change of the pitch of FBG, can be expressed in the below equation (1.9) which gives the wavelength shift for a ΔL change in the length of the fiber (Ramakrishnan et al. 2016). The same applies for changes in temperature ΔT which also alters the grating pitch due to thermal expansion of the fiber. This is given in eq. (1.10):

$$\Delta\lambda_\varepsilon = \lambda_B \cdot \left(\frac{1}{\Lambda}\frac{\partial\Lambda}{\partial L} + \frac{1}{\bar{n}}\frac{\partial\bar{n}}{\partial L}\right) \cdot \Delta L \tag{1.9}$$

$$\Delta\lambda_T = (\alpha + \beta) \cdot \lambda_B \cdot \Delta T \tag{1.10}$$

where α is the thermal expansion coefficient ($0.55 \times 10^{-6}/℃$ typical for silica core) and β ($6.6 \times 10^{-6}/℃$) is the refractive index variation with temperature.

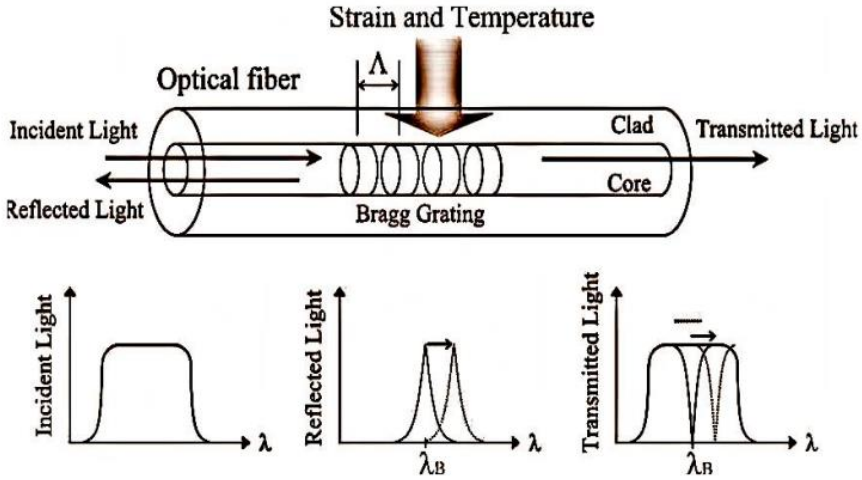

Figure 1.15 Bragg Grating Sensor (FBG)

Strain and temperature are predominant parameters measured by conventional FBG sensors, especially for CM where embedment of the optical fibers gives exceptional advantages. But this also has a negative aspect which is related to the cross-sensitivity between these two parameters. The magnitude of the effect of temperature depends. In Balageas et al. (2006) for example a shift of $1nm$ per $100℃$ for a central wavelength FBG of 1300nm is suggested. This needs to be compensated for accurate strain measurement as it is the common case in Strain Gauges. A special design of FBG sensor has been used for this reason called tilted fiber Bragg Gratings (TFBG), with the gratings being in angle in respect to fiber axis, separating, in this way, the temperature from the strain effects at the spectrum indications.

Plenty variations in the design are reported in literature specifically adjusted to the needs of application and the reader should refer to them for more information (see Ramakrishnan et al. (2016) and Fu et al. (2019) among others). For example, special FBG written in micro-structured fibers are reported for the cases when multi-axial strain is present in the structure and conventional FBG sensors are not able to distinguish them. These sensors can simultaneously measure these strains but in expense of cross-sensitivity between strain and temperature. Other designs mentioned in the same papers are phase-shifted FBG sensors for acoustic emission measurement and also for extremely small strain changes, and last, polymer FBG instead of classical silica fibers for higher temperature sensitivity, large strain range and lack of coating.

1.5.3 Fiber Optic Sensors in Composite Materials

The increased use of structures made of CM and the consequence demand for monitoring has made FOS a favorable option. FOS fulfills the demand of an SHM system for diagnosis, as well

as the goal of condition monitoring. This is possible due to some of their special merits (Staszewski et al. 2004), (Ramakrishnan et al. 2016), (Glisic et al. 2007):

- small size with diameter usually in the range 125–500μm
- embedment inside the structure
- low weight
- immunity against electromagnetic (EM) interference and electrical noise due to their non-electrical nature which makes them the appropriate solution when electromagnetic field, radio frequency (RF) and microwaves (MW) are present
- immunity to to corrosion
- naturally explosion proof which allow them to work in explosive environments
- multiplexing capability
- very high sensitivity
- wide operating temperature range
- low cost
- long distance measuring capability (tens of kilometers in magnitude) without the necessity of interfering other component between sensors and receivers

The greatest advantage of FOS is their embedding capability in CM. It offers great advantages in SHM, giving in that way the potential to the composite structure to act similar to the human nervous system, thus realizing the concept of smart material that has been mentioned before. Embedment offers better protection to the optical fiber itself from external conditions, augmenting the active lifetime of the monitoring system along with the potential of monitoring parts difficult to reach or to place sensors with their wirings, like internal structural areas. The lack of wirings at the outer surface of the structures also argues in favor of the embedding concept not only from a cosmetic point of view but also when clean surface are necessary like in aircrafts wings.

Every strain monitoring scheme follows in general the steps shown in Figure 1.16 in order to relate the output of the embedded FOS (specifically FBG) with the strain of the composite structure (Luyckx et al. 2011). The first step is to calibrate the output of the sensor (Bragg wavelength shift) so that it corresponds to the actual strain induced on the sensor. Theoretical and experimental understanding is necessary. In the second step the interaction between the optical sensor and the host material (which consist of materials with different mechanical properties) needs to be taken into account in order to determine the near field strain. Lastly, measurements in multiple points across the structure must be used for estimations on the far field strains.

In Ramakrishnan et al. (2016) some commonly fabrication methods for CM with embedded FOS are given:

- Fabrication Method of Composite Samples Embedded with FOS by Hand Layup and Pre-Preg Layup Methods (Figure 1.17 (a))

- Rotating Filament Wound Pressure Cylinder with FOS (Figure 1.17 (b)):
  FOSs are embedded either by a distinct rotating filament winding machine acting in parallel with the corresponding machine of the reinforcing fibers. FOS are positioned in the desired winding angles and between the appropriate layers and are drenched in the matrix material before or during the winding process. Specific applications of this method on composite shafts are given in next chapters (Konstantaki et al. 2021).
- Composite Panels Embedded with FOS (Figure 1.17 (c))
- Braided Composites Embedded with FOS

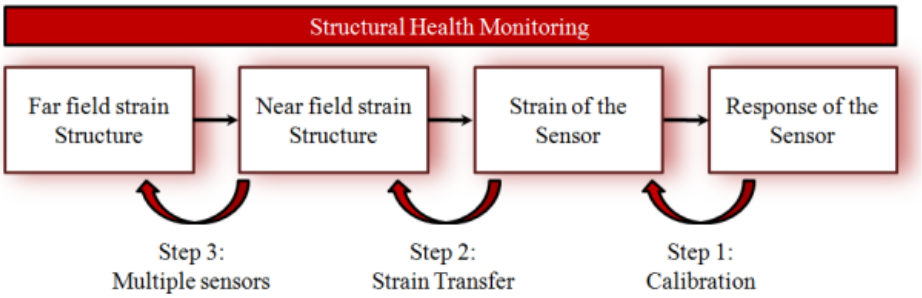

Figure 1.16. Steps for SHM with FBG

Although embedment of FOS into composite structures offers great merits, it is also affiliated to negative aspects. It is crucial that embedment of FOS does not threaten the structural integrity and the functionality of the structure and the FOS itself. The most important aspect is the possibility of degradation of the strength and modulus of the structure due to the appearance of the optical fiber. Degradation is directly related to areas inside the laminate which resin has been accumulated creating the so call resin-pockets. The recent advances in that area have shown that this is a function of the orientation of FOS in respect to the nearby reinforcement fibers especially for laminated composites. Shape and size of resin pockets can be minimized or even eliminated when FOS are parallel to the the adjacent plies of the structure as they will condense the resin-rich area around the FOS. Furthermore, there is a possibility that FOS ends inside the structure. The existence of this free end also has similar impacts to the structural integrity as the resin pockets. Both free ends and resin pockets have impact on the stress field and can potentially lead to delamination failure (Balageas et al. 2006). Sensors should not be located near free ends due to the effect of the stress field in the sensors' indication.

Another critical factor is the size of the embedded fiber. Common FOS diameters, coating included, range from 125mm to 230mm (Ramakrishnan et al. 2016) which is at least an order of magnitude bigger than the average reinforcement fiber. This fact should be considered in conjunction with the FOS orientation and the appearance of free ends for any potential effects on mechanical parameters of the composite structure.

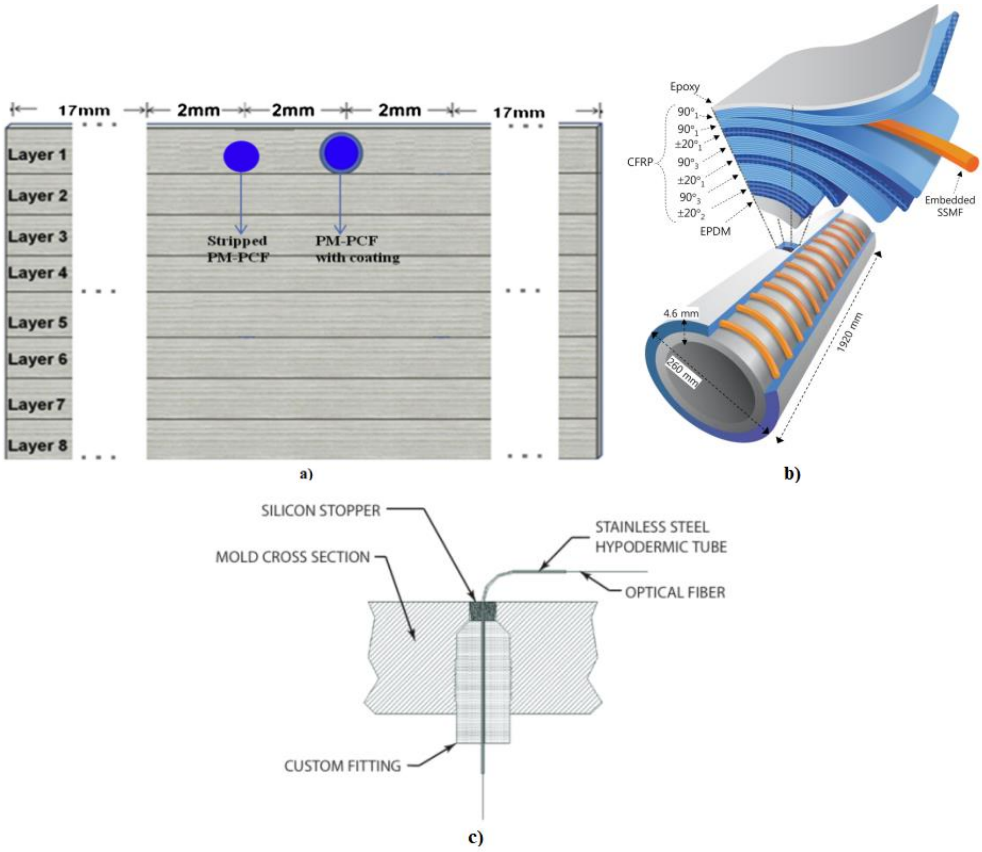

Figure 1.17. a) schematic FOS embedded in composite material;
b) schematic FOS embededd in composite cylinder and
c) schematic FOS inserted in the composite via tapered ingress

As far as the strength of the structure is concerned, it can be stated that in general it depends whether the embedment of FOS threatens it. In Lee et al. (1995) research has shown that the tensile strength is not significantly affected for tensile loads. The same applies for the tension region in bending loads but not for the compression region, which is FOS orientation depended. Obviously, the best way to embed the fibers is between unidirectional laminas. Fatigue resistance on the other hand, appears to be more prone in the presence of FOS under cyclic fatigue loads.

Connection spots of FOS with the external devices are also crucial. In these ingress/egress points the optical fibers, which are normally located in plane at the edges of the laminate, can become extremely fragile especially when mold are used for manufacturing. As the curing process takes place, the low viscosity resin can flow out of the laminate and gathered around the optical fiber (Kang et al. 2000). When cooled, this excess resin makes the fiber brittle which can lead to breakage of the fiber when mold or relevant curing tool is taken apart from the structure. Furthermore, difficulties arise when shaping the structure and smoothing the edges after the curing or when connections of FOS with the external equipment is made. Solutions in literature have been reported in such as: embedding thermoplastic sleeves and film adhesives which limit the resin flow at the ingress/egress points, reinforcement of the optical fiber at the ingress/egress points offering protection throughout the curing process, edge connectors with appropriate

ceramic ferrules. These methods though, are not suitable and fruitful for out of laboratory environment applications as after-curing processes may not be cost-effective in real-life structures. Appropriate manufacturing methods which make the need for trimming unnecessary (RTM, Sheet Molding Compound) are promising according to Balageas et al. (2006). Out of plane connections have also been studied. Designs based on free space couplings, meaning the ability to transfer the optical signal from the external interrogator to the fiber or backwards from few millimeters to few meters distance, have also promising prospects as reported in detail in Kinet et al. (2014), Ramakrishnan et al. (2016) and Qiu et al. (2009).

Lastly, **the reliability of the results** has to be checked as the presence of the optical fiber may lead to changes in the strain distribution field, at least at the area around and along the fiber. In the general case, it is reported that this has no significant effect on the normal strain field and thus the FOS response is equivalent to the case where no FOS is embedded (Valanduit et al. 2021). In Matveenko et al. (2017) numerical modelling results argue in favor of this although small, yet negligible strain disturbances exist. It has to be stated that the coating of the fiber acts as the median which transfers the strains from the host material to the optical fiber, thus choosing the appropriate (or in some cases omitting it) is important (Luyckx et al. 2011). However, peak splitting may appear in the indications of a FBG sensor, for example, when poor integration of the fiber has been made or non-uniform asymmetric loading of the sensor (Kuang et al. 2001). In addition, residual strains may be developed during the fabrication procedure which further complicates the reading of the results. However, embedded FOS is also a promising way to measure these process-induced strains.

1.6 Regulations on monitoring of shafts

As composite shafts have started to gain ground in the marine industry, Classification Societies have started to include in their ruleε and regulations sections for composite shafts. Related rules from some major classes (Lloyd's, DNV, BV) were thoroughly tackled in previous theses (Bilalis 2016, Vavatsikos 2016), thus they are presented again here in brief. Briefly, **Lloyd's Register (LR)** do not offer rules specifically concentrated to composite shafts, but rather general rules for the design, materials used and control and monitoring of shafting systems. It also gives rules for manufacture, testing and certification of composite materials. **DNV** has published a Class Programme (CP) for the type approval of "Composite drive shafts and flexible couplings – Non-metallic materials" which gives guidelines for the documentation, design, manufacturing and type testing applicable for type approval of composite shafts. CP provides demands that must be fulfilled for the type approval. Compliance with design requirements given in the Society's rules and/or other regulations and standards is also mandatory. **Bureau Veritas** offers a set of supplementary rules called Composite Shaft Line (Section 10 of Rule Note 546) for the scantlings check of hollow tubular composite shaft lines for main propulsion, having traditional design features.

Special consideration was given to find rules for structural monitoring of the shafting systems and relative guidance and requirements on the procedure to be followed, apparatus to be used etc., especially if strain measurement is included. Rules, guidance and requirements about torque measurement techniques, apparatus to be used etc. were also searched. Unfortunately, very few information is given by the classes. Specifically, all of them give rules and guidance for periodical surveys of the shafting systems. NDT method specifications are also included. Apart from these, requirements for condition monitoring and for condition-based maintenance systems of machinery of the ship are also given. These condition-based maintenance systems provide machinery condition related information as part of a machinery planned maintenance scheme for use as an alternative to machinery and equipment periodical surveys. Such condition monitoring schemes do not include strain-based (or other structural parameters) monitoring systems of the shaft but rather shaft bearing temperature, bearing wear down, lubricant analysis and other monitoring systems. Strain gauges (electrical resistance or even fiber optical in some shipping registers like in DNV and ABS) are also mentioned as typical sensors for hull monitoring, bearing monitoring (for shaft alignment) but not for the structural monitoring of the shaft.

Although **ABS** does not offer rules for shafts made of composite materials, on the other hand it was the only shipping register that was found to give rules about structural health monitoring and condition monitoring and specifications about the sensors to be used for various parts and components of a ship (e.g. hull monitoring) including shafts. ABS *Advisory On Structural Health Monitoring: The Application Of Sensor-Based Approaches* provides guidance on sensor-based structural health monitoring implementation divided into four sections. In the first section, called *Structural Health Monitoring Principles*, definitions and terminology are given while in the second section *Sensor-Based Monitoring Plans* sensor packages and specification requirements are given. Information about specific type sensors that are commonly used for measuring certain physical variables is given. For example, electrical resistance strain gauges and fiber optical strain gauges are mentioned for structural deflection and local strain/stress measurement and shaft torque meters for power output. Another Guide called *Guide for Hull Condition Monitoring Systems* covers motion monitoring, structural response monitoring and voyage data monitoring systems. Each system that complies with the requirements of this Guide can take a specific notation. For example, HM3 notation includes shaft monitoring systems requirements. Specifically, it requires that power output in term of shaft torque and revolution of each propulsion shaft to be directly measured and monitored continuously while the sensors used are to be documented and submitted for review. Warning and alarm levels are also to be submitted for review. Lastly, in the Rule called *Propulsion Shafting Alignment* bending moments/stresses and shear stresses measurement is proposed when shaft misalignment can be a detrimental factor, which is commonly done with strain gauges.

CHAPTER 2 OVERVIEW OF METHODS FOR STRAIN AND TORQUE MEASUREMENT ON COMPOSITE SHAFTS

In this chapter a review of recent advances in the field of strain and torque measurement on cylindrical structures is given, with special consideration on shafts made of composite materials that are under rotation, wherever that was possible. Strain measurements on shafts is strongly connected to measurement of torque. Strains comprise the effect of the application of torque on shafts and can be easily measured with strain gauges, optical fibers etc. as introduced in Chapter 1. Thus, these sensors are commonly used in torque transducers in many applications. Strain sensors are also used for structural and condition monitoring goals.

In the modern world, measuring torque is highly needed in many industries were rotating shafts are used such as the automobile, wind power plants and marine among many others. Relevant applications in such industries are the power measurement, the performance evaluation and process monitoring and control of combustion engines or electric motors, which arise from demands such as lower fuel consumption, greater operating safety, better reliability etc. (Schicker & Wegener 2002). Torque measurement sensors are typical transducers that convert the desired quantity (e.g. strain) into another physical quantity, commonly into an electrical signal, that can be measured, recorded and processed. This electrical output is proportional to the torque applied to the sensors. They can be divided into categories based on whether the sensor measure static torque or not (these are called reaction and rotary transducers respectively), whether the measurement is contactless or not and whether they are portable or permanently installed.

Reaction torque sensors are for static (non-rotating) torque acquisition. The torque of the rotating part is transferred to a static point (e.g. ground) and this reaction torque or force is measured there. Typical examples are process monitoring in agitatorsand similar types of mixing equipment or the force acting on the end of the lever arm using a force transducer. Rotary transducers are for in-line torque measurement on rotating shaft such as driveshafts. In this category, elastic tensile deformation is measured by translating the change of another quantity which is more suitable to measure (e.g. resistance). SGs are by the far the most common and widespread approach used for this reason. Optical methods can also be applied. Another approach is to measure the twist angle instead of the tensile deformation (Schicker & Wegener 2002). Figure 2.1 shows a scheme of a typical application of a drive shaft, where in-line torque measurement is used.

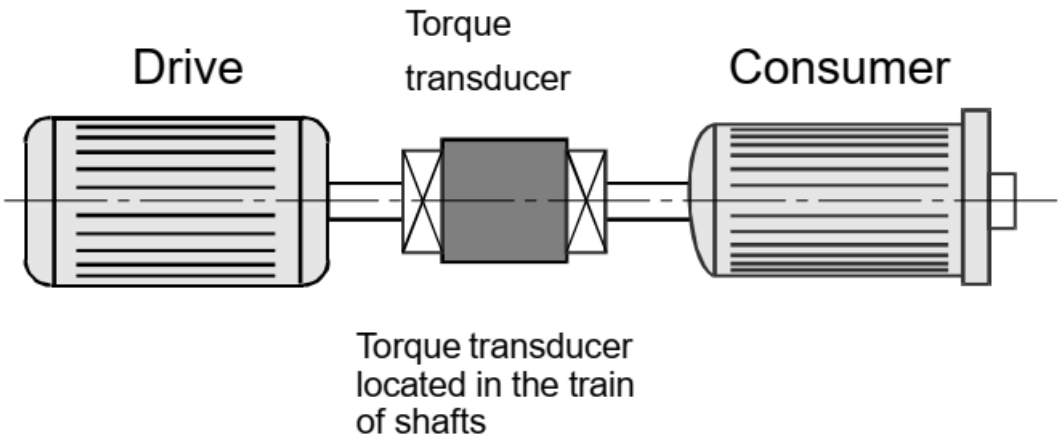

Figure 2.1 Schematic representation of a typical in-line torque transducer

In the sections of this chapter, papers available in literature are summarily presented in which methods of strain and/or torque measurement on composite material and rotating cylindrical structures (metal and composite) are examined. Care was given to hit on novel designs, devices and equipment which have the potential to realize the non-contact connection of the sensor attached on a rotating part (e.g. shaft) with the stationary signal receiver device. Market information was also briefly given where that was possible. It should be clear that in the context of this the thesis only typical examples of such methods are presented and not the full range of the applications that are available in the literature. The sections of the chapter were divided based upon the methods that are used for these purposes.

2.1 Strain Gauges applications

As already been mentioned before, SGs are the most common conventional strain sensors used until nowadays. Such sensors can be effectively used to measure strain at specific points of a structure (either consisting of composite materials or not). In that sense, SG have been extensively used as the baseline technique when evaluation and comparison of the results of other strain techniques in trials or laboratory tests is required, as they offer accurate and reliable results and their technology are well known to the users. There are plenty of such occasions in the literature.

SG has also been used for strain monitoring of the entire or an extensive area of a structure (e.g. hull). For example, SEA FIGHTER, an experimental littoral combat vessel fitted with a permanent monitoring system that was custom designed for the U. S. Navy used 100 metal foil strain gauges to measure hull strains (Phelps and Morris 2013). Commercial off-the-shelf systems for hull stress monitoring also include SG, such as HULLMOS® which has been installed in numerous ships. In Staszewski et al. (2004) some other cases of SG assemblies for load monitoring on aircrafts are also mentioned.

On the other hand, the use of conventional SGs for long-term monitoring of extensively large areas comes with some significant concerns, especially with the development of other sensors such as fiber optic sensors nowadays. For example, using a large number of SG on structures (e.g. airplanes, ships) would result in a very large number of wires needed which would result in a complex network. Despite that, long cables between the sensors and the DAQ device may also needed, which may affect the overall resistance of the SG assembly (Vanladuit et al. 2021). The data provided by the SG in such cases may also exhibit low signal-to-noise ratio. In addition, harsh environments pose a big threat for the safe and proper use of SG, especially when they attached on the surfaces of structures (which is the most common use). In such case, problems such as corrosion and debonding can commonly occur. For that reason, if long-term use of the SG assembly is desired, then extensive maintenance would be required which may not be cost-effective. Other drawbacks of SGs are their sensitivity to electromagnetic interference and regular need for is also needed regularly. SG applications on shaft are not excluded from the above limitations. The most widespread SG application on shafts on the other hand, is in torque transducers.

Torque transducers which utilize resistance SG for measuring torsional shear strain were firstly employed in 1952 according to Krimmel (2006). Mainly, SGs are attached on the shaft at $\pm 45°$ to the shaft axis where the principle strains occur in pure torsion loading. Commonly, four SGs connected into a Wheatstone bridge are attached on the shaft in pairs of two at opposite sides of the shaft in order to compensate for bending loadings that may affect the strain results. In addition, interference of other types of loads that produce strains on the shaft (e.g. compressive strains due to the thrust) is also eliminated. Modern SG rosettes integrate in one compact SG all of these four grids. Using SG in torque transducers offers some great advantages just like when used for pure strain measurements. Among other are the the capability for measuring static and dynamic torques, the long-term stability in proper environments and the high immunity against vibrations.

Apart from the sensing element itself that tis used, the main challenges that arise when torque transducers are used are power supply of the sensing element on the shaft and the data signal transmission from the rotating sensor. These cases are examined in the next sections below. Both contact and non-contact methods exist. A common contact method (and probably the oldest one) for both power supply and transmission of the data from the rotating shaft to the stationary data collector, are slip rings which are presented in the next section below. Non-contact torque transducers primarily use two ways: either induction or Radio Frequency (RF) telemetry. RF telemetry is solely used for data transmission and therefore, in such systems power supply can be done either inductively (non-contact) or with batteries in systems intended for short-term torque measurement applications.

2.1.1 Slip Rings

Slip ring is a typical example of such permanent installed, contact system for the signal transmission and the power supply between the rotor and the stator of a torque transducer. Slip rings are electromechanical devices that provide the power to excite the SG and to transmit the torque measurement back to the receiver through a set of appropriate brushes (or wipers) on the stator that are in constant contact with a set of rings on the rotor during rotation. In this way, an electrical contact is achieved. In Figure 2.2(a) two typical slip rings arrangements are schematically depicted: a cylindrical (drum) shaped one and a platter (pancake) shaped one. The selection is depended on application and the space requirements. The typical configurations of brushes on the other hand are depicted in Figure 2.2(b) and are selected according to requirements such as lifetime, size, power needs and ring arrangement. Noble metals are always used in the contact surfaces as they provide low resistant and eliminate contaminants.

With slip rings high data speed can be achieved, especially when Fiber Optic Rotary Joints (see Section CHAPTER 2) or non-contacting electrical slip rings are incorporated in the slip ring. In torque transducer with SG and slip rings the output torque signal is defined in mV/V and is boosted with appropriate amplifiers. Slip rings can be also used in cases when limited and no continuous rotating is desired (e.g. scanning mode). As it is obvious, slip rings exhibit enhanced performance, reliability and are more effective in terms of size and inertia compared to cable wraps in the case of static loading conditions. On the other hand, the major problem of slip rings is the wear of the contacts which mainly depends on the materials used. Great progress has been achieved in the field of the materials used and the design approaches in order to achieve minimal wear. Furthermore, resistive noise during rotation, which is the result of a slight variation in contact resistance, can be produced. Slip ring has a rotational speed limit, although this may probably not be an issue in all cases, and a power limit which depends on the size of the slip ring. Lastly, slip rings are prone to environmental contamination and thus contacts need appropriate sealing protection. Issues due to vibration must also be considered (see the first case of Figure 2.2(b) where spring applies pressure to the brushes in order to hold them in contact to the slip rings).

Slip rings assemblies are not solely used in torque transducers. In general, in any case where energy and signal transmission in rotating parts is required, slip ring is indisputably a reliable candidate. Such applications can be in aerospace - defense industry, for commercial - industrial (e.g. Ethernet connections, marine, wind turbines etc.), medical applications etc. Slip rings are commercially available either in pre-made compact torque transducers or in stand-alone assemblies which can be used for custom torque transducers. Some established manufactures and suppliers are:

- Moog which provides a huge amount of slip ring assemblies for a variety of applications fields but not torque transducers (https://www.moog.com/products/slip-rings.html). No market information was available.

- HBM provides one pre-made torque transducer which use slip rings: the T5 model (https://www.hbm.com/en/2386/t5-torque-transducer-with-cylindrical-shaft-stubs). Price in wholesale was found in 7500$.
- Cosmau from China which offers various types of slip rings but not torque transducers (https://www.cosmau-tech.com/products/slip-rings.html?gclid=Cj0KCQjwyOuYBhCGARIsAIdGQRNR_cAURlFboAphIEgMJkFpszdVJMlBrqG9Xc_zKJs8BIAGvT7eJ5IaAuiPEALw_wcB).
- SENRING Electronics from China which is exclusively a slip ring manufacturer (https://www.senring.com/products.html?gclid=Cj0KCQjwyOuYBhCGARIsAIdGQRPfOPWnab6-4q42uSuUeE1gzWea5EuuHxJleYnwaB4g7hruEDq5YBQaAjf8EALw_wcB).

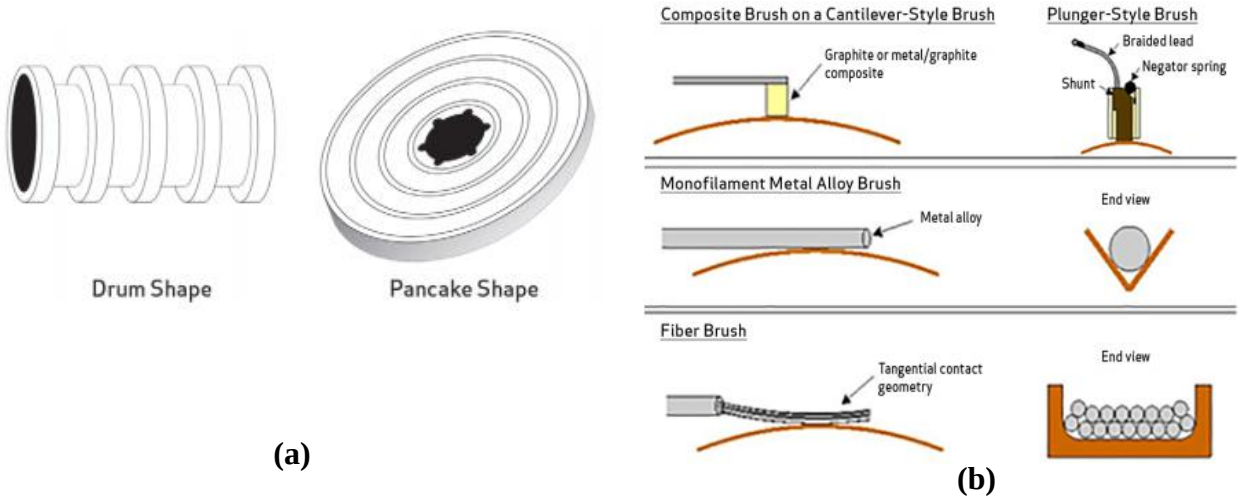

Figure 2.2 Slip ring (a) and brushes (b) arrangements (Source: Moog)

Even from a quick commercial investigation, it can be seen that torque sensors utilizing slip rings are not widely used nowadays. The main problem, as mentioned before, is the wear of the brushes which leads to the need of periodical maintenance. This entails for example, that a rotating shaft should be halted, which can lead to significant costs. This has made slip ring assemblies for torque sensors not a favorable option in the market.

Contactless methods, on the other hand, can tackle this problem and are generally employed in torque transducers. These methods are wear-free and therefore the need of maintenance can be eliminated. This can extend the lifetime of the torque transducer. Various types of such sensors are available and can be either permanent installed or for short-term measurements. As already mentioned before, non-contact techniques use induction, wireless RF telemetry or combination of these two. These methods are presented in the next sections. In order to be clearer how these systems work, two relevant devices that utilize these techniques and which are available in the LME in NTUA, Athens are also briefly presented. These are HBM T10F torque flange and Binsfeld TT10k. The last one was used in the static torsional test that was conducted for this thesis and presented in Chapter 4 and therefore it will be elaborated more thoroughly.

2.1.2 Inductive non-contact electrical signal transmission - Rotary transformers

Contactless transmission of energy and measurement signals in these cases is done inductively. The method of Inductive Power Transfer (IPT) is highly recommended in cases where moving parts much be supplied with electrical power without the need of wires. Systems aimed to transfer inductively electrical signals between two circuits that rotate near one another are called rotary transformers. Torque measurement is an application where such technology is used and most of the torque transducers commercially available, which are intended for permanent, long-term mounting around shafts, utilize this technique for power supply. In these systems, an inductive link is established between the stationary side (transmitter coil) and the rotating side (secondary coil). These coils are placed around cores so that a sufficient magnetic coupling between them is established. The first one is in the stator and is connected with the power source while the second is in the rotor and is connected the sensing element. When a current passes through the transmitter coil a magnetic field is generated which is then coupled to the secondary coil. When a change in the transmitter coil current occurs (Alternating Current-AC), a voltage is induced in the secondary coil according to Faraday's law which can be then used for power supply of the sensing elements or any other circuit as required (Figure 2.3). Typically, the axial rotary transformer is the most common design used where the two sides are placed coaxially around the shaft and constantly face one another. In that way, smooth operation can be achieved. The efficiency induction power transmission systems mainly depend upon the size (diameter), shape and resistance of the coils along with their relative distance and angle. Figure 2.4 depicts a typical scheme of an arrangement for torque measurement on a shaft which uses separate paths for the non-contact, inductive power supply and the signal measurement transmission. Other components are also depicted such as converter for AC to DC and vice versa, amplifiers etc.

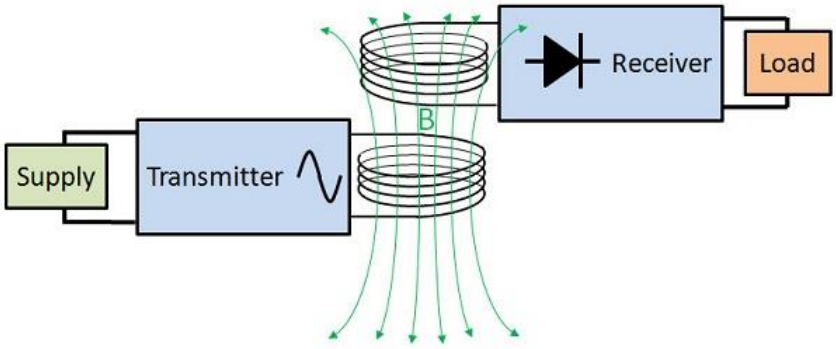

Figure 2.3 Schematic representation of Inductive Power Transfer principle (Schicker & Wegener)

Plenty of torque transducers which utilize the same technique for inductive electrical signal transmission are available in the market. There are many different designs of such sensors. Factors that vary in these designs are the geometry of the transducer or the way they are

connected with the shaft (e.g. flange, keyway shafts and others), the power supply (AC or DC voltage), the type of the transmitting signals (analog or digital signal transmission), the permissible rotational speed range or the maximum torque, the permissible working conditions and the temperature sensitivity, the overall accuracy and stability, the specific application which is intended for etc. Obviously, all the aforementioned factors also comprise the criteria for the selection of the desired torque transducers.

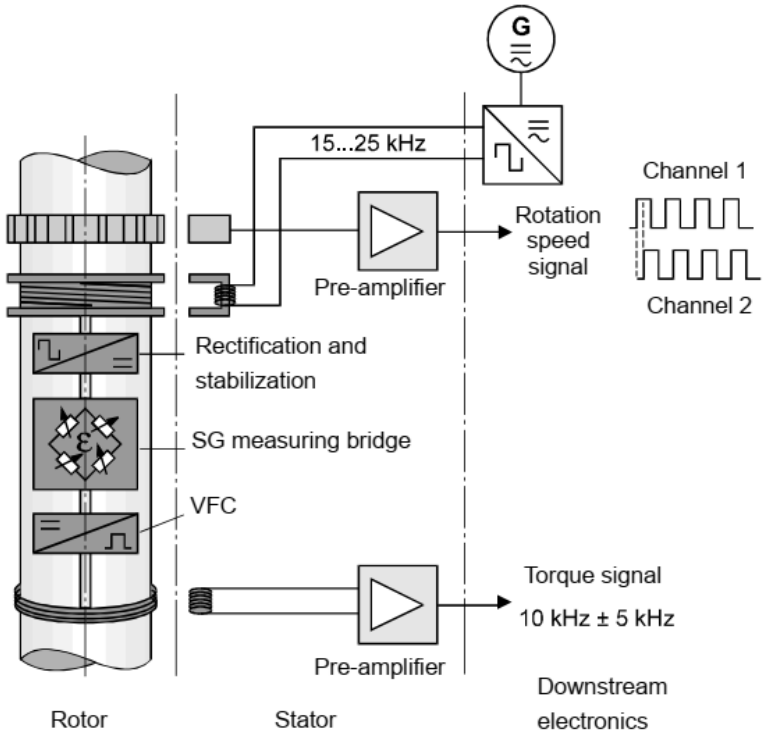

Figure 2.4 A contactless, inductive transmission arrangement for torque measurement on a shaft (HBM)

2.1.2.1 HBM T10F Flange

In the LME the T10F torque sensor from HBM is used (Schicker & Wegener). It consists of the rotor, which includes the measuring body and the adapter flange for connection with the shaft, and the stator. The measuring body has a tubular shape and contains four radial I-profile beams (shear spokes) used as shear elements on which the SG are attached (Figure 2.5). The nominal (rated) torque can range from 50 Nm to 10 kNm and depending on that the maximum speed can be up to 15000 rpm. The specific torque flange of the LME has a 2 kNm nominal torque and a 10000 rpm maximum permissible rotational speed. In some versions rotational speed measurement system is also included. Rotational speed is measure optically through a slotted disc. As mentioned before, the greatest feature of this transducer is that it is maintenance-free due to the non-contact transmission and the absence of bearings and slip rings. Furthermore, it has

extremely short design which can save space in the test rig or the engine room. High torsional, bending and lateral stiffness can be achieved and it can withstand high dynamic loads.

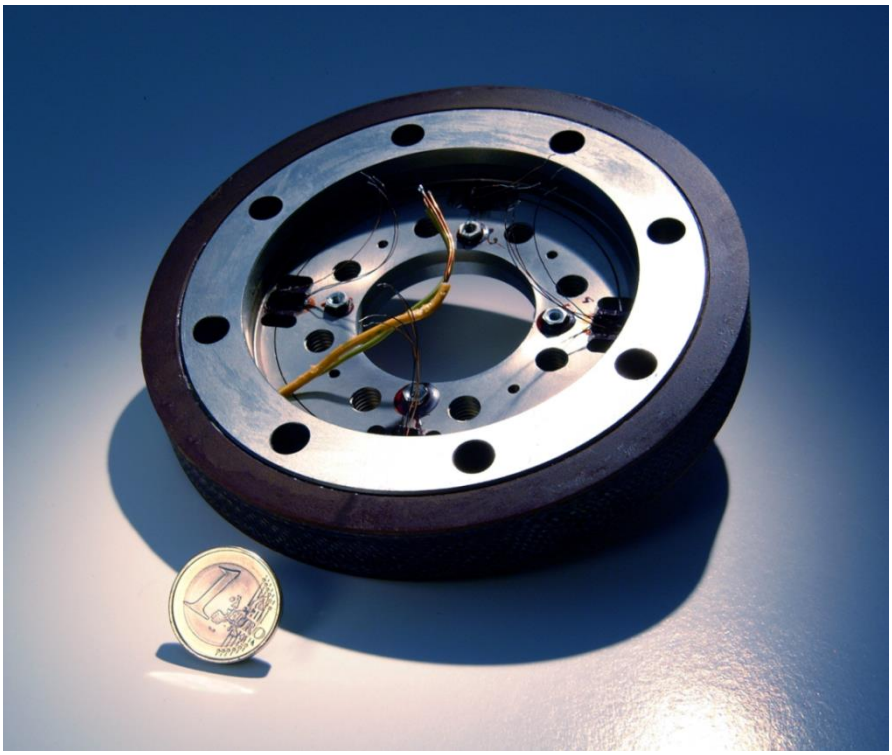

Figure 2.5 T10F measuring body with shear spokes

In this type of sensor a more compact way for the voltage supply (excitation bridge voltage of the SG) and signal transmission is utilized where one path is mechanically shared for the transmission of both signals. The transmitter coils are placed on the top outer surface of the measuring body of the rotor. An antenna ring mounted on the stator housing and placed concentrically around the rotor is used to transmit and receive the signal. The electronic system for voltage adaption and signal conditioning are included in the stator, along with connection plugs for the power supply and the torque and rotation speed signals. Figure 2.6 gives a scheme of this system and its components.

The power supply is inductively transmitted onto the rotor either as an AC voltage with a frequency of around 15 to 25 kHz or as an asymmetrical 18-30 V DC voltage supply in SF1 and SU2 versions. The last one (SU2) is owned by LME. The DC is transformed into AC to feed the antenna for the non-contact transmission. The output is a square-wave voltage with its frequency being proportional to the output bridge voltage and thus, proportional to the torque. This voltage output is transmit through a carrier signal and received from the antenna. After processing it is finally obtained from the connector in the form of a square-wave voltage of 10 kHz ± 5 kHz. The SU2 type which includes the DC supply can optionally have a ±10 V analog output for torque.

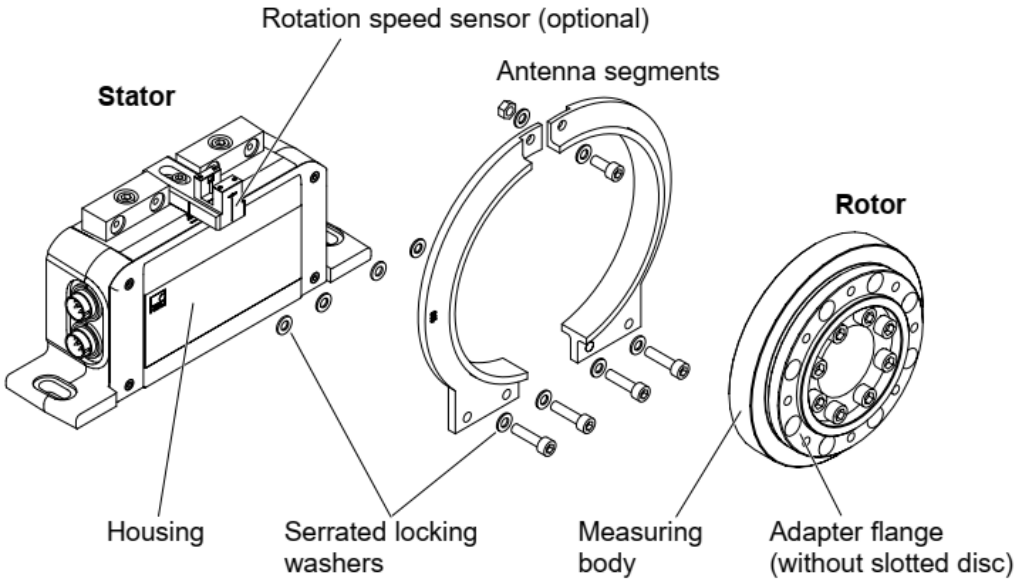

Figure 2.6 T10f (HBM) scheme

HBM offers plenty non-contact torque transducers with a variety of designs and features (https://www.hbm.com/en/0264/torque-transducers-torque-sensors-torque meters). T10F is one of the oldest versions offered by HBM. When it was purchased from LME, it was commercially available at around 10k €. T40/T40B model, with capability of digital signal transmission of torque measurement, released in 2008 and being in of the most established models offered from HBM, was found online at a cost around 12k to 22k $. T12HP was the last model released from HBM in 2017 offering very high precision. It was found online at a cost around 3k to 8k $.

Datum from UK is also a leading manufacturer and supplier of torque, load and shaft power measurement solutions worldwide. It offers plenty of different torque sensors designs, either for purely sensing application or integrated in a complete, compact system for shaft power measurement or shaft monitoring, especially for marine applications (https://datum-electronics.com/product/). Radio frequency telemetry signal transmission, which is presented in the next section, is also used in such devices. Prices were not online available.

Binsfeld offers TorqueTrak and Power Monitoring System (TPM2 series) which a rigged torque and/or power meter for permanent use on rotating marine shafts based on SG sensors. Inductive power supply and data signal transmission is used (Figure 2.7). It can be fitted to any size shaft up to 1220 mm in diameter without the need of modifying or disassembling the shaft.

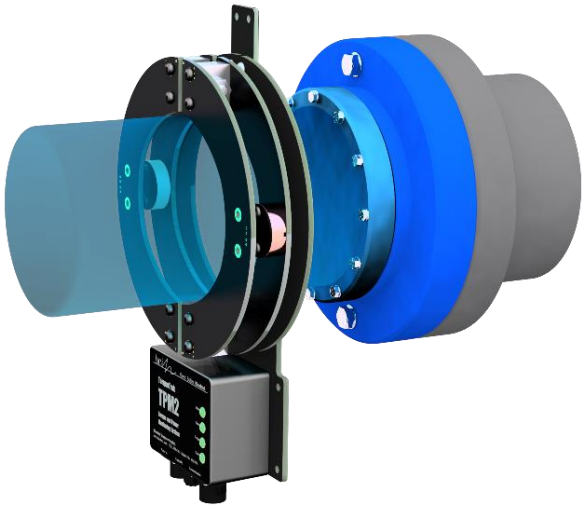

Figure 2.7 Binsfeld TPM2 torque meter

2.1.3 Wireless RF Telemetry

2.1.3.1 General

Wireless communication based on Radio Frequency (RF) is the leading method for wireless data transmission and is being used in many everyday applications such as television, radio, cellphones, radar etc. RF telemetry uses high-frequency waves to transmit the signal, primarily in the radio spectrum but also in higher frequencies like in microwaves or infrared spectrum. Every RF telemetry system primarily consists of a receiver and a transmitter located at different places. An antenna mainly serves this purpose. The original signal (e.g. voice, electrical etc.), which is intended for transmission, is superimposed on a carrier signal (a sinusoidal signal) which is generated in the antenna and modifies its properties. The carrier signal then contains the information of the original signal. This process is called modulation. The carrier signal is then transmitted through the air and received by the antennas. At the receiver the reverse process is followed and the information contained in the original signal is extracted. This process is called demodulation. Systems that use RF telemetry technologies can either be analog or digital.

In analog systems the modulation process is either done by modifying the frequency of the carrier signal (FM) or the amplitude (AM). The information of the original signal is then contained in the change of the frequency or the amplitude of the carrier signal respectively. In digital systems the signal is not continuous as in analog signals but divided into small discrete parts. The digital signal is generated by sampling the analog signal in discrete time steps in order to approximate the values of the analog signal (Figure 2.8). Modulation of digital signal is more complicated than that of analog signal. Modulation techniques are frequency division multiple access (FDMA), Time Division Multiple Access (TDMA) and Code Division Multiple Access (CDMA). Digital telemetry technology is used for example in 3G and 4G LTE cellular communications. The main advantage of digital systems compared to analog systems is that the can accommodate more users in the available bandwidth.

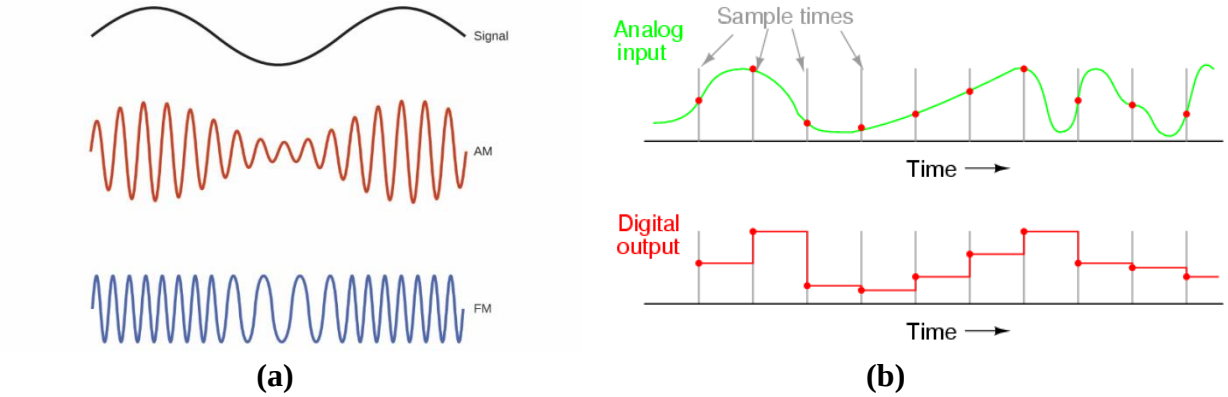

Figure 2.8 (a) Analog signal modulation FM and AM
(b) Analog to digital signal

RF telemetry technology is highly used in sensor applications where the physical quantity that is being measured is converted to an electrical voltage signal. This is the original signal which is superimposed on the carrier signal. Especially for torque (or purely strain) transducers on rotating shaft such technology is highly used as it offers an effective solution in the problem of the non-contact transmission of the measured torque data. In that way, the sensor system becomes less complicated as no extensive wiring is required, reducing in that way the installation and maintenance efforts and costs.

The rotating part of such transducers contains the sensing element, which is mainly a SG and its output voltage is the original signal, the transmitter for sending the signal to the stationary receiver and the electronic for the power supply which can done either with a contact method, such as slip rings or a battery attached on the transmitter and connected with wires (see Binsfeld TT 10k in the next section), or with a non-contact method such as electromagnetic induction. The stationary part contains the receiver and probably a DAQ system and the inductive system for the power supply of the rotating part.

In the next section the TT10k from Binsfeld Torque Telemetry System is presented as a representative example of torque transducers based on RF wireless telemetry. This system was used in the experimental static torsional test described in Chapter 4 and thus its basic features, components and working principles will be elaborately presented. Other systems and commercially available devices are also mentioned in the end of the next section.

2.1.3.2 Binsfeld TorqueTrak - 10k (Wireless telemetry)

The TorqueTrak 10K (TT 10K) Torque Telemetry System from Binsfeld (https://binsfeld.com/torquetrak/temporary-torque-measurement/torquetrak-10k/) is a common, frequently used tool for torque measurement which utilizes the proven digital RF wireless telemetry technology to transmit a single data signal from a strain gauge in relevant close distance, thus realizing a non-contact way to measure torque on a shaft of any size. Batteries are also attached on the shaft and wired with the transmitter for the power supply (Figure 2.9). This

type of transducers is usually employed for short-term application, like for diagnostic tests of existing shaft or under laboratory conditions. For more detailed information along with guides on how to specifically use and manage each component and operation of the TT 10K, the User's Guide shall be consulted. The specifications of each component can also be found there.

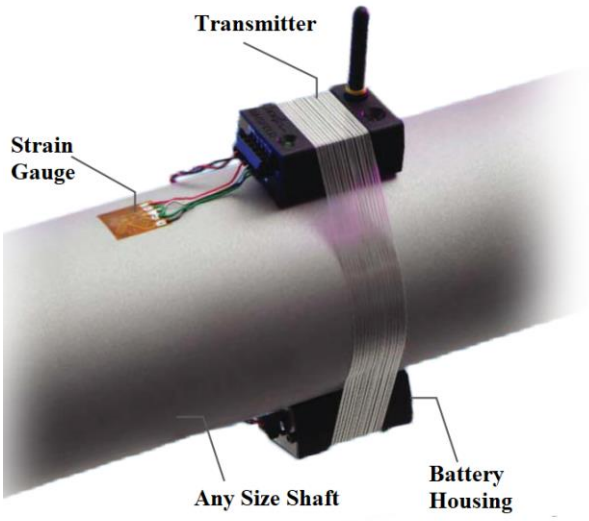

Figure 2.9 The TX 10K-S Transmitter

TT 10K consists of three main components:

The *RX10K Receiver* (Figure 2.10): The device which receives the signals from TX10K-S Transmitter and displays them in 3 ways: text & graphs on a screen on the front panel, analog voltage signal output with ±10V nominal range (±12V maximum range) and digital voltage signal output of RS-232 type. On the rear panel (Figure 2.12) binding posts for the analog Voltage Output, a Com connector for the digital data signal are located the On/Off Power switch, a jack for 12VDC Power Input, a Fuse housing and a connector for attaching the Receiver Antenna are also located there. The settings of the system consist of seven user-configurable parameters which can easily be adjusted through the receiver to the requirements of each application (Section 3.2.2). Via the arrow keys of the buttons "Select" and "Adjust", which are located on the front panel (Figure 2.11), all the parameters can be selected and adjusted.

Reicever

Figure 2.10 RX 10K Receiver

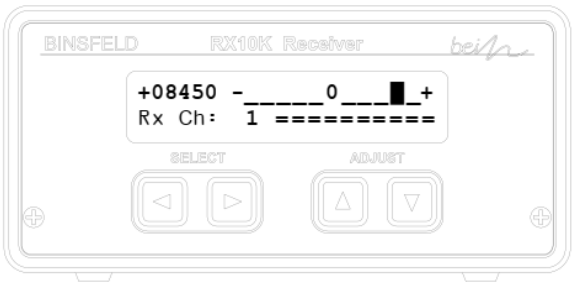

Figure 2.11 Front panel of RX 10K schematically

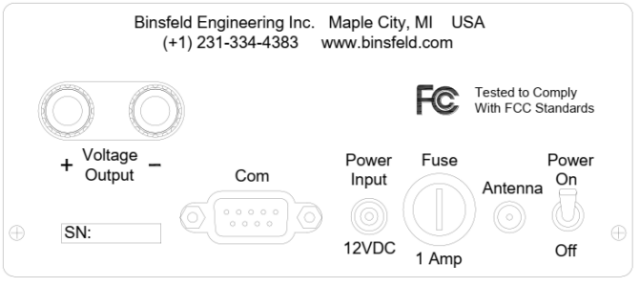

Figure 2.12 Rear panel of RX 10K schematically

TX 10K-S Transmitter (see Figure 2.9): It acts both as the transmitter of the signal to the receiver and also as the connector of the strain gauge with its power excitation. For that reason, the Transmitter is accompanied by a battery housing which holds a 9V lithium battery. A 2-conductor power cable connects the battery housing and the transmitter. The TX 10K-S includes a Status Indicator light, an Infrared Receiver lens, a Transmitter Antenna connector, and a screw terminal block for making power and sensor input connections (Figure 2.13). It has 16 distinct RF Channel settings and 6 Gain settings which are introduced in the next section. The sample transmission rate of the digital data is 2400 samples/second and the resolution is 14 bits. Lastly, in order to check the calibration of the system, TX 10K-S can also simulate strain values and send reference signals to the receiver with the aid of internal shunt resistors.

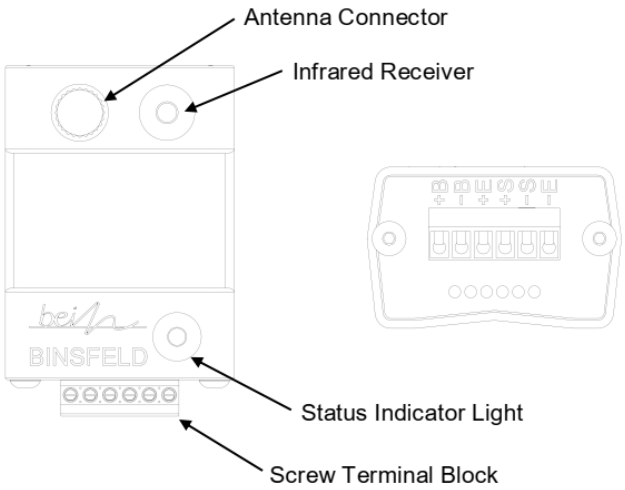

Figure 2.13 Drawing of the transmitter

RM10K Remote Control (Figure 2.14): Operates similar to a common TV remote control, emitting an infrared signal by pressing the proper button which transmits commands to the TX10K-S when pointing to it. TX10K-S shall be stationary but is also able to work at slow rotation speeds, typically less than 100 rpm. RM10K also needs to be within 150 mm of the TX10K-S for the signal to be received but high infrared power mode is also feasible which increase the distance up to more than 6 m which is useful in cases where the TX10K-S is difficult to reach. Through RM10K some parameters of the TT10K can be remotely changed and standby mode can be selected battery conservation. Lastly, two reference signals which simulate specific strain values (100 με and 500 με respectively) can be also activated. In Figure 2.15 a schematic image is shown.

Figure 2.14 RM 10K Remote Control

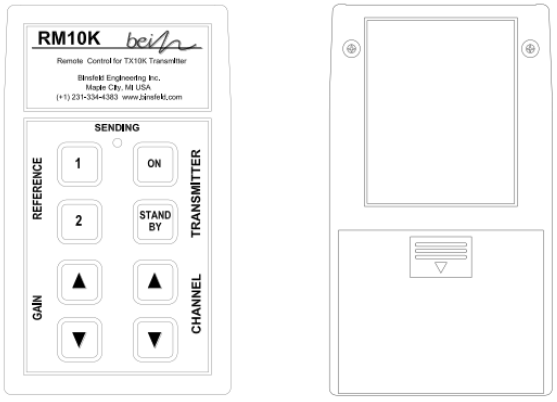

Figure 2.15 Drawing of the Remote Control

Settings

As already mentioned before, seven parameters comprise the settings of the RM10K. This are

briefly described below. The User's Guide has more detailed descriptions and instructions on their use.

Channel: In order to match the RF channel of the TX10K-S with the receiving channel of the RX10K this parameter shall be altered. There are 16 different RF channels listed in Table 2.1. The channel with the strongest strength signal shall be selected.

Table 2.1 RF frequencies of channels

RF Channel	Frequency (MHz)	RF Channel	Frequency (MHz)
1	902.62	9	914.62
2	904.12	10	916.12
3	905.62	11	917.62
4	907.12	12	919.12
5	908.62	13	920.62
6	910.12	14	922.12
7	911.62	15	923.62
8	913.12	16	925.12

Input: This parameter defines which input value the RX10K receives. The default value and the commonly used for every application is the "Transmitter" value as it is obvious. Beyond this, other input parameters can be selected to simulate specific values that the TX10K-S can transmit in order to check how the RX10K-S responds and operates at these specific signals. E.g. "+FS" value simulated positive full scale input etc.

Filter: With this option the high frequency data transmitted by the TX10K-S can be reduced. In this way the output range of the signal is strictly defined and the possible noise is eliminated. The upper value of the output frequency range can be selected from the below values: 500, 250, 120, 60, 30, 15, 8, 4, 1 Hz.

Polarity: This parameter gives the option to change the polarity of the output signal. Can take either "Positive" or "Negative" value.

Input AutoZero: When this parameter is applied ("On"), the initial offset of the output signal, prior to the beginning of the TT10K operation, is compensated and becomes the input zero. This offset is usually attributed to pre-strains of the gauge sensor. This option should be activated prior to application of the Gain parameter (see "Gain" below) which otherwise would change this initial offset. Furthermore, this offset output value shall be stable in order to appropriately apply the Input AutoZero parameter, which can be accomplished by a lower frequency Filter value.

Gain: The Gain parameter is the scale factor applied to the input values that the RX10K receive from the TX10K-S which affects the output values displayed to the front panel of the RX10K, the Voltage Output signal, and the digital (RS-232) output signal. The Gain parameter

consists of two parts: the "Transmitter Gain" displayed on the left and the "System Gain" displayed on the right of the front panel of RX10K.

Table 2.2 Transmitter Gain Setting
(for Torque or Bending, Full Bridge, 4 Active Arms)

Transmitter Gain Setting	Full Scale Strain (Full Bridge, με)
500	±4000
1000	±2000
2000	±1000
4000	±500
8000	±250
16000	±125

The "Transmitter Gain" value depends on the microstrain (με) range expected during a given test (Table 2.2). When torque on round shafts is measured and the Full Bridge with 4 Active arms gauge pattern is used, this table is used to select the "Transmitter Gain". The "System Gain" range from ¼ to 4 times the "Transmitter Gain" and is used for convenient output scaling and calibration. In Section 0 its use on the calibration of torque measurement on a shaft is better explained. The basic equation relating the measured strain to the Voltage Output of the RX10K is the eq. (2.1) below and the terms used in it in Table 2.3. It derives from eq. (1.7) in the case where the active arms of gauge are four. The "Transmitter Gain" is changed using the RM10K while the "System Gain" by using the RX10K arrow keys in its front panel.

$$\varepsilon \times GF \times V_{EXC} \times System\ Gain = RX10K\ Voltage\ Output\ (V) \qquad (2.1)$$

Table 2.3 Terms in eq. (2.1)

$\boldsymbol{\varepsilon}$	Measured strains (με)
$\boldsymbol{GF}$	Gage Factor (specified on strain gage package)
$\boldsymbol{V_{EXC}}$	Bridge Excitation Voltage = 2.5 Volts

Output Offset: The last parameter Output Offset offers the possibility to adjust the initial offset or "move the zero" of the output of the RX10K. The zero value can be moved anywhere within the maximum voltage range of $\pm$12V. It affects the output values displayed to the front panel of the RX10K, the Voltage Output signal and the digital (RS-232) output signal. This parameter should be activated after the Gain parameter has been applied.

The Default RX10K parameters are listed below in Table 2.4.

Table 2.4 Default Settings

Default	Description
RX10K Channel	1
Input	Transmitter
Filter	500Hz
Input AutoZero	Off
Polarity	Positive
Gain	T=S
Output Offset	0

The standard process that the RX10K follows each time a signal from the TX10K-S is received is presented below (User's Guide):

1. Receive signal from TX10K-S
2. Check for errors and display if any detected
3. Check for simulated signal and apply if enabled
4. Apply Filter
5. Apply AutoZero
6. Apply Polarity
7. Apply Gain
8. Apply Output Offset
9. Send signal to display, voltage output, and digital output

Calibration

The most important step of the procedure of measuring the torque (or merely strains) of a shaft with TT10K is the calibration of the voltage output signal. In that sense, a relationship between the TX10K-S input signal, i.e. the measured voltage from the strain gauge, and the output of the RX10K (RS 232, analog output) shall be defined. This will be examined in this Section.

Beyond that, the RX10K calibration should also be checked separately annually, meaning that the output values, displayed by the RX10K, have to be true. For that, the Input parameter has also seven other choices except the "Transmitter" input. These are presented in Table 2.5. By applying one of them the real output value, which has to be checked by an external attached voltmeter via the Voltage Output terminal on the rear panel of RX10K, should be within the Output range; otherwise the system needs to be returned to the manufacturer for calibration according the User's Guide.

Table 2.5 Input parameters and output values for the check of the calibration

Input	Output
+FS	10.000 ± .010 VDC
Zero	0.000 ± .005 VDC
-FS	-10.000 ± .010 VDC
+FS/2	5.000 ± .005 VDC
-FS/2	-5.000 ± .005 VDC
+FS/4	2.500 ± .005 VDC
-FS/4	-2.500 ± .005 VDC

For torque measurement, shear strain gauges with four grids at 45 degrees orientation with respect to the shaft axis are required (full bridge, 4 active arms). Different SGs can be used for different shaft materials, (e.g. composite). Figure 2.16 shows schematically how the rosette strain gauge should be attached on the shaft in relation to the orientation of the applied torque in order to have a positive output signal. In addition, the taps of the strain gauge and their corresponding wire connections are also shown.

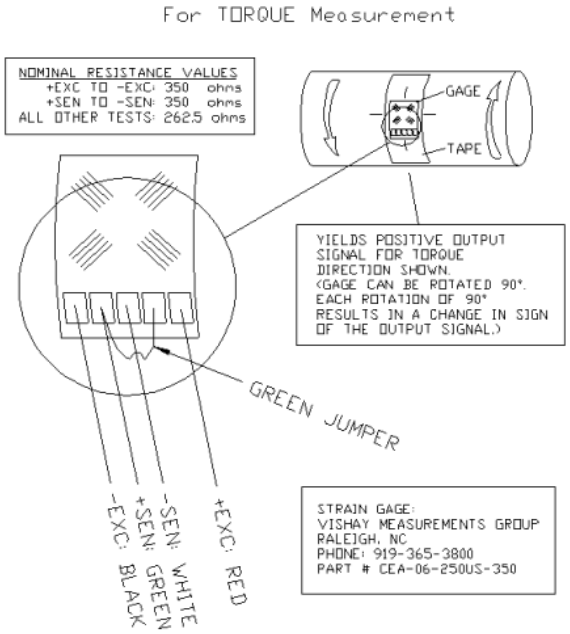

Figure 2.16 Schematic representation of strain gauge for torque measurement according to TT10K User's Guide

In order to achieve the proper calibration, three steps are required. In step 1 is the calculation of the Full Scale Torque, meaning the torque that corresponds to the system maximum voltage (10V), which depends on the shaft characteristics, sensor parameters (Gauge Factor) and the Transmitter Gain selected. Then, in step 2 the scale factor is calculated, which makes the

adjustment of the maximum voltage output (10 V) to the desired Full Scale Torque. In this way the System Gain can then be determined. Lastly, in step 3 the calibration of the installation is performed and the System Gain is readjusted. Calibration is done either by a deadweight calibration or by shunt calibration and is introduced later.

In step 1, the Full Scale Torque for hollow shaft in metric units is given in eq. (2.2). The terms of eq. (2.2) are listed in Table 2.6.

$$T_{FS} = \frac{V_{FS} \cdot \pi \cdot E \cdot 4 \cdot (D_0^4 - D_i^4)}{V_{EXC} \cdot GF \cdot N \cdot 16000 \cdot (1 + \nu) \cdot G_{XMT} \cdot D_0} \tag{2.2}$$

Table 2.6 Magnitudes of eq. (2.2)

$\boldsymbol{D_i}$	Shaft Inner Diameter (mm) (zero for solid shafts)
$\boldsymbol{D_0}$	Shaft Outer Diameter (mm)
$\boldsymbol{E}$	Modulus of Elasticity (for steel: $\boldsymbol{206.8 \times 10^3\ N/mm}$)
$\boldsymbol{GF}$	Gage Factor (specified on strain gage package)
$\boldsymbol{G_{XMT}}$	Telemetry Transmitter Gain (user configurable, typical is 4000 for ±500 microstrain range)
$\boldsymbol{N}$	Number of Active Gages (4 for torque)
$\boldsymbol{T_{FS}}$	Full Scale Torque (N·m)
$\boldsymbol{V_{EXC}}$	Bridge Excitation Voltage = 2.5 volts
$\boldsymbol{V_{FS}}$	Full Scale Output of System = 10 volts
$\boldsymbol{\nu}$	Poisson's Ratio (0.30 for steel)

Eq. (2.2) derives from equations of classical mechanics which relate the applied torque with the developed strains on the external surface of a hollow shaft (eq. (2.3) - (2.5)):

$$\tau = G \cdot \gamma = G \cdot 2\varepsilon \tag{2.3}$$

$$T = \frac{I_P}{\frac{D_0}{2}} \tau \tag{2.4}$$

$$I_P = \pi \frac{(D_0)^4 - (D_i)^4}{32} \tag{2.5}$$

The strain ε on the external surface of the shaft can then be calculated from eq. (2.6). This equation is used on the online calculator provided by Binsfeld in order to estimate the expected strain range and thus select the appropriate Transmitter Gain value (see Section 4.4).

$$\varepsilon = \frac{T \cdot \frac{D_0}{2}}{2 \cdot G \cdot I_P} \tag{2.6}$$

The developed strain is calculated from eq. (2.7) which is identical to eq. (2.1) but also contains the gauge factor and the System Gain is also used instead of the Transmitter Gain.

$$\varepsilon_{FS} = \frac{V_{FS} \cdot 4}{N \cdot V_{EXC} \cdot GF \cdot G_{XMT}} \tag{2.7}$$

For isotropic materials eq. (2.8) is applied.

$$G = \frac{E}{2(1+\nu)} \tag{2.8}$$

On the other hand, for orthotropic materials, hence for shafts made from composite materials, more complicated relationships between mechanical constants are in effect and eq. (2.8) cannot be applied.

Eq. (2.2) derives from the combination of eq. (2.3)-(2.5) and eq. (2.7)-(2.8). For orthotropic shafts though, eq. (2.8) cannot be applied and the shear modulus G cannot be replaced by its equivalent relationship in eq. (2.8). Thus, eq. (2.9) should be used in the case of shaft made of composite materials. The validity of this equation is examined in Chapter 4.

$$T_{FS} = \frac{2 \cdot V_{FS} \cdot \pi \cdot G \cdot 4 \cdot (D_0^4 - D_i^4)}{V_{EXC} \cdot GF \cdot N \cdot 1600 \cdot G_{XMT} \cdot D_0} \tag{2.9}$$

In step 2 the Scale Factor is calculated. If the calculated value of the Full Scale Torque (T_{FS}) needs to be altered so that the maximum voltage value of 10 V corresponds to a different, more convenient torque (T_{REF}), probably with a rounded off value, then their ratio is calculated using eq. (2.10). This value is the Scale Factor.

$$Scale\ Factor = \frac{T_{FS}}{T_{REF}} \tag{2.10}$$

The System Gain is then defined by eq. (2.11) and can be set from the front panel of the RX10K. As can be seen, in most cases the System Gain will diverge from the Transmitter Gain, in contrast to the Default settings.

$$System\ Gain = Transmitter\ Gain \times Scale\ Factor \tag{2.11}$$

For example, if eq. (2.2) gave a full scale (10V) value of $4901\ Nm$ and we want a more convenient value like $5000\ Nm$ torque, then from eq. (2.10):

$$Scale\ Factor = \frac{4901}{5000} = 0.9802$$

The System Gain is then (for a typical Transmitter Gain of 4000 which corresponds to ±500 με full scale strain range):

$$System\ Gain = 4000 \times 0.9802 = 3920$$

Finally, in step 3 the calibration is carried out. It is the necessary process so that the indication of torque from the RX10K is equal to the real applied torque. As already mentioned before, two methods of calibration are proposed in the User's Guide.

Deadweight Calibration: In this way a torque is applied with a precise known value. This can be achieved either by suspending a mass at a certain distance from the center of the shaft or by fitting the shaft on a normally operating torsion machine and apply a specific torque. The System Gain can then readjust so that the indicated value of the RX10K corresponds to the applied torque. The applied torque should be close to the expected one during the test or at least at 10% of the range. This method, although may not be practical on every occasion, is the most precise and the one recommended.

Shunt Calibration: An easier way to calibrate the output is to perform the Shunt calibration. It is already known that the Transmitter has two internal resistors with different resistances which are called reference shunt resistors (Reference 1 and 2) and can be activated from RM10K-S. They are placed parallel with one arm of the bridge and together with a 350Ω gage and a 2.0 gage factor, the values simulate input strains equivalent to 100 and 500 microstrain respectively in the positive direction. In the same way a torque load can also be simulated. Eq. (2.12) gives the relationship between the shunt resistance and the corresponding simulated strain value.

$$R_C = \frac{R_G}{N \times GF \times \varepsilon} \tag{2.12}$$

where:

R_C: Shunt Calibration Resistance (kΩ)

R_G: Gage Resistance (Ω)

In the previous example, the Reference 1 resistor (100 με) simulates the 20% of the Full Scale before the application of the Scale Factor $Z = 0.9802$. After the application, the voltage output is given by eq. (2.13):

$$V_S = (\frac{\varepsilon_S}{\varepsilon_{FS}}) \times Z \times V_{FS} \tag{2.13}$$

The terms of eq. (2.13) are presented in Table 2.7. Then, the System Gain should be readjusted to correspond to the value obtained from eq. (2.13) and the calibration is done.

Table 2.7 Terms of eq. (2.13)

V_S	Voltage Output with Shunt Applied (V)
ε_S	Strain Simulated by Shunt (με, GF = 2.0)
ε_{FS}	Full Scale Strain (με, GF = 2.0)
Z	Scale Factor (one if no scaling)
V_{FS}	Full Scale Voltage Output (V) (10V)

Pros and cons

The most predominant advantages that TT10K offers are:

- Easy usage, as it can be fitted to any size shaft without any alteration or disassembly on its arrangement.
- The RX10K front panel screen and keypad along with the RM10K which provide a user-friendly environment and interface.
- The capabilities offered by the RM10K remote control including channel select, gain/range, shunt calibration and low-power standby mode
- Both analog voltage output and digital data output (RS-232) which provide with clean, noise-free data signal.
- Battery standby mode which can extend the Transmitter battery life without the need to disconnect it.
- Multiple channels along with the capability to simultaneously use multiple devices on the same shaft even at very close distance.
- Rigidity of the Transmitter which features reinforced, injection-molded housing which ensure that the Transmitter mounted on the shaft can withstand up to 3000 G's force. V-groove and tape slot are also used for secure mounting. These are of high importance for demanding applications.
- The Gain parameter which scale the output to the desired level for each application.
- The easy and fast transfer of the device to any place with the carrying case provided which also offers watertight protection.
- The capability to use it to harsh and moist environment with the aid of specific coatings on the strain gauge and a watertight kit (not contained in the standard edition) which contains tools to make the device (housing, power connections etc.) water-resistant.

On the other hand, the main disadvantage encountered when TT10K is used, is the relative low battery life. According to TX10K-S specifications and for the case where a 350 Ohm bridge for the strain gauge is used, which is typical, at Transmit mode the battery lasts for up to 24 hours while in Standby mode up to 240 hours approximately. This inhibit the potential use at out of laboratory environments, like on shafts of merchant ships while they are in commission on long-

voyages, without the need to halt the operation of the shaft and replace the 9V battery. This demand can be met though in short distance voyages of passenger ships.

TT10K has already been used in LME facilities (Figure 2.17) on a metal shaft which connects a Diesel engine with a dynamometer. It has also been examined in previous thesis (Mavrakis 2015) again on metal shafts. Its use on composite materials shaft and the corresponding nuances that may arise has not yet been investigated in the author's knowledge. As mentioned previously, an attempt was made in this thesis on a carbon epoxy drive shaft under static torsion load which is presented in Chapter 4.

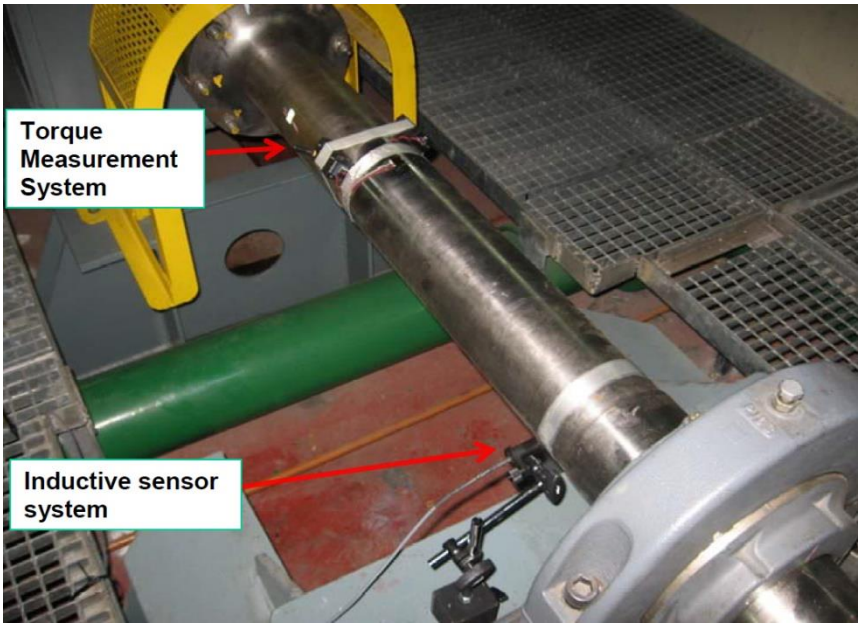

Figure 2.17 TT10K on metal shaft in LME facilities

2.1.3.3 Other RF wireless telemetry systems

Other torque transducers that use SG and RF telemetry have been produced by various manufactures. Despite specific differences in the design, the basic features and the working principle of them are similar to that of the TT 10K. To name a few:

- Kyma Shaft Power Meter (https://www.danelec.com/products/ship-performance-monitoring/) which offers a well proven full package for torque, rotational speed and trust measurement on marine shafts (150 mm or greater diameter) for permanent use. Inductive power supply and RF wireless telemetry signal transmission are used
- Althen offers some various rotary torque transducers for permanent mounting mainly based on digital wireless RF telemetry and inductive power supply. Most of them are intended for small shafts with low torque measurement range (up to 2kNm). An interesting model was 90415 IRT intended for applications such as dynamometer and test stands which transmit torque data into digital format via infrared (IR) diodes and receivers (Figure 2.18).

Figure 2.18 90415 IRT from Althen (digital transmission in the infrared spectrum)

- Michigan Scientific Corporation offers some digital wireless telemetry systems with unique designs for non-contact signal transmission of SG data on rotating shafts. They have the advantage that can easily mounted and dismounted on any shaft with diameter of 1.0 inches or larger. They are power either inductively (CIT-Clamping Induction Telemetry and TEL-SC Split Collar Telemetry and Induction System) or by battery (CBT-Clamping Battery Telemetry) (https://www.michsci.com/products/telemetry_systems/).
- Tecat Performance Systems have released Wise 4000 and 8000 version of RF wireless telemetry strain and torque sensors parameters (https://tecatperformance.com/).

2.1.3.4 Conclusions

All the torque transducers that were presented previously had a common feature: they use SG for measuring shear strains in order to extract torque data. The SG are either attached on the shaft or integrated into the measuring body of the torque transducer in compact designs. For the power supply, either non-contact induction or wiring with batteries are used. For the transmission of the torque measurement, signal induction or RF telemetry are used. Combination of induction for power supply and RF wireless telemetry is also widely used. These are typical torque transducers that are mainly used in commercial applications in various industries.

2.1.4 Strain Gauges on composite shafts

Torque transducer based on SG can also be used on composite shafts. Further to what has been discussed in Sec. 1.4, SG application on CM has several concerns, mainly regarding the influence of the orthotropic behavior of the shaft on the SG measurements. The direction-depended deviation of the mechanical properties as a result of this orthotropic behavior is a major

difference compared to isotropic materials which affect the conventional, well-known application of SG on shafts. The fabrication process and the formulation of the composite structure may also lead to deviations from the desired mechanical properties. As a consequence, the proper alignment of SG is crucial. Surface preparation is also a special aspect of SG installation on CM compared to isotropic materials and manufacturers' guidance should be followed.

For torque measurement on compsoite shafts the stress-strain relationships, which are dictated by the stiffness of the shaft, is the most complicated part in general. For that reason, the shear modulus at least should be determined with the highest accuracy possible. This may not be always achievable though and some deviations from the real valued may be present. According to the study of Guijs (2018) where the problem of power measurement of marine composite shaft was examined, various identical shafts manufactured by (https://www.vulkan.com/en/) exhibited a deviation of $\pm$10% in their stiffness values which was mainly caused by the production process. Furthermore, accurate estimations of the internal and external diameters are also necessary as fluctuation of the outer diameter is a common problem.

Theoretical studies have been also conducted for composite shafts under pure torsion in order to derive and analyze relationships of torque vs angle and torque vs strain. A typical one was presented in Zhao & Pang (1995) where a cylindrical, laminated thin shell under pure torsion was studied. In Figure 2.19 a scheme of the cylindrical coordinate system of the shaft is depicted along with positive stresses directions.

Initially, assumptions were made which are given in eq. (2.14) and eq. (2.15) which was derived from the general form of stress vs strain relationships for a composite lamina:

$$\varepsilon_{z\varphi} \neq 0, \qquad \varepsilon_{others} = 0 \tag{2.14}$$

$$\sigma_{z\varphi} = \bar{Q}_{66}\varepsilon_{z\varphi}, \qquad \sigma_{others} = 0 \tag{2.15}$$

where $\bar{Q}_{ij}$ represents an element of transformed reduced stiffness matrix $[\bar{Q}] = [T]^{-1}[Q][T]$, where $[Q]$ is the matrix of material properties - stiffnesses of a layer and $[T]$ is the matrix of coordinate transformation principal directions of material (one layer) to the principal direction of the structure. If the shaft is fixed at one end the subjecetd to a torque at the other the shear strain can be written as in eq. (2.16):

$$\gamma_{z\varphi} = \frac{\partial u_{\varphi}}{\partial z} = \frac{\varphi}{L} r \tag{2.16}$$

where $\gamma_{z\varphi}$ is the mechanical shear strain ($\gamma_{z\varphi} = 2\varepsilon_{z\varphi}$), u_{φ} is the angular displacemen, φ is the torsional angle at the end of the pipe, L is the length of the shaft and r is the radius of the lamina.

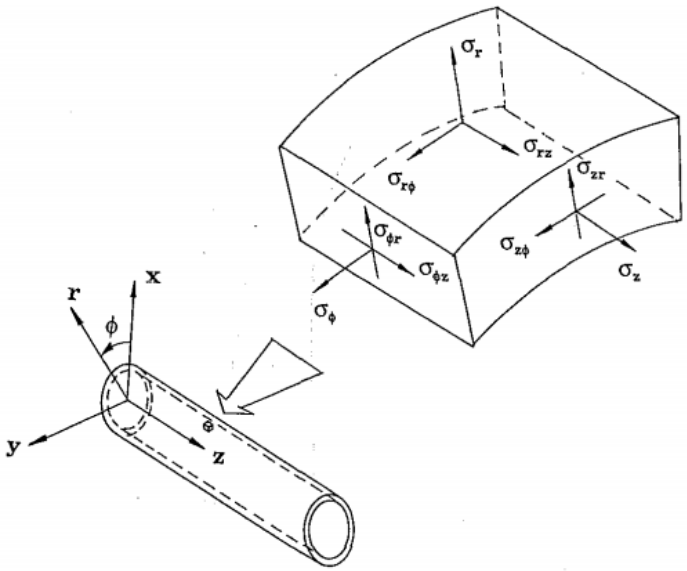

Figure 2.19 Cylindrical coordinate system and positive stresses

Torque and rotation angle φ relationship could then be obtained through equilibrium equation and is given in eq. (2.17) where R_o and R_i are the outer and inner radius and k is the index of each lamina of the composite. The same equation can be found in other studies too (for example in Geng et al. 2021).

$$T = \int_{R_i}^{R_o} \sigma_{z\varphi} 2\pi r^2 dr = \\ = \int_{R_i}^{R_o} (\bar{Q}_{66})_k \cdot \gamma_{z\varphi} 2\pi r^2 dr = \\ = \frac{2\pi\varphi}{L} \int_{R_i}^{R_o} (\bar{Q}_{66})_k \cdot r^3 dr \tag{2.17}$$

Eq. (2.18) gives the same relationship in the form of summation instead of foregoing integration with $r = R_i + kt_o$, t_o the uniform thickness of each lamina and n the total number of layers.

$$T = \frac{2\pi\varphi}{L} \sum_{k=1}^{n} (\bar{Q}_{66})_k \cdot (R_i + kt_o)^3 dr \tag{2.18}$$

The shear strain at each radius in terms of torque can then easily be obtained by substituting eq. (2.16) into eq. (2.18). Eq. (2.19) was then derived.

$$\gamma_{z\varphi} = \frac{Tr}{2\pi \sum_{k=1}^{n} (\bar{Q}_{66})(R_i + kt_o)^3 t_o} \tag{2.19}$$

In the same study experimental investigation on five pipe samples was made. The shear strain experimental results were compared with the results from the analytical solution of eq. (2.19) and from FEM analysis. Maximum deviation of 17.5% between the experimental and analytic data and 9.8% between the experimental and FEM analysis data were observed. The analytic solution of eq. (2.19) was also evaluated in the static torsion experiment conducted in LME facilities in the context of this thesis which is presented in Chapter 4.

In Guijs (2018) installation of two SG rosettes on a carbon shaft was made and this set-up was found to be functional (Figure 2.20). No torsional tests were conducted though. Other alternative solutions were also proposed when SG application on a composite shaft may not be possible or reliable. This may occur for example when SG cannot be placed away enough from a potential stress concentration area or an edge, when the proper attachment of the SG is difficult to achieve (accurate alignment, surface preparation) or may lead to problem (e.g. bad soldering can introduce local strain), or when mechanical properties are not a priori known or is difficult to calculate. Such alternatives include the attachment of the SG on the metal flange or hub of the shaft. This is also recommended from manufacturers of SG or torque transducers (e.g. Micro-Measurements-VPG, Binsfeld, https://binsfeld.com/support/torquetrak-support/torquetrak-support-strain-gage-installation/).The metal part which connects the flange with the shaft (Figure 2.21) is also an area where SG could be placed. If the length is not sufficient it could be increased although this would alter the initial design of the shaft system. Stress concentrations may present in such areas because they are at the end of the shaft and due to presence of bolts. FEM analysis may be required to determine the exact position. Another option could be the installation of a metal ring as shown in Figure 2.21 with accurately known properties around the shaft, which will create a uniform stress distribution on it (if it has a sufficient length) and thus the strain measurement will be performed on it. Another solution would to add a spool at the end of the shaft (Figure 2.21) close to the load (e.g. propeller) and attach the SG on it. This may lead to an increased whirling though. Lastly and foremost, torque transducers, like the one presented previously (HBM T10F), is a proven technology which offers a compact and reliable solution with high quality results. All of the above alternative options skip the direct installation of SG on the composite, orthotropic shaft and the associated problems, and perform the measurement on an isotropic part.

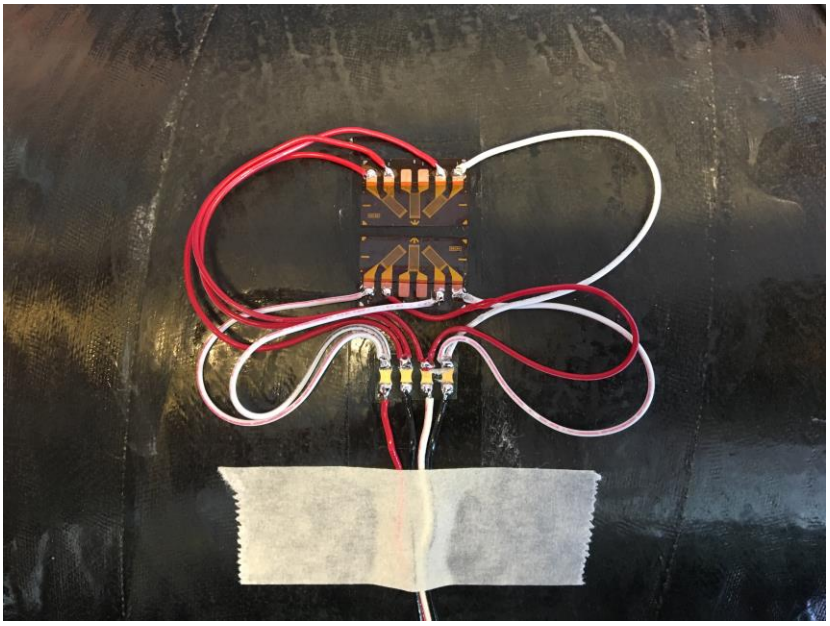

Figure 2.20 3-grid SGs on a carbon shaft (Guijs 2008)

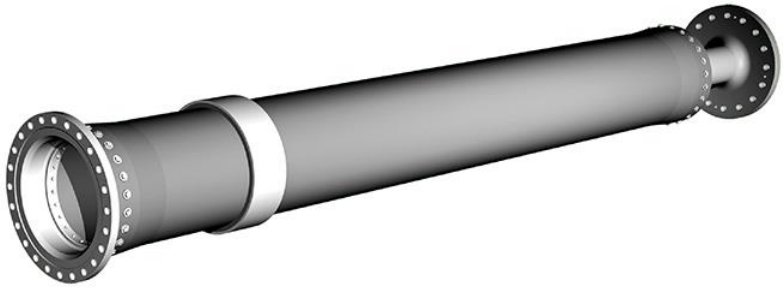

Figure 2.21 Composite shaft. The flange and its metal, connection part is shown at the left end. The metal ring is also visible. At the right end the spool is shown.

2.2 Fiber Optic Sensors Applications

The range of applications of FOS (and mainly FBG) in strain measurement in composites is enormous. From a comprehensive research it can be stated that much literature exists for lab-level testing of composite structures with FOS (mainly FBG) attached or embedded, but few for public domain applications in real structures. In this section, some representative applications, which realize smart composite structures due to their integrated network system of FOS, are briefly presented. Generally, FOSs in composites are almost solely used for structural and condition monitoring. The driving force for using FOS is their comparative advantages to conventional strain monitoring systems, mainly their small size, weight and anti-electromagnetic interference.

A completely review of all the applications of such sensors is unattainable in the context of this thesis. Thus, some representative applications are presented below which are related to the airspace industry, which extensively uses composite materials to components of their structures and the marine industry. Lastly, application of FOS for strain measurement on a composite shaft is presented, which consist the core of the objective of this thesis. It has to be mentioned that

although the rapid development of this technology in the last decade, it has not yet reached its limits. New aspects constantly arise and previous ones are still investigated and enhanced.

2.2.1 General Applications

In the airspace and aviation industry, in the not far past, it has been realized the importance and the necessity of real-time dynamic strain measurement of aircraft during flight conditions. The example of "Helios" solar powered UAV from NASA (Ma & Chen 2018), which suddenly broke up due to wing disintegration during test flight, is characteristic (Figure 2.22).

Figure 2.22 Helios (Ma & Chen 2018)

In that sense, wing shape deformation is critical for the safe operation of aircraft. Thus, the monitoring of the dynamic deformation of wing is critical. FOS embedment has been investigated and used as an alternative to traditional techniques such as SGs, which although convenient, they have the disadvantage of extensive transmission cables which combined with the signal processing units, add non-negligible weight to the whole structure. Furthermore, network with conventional SGs cannot be used for extremely long-time period. As reported in Ma & Chen (2018), NASA Langley Research Center tested the application of a FOS system for wing shape measurement of a UAV (Ikhana, see Figure 2.23) for the first time in 2008. One more investigation has been done on an experimental remotely piloted aircraft (X56, 2017, see Figure 2.24). In the first case the results were in excellent agreement with SG while in the second, the results for the wing deflection were far more than satisfactory.

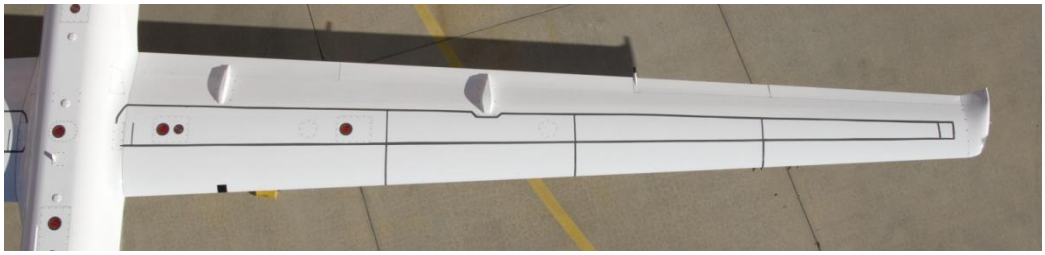

Figure 2.23 Ikhana (NASA.gov)

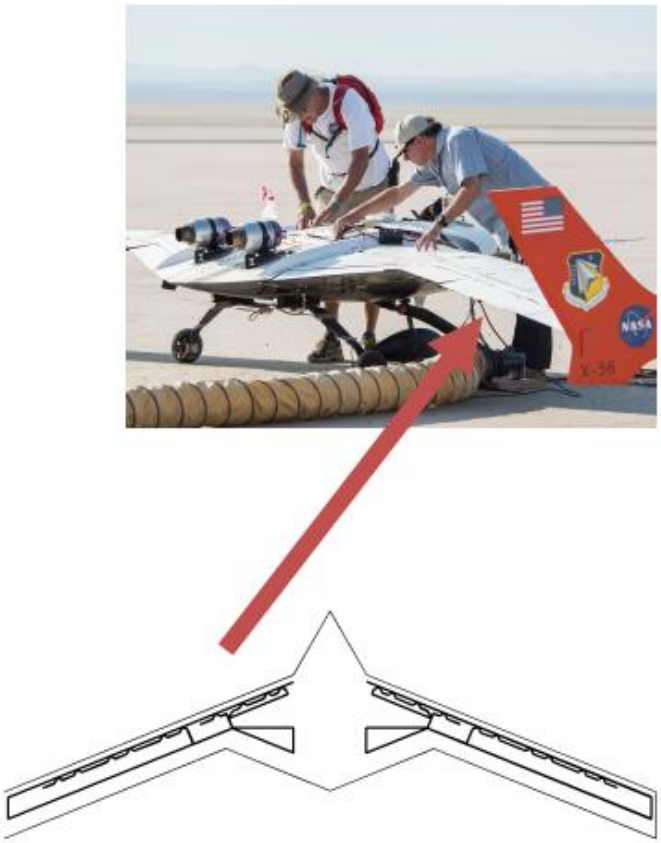

Figure 2.24 X56

In Nicolas et al. (2016) an operational application was demonstrated. A 5.5 m wing of an ultralight aerial vehicle was fabricated from carbon fibers with two optical fibers attached along the main spar on the upper and lower skin respectively (Figure 2.25). This resulted in 388 sensors on the upper skin and 390 on the lower skin. 4 conventional strain gauges and a tip displacement gauge were also attached. Two algorithms, based on classical beam theory and considering only pure bending, were used, in order to estimate the deflection and load based on the measured strains. Then, the strain results from FBG sensors were used to estimate the wing shape and the out-of-plane load, under concentrated and distributed loading scenarios from a three-tier whiffletree mechanism. The results showed that the total computed load based on FBG strains is within 1.62% of the applied load, while the computed out-of-plane loads is within 2% of the applied load. The calculated deflections, based on the FBG strains for several load levels, and the predictions are within 4.2% of the measured data and the computed FBG-based loads are within 4.2% of the measured applied loads. From the experimental results it was concluded that the high spatial density of the FBG measured strains can give detailed information for the defected shape of the wing and the out-of-plane loads, especially when compared to the results of the SG. Thus, this FOS system is able to determine the health state of the composite wing.

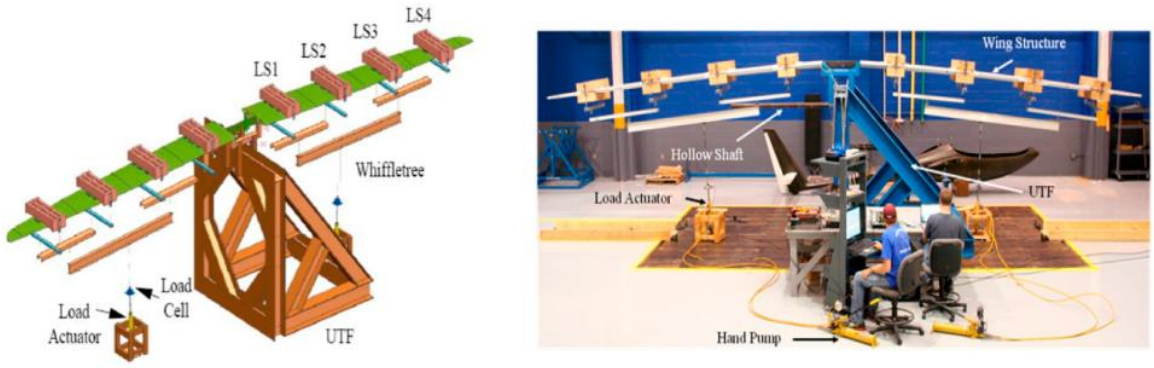

(a) (b)

Figure 2.25 (a) Scheme of the test frame with the Loading Stations (LS) visible, (b) real phot of the wing under whiffletree loading

As composite materials have started to be used more and more in structures in marine industry so has the application of FOS on them for SHM. This is necessary in order to monitor in real-time the integrity of the ships and improve maintenance programs, which can enhance the operational availability and safety of the ships (Qiu et al. 2013). The military was the first which showed great interest in exploring the use of FOS systems (mainly FBG) to ships and military (or relative) vessels made of composite materials were probably the first case where such sensors were tested and employed in the author's knowledge. Specifically, composite hull embedded sensor system (CHESS) project of USA Naval Research Laboratory and Norwegian Navy in 1996 reported the preliminary development of a system of FBG on the composite hull of minehunter vessel for monitoring of transient strains due to wave slamming (Kersey et al. 1997). The same project also developed a system of distributed fiber optic sensors for hull structure monitoring of the pre-series fast patrol boat (MTB) KNM Skjold (Figure 2.26). This was a 45 m long twin-hull surface-effect ship made fiber reinforced polymer sandwich composite which was delivered to the Norwegian Navy. The system was employed in sea-keeping trials giving important results. Another application conducted on the same vessel was the continuous measurement of global loads (sagging/hogging moment, the horizontal bending moment, and longitudinal twisting moment) acting on it, through a network of FBG attached on the inside of hull panels at specific positions (Jensen et al. 2001).

Figure 2.26 Pre-series fast patrol boat (MTB) KNM *Skjold*

FOS system has also been tested and successfully implemented for SHM of the metal hull or other components of commercial ships. Example of such application are the 100.000 DWT tanker "Four Island", where a network of 48 FBG sensors was used on its hull for determination of the elastic deformed shape and evaluation of the cycles of fatigue (Kotsidis 2012), or the HULLFIB system where FBG sensors where place on the deck of an LNG carrier in order to provide real-time information on stress levels due to longitudinal bending moment and give warning when undesired level of stresses have been reached (Figure 2.27). Nowadays, many commercial off-the-selves (COTS) hull structural monitoring systems have been produced which either use SGs or FOS (among other components such as accelerometers etc.). A representative list of them is given in Phelps & Morris (2013). Use of FOS technology for the real time monitoring of cargoes and cargo handling systems (temperature/humidity readings at cargo space and in refrigerated containers, draught readings for measuring the weight loaded or unloaded, liquid level on tanks sounding pipes) has also been proposed in Ivce et al. (2004).

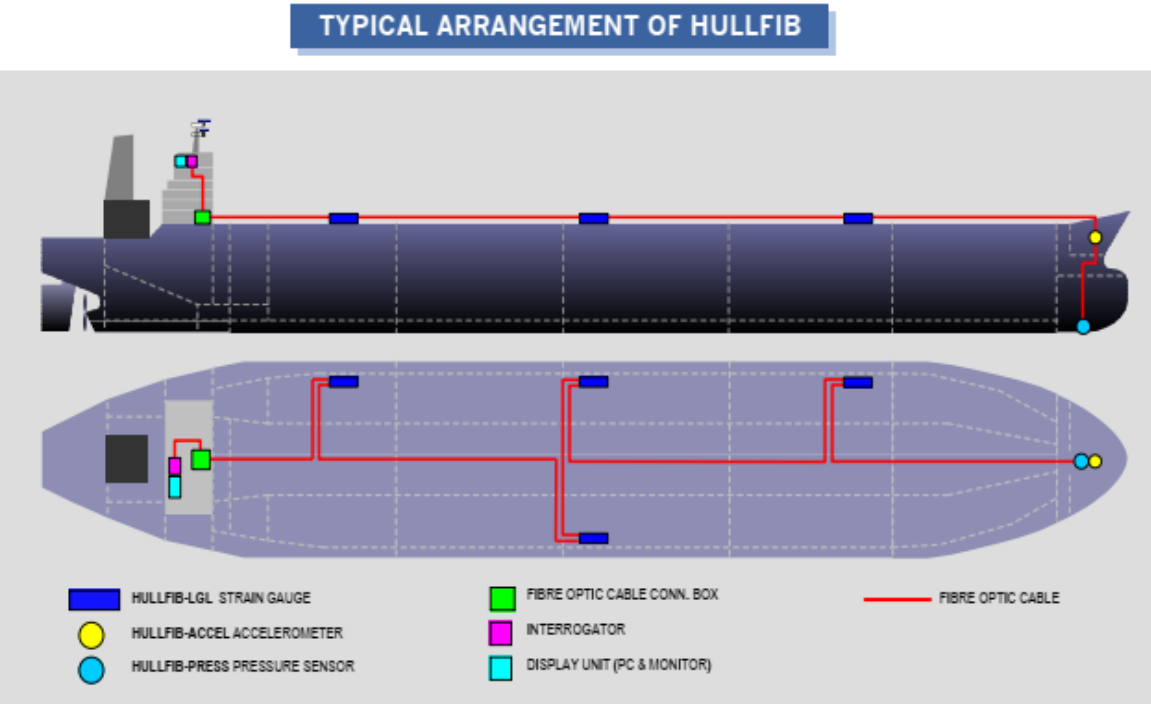

Figure 2.27 HULLFIB system arrangement
for real-time monitoring of stress levels on the deck of an LNG carrier

2.2.2 Applications on cylindrical structures (shaft, pipes etc.)

FOS were firstly used on cylindrical structures for torsion and torque measurement approximately two decades ago. Despite their advantages over conventional methods using SG that have been previously mentioned, they still remain in an experimental level and are not yet used in commercial application (e.g. driveshaft of ships) in the author's knowledge. In the followings, some typical examples of the use of FOS (FBG commonly) on cylindrical structures are presented. Both metal and composite shaft applications with FOS were found. Special consideration was given in technology and devices that can contactless transfer the optical signal outside from the shaft.

In Tian & Tao (2001) FBG on metal shafts were studied. The main aim in this paper was to obtain the torsional deformation (angle φ) through the strain induced on the FBG that was helically attached on the surface of the shaft. In Figure 2.28 a schematic configuration of the shaft with R radius with the FBG helical angle α is depicted. Theoretical calculations were made and a relationship between the torsional angle φ and the strain induced on the FBG sensor ε_s was established in eq. (2.20). In this equation H is the length of the shaft, M is the torsional moment applied, R is the external diameter of the shaft where the FBG is attached and r is the diameter of the optical fiber (commonly R ≫r). It can be seen that the helical angle of the FBG sensors bonded on the shaft affects the results. Estimation of the optimal angle where also made. Taking as a reference the shaft in **Figure 2.28** it was concluded that an $\alpha = \pi/4$ angle resulted in the highest (tension) strain ε_s in the FG sensors while $\alpha = 3\pi/4$ in the smallest (compression) strain.

Axial strain ε_s is obtained from the FBG principles which for constant temperature is given in eq. (2.21), where $\Delta\lambda$ is the Bragg wavelength shift, λ is the Bragg wavelength and f is the photoelastic constant which is a sensitivity factor related to the optical characteristic of the optic fiber and to the deformation status.

$$\frac{\varphi}{H} = \frac{2\varepsilon_s}{(R+r)\sin 2a} \tag{2.20}$$

$$\varepsilon_s = \frac{\Delta\lambda}{\lambda \cdot f} \tag{2.21}$$

An experimental test was contacted in order to validate the results of the above theoretical analysis. In a copper shaft a static torque was applied by a torque tester which also recorded the torsional was recorded from this device. Two FBG were attached on the surface in different directions, one at 45 degrees (sensor 1) and one at 35 degrees (sensor 2). As it can be seen in Figure 2.29 the calculated angle from sensor 1 is much closer to the tested one (recorded from the torsion meter) than the calculated angle from sensor 2. This was mainly related to then helical angle of the FBG sensor but also to the bonding conditions and the accuracy of calibration procedure. From the above results, the feasibility of using FBG for measuring torsional deformation was concluded.

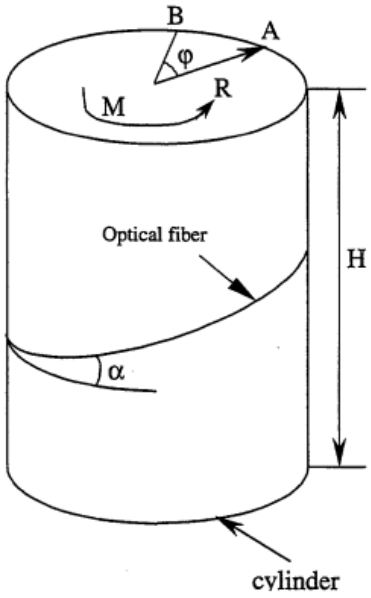

Figure 2.28 Scheme of a shaft with FBG helically attached on its surface Tian & Tao (2001)

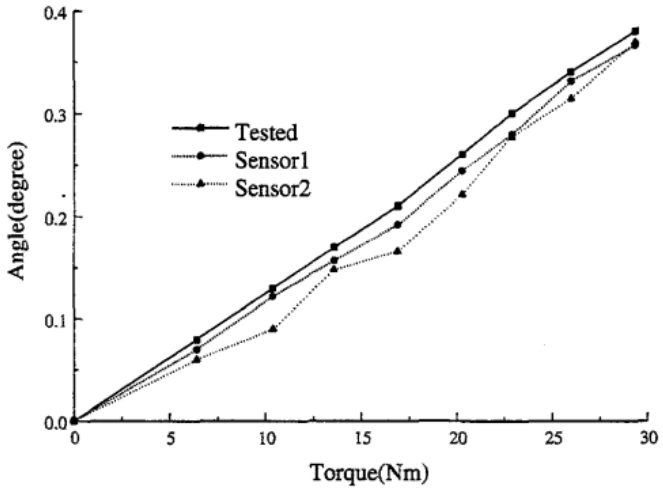

Figure 2.29 Angle vs Torque diagram with FBG (sensors 1 and 2) and torsion meter results (Tian & Tao 2001)

Another application of FBG on metal shafts is reported in Kruger et al. (2004). A novel non-contact measurement method of torsion on a rotating steel shaft was presented there. This method involves FBG sensors along with Graded Index (GRIN) lenses for the contactless transmission of the optical information from the light source to the gratings and then back to a spectrum analyzer. This offers a great advantage over conventional methods involving slip rings. The sensor system is relatively insensitive to temperature changes and electromagnetic interference, and it has twice the strain sensitivity of a single Bragg grating.

Two gratings are mounted on the surface of the shaft at 45° with respect to its axial direction (Figure 2.30), to measure pure tensile and pure compressive strain (principle strains of opposite sign). A light wave propagates from a broadband optical source such as a super luminescent diode (SLD) or a scanning narrowband optical source along an optical fiber. The optical power is guided through a device that is able to separate the paths of the incident optical excitation and the returning signal from the measurement transducer. An optical circulator performs this function in the embodiment. The coupling between the stationary part of the system and the rotating part occurs through a set of suitably aligned lenses (GRIN) (Figure 2.31). In the author's opinion, this technique is of great interest for the objective of this thesis, thus it is further discussed later in this section.

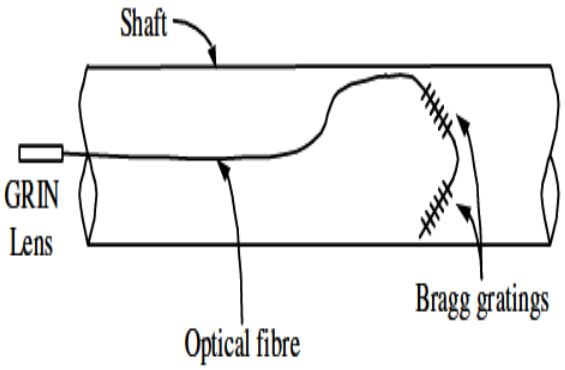

Figure 2.30 Details of Bragg gratings on a rotating shaft

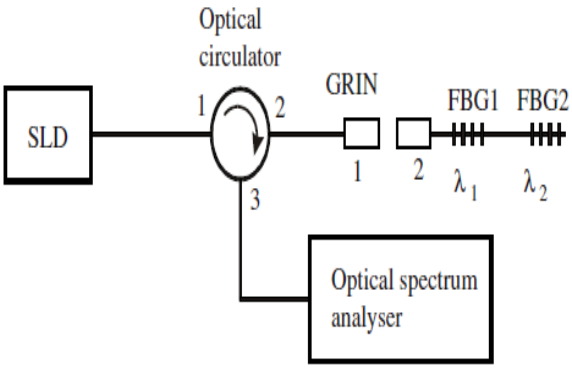

Figure 2.31 Optical set-up for non-contact torsion measurement

The Bragg gratings have different center wavelengths λ_1 and λ_2. It was proposed and examined if the change in the difference in the two center wavelengths of the Bragg gratings (differential-mode signal) was proportional to the torsion applied and whether the change in the mean value of the wavelengths (common-mode signal) was proportional to the common temperature of the Bragg gratings on the shaft. Experiments were performed on rotating propeller shaft of a micro-light aircraft. One end of the shaft was clamped in the lathe chuck, and the other end was fixed to a drum brake system (Figure 2.32), allowing the application of torque to the shaft which was independently measured on the brake system by two watt meters and a phototachometer. Torsion measured by the gratings was compared to theoretical estimations and the results were in close agreement. The differential wavelength change was then 7.4 pm N^{-1} m^{-1} (Figure 2.33). The low and steady temperature sensitivity of this dual-grating torsion sensor on the differential mode wavelength was also confirmed by mounting the shaft into an oven and varying the temperature stepwise. More accurate alignment of the GRIN lenses could better reflect the light to the optical spectrum analyzer and thus further improve the final spectrum image. It is concluded that this method can successfully measure torsion (and therefore torque) with the ability to separate the temperature effects.

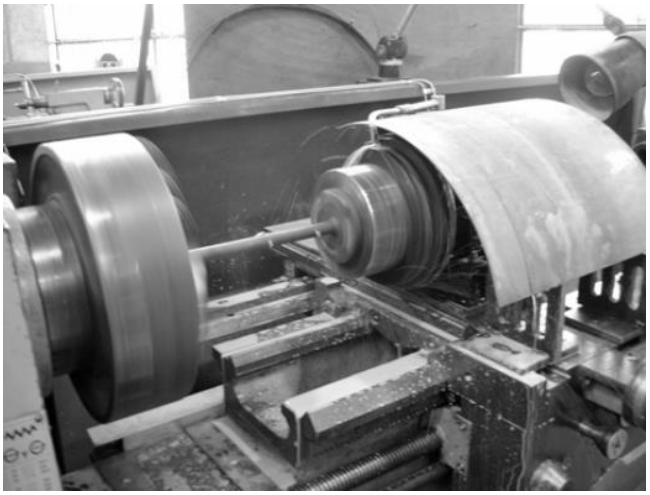

Figure 2.32 Mechanical experimental set-up showing the chuck (left), shaft (center) and the water-cooled brake on the right

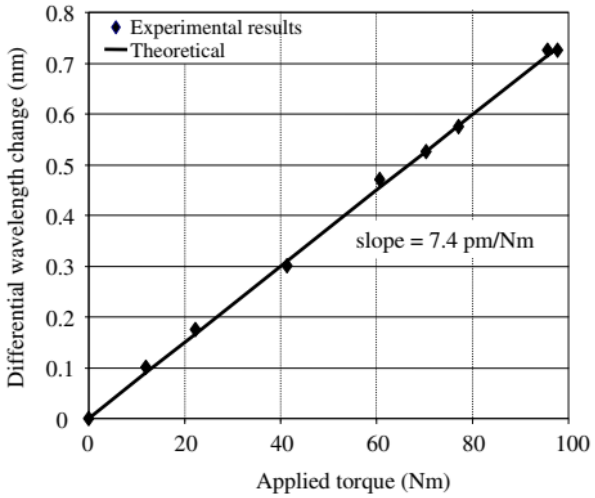

Figure 2.33 Changes in the differential-mode wavelength as a function of applied torque

In Swart et al. (2006) the same method of the dual-Bragg gratings was further analyzed in respect to its theoretical background. The dependence of torque and temperature on the differential-mode wavelength and the common-mode wavelength was elaborated. In addition, the effect of the misalignment error on these dependences was also investigated and expressions were derived. Next, a static torsional test of a metal hollow shaft was made, with two FBG on its surface at +45° and -45° with respect to the axial direction. The reflectance spectrum was recorded for several combinations of torque and temperature. A schematic representation of the shaft arrangement is depicted in Figure 2.34.

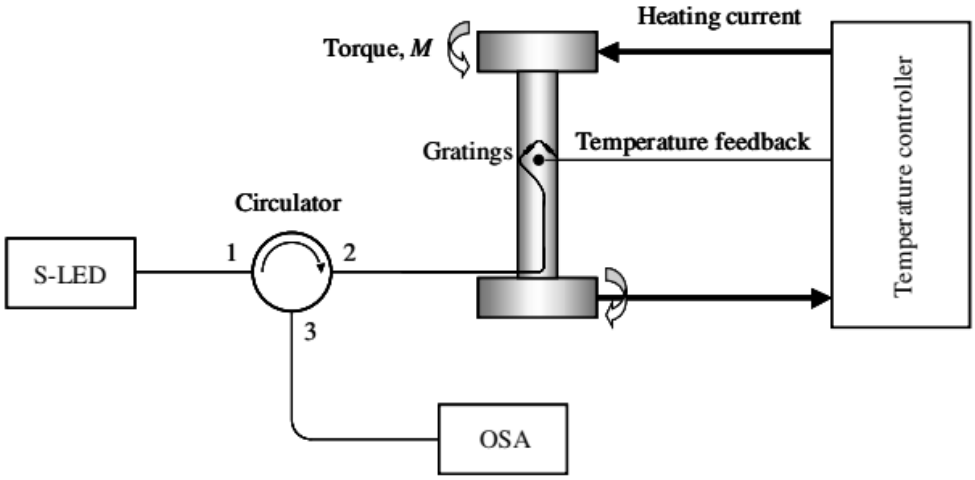

Figure 2.34 Schematic representation of the shaft arrangement (S-LED: super-luminescent diode; OSA: optical spectrum analyzer)

The experimental results again confirmed the observation that the changes in the wavelength difference between these double gratings is proportional to the applied torque, while the change in the mean resonance wavelength of the gratings was proportional to their common temperature.

The torsion and temperature sensitivity for the differential-mode wavelength was measured at 19.4 pm $(Nm)^{-1}$ and -0.36 pm $°C^{-1}$ which was better than the results reported in Kruger et al. (2004). For the common-mode wavelength the torsion and temperature sensitivities were -0.19 pm $(Nm)^{-1}$ and 25.3 pm $°C^{-1}$ respectively. Thus, independent torsion and temperature measurements can be made with this method.

Gradient Index (GRIN) lenses are commonly used for non-contact transmission of optical signals and are vital components in relevant devices (e.g. FORJ see Section CHAPTER 2) or in other similar techniques (as the one presented previously in Kruger et al. 2004). According to the Encyclopedia provided by RP Photonics company (https://www.rp-photonics.com/gradient_index_lenses.html), in order to make the the output optical beam either converge or diverge in any on lens, phase delay of optical waves passing through the lens on the radial direction must vary. In contrast to classical lenses though, where the optical phase varies radially due to the variation of the thickness, in GRIN lenses the thickness remains constant. What changes radially is the refractive index within the lens material. The refractive index is highest near the center and lower outside in order to focus the light beam and vice versa for defocusing. The radial change of refractive index is usually approximately parabolic. A parallel input ray is oscillated (approximately sinusoidal) in the propagation path inside a focusing GRIN lens). The pitch of a focusing GRIN lens is defined as the number of oscillation cycles of such a ray which can occur over the whole length of the lens. Full-pitch, half-pitch (for output image inversion), quarter-pitch (can be used as a beam collimator) lens or any other pitch values can be achieved. GRIN lenses have usually a cylindrical rod shape (Figure 2.35).

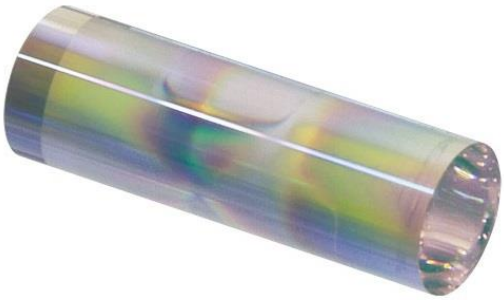

Figure 2.35 GRIN lens (Source: Thorlabs)

Common fabrication methods are ion exchange methods, partial polymerization, direct laser writing, chemical vapor deposition and neutron irradiation. Some great advantages of GRIN lenses are that they can have very small size and flat surfaces, which make them suitable to handle and for integration to other optical components. On the other hand, optical aberrations (spherical aberrations and chromatic dispersion), parasitic reflections and birefringence may occur in these lenses. Beyond fiber-to fiber coupling applications (e.g. FORJ), GRIN can be also used in fiber collimator, focusing (e.g. for optical data storage), imaging (objectives for endoscopes), ophthalmology applications etc.

Edmund Optics from USA with worldwide presence is a leading global manufacturer and supplier. GRIN rod lenses are offered for focusing applications with small working distance or for collimation of single and multi-mode optical fibers and laser diodes with zero working distance. Prices range approximately from 55€ to 80€ in retail. One type of 3-D printed GRIN lenses are also offered used for defense application such as night vision systems (https://www.edmundoptics.com/search/?criteria=GRIN&SearchPartNumbers=false&Tab=Products).

Thorolabs is also a global leading manufacturer and supplier of GRIN lenses among others such as GRIN lenses for imaging applications and for collimation and focusing (https://www.thorlabs.com). Pigtailed glass ferrules with or without connectors and with single mode, multimode or polarization-maintaining fiber pigtails designed to be paired with GRIN lenses are also offered (Figure 2.36) which satisfies many experimental needs. GRIN lenses are available with either 0° or 8° face angle. The 8° versions (Figure 2.37a) maximize the return loss by back reflecting the incident light at a non-normal angle and are recommended for building collimators. In contrast, the 0° versions are easier to align but are only recommended for general fiber-to-fiber coupling (Figure 2.37b).

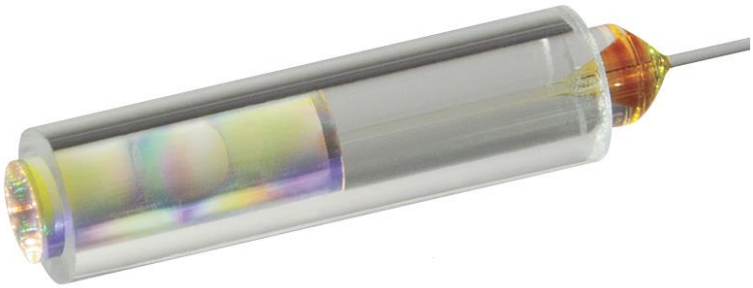

Figure 2.36 GRIN lens (left) and pigtailed ferruled (right) coupled

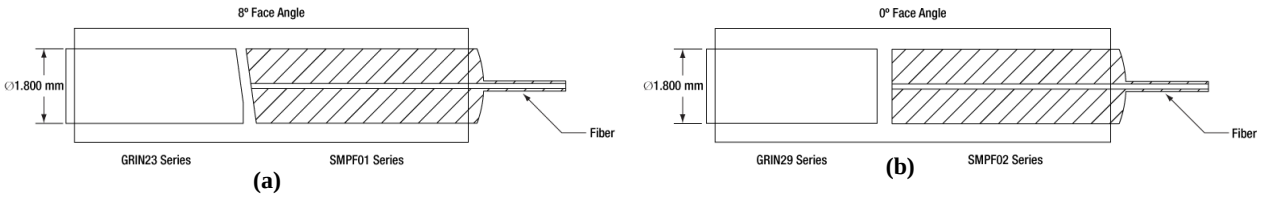

Figure 2.37 Schematic representation of 8 degrees (a) and 0 degrees (b) GRIN lenses coupled with pigtailed ferrules

C-lenses are another category of such lenses which have similar overall working principle and structure to GRIN lenses, with a small difference in theirs shape though. The rear end of these lenses is spherical and not planar like in GRIN lenses (Figure 2.38). Low cost, low insertion loss in long working distances and a wide working distance range are some advantageous characteristics of C-lenses compared to GRIN lenses. Such lenses are typically used for fiber

optics applications such as collimators, isolators, switches, MEMS, collimator arrays and laser assemblies (Jing et al. 2004).

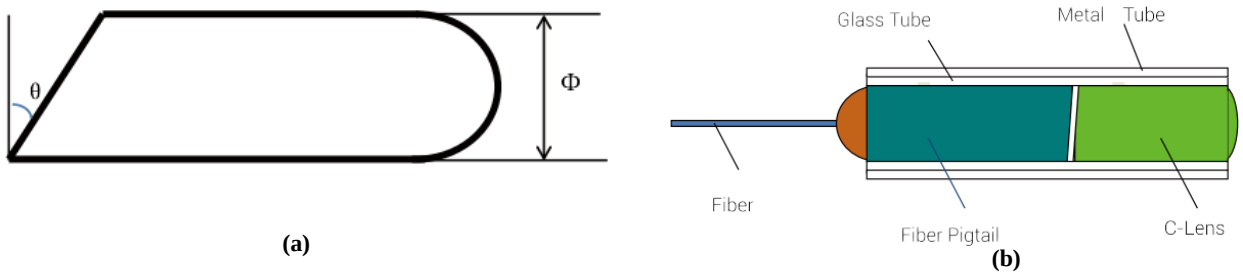

(a) **(b)**

Figure 2.38 (a)C-lens scheme (spherical rear end)
(b) Scheme of C-lens acting as a collimator coupled with a ferrule of a pigtailed fiber in a glass tube

In Lee & Hwang (2008), C-lenses were used in a rotary optical coupler for continuous transmission of optical information about strain data measured with FBG on a wooden blade (see Figure 2.39). In that way, the cross-sectional area of the optical connection was widened and the light could travel parallel to the lens axis. This renders the optical connection less prone to break when the shaft is rotating and improves the insertion loss and the mechanical tolerance.

In Figure 2.40 the sensor on a rotating shaft can be seen. The rotary optical coupler consists of two coaxial lenses. The right one is placed in the center of the rotating shaft end, while the left lens at the stationary part with a small air gap. Figure 2.39 gives a close-up view of the lenses. A reference FBG was also placed near the right lens, in the axial direction of the shaft. This is a special treated sensor which was designed to be insensitive to deformation. In that way, the light intensity loss change is compensated. The sensor arrangement described in this study mainly tackles the intensity loss change problem encountered in FORJ, where the magnitude of light intensity loss varies with the rotational angle due to mechanical and optical errors. Furthermore, the rotational speed limit of FORJ is also addressed. Lastly, it is recommended in cases where the room required for the installation is relative small. Although the test conducted in this study was on wooden blades, this sensor arrangement can be practically implemented in any rotating part and is greatly promising for condition monitoring of rotating parts and detection of external impacts.

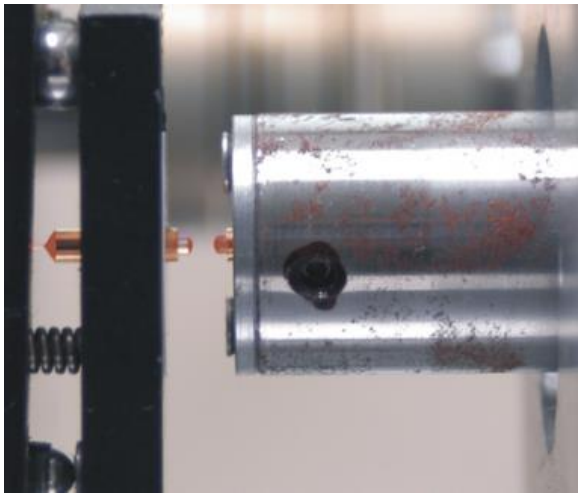

Figure 2.39 Close-up view of the lenses of the rotary optical coupler

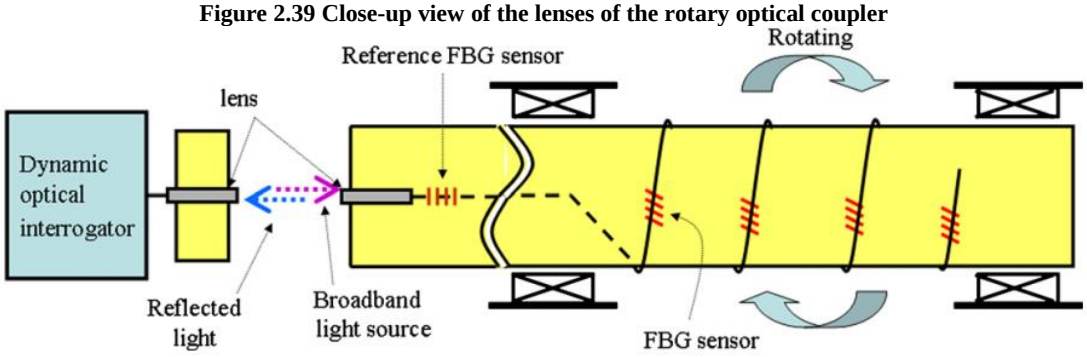

Figure 2.40 Arrangement of the rotary optical coupler and the FBGs

2.2.2.1 Composite cylindrical structures

Composite cylindrical structures, such as drive shafts, pipelines, fuselages etc., are widely used in many industries due to their previously mentioned excellent properties such as low weight and thus high specific strength and stiffness. For the requirement of continuous monitoring during manufacturing processing and for in-service SHM of such structures, FOS is a promising option that is constantly developing. The embedding capabilities and the easiness of the embedding procedure of such sensors in a composite structure, argue in favor of using FOS for SHM needs.

A characteristic study on the field of composite drive shafts under torsion was recently made in Konstantaki et al. (2021). FBG sensors were used on a CFRP shaft under torsion for the purpose of developing an SHM system through residual and torque-induced strain monitoring. A hollow CFRP 2.2 m long shaft was fabricated at the premises of B&T Composites S.A., Florina Greece with an external diameter of 49.5 mm and a nominal wall thickness of 2.0 mm. This shaft was equipped with embedded and surface-mounted FBG sensors during filament winding manufacturing procedure, at various orientations with respect to the shaft axis (longitudinal, parallel to the reinforcing fibers at 55° and circumferential) and at different longitudinal positions. Then this shaft was cut into two pieces with a diamond-coated disk. Two sub-shafts were then produced (shaft A: 89 cm and shaft B: 114 cm). Figure 2.41 schematically depicts the

FBG sensors on each shaft. Through special steel fittings attached at the edges of each shaft, one end was clamped while the other was mounted on a torque wrench for the application of static torque. The reflection spectra of the FBG were acquired in real-time through a 2×1 couple and a spectrometer (Figure 2.42) and then the results were analyzed. Temperature variation was negligible and thus no compensation was needed.

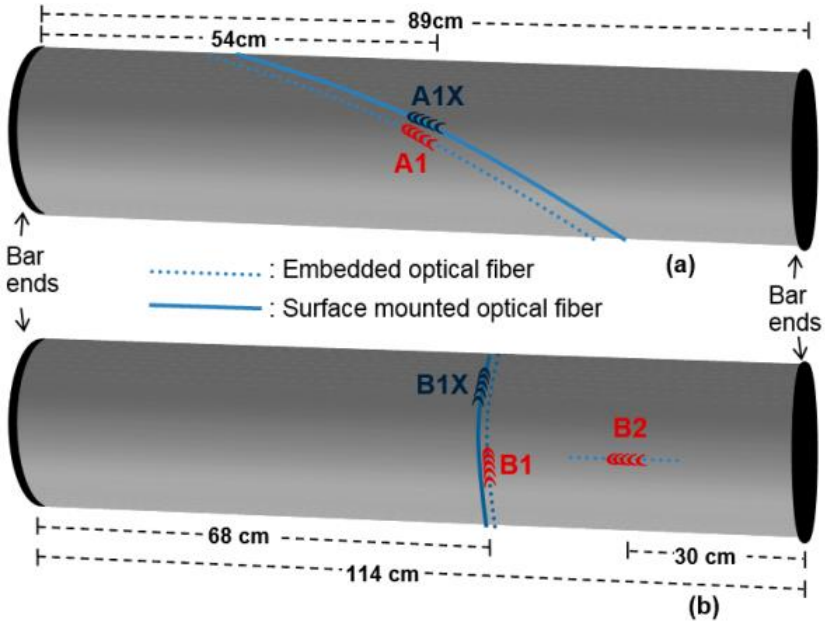

Figure 2.41 (a) Shaft A with FBG at the orientation of the external carbon fibers, (b) shaft B with FBG at circumferential and longitudinal orientations

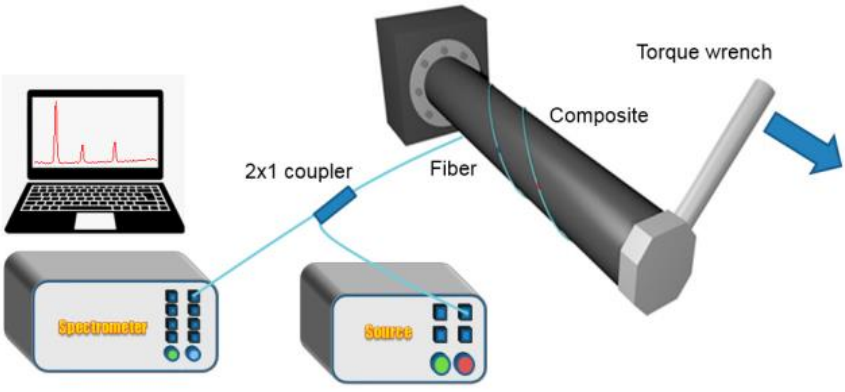

Figure 2.42 Scheme of the experimental set-up (Konstantaki et al. 2021)

After the curing process, the spectral signals of the only embedded FBGs (A1, B1 and B2) were monitored in order to compare them to their initial spectral signals. A blue-wavelength-shift (reduction of the wavelength) was observed in all FBGs which indicates compression on the fibers. This is mainly attributed to the thermal shrinkage of the resin after the curing. Then, torque was applied up to 800 Nm. Numerical analysis with a homogenized material model was also conducted for comparison. As a conclusion, it was stated that FBG can attribute in SHM

methods on composite shafts under torsion. For optimal strain transfer from the composite material to the optical fiber, FBG parallel to the reinforcing fibers should be placed. For the embedded FBGs, the sensitivity of A1 (parallel to reinforcing fibers) was four times greater than B1 and B2 (circumferentially and longitudinally place respectively). Moreover, surface mounted FBG compared to embedded FBGs are proposed as the most viable solution. However, this is application dependent. For example, for delamination monitoring or residual strain measurements embedded FBG are required. Factors such as ease of installation, protection etc. should be considered prior to the decision. It should be also stated here an interesting observation about the possibility of implementing this technology in rotating shaft although no such application was investigated there. As on would expected, the crucial part is the connection between rotating and stationary part of the equipment. Fiber optic rotary joints (FORJ) are proposed and this technology is briefly discussed below.

Fiber optic rotary joints (FORJ) are passive opto-mechanical components which provide a continuous, non-contact fiber optic connection between a rotating and a stationary part. They are also called fiber optic slip rings as they are the optical equivalent of the electrical slip rings (Snow 1998). With the increasing use of fiber optics the last four decades approximately, the need for transferring the optical signal across a rotating surface has been emerged in a variety of diverse applications in defense, engineering (including marine), robotics, medical, renewable energy industry, such as radar pedestals, armored vehicle turrets, remotely operated (underwater) vehicles (ROVs), wind turbines, electro-optic sensors and others. With FORJs digital data are transferred in the majority of these applications although in some cases analog signal transmission is also preferred (some radar systems, fiber optic distributed applications).

FORJs can be divided into classes based on the mode of operation, which include passive or active, and the number of passes (number of physical fibers), which include single or multi-pass. Passive FORJs transmit the optical signal from the rotating to stationary structure without any electronics for processing although components such as filters and lenses can be used to "process" the optical signal. This type of FORJs is the most common used for widespread applications. On the other hand, in active FORJs an electrical signal is optically transmitted across the gap, thus an electrical to optical (E/O) convertor is required. Other electronics are used for the processing of the signal in order to enhance transmission properties. Such procedures may include amplification, signal conditioning and re-clocking. Active FORJs can be considered as directly, non-contact substitutes of conventional electrical slip rings. For specific applications, customized FORJ can be designed which include slip rings for the power supply of electronics (Dorsey & O'Brien). An interesting application in the medical field is the FORJ used for optical signal transfer when hollow bore is required like in CT scanning imaging machines. There, X-ray image data from the rotating machine are optically transmitted through rotating lenses to the pick-up lenses and then to the stationary image processor (Figure 2.43). Although such design has not been reported in any other application, the potential use in rotating shafts could be realized in the future.

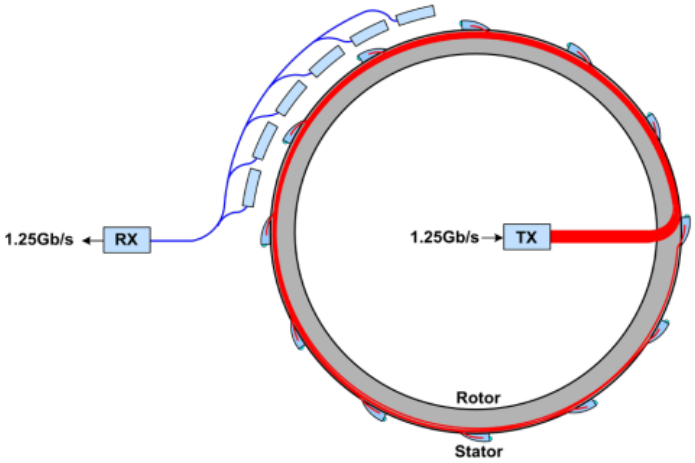

Figure 2.43 Hollow bore active FORJ achieving 1.25 Gbps

Single pass FORJ is the simplest configuration for FORJs. In each side of FORJs (rotor and stator) a single optical fiber is used. The fibers lead to lenses at both opposing sides of the interface for the coupling of the light. One fiber-to-lens part is able to rotate using a suitable bearing configuration. Lenses and fibers orientation is coincident to the rotation axis of the FORJ. Such lenses are the Graded index – GRIN lenses which were first used in FORJs with a ¼ pitch for collimating the beam of light (Figure 2.44) or the C-lenses which were used in Lee & Hwang (2008) and Jing et al. (2004) with very good characteristics. Merits of these designs are low insertion loss and relaxed mechanical tolerances compared to single fiber without lenses and fiber bundle designs, which can be also used for the signal transfer. Fiber with large diameter can also be used but they are not so common.

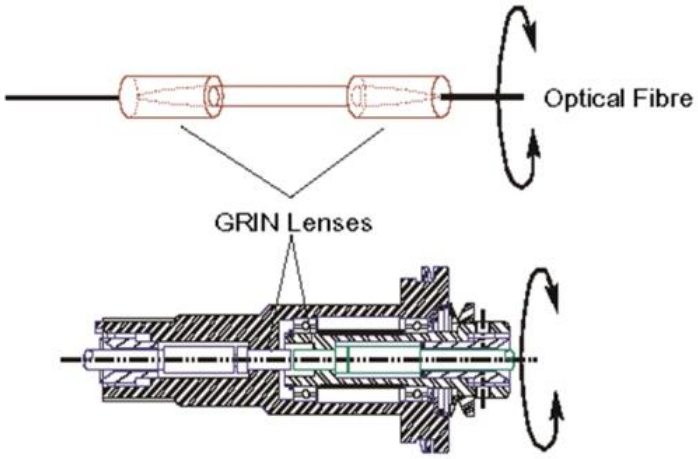

Figure 2.44 Single pass FORJ with ¼ pitch Grin lenses (Dorsey & O'Brien)

In multi-pass techniques optical signal are coupled between specific pairs of fibers from each side of the FORJ. Coaxial designs where the lenses operate just like in the case of single pass

FORJ (Figure 2.45) are the most commonly used. In general, these designs are more mechanically complicated and have larger size.

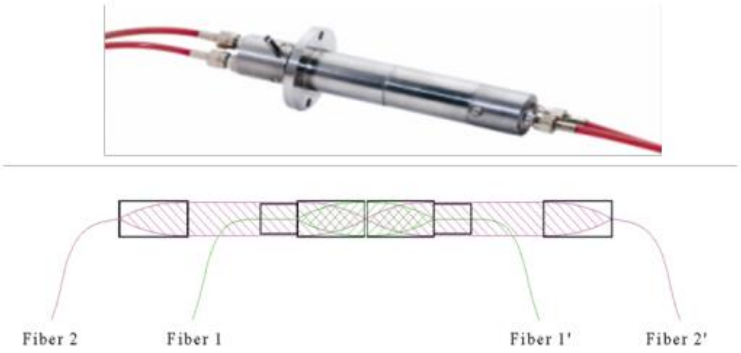

Figure 2.45 Two-pass lens based FORJ

Apart from multi-pass FORJs, multiplexing is also an option for multi-channel transmission which exploits the capability of a single fiber to have unlimited bandwidth. Multiplexing has significant advantages like the reduction of the complexity of the system and cost-effectiveness compared to the multi-pass system. Figure 2.46 below illustrates a common multiplexing configuration for the transmission of a bidirectional communication signal through a single fiber using two wavelengths of light simultaneously. More wavelengths can be used to transfer different optical signals with the wavelength division multiplexing (WDM) technique. Full duplex Ethernet connection usually implements this technique.

Figure 2.46 Schematic representation of bidirectional signal multiplexing configuration using two separate wavelengths

The main problem encountered in fiber optic transmission lines in general, including FORJ, is the losses in the line which affect in the magnitude of the signal. The FORJ insertion loss should therefore be carefully taken into consideration. Lateral misalignment, axial separation, and angular tilting are crucial factors in order to keep the insertion losses as low as possible (Figure 2.47). On the other hand FORJ have some major advantages, according to manufacturers:

- No contact and friction, long life, up to 10 million rpm (more than 100 million rpm for signal channel)
- Thin and lightweight compared to copper wire cables.
- Flexibility which allows them to be used in flexible digital cameras in medical applications, mechanical imaging, plumbing etc.

- Ruggedized for harsh environments
- Can combine multiple signals such as video, series, Ethernet signal, etc.
- Use of optical fibers to transmit information with no leakage, no electromagnetic interference and low signal degradation
- Can carry digital signals
- The transmission bandwidth is much larger than the electrical connector, and it can be used to double the bandwidth with the wavelength division multiplexer.
- Large amounts of data transmitting, up to hundreds of Gbps
- Compact size that is easy to integrate with electric slip ring and easy to upgrade and change
- Multiple channels on customer request.
- Photo-electric integrated rotary joint available

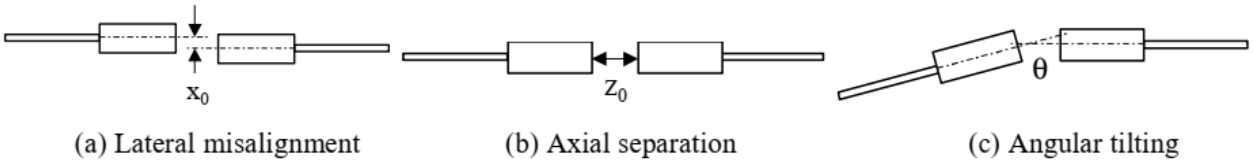

Figure 2.47 Factors that affect the insertion losses in FORJs

Applications on drive-shafts which interest us, for example for ship propulsion, have not been found in the literature. In such cases, the egress point of the optical fibers of the stationary part of the device (considering that the FORJ will be somehow mounted coaxially in the center of the hollow shaft) will be an interesting problem to tackle.

FORJ are mainly supplied in compact form with the optical fibers integrated. Some well-established FORJ manufacturers and/or suppliers are listed below.

- Moog from USA and offices all around the world. One of the leading manufacturers which supplies plenty of industries. Hybrid (electrical and optical) and complete (fluid rotary joints integrated) rotary joints are available (https://www.moog.com/products/fiber-optic-rotary-joints.html). Large bore active FOJRs are provided (https://www.moog.com/products/slip-rings/commercial-industrial-slip-rings/large-diameter-slip-rings.html).
- BGB from UK. Offers a variety of products available including unique designs such mini, L-type and even capacitive FORJs (https://www.bgbinnovation.com/optilinc/)
- MOFLON from China with sales and service network all over the world (https://www.moflon.com/mfo.html)
- RION from China with sales and service network all over the world (http://www.rionsr.com/products/fb_list.html)

- JINPAT Electronics from China (https://www.slipring.cn/h-pd-15.html" \l "_jcp=2&_pp=122_0)
- SENRING Electronics from China (https://www.senring.com/fiber-optic-rotary-joints/)
- Mortek, supplier in Greece mainly engaged in telecommunication industry (https://www.mortek.gr/).

For more information on the available products of their catalogue, their website should be explored. When price information was available (although in almost all case this was not true), prices ranged from around 700 $ to 22000$ in retail with increasing complexity of the product (more channels, multimode optical fibers, flange mounting etc.).

Another SHM approach for composite cylindrical structures was implemented in Shamsuddoha et al. (2021). Thermoplastic composite tubes with cut-outs (Figure 2.48), manufactured robotically with an Automatic Fiber Placement (AFP) machine, were tested under axial compression, torsion and biaxial (compression and torsion) loads in an Instron 8852 servo hydraulic machine and with a novel biaxial jig. For the monitoring of the deformation of the structure, a distributed fiber optic sensor was used, equipped with an optical backscatter reflectometer (OBR) interrogator with sub-centimeter spatial resolution. The optical fiber was placed close to the cut-out at the longitudinal direction (Figure 2.49). A strain gauge rosette was also attached at the opposed side of the optical fiber to the cut-out and digital image correlation (DIC) was also used for the full field strain measurement of the tubes. This method is further discussed in the Section 2.4.

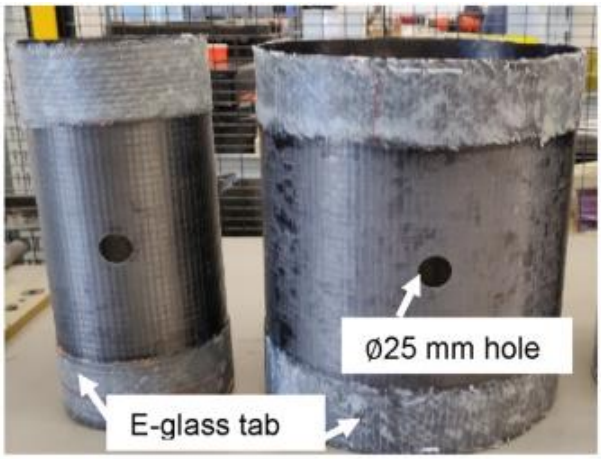

Figure 2.48 Manufactured tubes (Shamsuddoha et al. 2021)

The results of the distributed sensor were compared with the results of an FE analysis (Figure 2.50). A laminated composite cylinder model was created. In general, good agreement was observed. In addition, the experimental results show smoother gradients compared to FE results which is probably due to the poor strain transfer between the soft acrylate coating of the fiber and its core. Removing of the coating in the locations of the sensors is proposed. On the other hand,

the general deviation of the results is mainly attributed to the manufacturing method (AFP), which created surface undulation. This led to grids of overlapped or elevated layers in the surface which affected the bonding of the optical fiber and thus the strain transfer. This induced the relative strain mismatching compared to the ideal FE model. The same observations were also true for the strain rosette results. Lastly, an interesting finding was that the directional deformations around the edge of the cut-outs (longitudinal, radial or rotational deformation) induced by the axial compression and the torsion can be superimposed to give the biaxial deformation. Overall, the DOFS proved to be an effective SHM tool of composite tubes.

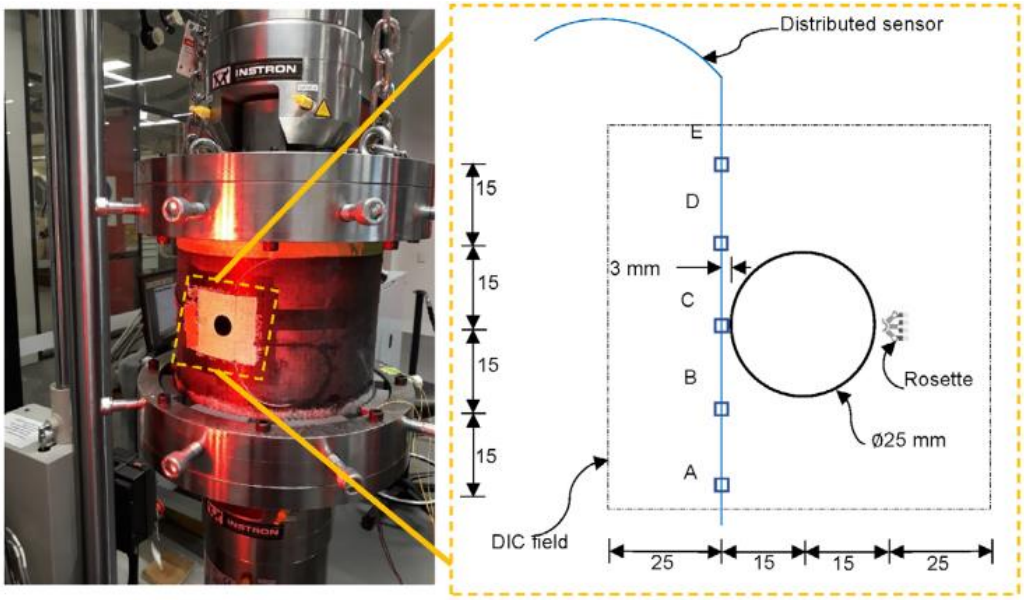

Figure 2.49 Sensors location (Shamsuddoha et al. 2021)

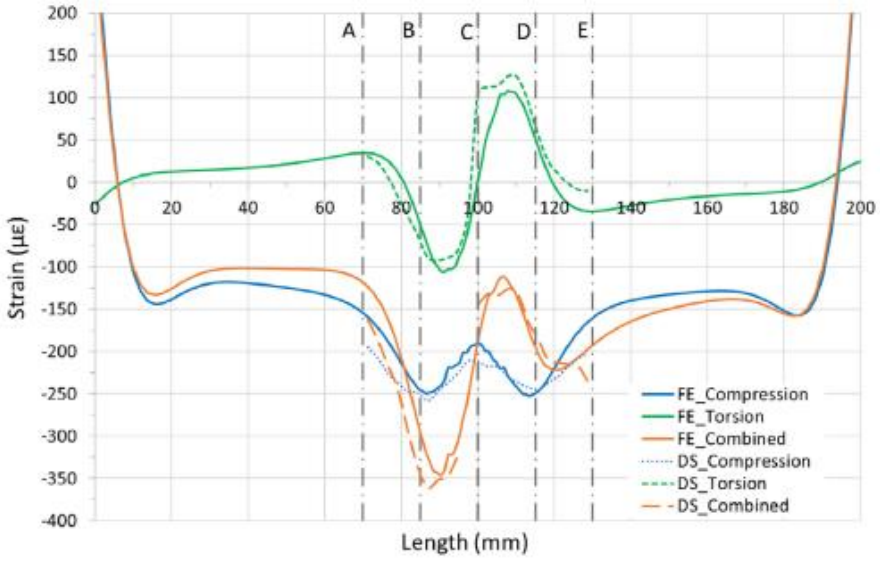

Figure 2.50 Strain obtained from FEA and distributed optical sensors versus length of the tube for the applied loads (Shamsuddoha et al. 2021

2.3 Twist Angle

Another conventional method for torque measurement is the one based on the twist angle of the shaft. Eq. (2.22) gives the well-known relationships between the applied torque T on a circular shaft and the twist angle θ, with G being the shear modulus of the shaft material, J the polar moment of inertia and L the length of the shaft.

$$T = \frac{GJ}{L}\theta \tag{2.22}$$

Such methods are based on the measurement of the relative torsion angle between two distinct sections along the length of the shaft with known mechanical properties. To do that many techniques have been used or investigated by researchers. The majority of them are based on the twist angle measurement of two discs (encoders) placed around the shaft at different axial positions. Electromechanical or optical technologies are deployed for that reason. The part in between these two sections can either be part of the shaft, with the two discs mounted after the shaft assembly, or can be an extra torsion bar inserted in the shaft in-between the motor and the load. The amount of such techniques that can be found in literature is large, thus some typical cases are mentioned below. The main advantage of these systems is that they are independent of the local strain of the shaft and the local condition of its surface. In addition, the material of the shaft and particularly its orthotropic behavior, does not affect the twist angle measurement (Guijs 2018). The shear modulus of the shaft should be known though, as eq. (2.22) shows.

A solution proposed in de Silva (2015) for measuring the twist angle is through two toothed gear wheels placed at two axial locations of the shaft (Figure 2.51). These gear wheels are made of ferromagnetic material in order to comply with the non-contact, magnetic induction type (self-induction or mutual induction) proximity probes. Other types of such sensors can be used such as eddy current proximity probes and Hall-effect proximity probes. These sensors are firmly placed radially around the gear facing their teeth. The output electrical signal of each sensor is in pulse form. The relative phase shift of these two signals reflects the twist angle between these two gear wheels, with the assumption that under zero torque the two probes signals are synchronized. The direction of the torque can also be determined in that way. If the phase shift is φ, the twist angle θ and the toothed gear wheel has n teeth, then $\theta = \varphi/n$ and eq. (2.23) becomes:

$$T = \frac{GJ\varphi}{Ln} \tag{2.23}$$

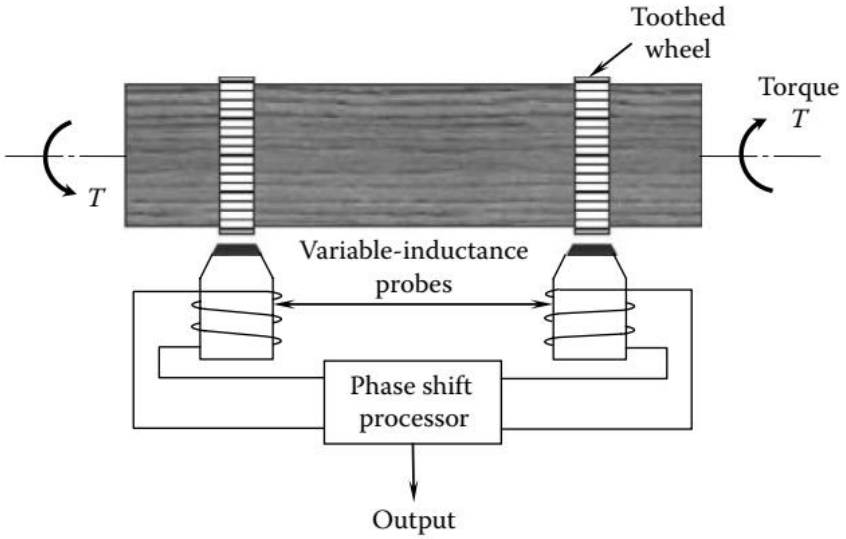

Figure 2.51 Scheme of the sprocket wheel and proximity sensors configuration

Optical methods employ systems that have two "code" discs mounted on the shaft, a light emitter and photodetector. Commonly, these discs have a pattern of slots or small windows on their plain surface where the light passes through (Figure 2.52). As torque is applied, the two discs relative positions change which lead to a change in the amount of light passing through them. This change is proportional to the applied torque and can be detected through the photodetectors. Other optical methods have a setup that resembles the technique of the magnetic proximity sensors mentioned previously. For example, in Pantaleo et al. (2006) a torsion bar with two discs on its end is inserted on a shaft. On each disc a black strip is marked through its thickness and two commercial high resolution optical reflective sensors are placed above them as schematically depicted in Figure 2.53. These sensors are able to detect these black strips and produce a current pulse when they cross their detection area. Two signals generated of which their frequency is inversely proportional to the shaft speed and the phase difference is proportional to the angular twist θ.

Some interesting commercially available system for twist angle measurement which utilize a variety of different methods mainly for marine applications, are reported in Guijs (2018) such as inductive encoders from Zettlex (https://www.celeramotion.com/zettlex/) optical with slotted wheels with LEDs from Kongsberg (https://www.kongsberg.com/maritime/products/engines-engine-room-and-automation-systems/Machinery-Instrumentation/engine-monitoring systems/metapower-quad/, Figure 2.52) optical with linear precision position encoders from Chris-Marine (https://chris-marine.com/products/monitoring-of-diesel-and-gas-engines/permanent-shaft-power measuring-system-shaftpower/) optical by VAF instruments (https://www.vaf.nl/products-solutions/overview/t-sense-shaft-power-torque-meter/) and acoustic vibrations sensors from Hoppe (https://www.hoppe-marine.com/product/measuring-solutions/maihak-shaft-power-meter).

In general, this type of torque transducer with the two discs mounted on the shaft and the two sensors is usually more suitable for installation on already existing shaft systems without the need to dismantle them. In addition, there is no limit on the shaft size and the cost for proximity sensors is very low. On the other hand, the additional inertia added on the shaft due to the circumferentially distributed mass of the sprocket wheels should be taken into account in some cases. Space limitations may also be a prohibitive factor for using this sensor configuration when the sprocket wheels have large diameters. Furthermore, environmental factors affecting the sensors, such as dust, humidity, temperature or even lubricants which can blind the sensors should also so be taken into account. Vibrations, shaft tilts or misalignment of the discs-sensors system may also affect their performance. The calibration constant $\frac{GJ}{L}$ as can be seen in eq. (2.22), need to be as low as possible in order to have large twist angles and thus achieve high sensitivity and resolution. Torsion bars with a proper selected material with low torsional stiffness can fulfill this requirement. Lastly, in general the cost of these twist angle based system is relatively high.

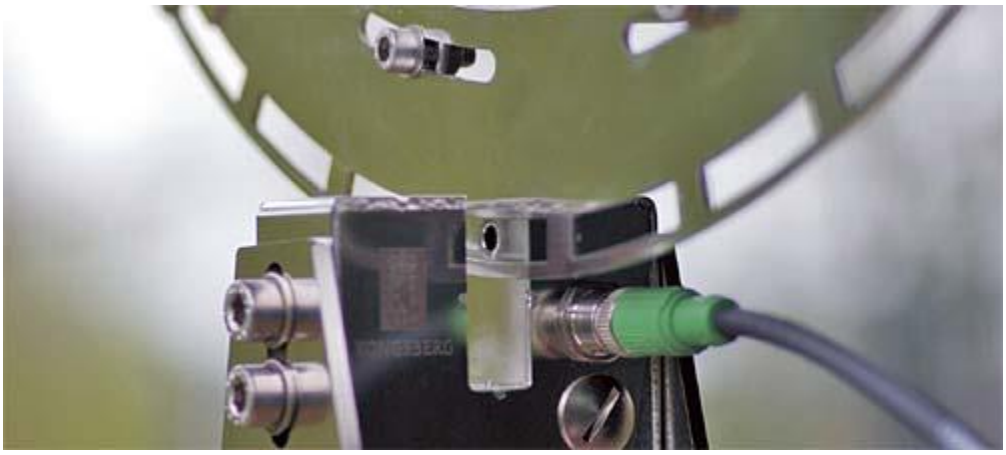

Figure 2.52 Slotted disc and LED for twist angle measurement (MetaPower from Kongsberg, source: Guijs 2018)

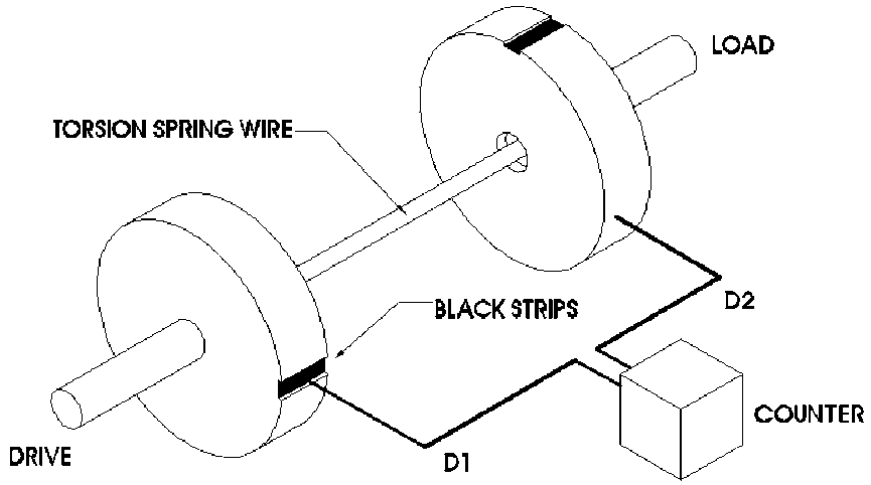

Figure 2.53 Scheme of a system consisting of two discs with black strips inscribed on them and two optical sensors (D1 and D2) (Pantaleo et al. 2006)

Another novel technique for measuring torque on a rotating shaft based on twist angle was presented in Garinei & Marsili (2017). This technique utilized the laser speckle contrast method. This method relied on the measurement of torsional displacement of two distinct section of the shaft through the measurement of their roughness with the aforementioned method. The different phase shifts of incident light beams on a rough surface result in a diffuse reflection composed of light and dark points which is called speckle (Figure 2.54). Through an optical fiber and a photodiode, information about the speckle, and thus the roughness, can obtained from the scattered light in the form of an electrical signal. Cross correlation of the roughness profiles of the two sections is conducted for the unloaded and the loaded conditions. The maximums in time of the functions carried out from the cross correlations for both loading conditions can be then used for the calculation of the angular shift $\Delta\vartheta$ from eq. (2.24), where t is the maximum time from the cross-correlation function, ω is the rotational velocity monitoring and the subscripts up and dw correspond to the uploaded and unloaded condition respectively.

$$\Delta\vartheta = \left(\frac{t_{up}}{\omega_{up}}\right) - \left(\frac{t_{dw}}{\omega_{dw}}\right) \tag{2.24}$$

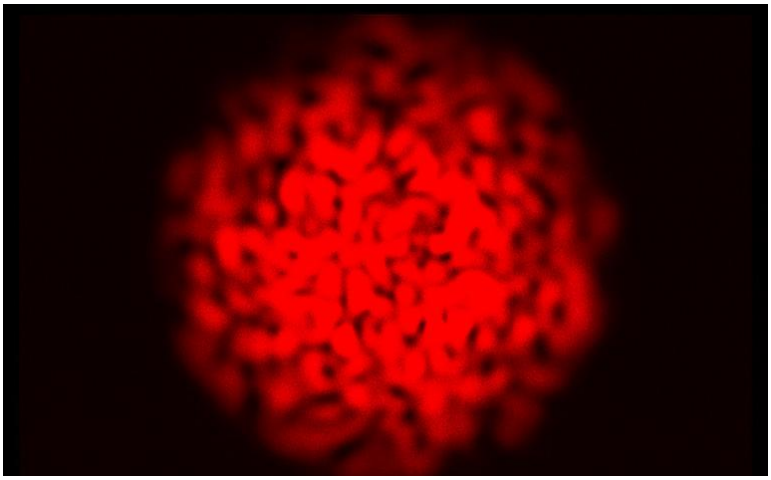

Figure 2.54 Speckle distribution (Garinei & Marsili 2017)

The measurement chain is depicted in Figure 2.55 which was evaluated through a number of tests. It is shown that an in-fiber beam splitter was used which was connected with two multi-mode fibers which strike the target surfaces. Two other multi-mode fibers received the back-reflected light which then entered the photodiodes. The incident angle and target distance from fiber head were found to be factors that affect the optimization of the back-reflected signal intensity. In addition, the target roughness, incident angle value and incident light wavelength were factors that affect the spatial resolution as they modulate the speckle distribution and intensity. The material used was also a critical factor due to the dependence of the scattered light from the conductibility. An experimental setup was created as schematically depicted in Figure 2.56 in order to measure the torque on a rotating shaft with the non-contact method giving promising results. The shaft torsional stiffness was obtained through a FEM of shaft model. In order to boost the performance of this system many aspects could be enhanced in the future such as the power of the light source and its wavelength, the relative position of the emitting and receiving fiber and the optical alignment improvement using fiber coupled components. The big advantage though of this novel system is that only an incident coherent light beam on the shaft is required. No additional equipment needs to be mounted on the shaft and thus is easier to be applied compared to other conventional non-contact techniques. However, practical application may face difficulties as shaft displacement or tilt may lead to decorrelation of the speckle pattern.

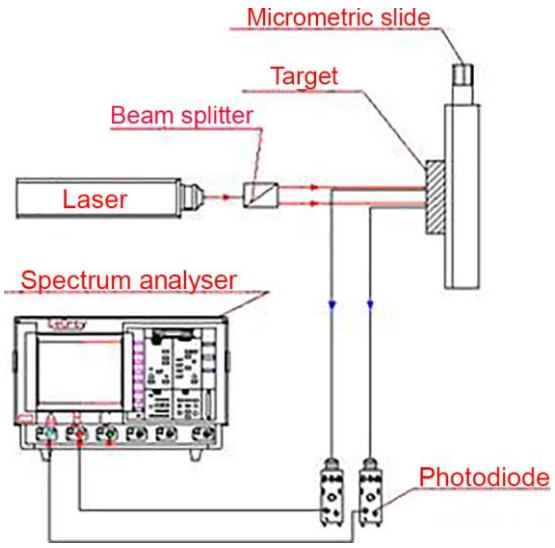

Figure 2.55 Measurement chain

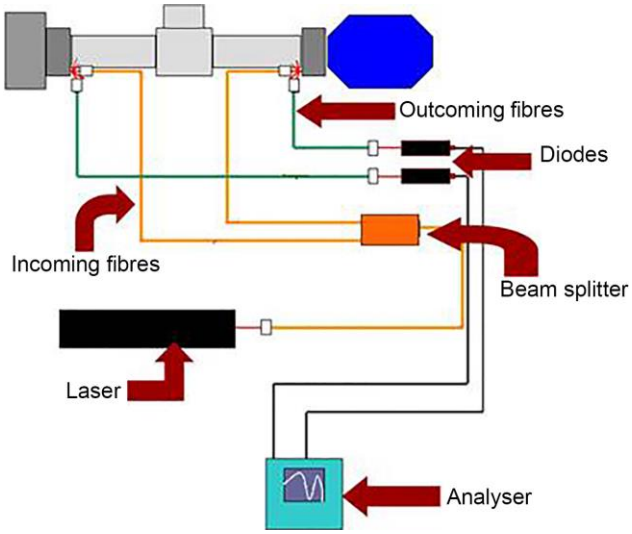

Figure 2.56 Scheme of the experimental setup

Another novel contactless, non-intrusive system for torque measurement on a rotating shaft based on the twist angle estimation was reported in Zappalá et al. (2018). A system consisting of two zebra tapes with equidistant black and white stripes attached around the periphery of the shaft and two optical probes pointing to these zebra tapes was employed (Figure 2.57). Each probe generated a pulse train signal proportional to the light intensity reflected by the zebra stripes (light intensity from the white surfaces was significantly larger than that from the black surfaces). By measuring the phase difference (time shift) of the two distinct pulse signals the twist angle of the shaft under torque can be obtained and consequently the torque.

Experiments were made for calibration and validation of the proposed system. Figure 2.58 depicts the test rig and Figure 2.59 gives a closer look on the contactless system of one optical probe and zebra tape. A conventional in-line torque meter was mounted on the shaft for calibration and comparison. An electrical generator and an electrical motor were used for varying the torque (0-16 Nm) and the rotational speed (up to 2100 rpm). The voltage output of the optical probes went through a Schmitt trigger which converted it into a train of constant amplitude square pulses. The data were collected by a DAQ system. The signals were processed with two distinct methods in order to estimate the absolute twist of the shaft: rising edge detection and cross-correlation approach, which determined the time shift between the two pulse signals. Measurement uncertainty evaluations was also made according to the ISO GUM (Guide to the expression of uncertainty in measurement) with Type A uncertainty analysis of the experimental data and Type B (Monte Carlo method) for the statistical variations of the parameters affecting system performance under real-world operating conditions with results around $\pm 1\%$ (cross correlation method was the worst case).

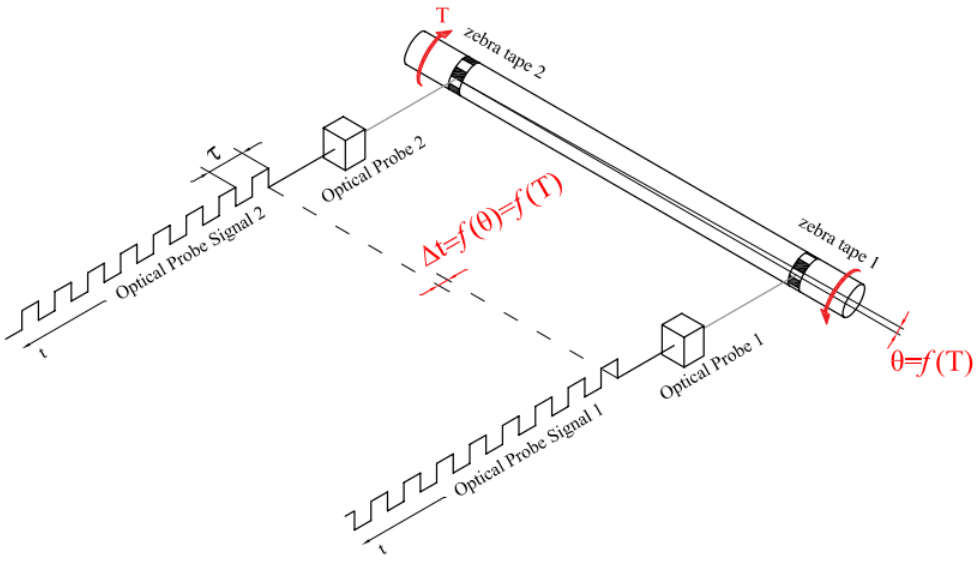

Figure 2.57 Schematic representation of the operating principle of the system (Zappala et al. 2018)

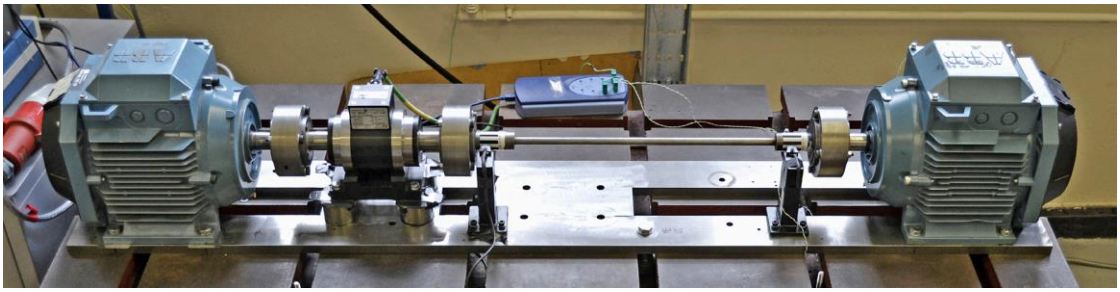

Figure 2.58 Torque test rig (Zappala et al. 2018)

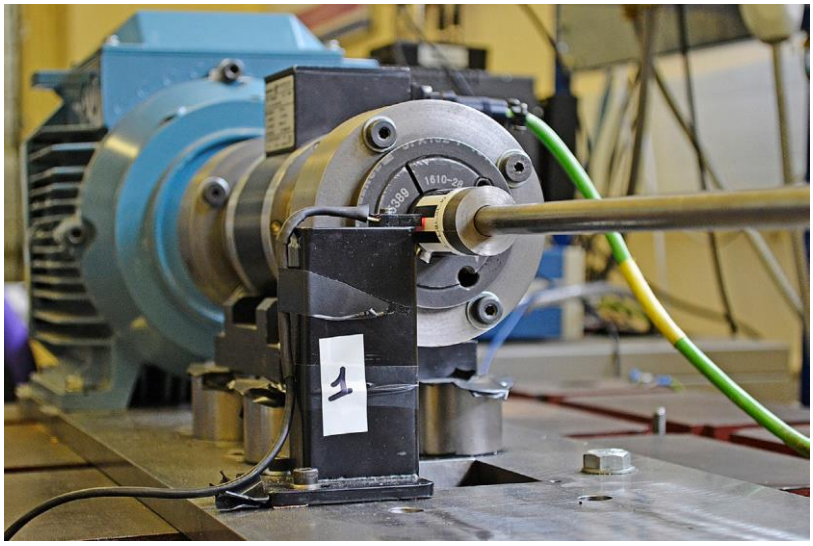

Figure 2.59 Optical probe and zebra tape (Zappala et al. 2018)

Calibration under steady state conditions showed a linear relationship between the torque and twist angle as expected from the theory. Tests under steady state (at 1700 rpm, 4N m and

1900rpm, 10N m) and variable state conditions were also made which gave results very close to that from the in-line torque meter. Cross correlation approach gave higher level of noise especially. Low pass digital filters were recommended to compensate this noise.

Compared to conventional twist angle based torque meters, this novel technique offers significant advantages such as less intrusiveness, robustness, easy and quick application, suitability to a large range of industrial application even in non-friendly environments. Rotational speed can also be obtained through the period of the pulse signal which diminishes the number of sensors in the system. This is quite important for example in naval applications where the space around the shaft is confined. In addition, the zebra tapes can be attached to any shaft diameter and can be quickly removed and placed to any other system. As also shown from the experiment conducted, accurate results are also obtained. Accuracy and sensitivity can be easily adapted or increased by carefully designing the zebra tapes or by simply modifying the distance between the two zebra tapes along the shaft, if that is possible. Lastly, this solution is considered cheaper than other conventional approaches. High-quality, laser-printed zebra tape were glued on the shaft (no market information available) and two Optek OPB 739 RWZ reflective line reader sensors were placed opposite to them. These sensors were found at a bulk price of 15∼16 € each. The most expensive item was the National Instruments (NI) 16-bit data acquisition system (USB-6211 DAQ) driven by the LabVIEW data acquisition environment. This was found at a price of approximately 1000 $.

2.4 Other methods

2.4.1 SAW

Surface Acoustic Waves (SAW) sensors are another option for non-contact strain and torque measurement on rotating shaft which is frequently used. Many manufacturers have designed and developed sensors based on this technology which are employed on existing drive shafts. SAW (or Rayleigh waves) are sound waves travelling parallel to the surface of an elastic material. Such waves have found widespread use in sensors, filters, oscillators, transformers etc. due to piezoelectric components integrated in such devices. SAW sensors typically consist of a piezoelectric substrate and interdigitated electrodes or transducers (IDTs) which can together convert receiving electrical energy to mechanical energy in the form of SAW. IDTs are formed in a grating-like pattern (which resembles fingers) on the piezoelectric substrate, as schematically depicted in Figure 2.60, and are essentially the electromechanical coupling between the input electrical signal and the piezoelectric substrate. An electrical interrogating signal is received through an antenna which then is converted to a SAW in the input IDT. The generated SAW propagates through the sensing zone (also called delay line in some SAW designs) and via the surface of piezoelectric substrate which in turn interacts with the gratings of the IDT and produces electrical signal through the reverse electromechanical mechanism of the piezoelectric effect. Changes in different physical parameters of the propagating SAW (commonly frequency

and amplitude) can reflect changes in other physical quantities of the structure on which sensor is integrated or the environment around the structure such as strains, pressure, temperature, humidity etc. SAW devices are therefore widely used in mechanical, chemical, electrical, physical science, and biological applications (Mandal & Banerjee 2022).

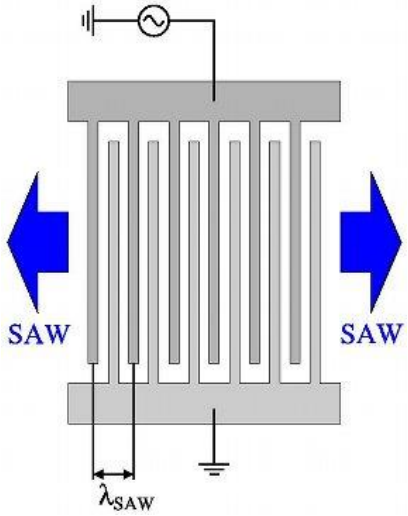

Figure 2.60 IDT pattern (λ_{SAW} is the pitch of IDT)

In general, different configuration of the IDTs and the SAW sensor can be designed based on the application for which is intended. The most common design for general SAW applications (including strain measurement) is the one which contains two IDTs (Figure 2.61): one for the input of the applied electrical signal and the other for the output where an electrical signal is produced from the waves. The space between them is called delay line and contains sensing films. Another design includes addition electrodes (reflective gratings) acting as a resonator which can be added on the delay line or at the side of an IDT without delay line. This design is typically used for strain measurement. The resonator SAW can be found in one-port configuration, where one IDT serves as the input and the output simultaneously, or two-port configuration with two IDTs. These designs can boost the performance (Q-factor) of the SAW sensor.

When two (or even more) IDTs are used, a standing wave in the resonance frequency is created in the cavity between the two reflecting gratings (Figure 2.62). The resonance frequency is determined by the surface wave velocity (u_s) and the electrode pitch p (λ_{SAW} in Figure 2.60) by the well-known formula (Donohoe et al. 2011) in eq. (2.25). Typically, the resonance frequency is in the UHF range (normally 430 MHz to 440 MHz). Strain applied on the structure affects both of these quantities and thus changes the resonance frequency. This can be detected by the output electrical signal which had been generated from the reflected acoustic wave formed in between the reflectors. The interrogation signal is a RF pulse and when the burst stops the decaying response RF can be obtained in the output for processing.

$$f_c = u_s/p \tag{2.25}$$

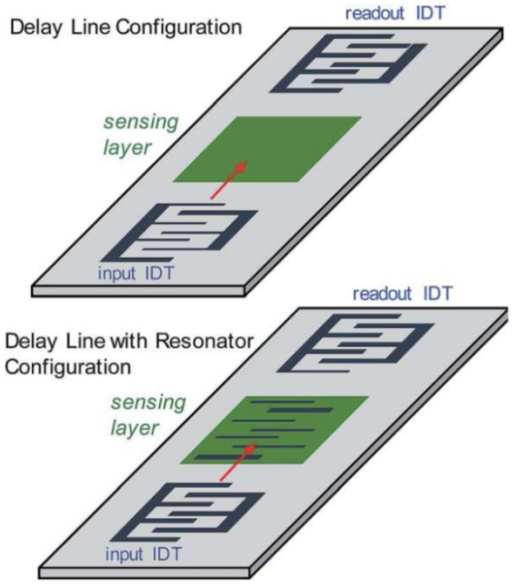

Figure 2.61 Delay line of SAW sensors with and without resonator

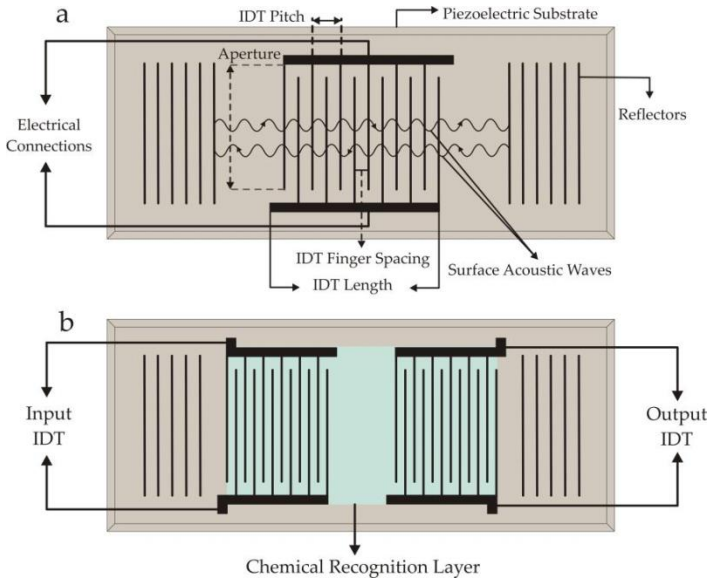

Figure 2.62 One-port and two-port SAW resonant sensors scheme

Torque measurement using SAW sensor is one of the common application of such sensors, although developed later (approximately the last two decades) compared to other SAW applications. SAW sensors in torque transducer act similar to a strain gauge attached on a shaft. Two SAW resonators are used in a half bridge configuration where one is positioned parallel to the principal compressive strain direction and the other at the principal tensile strain direction as schematically depicted in Figure 2.63. Due to this reason, the two resonance frequencies change in opposite directions when a torque is applied. The difference of these two frequencies is

proportional to the applied torque. Two SAW devices can be attached at diametrically opposite sides for bending compensation and more accuracy. Non-contact transmission of the interrogation signal from and towards the rotating shaft can be achieved with RF rotary coupler and without the need for batteries (passive).

Other SAW-based torque sensors with variations in the design may also be found in the literature available online. SAW-based torque sensors with the typical design described previously are commercially available by some manufactures due to their robustness, compact size, low cost, wireless passive sensing, immunity to magnetic fields and ability to work in harsh environments. The most established company which manufactures and licenses innovative, advanced, patent-protected SAW-based sensing systems for torque, force, pressure and temperature measurement for many industries (automotive, aerospace, marine, railway etc.) is Transense Technologies plc in Oxford (https://www.transense.com/). Off the shelf products were not available in the site of the company. Other manufacturer and suppliers such as Sensor Technology Ltd and Althen Sensors & Controls also mention that use SAW technology in some of their torque sensors.

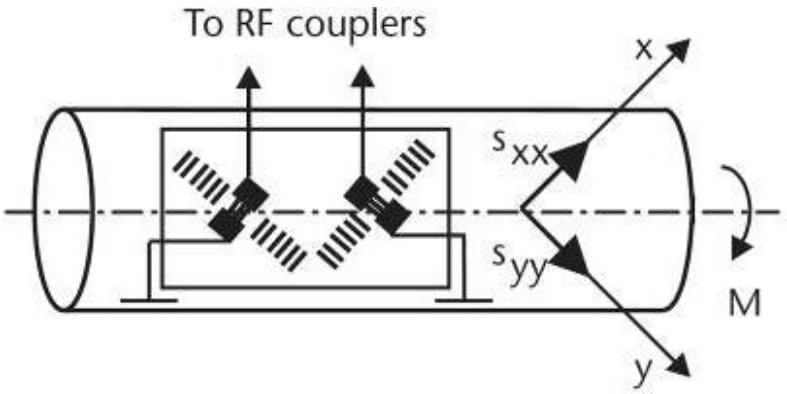

Figure 2.63 Scheme of a torque sensor on a shaft with two SAW resonators (Lin et al. 2012)

2.4.2 DIC

Another innovative non-contact optical technique for full-field displacement and strain monitoring of structures, including composites, is the Digital Image Correlation (DIC). In this technique, first established in the early 1970s, images of the inspected object are captured at different deformation instants and through image analysis techniques they are compared to give strain results. The surface of the component should be ideally covered with a random, non-repetitive, high-contrast speckle pattern of black and white color (Figure 2.64). Typical image sources are conventional CCD or consumer digital cameras, high-speed video, macroscopes and microscopes, including scanning electron and atomic force microscopes (Shadmehri & Hoa 2019). Full-field 2D and 3D (two or more cameras) strain maps can be obtained in that way. In 2D DIC only planar components can be examined. On the other hand, in the 3D DIC system, with a stereoscopic sensor setup, each point of the examined area corresponds to a specific pixel in the camera plane. Thus, the 3D position and deformation of any point can be determined, even

for out-of-plane displacements, if all the extrinsic (camera relative orientation) and intrinsic parameters (internal camera parameters such as focal length) of the set-up are known. Strains at each point are calculated trough a triangular mesh which is created from the DIC data of the adjacent points. Any structure shape can be examined in 3D DIC.

Figure 2.64 Random speckle pattern on a composite tube in Shadmehri & Hoa (2019)

In Elmahdy & Verleysen (2018) an experimental investigation of high speed 2D and 3D DIC systems was made for the characterization of unidirectional carbon fiber reinforced epoxy composites in high strain rate tension, in terms of strain resolution and detection of strain concentrations (Figure 2.65). It was concluded that high speed 2D DIC technique had greater resolution compared to 3D DIC, while 3D DIC could measure strain localization in the gauge section.

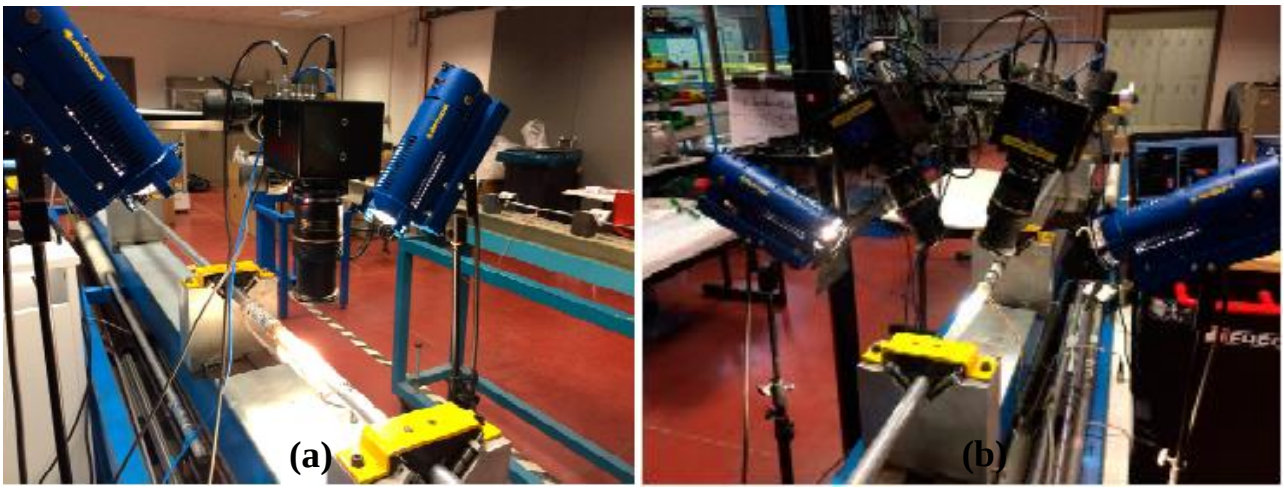

Figure 2.65 2D DIC (a) and 3D (b) system in Elhmady & Verleysen (2018)

DIC is in general a low-cost, effective and accurate monitoring technique, suitable for in-situ inspection of the structure. In addition, no special and surface preparation and lighting is required

for DIC implementation in general (McCormick & Lord 2010). However, some challenges arise. Firstly, DIC is not aimed for continuous monitoring. Strain results are acquired through the comparison of images captured between the surveys. Furthermore, in order to the 2D DIC systems measure accurately, the camera should be placed perfectly perpendicular to the component. Out-of-plane displacement may also affect the results (Elhmady & Verleysen 2018). In addition, environmental effects on the surface condition of the structure or non-optimal views of the surface due difficulty in accessing the inspected area may lead to inaccurate results.

Apart from small scale applications for material testing, in recent years, DIC have been implemented in real, large scale composite structures mainly in the wind energy and the aerospace fields for static and dynamic testing (Janeliukstis & Chen 2021). These cases face difficulties that are not encountered in small scale application. One of them is the need to move the camera in order to capture the whole structure and then combine all the images taken. Another matter is the point of view of the cameras and the necessity to joint synchronization and appropriate calibration of the multiple camera system which increases the complexity of the procedure.

In composite cylindrical structures, DIC has been implemented in tubes under buckling or bending loadings. In Shadmehri & Hoa (2019) buckling under an axial compression test was conducted on a graphite/epoxy pre-preg cylinder and a stereo DIC system was used. Random speckles were painted on the outer surface of the cylinder for that reason (see Figure 2.64). Comparison with the results of strain gauge showed good agreement prior to the buckling but poor correlation after the buckling had occurred. This was probably owed to two reasons: the failure of the bonding of the strain gauge and the accuracy of the DIC system which was affected by a number of factors including speckle size and quality, lighting, camera and lenses quality etc. Furthermore, a two-point bending test was also conducted on a thick-walled thermoplastic, carbon fiber reinforced tube with a random pattern of speckles printed on its surface. Two pairs of DIC cameras were used. The deformation results revealed the axial compression and tension zones of the tube. The strain results were reasonable and the maximum axial strain values at the top and bottom were almost equal to the ones expected for a typical bending test like this.

Figure 2.66 DIC for tube under an axial compression test (Shadmehri & Hoa 2019)

In Shamsuddoha et al. (2021), which has already been presented previously, a composite tube with cut-out was tested in axial compression, torsion and biaxial (compression and torsion) loads. In Figure 2.49 the tube mounted on the testing machine is depicted. The stochastic pattern of speckles can be seen around the cut-out area. The DIC system was consisted of two cameras. The area was also illuminate by a LED light source. DIC displacement results in the biaxial loading case were in very good agreement with the FEA results, although slightly higher values were recorded. It was concluded that DIC could be used as a reliable tool for deformation measurement of tubes under biaxial loads.

When it comes to DIC implementation on rotating shaft, no specific studies have been found in the literature in the author's knowledge. Despite that, DIC on a moving target in dynamic conditions, such as rotating components, have started to be investigated in the recent past. In these cases, two major issues arise: firstly, the camera and the stroboscope must be synchronised with the periodic rotation and secondly, the effect of motion blur must be eliminated (Li et al. 2017). These may impose additional requirements to the camera, for example, for high frame rate (high-speed camera) which usually comes in expense of the resolution and the accuracy (Janeliukstis & Chen 2021). Attempts have been done either to quantify the uncertainty induced by the rotation of the component (Zappa et al. 2014) or to compensate the consequent blur of the images due to this rotation (see studies that are mentioned in Lich et al. 2019). In general though, more need to be done to tackle these issues.

2.4.3 Random

Other approaches for strain and/or torque measurement on cylindrical structures (either metal or composite) that use unique techniques are also under development, although they are still mainly in laboratory-level. Some of these novel techniques, which have been found in the literature, are presented below.

In Bonislawski et al. (2019) a novel system intended for power monitoring of the main shaft of modern ships was presented. Torque and speed measurements were performed. In general, the working principle of this system was similar to that of a conventional system as presented previously. The energy was wirelessly supplied from a stationary to a rotating part which fed a SG, and the measurement data were transferred with radio-based telemetry. In contrast to conventional systems though, the wireless power supply system had a special setup consisting of flexible printed circuit board (PCB) coils. To be clearer, the main parts of the system were the stationary part, the rotating part and the GUI (Figure 2.67).

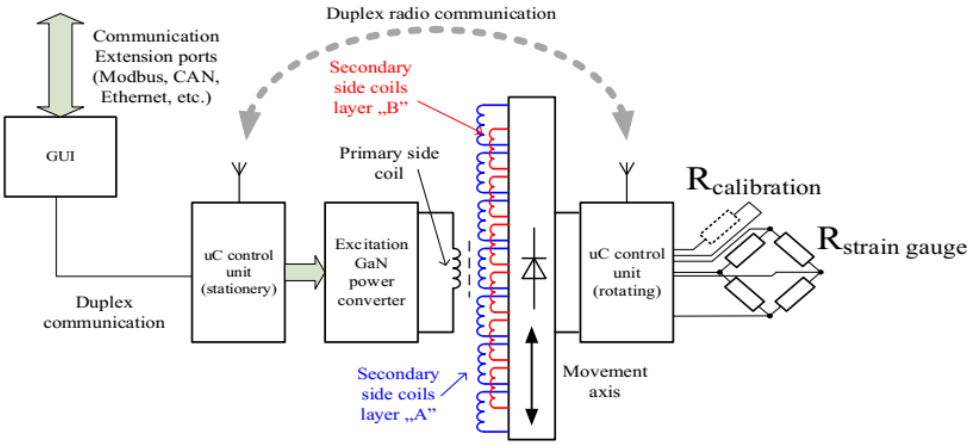

Figure 2.67 Schematic construction of the system (Bonislawski et al. 2019)

The stationary part was intended to wirelessly transmit the power supply and establish the real-time, bidirectional radio-communication with the non-stationary part and the Modbus communication to transfer the measurement results to the graphical user interface (GUI). Control of the wireless power supply was also performed. A microcontroller platform (ST STM32L0) was integrated for the proper operation of the unit. A resonant inductive coupling system was used to wirelessly transfer the power supply. Compared to conventional inductive coupling systems these systems have higher energy transfer efficiency and can operate at much bigger distance (between transmitter and receiver) due to strongly enhanced resonant magnetic field. In order to achieve a more compact system, the transmitter coils of the stationary part (Tx) were arranged on a flat planar core, while the receiver coils (Rx) were manufactured as a flexible, two-layer printed circuit board (PCB) attached the shaft. These are depicted in Figure 2.68 (a) and (b). Such arrangement can be attached on shaft of various diameters and used in either standstill or rotating conditions. In addition, it can operate even if a number of single coils are damaged. High energy transmission efficiency, easy coil alignment procedure and pre-mounting preparation are some extra advantages of this wireless power transfer system.

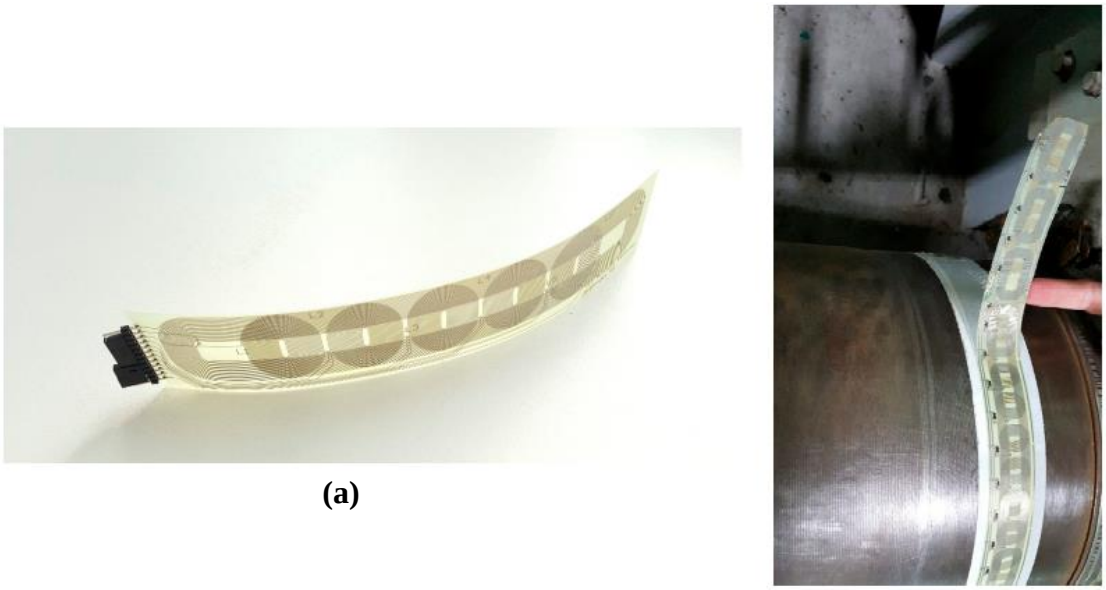

(a) **(b)**

Figure 2.68 (a) Receiver coils (Rx) and (b) the Rx arrangement on the marine shaft (Bonislawski et al. 2019)

Figure 2.69 depicts the non-stationary part. It is connected to the Rx coils for the wireless power supply and the rotational speed reading. The strain gauge are also connected and powered and the measurement data are transmitted through real-time radio communication. The same microcontroller is used for the operation of this unit as in the stationary part. Due to the A/D converter the sampling rate range was limited and thus a rate of 90 samples per second was selected.

Figure 2.69 Non-stationary part and its components (Bonislawski et al. 2019)

Lastly, GUI unit had a touch-screen and I with full programmable logic controller. It also had extension ports for analog or digital output in order to be able to communicate with various other marine control units. In Figure 2.70 the whole system after the assembly is depicted mounted on a main propulsion shaft.

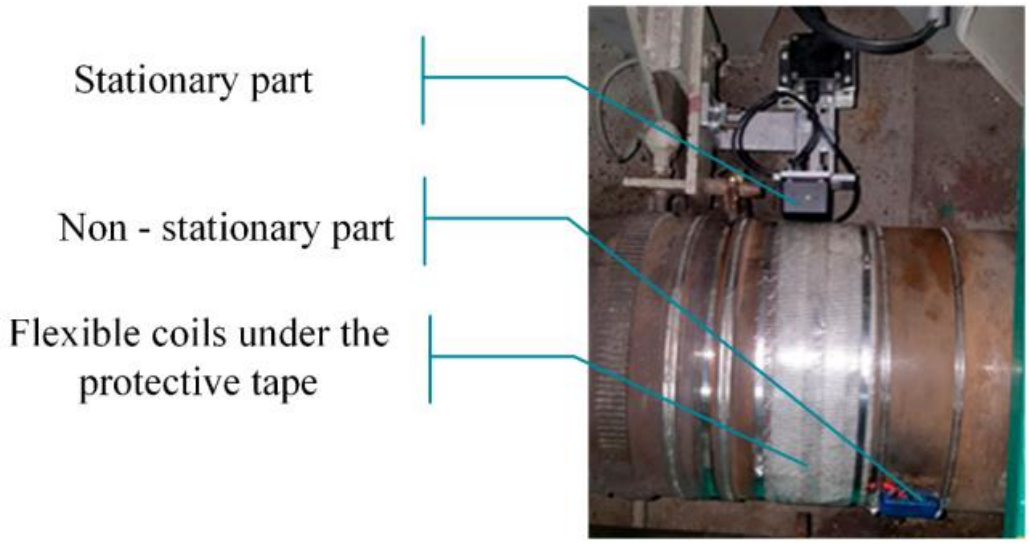

Figure 2.70 Final assembly on a main propulsion shaft (Bonislawski et al. 2019)

Validation of the system was made through a test bed examination the excellent accuracy of the results was pinpointed by comparison to the indications of a dynamometer. Installation of the system on a passenger Ro-Ro ship operating in the Baltic Sea was also made for a period of several months for power recording and ship performance (SFOC) evaluation with precise and steady results.

In conclusion, the above system although still in a preliminary stage, offers some major advantages such as: small size-weight, very low energy consumption, simple and easy mounting and preparation, resistant toy harsh operating conditions, wireless power and data transmission with high energy efficiency and user-friendly GUI. The cost of the setup was considered low but no market information could be obtained as the exact details of the components (e.g. for the Rx coils which were an important components) were not given except for the microcontroller.

Another interesting approach was recorded in Micek & Grzybek (2020) and Grzybek & Micek (2019) for a novel contact yet wireless (meaning without the need of slip rings), method of measuring stress (from the developed strains) on a rotating shaft is discussed. This sensor was tested under laboratory conditions. It consisted of a piezoelectric energy harvester and a radio transmission system. The piezoelectric harvesting system contained a patch of Macro Fiber Composite (MFC) from Smart Material Corporation (P2 type) attached on the surface of the shaft and the EH310A device (Series EPAD® Energy Harvesting™ Modules) from Advanced Linear Devices Inc. (USA) in which the energy storage system (containing a Graetz bridge and capacitor) and the energy transfer control were included (Figure 2.71) and which is intended for low power intermittent duty cycle sampled data or condition-based monitoring/extreme lifespan applications.

Micro Fiber Composite (MFC) is a smart material invention originally proposed by NASA in 1999 and first commercialized by Smart Material in 2002 as NASA's licensed manufacturer and distributor (Figure 2.72). MFC can be used either as actuators or sensors. The core of MFC is the

piezoelectric materials which are used due to their unique characteristic and various advantages such as strong electromechanical coupling and quick response time. It consists of an active layer of rectangular piezoceramic fibers (rods) or piezoelectric composite (piezocomposite) fibers in some cases, embedded in polymer matrix sandwiched between electrodes and protective polyimide film (Figure 2.73). The electrodes are attached to the film in an interdigitated pattern which transfers the applied voltage directly to and from the ribbon-shaped rods. In that way, when voltage is applied the MFC acts as an actuator and will bend or distort materials, counteract vibrations, or generate vibrations. On the other hand, it can act as a very sensitive strain gauge sensor which produces voltage when deformed. In general, it is used for energy harvesting applications, in structural health monitoring schemes and in vibration and shape control. What makes MFC a great option is the mechanical flexibility, increased strength, reliability, environmentally sealed packaging, ease surface attachment or embedment (in composites), the variety of piezoceramic materials available, the directional actuation and sensing capabilities, cost-effectiveness etc.

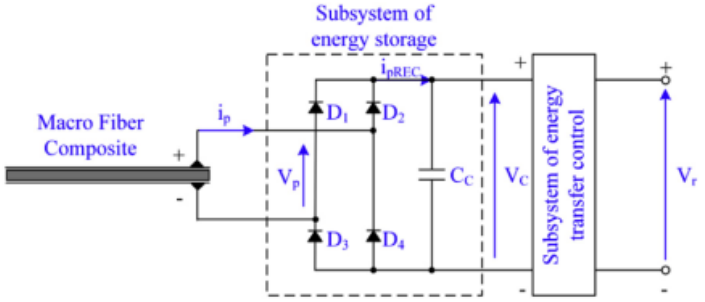

Figure 2.71 Schematic representation of the energy harvesting and transfer system (Micek & Grzybek 2019)

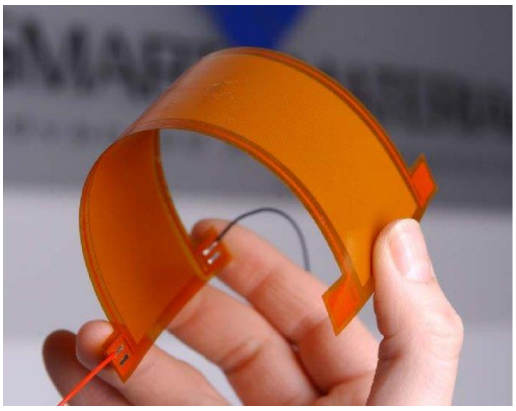

Figure 2.72 MFC (Smart Material)

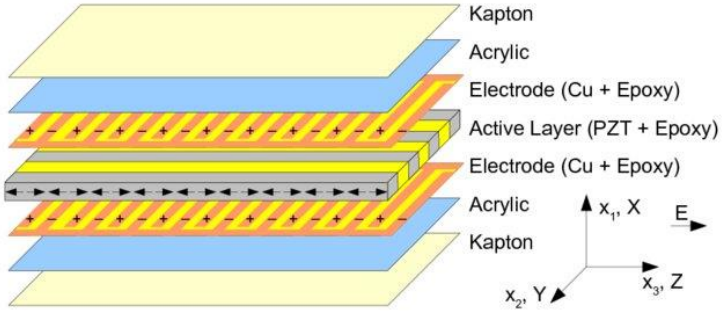

Figure 2.73 Schematic representation of a typical structure of a MFC (d_{33} type)

The MFC supplied packets of energy to the capacitor in the form of electric charge impulses each time when the maximum value of the voltage storage capacity (5.2 V) was reached. The energy transfer control system then supplied the radio transmitter with voltage from the capacitor and each time the minimum voltage (2.1 V) was reached recharging was taking place. The innovative part of the sensors was that the stress on the shaft was monitored via the number of

radio signal per second (output frequency) of the radio transmitter. Each time the capacitor was charged to each maximum capacity, the energy was supplied to the radio transmitter and signal were sent to the static radio receiver nearby (Figure 2.74). The faster the charging procedure was, the smaller the interval between two consecutive signal transmissions. The charging time in turn depended on the current generated from the MFC due the stress or the rotating speed of the shaft. A higher current value led to faster charging of the capacitor and smaller time between two consecutive signals (output frequency of the radio transmitter). Thus, through a calibration procedure, the relationship between the output frequency and the stress and rotational speed could be established for a specific shaft.

This stress was induced by the application of a lateral (to the shaft) force from a moving frame on which the shaft had been placed and not the shear stress developed on the shaft from torsion. Experiments were made on metallic shaft with different rotational speeds and different lateral forces. The experimental arrangement is schematically shown in Figure 2.75 and in reality in Figure 2.76.

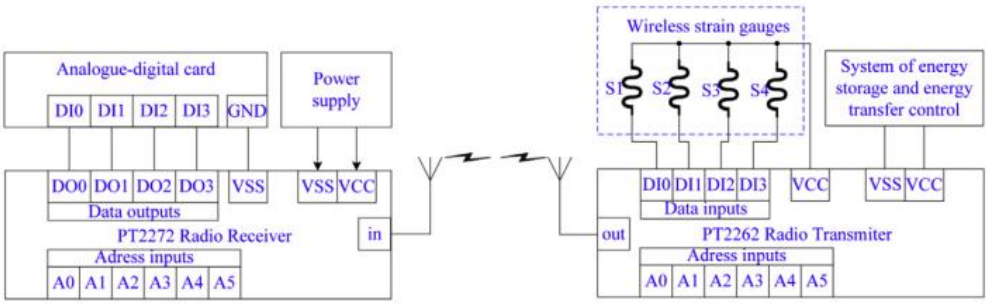

Figure 2.74 Piezoelectric wireless sensor, wireless SG and radio receiver (Micek & Grzybek 2019)

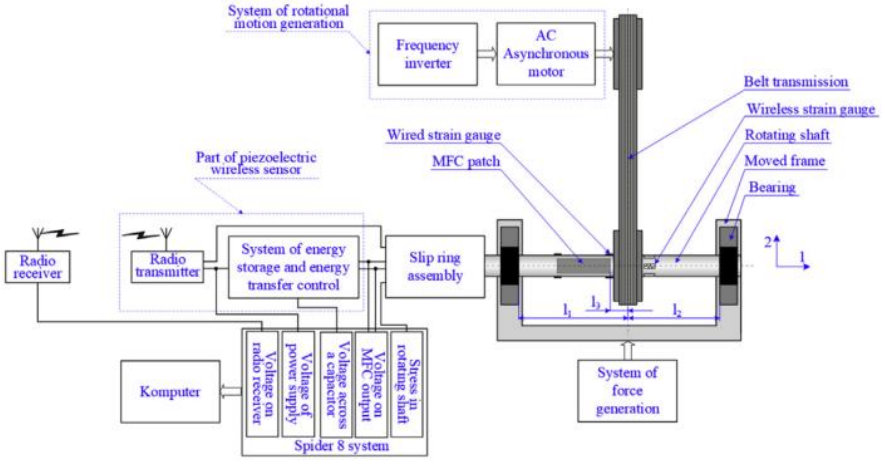

Figure 2.75 Shematic representaion of experimental set-up (Micek & Grzybek 2019)

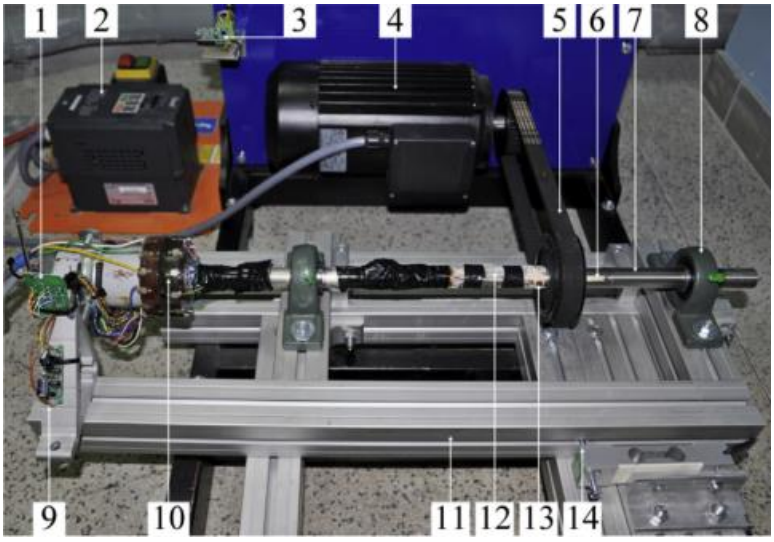

Figure 2.76 Photo of experimental set-up (Micek & Grzybek 2019):
1 – radio transmitter, 2 – frequency inverter, 3 – radio receiver, 4 – asynchronous motor, 5 – belt transmission, 6 – wireless strain gauge, 7 – rotating shaft, 8 – bearing, 9 – system of energy storage and energy transfer control, 10 – slip ring, 11 – moved frame, 12 – Macro Fiber Composite, 13 – wired strain gauge, 14 – system of force generation

In the calibration procedure mathematical relationships were derived from which appropriate coefficients were calculated and thus the connection between the output frequency and the stress could be made, in conjunction to the rotational speed of the shaft. The tendency that was notice was the the bigger the stress, the bigger the current generated from the MFC and thus the smaller the charging time of the capacitor. This increased the output frequency. The same behavior was observed when the rotational speed was increased. The stress for the calibration was independently measured from four wired SG connected through a slip ring with the DAQ system For a more "active" use of the SG, a crack detection application was briefly discussed in which four wireless SGs (meaning that they were not connected with a slip ring) were connected with the radio transmitter. In the case of a crack on the shaft surface, if the connection of a SG failed, this consequently will alter the signal received from the radio receiver and thus the crack would be detected.

Despite the fact that the measurement of shear strain (and thus shear stress and torsional torque), is not directly considered in that study, the sensor design could be altered for stress monitoring of a shaft under pure torsion and without later force application. The MFC would again charge the energy storage system based on its pure shear deformation. The orientation that the MFC would be glued on the shaft, the calibration procedure of the sensor and the mathematical description of the relation between the output radio signal frequency and the shear strain, would be an interesting future task, yet not completely different from the one described in this paper.

Another interesting approach for measuring torsion on a metal shaft was reported in Cheng et al. (2016). Instead of optical fibers, coaxial cables were used in that case. Coaxial cables have the same electromagnetic principles with the optical fibers but the signals are transmitted in the radio

frequency (RF) range are through them. It has been found that these cables are appropriate when distributed sensing is needed, as the phase of the RF signal can more easily be obtained for example with a vector network analyzer (VNA). With these cables sensors that resemble with other common optical sensors, such as FBG and Fabry-Perot interferometers (FPI) can be made. That was done in this study where a FPI distributed torsion sensor is reported.

A schematic representation of the sensor is depicted in Figure 2.77. The coaxial cable, consisting of a series of reflectors at intervals along the length of the shaft, is wrapped around the shaft forming a helix. Two adjacent reflectors form a FP cavity. The partially reflected signals from two adjacent reflectors are superimposed and form an interference pattern (interferogram). When a strain is applied, a shift proportional to this strain can be observed in the interferogram. This is due to the change of the cavity length and the dielectric constant of the insulating material. Using multiple reflectors, the strain of the cable at each section can be calculated and thus, the distributed strain along the length of the shaft. In that way, the torsional agnle can be obtained. This calculation method is described in the paper.

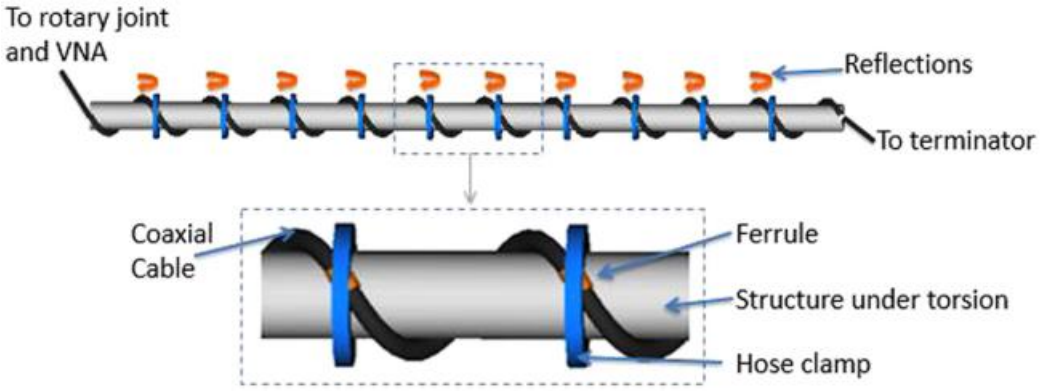

Figure 2.77 (a) Schematic representation of the sensor on a shaft,
(b) close view of a section of the sensor between two FP cavities (Cheng et al. 2016)

As can be seen in Figure 2.77(b), each reflector is a ferrule clamped at the specified intervals. Theses ferrules induced deformation on the dielectric material of the cable and thus an impedance discontinuity. This deformation is proportional to the magnitude of the reflection and thus can be controlled through the clamping force. Hose clamps were used to fix the ferrules and the cable to their position relative to the shaft. The sensor was examined in two ways. Firstly, a single-section of the sensor was used on the shaft in order to validate its response to the torsion, and then the distributed sensing capability of the sensor was tested with three sections. The experimental set-ups for these cases are schematically shown in Figure 2.78 and Figure 2.79 respectively. A wide range of twisting angles could be achieved as the the material of the shaft was soft and easy to twist.

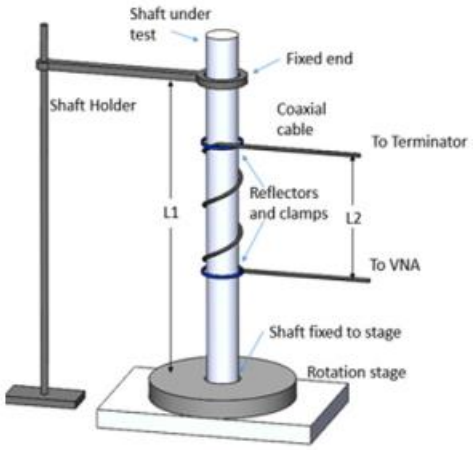

Figure 2.78 Experimental set-up for the single-section case (Cheng et al. 2016)

For the single-section sensor, the rotational angle was increased in steps of 5 or 10 degrees and the results were processed in each stage. As the angle increased, the central frequency of each interference valley decreased due to the increase of the cable length between the two reflectors. A linear response was observed with a sensitivity of 1.834 MHz $(rad/m)^{-1}$. In the other case (Figure 2.79) it can be seen that some space was added in between each section in order to avoid cross-talks, although this may not be mandatory in real-time applications. The torque was applied in the 2^{nd} section areas in order to validate the distributed capability of the multiple-section arrangement. Again, the response of the 2^{nd} section was similar to the single-sections case. The other sections exhibited more weak response (Figure 2.80) with some small cross-talks. It has to be mentioned here that the number of sections that can be used is limited by the reflectivity R% of each reflector and the noise and loss along the cable. It was finally concluded that this distributed sensing capability offers the possibility of SHM, damage detection or merely torque measurements on shafts.

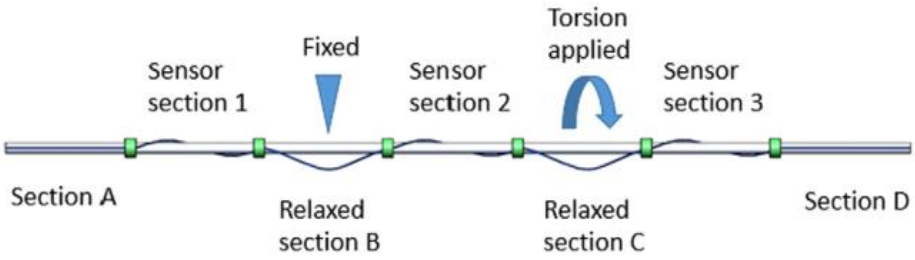

Figure 2.79 Experimental set-up for the multiple section case (distributed torsion system) (Cheng et al. 2016)

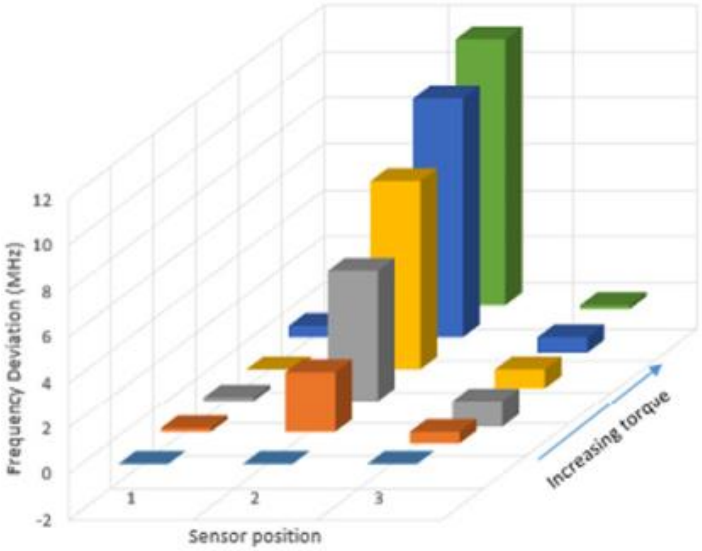

Figure 2.80 Response of the three sections to the applied torque at the 2nd section (Cheng et al. 2016)

In Chen et al. (2020) a system for non-contact torque and rotational speed measurement on a rotating shaft based on a novel resistance and capacitance coupling method was proposed. This system combined two strain gauges attached on the shaft in $\pm 45°$ in relation to the shaft axis and a capacitive grating sensor. The latter is a novel sensor based on the capacitance sensor and is composed of a grating-like moving capacitive grating and a stationary capacitive grating mounted on the shaft and on a sleeve respectively. Each side of the capacitive grating sensor consisted of two parts A and B made of corroded copper which were complementary and insulated. Hence, four capacitors were created. Figure 2.81 gives the nomenclature of the capacitors formed by the stationary and rotating parts of the grids which was: The stationary and moving grids of part A form capacitor C_{1a},the stationary grid of part A and the moving grid of part B form capacitor C_{1b}, the stationary grid of part B and the moving grid of part A form capacitor C_{2a}, and the stationary and moving grids of part B form capacitor C_{2b}. Omitting edge effects and parasitic capacitances it was: $C_{1a} = C_{2b}$ denoted as C_a and $C_{2a} = C_{1b}$ denoted as C_b.

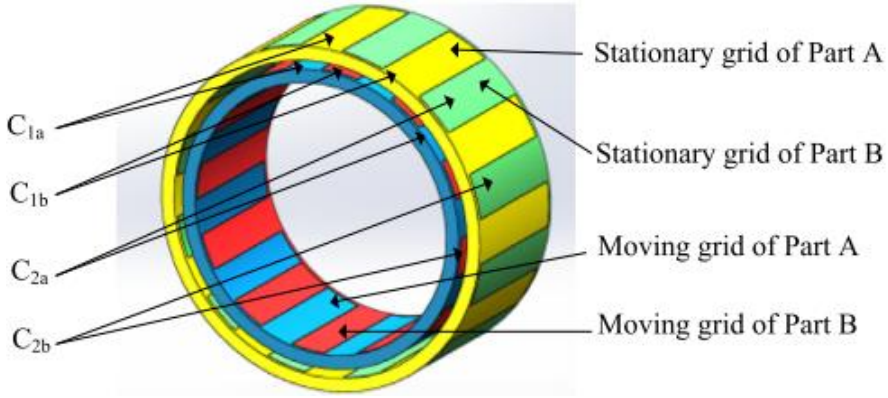

Figure 2.81 Model of the capacitive grating sensor and the capacitors formed (Chen et al. 2020)

As the SGs were stretched, they obtained the torque information while the capacitive grating sensor dealt with the transmission of the output signal. As it will be shown, this system eliminates the need for power supply on the sensor. As depicted in Figure 2.82 one ends of the two SGs were connected on the rotating shaft (and therefore to the ground through the connection of the shaft with the vehicle) and the other ends were connected to the rotating capacitive grating. Equivalent resistances and capacitances were obtained through multivariate function relationships by complex impedance. As the shaft rotated it caused the capacitances C_a and C_b to change due to the change of the relative are between the grids (dielectric material remained constant (air)) which in turn affected the charging time constants. SGs deformations under torque also changed their resistances. The maximum difference of the charging time constant of the two equivalent capacitors was found (and confirmed by simulation experiments) to be proportional to the difference of the SGs resistances ΔR and the maximum capacitance difference (C_a - C_b) as given in eq. (2.26). This difference was essentially the output signal that carried the information of the torque applied on the shaft. This signal was connected with a pulse-width modulation (PWM) circuit and altered the duty ratio of the output pulse signal. Through the use of circuits, such as difference subtraction and low-pass filter circuits, a sinusoidal signal was obtained and monitored by an oscilloscope of which the voltage amplitude reflected ΔR, hence the torque, and the frequency reflected the rotational speed.

$$\max(\tau_1 - \tau_2) \propto \Delta R \cdot \max(C_b - C_a) \tag{2.26}$$

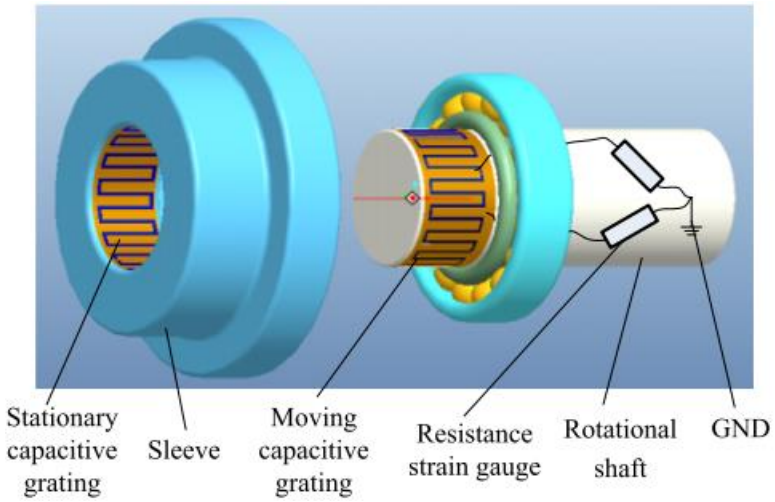

Figure 2.82 Model of the sensor arrangement (Chen et al. 2020)

Simulation of the proposed circuit model was carried out in an appropriate environment called Multisim which confirmed the correlation between the change of the SGs resistances and the change in duty cycle of the PWM. A simulation experiment was also performed with the stationary and rotating grids depicted in Figure 2.83 and the test rig depicted in Figure 2.84. In order to verify that the output signal of the PWM is positively correlated with the resistance

change, adjustable resistors were used instead of resistance SGs which give weaker signals. The stationary grating was fixed on a bracket and the rotating shaft was driven by a speed motor. At constant rotational speeds (100 r/min, 200 r/min and 300 r/min) and by varying the proportion of the adjustable resistors at each speed, the recordings qualitatively confirmed the correctness of the theoretical analysis.

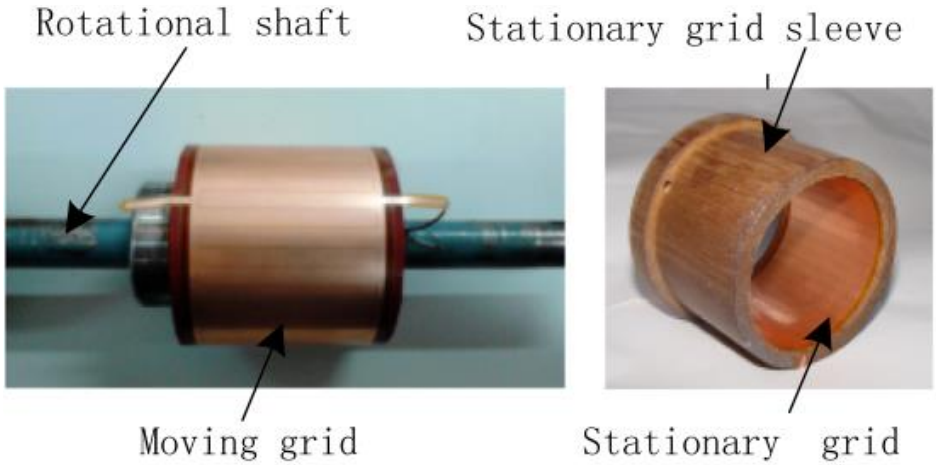

Figure 2.83 Stationary and rotating grids (Chen et al. 2020)

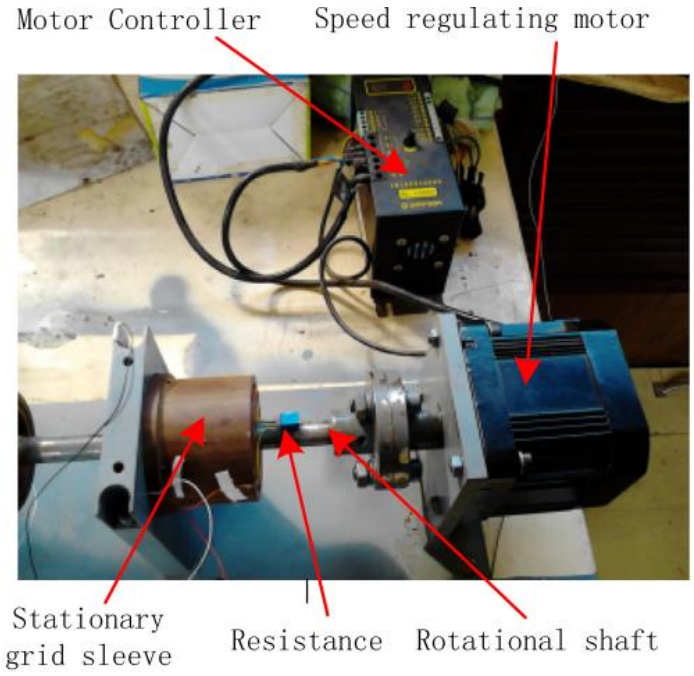

Figure 2.84 Test rig (Chen et al. 2020)

Although this system is still at a very preliminary stage and further validations need to be done, the feasibility of the basic working principle was confirmed. It offers a novel way to solve the power supply and signal transmission issues related to torque meters. Another advantage is that the components of the system can be integrated in other structures such as bearings, hence

diminishing assembly problems and making it a promising solution for applications where the available space around the shaft is confined.

Some other unique approaches for in-process damage-state monitoring of composite rotating structure, and specifically composite rotors, had been investigated in a number of studies (Kuschmierz et al. 2015, Phlipp et al. 2016). Although the main parameter to determine was the radial expansion (in-plane deformation) of the rotor and not the torsional deformation, the technique used there was interest. Different set ups of Laser Doppler Distance (LDD) sensors were used which were distributed around the circumference of GFRP rotor in order to capture its shape deformation, which was expected to be elliptical due to the anisotropy of the composite materials (Figure 2.85). Also the whirling motion of the rotor could be separated from the results. Through the monitoring of the rotor expansion, the initiation and progression of damage in the rotor could also be captured

In the first study, the validity of a system consisting of 3 LDD sensors for the determination of in-process, angle-dependent expansion of a high speed rotor was affirmed. This system could measure the radial expansion with 95% confidence below 10μm. Comparison with a numerical solution also showed good agreement.

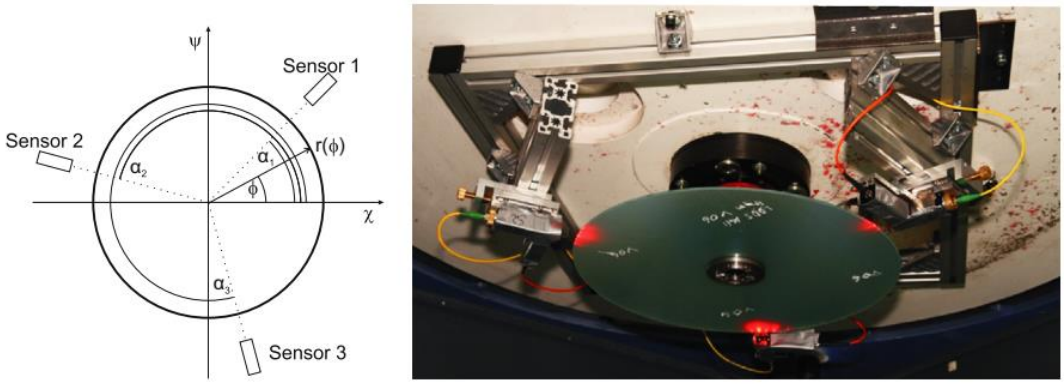

Figure 2.85 Schematic depiction (left) and real photo (right) of the 3 LDD sensor set up

2.5 Conclusions

In this chapter methods and techniques to measure strain and torque on shafts and cylindrical structures were presented with special consideration on rotating driveshafts made of composite materials. Among the conventional methods, the most common is the one which involves SG attached on the shafts. Despite that SGs have also been used in structural monitoring schemes in other structures (e.g. hulls), when it comes to shaft application their main utilization is in torque transducers and most of the commercially available transducers are based on SGs. Techniques for the non-contact transmission of the signal received from the SGs are slip rings, which though seem obsolete nowadays, inductive power and/or signal transmission and wireless RF telemetry. High accuracy, reliable results and ease of installation of such torque meters on any shafting

systems, in many cases without the need to disassemble them, are some basic features that have made SG-based torque transducers the most favorable and predominant solution in the market. Many COTS systems offer compact solution with the SG attached on their measuring body (e.g. T10F torque meter flange from HBM) which are independent of the materials of the shaft and can solve or at least moderate some of the disadvantages of SG such affection from the environment condition, E/M interference etc. Strain and torque measurement with SG on composite shaft, although entails some difficulties, is also feasible.

Other commercially available torque meter systems measure the twist angle between two sections along the length of the shaft with various ways (induction proximity or optical sensors) which are independent of the material of the shaft and in many cases is a great solution for installation on already operating shaft systems. Many interesting novel systems based on twist angle measurement have been also examined but are still in laboratory level.

Other novel systems are also under development. The most promising ones use FOS for strain measurement (mainly FBG sensors) of the structure as they exhibit great accuracy and sensitivity, robustness and resistance in E/M interference. In general, FOS have been widely used for structural health monitoring of various structures. In shaft application they have been tested in measuring torsion on metal shafts but yet not used in torque transducers. Lately, FOS have been also examined in composite shafts or general in cylindrical structures for measuring torque-induced strains for SHM. One of their major advantages is that they can be embedded inside the composite shaft or tube during manufacturing without having a big impact on their structural integrity. This offers great prospects for SHM during operation. A crucial aspect is the non-contact transmission of the optical signal between the rotating and stationary part. FORJ (optical slip ring) and special designed lenses are promising solutions with plenty of merits which are already used in various other applications but yet not in driveshafts. Other novel systems using SAW, DIC or other more general techniques for strain and/or torque measurement have also been tested on rotating shafts but are still in laboratory level. SAW-based torque sensors have also been produced by some manufacturers.

In conclusion, it can be stated that strain and torque measurement methods on shafts have been constantly developed. Despite the fact that conventional methods are still the predominant solution in the market, new novel techniques can be a possible future way to tackle some problems encountered in conventional methods. Especially with the growing use of composite material shaft, techniques such as FOS with their embedding capabilities can establish a SHM system of rotating shafts during operation.

CHAPTER 3 THEORETICAL CALCULATION AND EXPERIMENTAL MEASUREMENT OF THE EQUIVALENT MECHANICAL PROPERTIES OF A CFRP SHAFT

In this chapter the theoretical and experimental calculation of the equivalent modulus of elasticity in the hoop direction E_2 and other equivalent mechanical properties are given. These were necessary for the experimental static torsional tests which were conducted on a Carbon Fiber Reinforced Polymer (CFRP) shaft in the facilities of LTM of the School of Applied Mathematics and Physical Sciences and the implementation of TT 10k on this composite shaft (see Ch.5).

3.1 Shaft Specifications - Analytical Calculation

The aforementioned CFRP shaft was manufactured in the premises of B&T Composite in Florina, Greece, with the method of filament winding (Figure 3.1). The lay-up of the shaft was identical to that used in a previous thesis (Vavatsikos 2020) conducted in Shipbuilding Technology Laboratory (STL): [± 12° / ± 12° / ± 80° / ± 12° / ±12°], with the typical layers thickness, as provided by the manufacturer, being for ± 12° layers equal to 0.95 mm, for ± 80° layers equal 0.32 mm and for the outmost ± 12° layers equal to 0.52 mm. This gives a total thickness of 3.69 mm. However, ultrasonic Thickness Measurement (UTM) and Caliper Measurement on the shaft tested by Vavatsikos (2020) gave a rather different measurement of the thickness of the shaft and its longitudinal and circumferential distribution. Measurements were made at 11 different cross sections per 10 mm and at 4 points per 10 mm circumferentially. The average thickness value was calculated equal to 4.52 mm with a 3.35% CV. Due to absence of more details, the difference in thickness between the initial estimation and the actual one was equally distributed on the layers. Table 3.1 shows the initially layer thicknesses proposed by the manufacturer and the ones obtained after measuring the total thickness. The latter were considered as the real ones and were used in the calculations.

Table 3.1 Layers' thicknesses

Layer	Proposed thickness (mm)	Measured thickness (mm)
±12	0.95	1.12
±80	0.52	0.69
±12 (outer layers)	0.32	0.49

The difference in the thicknesses between the internal and outmost layers of ± 12° angle orientation was due to the different properties of the fibers used. Specifically, the outmost fibers were made from rovings of 12K (12 thousands fibers per tow) while the inner ± 12° fibers were

made from 24K rovings. The mechanical properties of each lamina made from these fibers (12K and 24K) and epoxy resin in the principal material orientations (Figure 3.2) are presented in Table 3.3.

Figure 3.1 CFRP shaft

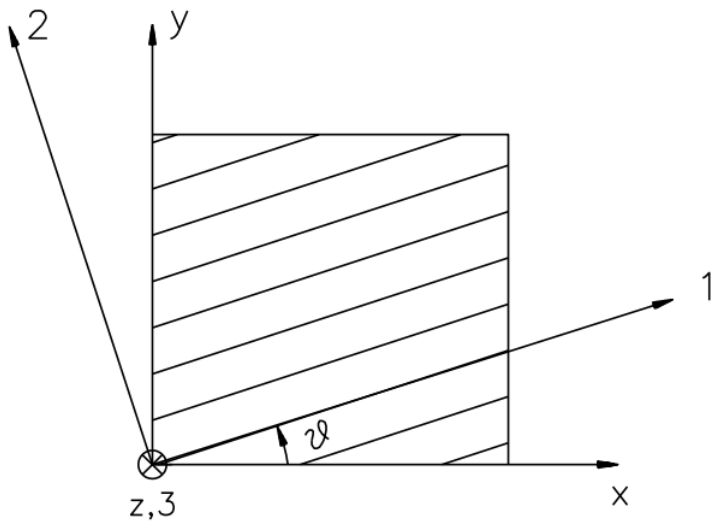

Figure 3.2 Principal material (1-2) and geometrical (x-y) system of a lamina

The shaft principal dimensions are in Table 3.2:

Table 3.2 Shaft's principal dimensions

Total length (end fittings not included) (mm)	External diameter (mm)	Internal diameter (mm)	Thickness (mm)
1.255	119.0	110	4.52

Table 3.3 Mechanical properties of 12K and 24K fibers UD layers

	Mechanical properties of 12K	**Mechanical properties of 24K**
$\boldsymbol{E_1}$ (GPa)	143.7	135.4
$\boldsymbol{E_2}$ (GPa)	9.2	9.2
$\boldsymbol{E_3}$ (GPa)	9.2	9.2
$\boldsymbol{G_{12}}$ (GPa)	3.4	3.4
$\boldsymbol{G_{23}}$ (GPa)	1.7	1.7
$\boldsymbol{G_{13}}$ (GPa)	3.4	3.4
$\boldsymbol{\nu_{12}}$	0.32	0.32
$\boldsymbol{\nu_{23}}$	0.46	0.46
$\boldsymbol{\nu_{13}}$	0.32	0.32
$\boldsymbol{\nu_{21}}$	0.02	0.02
$\boldsymbol{\nu_{32}}$	0.46	0.46
$\boldsymbol{\nu_{31}}$	0.02	0.02

The $\nu_{12}, \nu_{32}, \nu_{31}$ values in Table 3.3 were obtained from the reciprocal relations in eq. (3.1):

$$\frac{\nu_{ij}}{E_i} = \frac{\nu_{ji}}{E_j} \; i,j = 1,2,3 \tag{3.1}$$

In order to calculate the equivalent modulus of elasticity of the composite laminate structure in the hoop and the longitudinal direction, the extensional stiffness matrix [A] of the laminate was necessary. Its elements are given by eq. (3.2), where $\left(\overline{Q_{ij}}\right)_k$ represents the elements of the $[\bar{Q}]$ matrix of the k[th] layer of the structure, which is given by eq. (3.3) and z_k is the upper end of the layer (the interlaminar surface between the k^{th} and the $(k+1)^{th}$ layer) measured from the mid-surface.

$$A_{ij} = \sum_{k=1}^{N} \left(\overline{Q_{ij}}\right)_k (z_k - z_{k-1}) \tag{3.2}$$

$$[\bar{Q}] = [\mathrm{T}]^{-1}[\mathrm{Q}][\mathrm{T}] \tag{3.3}$$

In eq. (3.3) [T] is the matrix of coordinate transformation from the principal directions of one layer to the geometrical directions of the structure, and $[Q]$ is the matrix of material properties - stiffnesses. With the assumption of plane-stress conditions, its elements Q_{ij} for orthotropic material (as generally the CFRP is considered) are given in eq. (3.4) - (3.7):

$$Q_{11} = \frac{E_1}{1 - \nu_{12}\nu_{21}} \tag{3.4}$$

$$Q_{12} = \frac{\nu_{12} \cdot E_2}{1 - \nu_{12}\nu_{21}} = \frac{\nu_{21} \cdot E_1}{1 - \nu_{12}\nu_{21}} \tag{3.5}$$

$$Q_{22} = \frac{E_2}{1 - \nu_{12}\nu_{21}} \tag{3.6}$$

$$Q_{66} = G_{12} \tag{3.7}$$

These Q_{ij} values were then calculated for each type of fiber (12K and 24K) and the results are given in Table 3.4:

Table 3.4 Stiffness matrix [Q] elements of 12k and 24 fibers

Stiffnesses 12k fibers (GPa)	Stiffnesses 12K fibers (GPa)	Stiffnesses 24K fibers (GPa)
$\boldsymbol{Q_{11}}$	144.65	136.95
$\boldsymbol{Q_{12}}$	2.96	2.96
$\boldsymbol{Q_{22}}$	926	9.26
$\boldsymbol{Q_{66}}$	3.40	3.40

The equivalent mechanical properties of the shaft are given from equations (3.8) - (3.12) (Rangaswamy and Vijayarangan 2005). These equations are referred to composite plates but they can also safely used in the problem of the shaft. They are used to transform an orthotropic multilayered plate into a homogeneous orthotropic plate.

$$\nu_{YX} = \frac{A_{12}}{A_{11}} \tag{3.8}$$

$$\nu_{XY} = \frac{A_{12}}{A_{22}} \tag{3.9}$$

$$E_X = \frac{A_{11}(1 - \nu_{XY}\nu_{YX})}{t} \tag{3.10}$$

$$E_Y = \frac{A_{22}(1 - \nu_{XY}\nu_{YX})}{t} \tag{3.11}$$

$$G_{XY} = \frac{A_{66}}{t} \tag{3.12}$$

where X orientation is parallel to the shaft axis and Y the hoop direction. E_X and E_Y are the Young's modulus of the shaft in the respective directions and G_{XY} and ν_{XY} are the shear modulus and Poisson's ratio of the composite shaft in xy-plane respectively.

As can be seen, only the elements of matrix [A] were necessary to be calculated. This meant that the respective elements of matrix $[\bar{Q}]$ should also be calculated. The elements of $[\bar{Q}]$ matrix are given in eq. (3.13) - (3.16) below, where $m = cos\theta$ and $n = sin\theta$ and θ is the angle between the fiber orientation of each ply with respect to the structure (laminate) geometrical directions (Figure 3.2) where positive angle is in anticlockwise orientation.

$$\overline{Q_{11}} = Q_{11}m^4 + 2(Q_{12} + 2Q_{66})m^2n^2 + Q_{22}n^4 \tag{3.13}$$

$$\overline{Q_{12}} = (Q_{11} + Q_{22} - 4Q_{66})m^2n^2 + Q_{12}(m^4 + n^4) \tag{3.14}$$

$$\overline{Q_{22}} = Q_{11}n^4 + 2(Q_{12} + 2Q_{66})m^2n^2 + Q_{22}m^4 \tag{3.15}$$

$$\overline{Q_{66}} = (Q_{11} + Q_{22} - 2Q_{12})m^2n^2 + Q_{66}(m^2 - n^2)^2 \tag{3.16}$$

The obtained values are presented in Table 3.5:

Table 3.5 $[\bar{Q}]$ matrix elements

$[\bar{Q}]$ **matrix elements (GPa)**						
	12K fibers				**24K fibers**	
	+12°	**- 12°**	**+ 80°**	**- 80°**	**+ 12°**	**- 12°**
$\overline{Q_{11}}$	125.64	125.64	9.41	9.41	133.24	133.24
$\overline{Q_{12}}$	8.18	8.18	6.65	6.65	8.52	8.52
$\overline{Q_{22}}$	9.54	9.54	128.83	128.83	9.56	9.56
$\overline{Q_{66}}$	8.61	8.61	7.09	7.09	8.96	8.96

The [A] matrix elements from eq. (3.2) are given in Table 3.6:

Table 3.6 [A] matrix elements

A_{11} (GPa·mm)	A_{12} (GPa·mm)	A_{22} (GPa·mm)	A_{66} (GPa·mm)
514.01	36.46	101.12	38.43

Finally, the mechanical properties obtained from eq. (3.8) - (3.12) and are presented in Table 3.7:

Table 3.7 Equivalent homogeneous orthotropic mechanical properties of the CFRP shaft

Equivalent Mechanical Properties	
$\boldsymbol{\nu_{XY}}$	0.36
$\boldsymbol{\nu_{YX}}$	0.07
$\boldsymbol{E_X}$ (GPa)	110.81
$\boldsymbol{E_Y}$ (GPa)	21.80
$\boldsymbol{G_{XY}}$ (GPa)	8.50

In the direction of the shaft axis the E_X modulus is quite higher than the E_Y modulus in the hoop direction. This is obviously due to the lay-up of the shaft, where plies of ± 12° orientation are predominant against ± 80° plies.

3.2 Split Disk Test - Material Characterization

3.2.1 Specimens, test set-up and procedure

Split disk tests were carried out in order to experimentally estimate the homogeneous orthotropic elastic modulus in the hoop direction E_Y of the shaft tested in static torsional test (Ch.5). Aim of this procedure was not to study how the various manufacturing and geometrical parameters affecting the final calculation of E_Y. This was already done in previous thesis carried out in STL (Chatzinas 2020, Themelakis 2017) in which the effect of diameter, thickness, width, fibers material, number of tows and tensile winding force were investigated. Here, the tested shaft was examined in order to get a quick estimation of E_Y. The relative apparatus, procedures and process and analysis of results are briefly described.

The spilt disk test according to the standard ASTM D2290 is focused on measuring the hoop Young's modulus in the hoop direction and the apparent tensile strength of ring-shaped specimens made from plastic materials. This test method is applicable to ring specimens, extracted by composite pipes which consist of thermosetting resin, regardless of fabrication method (ASTM D2290). Thus, shaft made from filament winding procedure and consisting of epoxy resin are acceptable parameters, as it was in our series of specimens. Specimens from pipes of different resins can also be included but slightly different procedure is followed based on the standard.

Specimens were cut from a previously used CFRP shaft, identical to the one used in the torsional test in this thesis, in two ways: by reciprocating saw of the STL and by band saw of the Laboratory of Marine Engineering. In total, seven specimens were cut, three of which had 20 mm width and four had 10 mm width. All of them had an inner diameter of 110 mm and were approximately 4.52 mm thick. As it is obvious in Figure 3.3a and Figure 3.3b specimens cut by the reciprocating saw were flawed as they were not appropriately cut. In fact, the fibers on the specimens appeared to be pulled out from the rest part of the shaft (Figure 3.3c) and then cut or break which consequently led to break of the fibers and matrix bond. These specimens were

excluded from the analysis of the results. On the other hand, specimens cut by the band saw had a smooth cut surface (Figure 3.4).

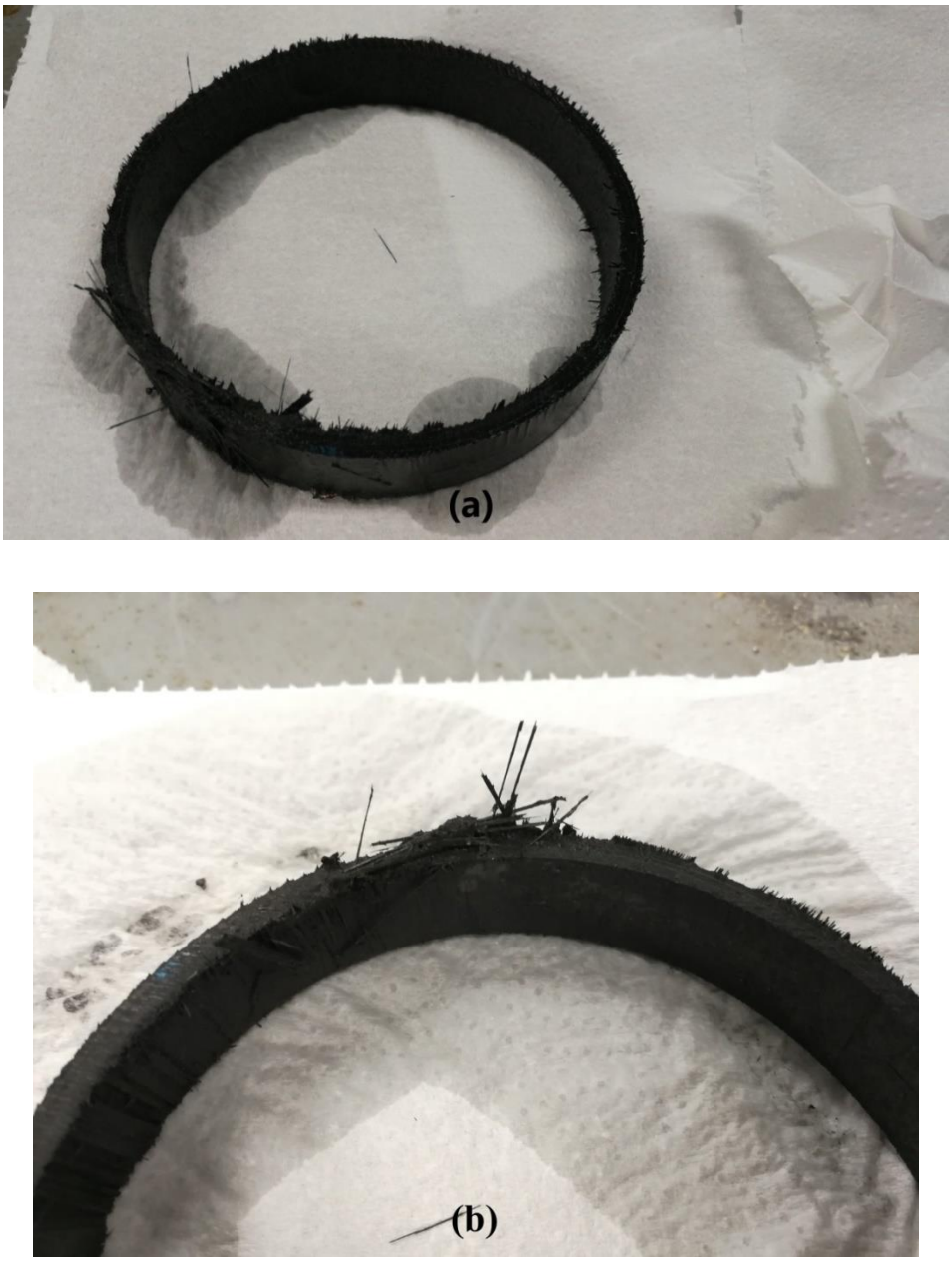

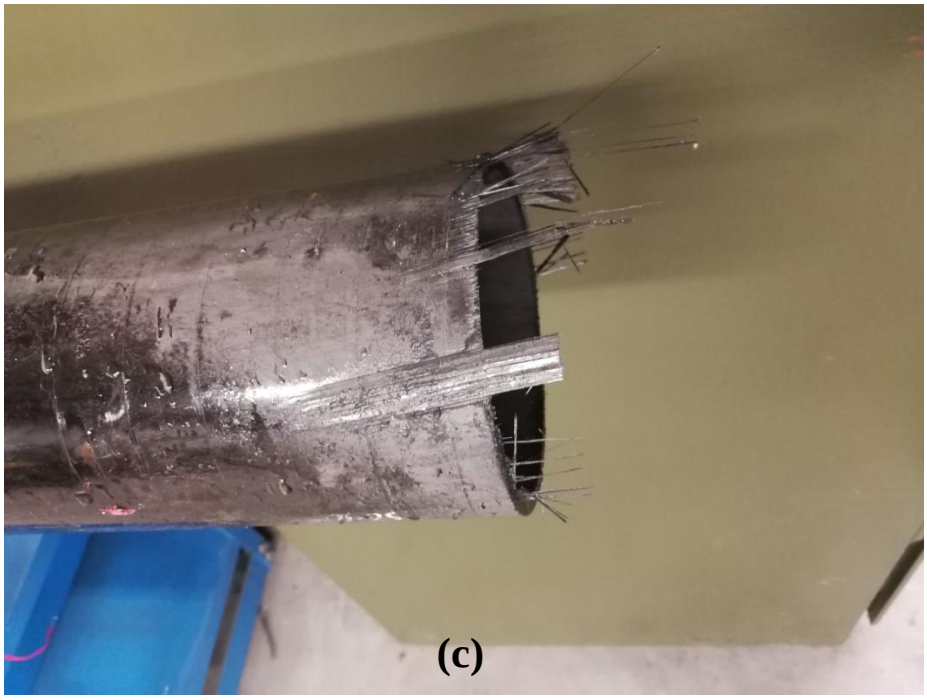

Figure 3.3 (a)-(b) Cut ring-shaped specimen by reciprocating saw, obviously plucked out and (b) shaft after cut where pull-out fibers are visible

Figure 3.4 Smooth cut specimens by band saw

The apparatus used for the split-disk test is schematically shown in Figure 3.5a. This is the typical fixture used for these tests according to ASTM D2290. The real one that used in the facilities of STL is shown in Figure 3.5b. It consisted of two half split disks with diameter approximately equal to the inner diameter of the ring specimens. Each of them had a hole where a pin comes in and connected each disk with a flange. These two flanges were then attached via

grips to the MTS hydraulic tensile machine of the laboratory which has a maximum loading capacity of 250 kN. All parts of the fixture were made from high strength S355 steel.

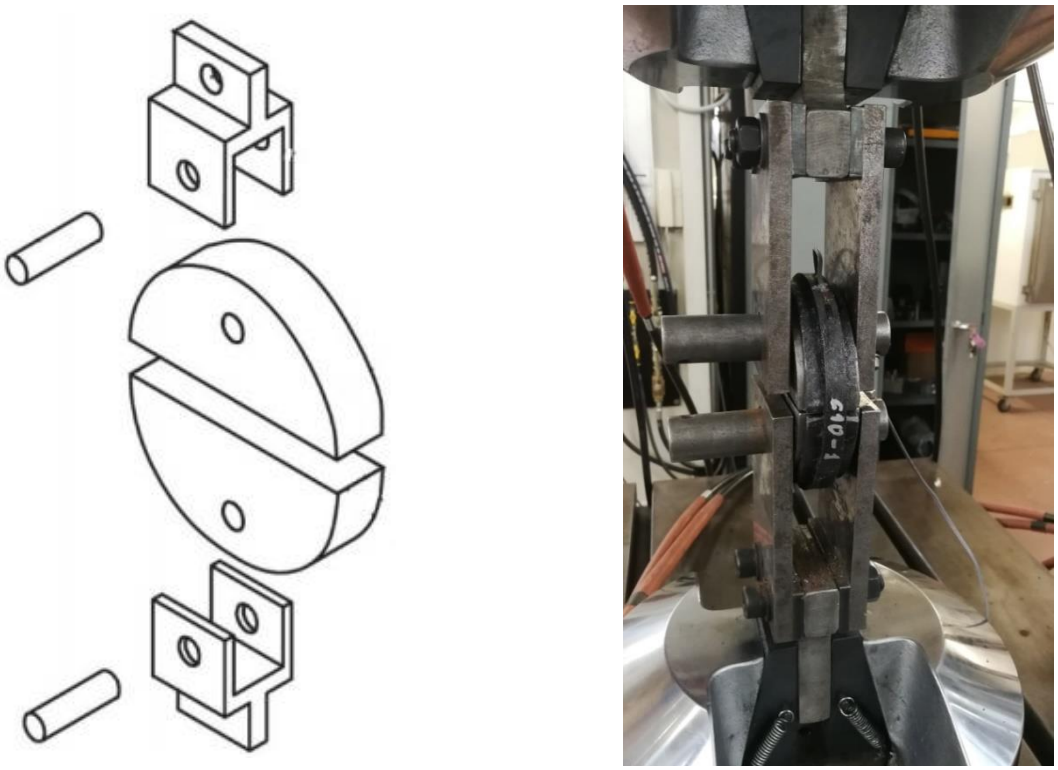

Figure 3.5 Split disk typical fixture (a) schematically and (b) the one used in STL facilities

According to ASTM D2290 standard, specimens shall have one or two reduced-width areas located 180° apart. Our specimens did not comply with this this demand in order to avoid the appearance of discontinuities of stresses and the strain measurements be reliable as proposed in Themelakis (2017).

Furthermore, due to the fact that the disks diameter was smaller than the specimens' diameter, two extra half ring-shaped metallic chocks were placed in between the disks and the specimens in order to achieve a better fitting. This is shown in Figure 3.6 where the specimen and these chocks have been placed around the disks before the test procedure begins. In addition, a small preload was applied before the main loading to failure took place and respective initial offset was set to zero. This was done so that the specimen fit well on the fixture and to prevent a loose fitting (Chatzinas et al.).

Before the specimens fit on the disks, grease was applied on the inner surfaces of the ring specimens to minimize the friction. Although we cannot completely eliminate the friction and in order to minimize its effect on the test results, Yoon et al (1997) proposed to unload directly after certain, low limit of strain has been reached during loading and then calculate the average value of the Young's modulus at the loading and unloading phases. In our case though, load was directly applied without an unloading phase. This was in compliance with the ASTM standard.

Figure 3.6 Ring specimen and the disks with the chocks.

During the test procedure the tensile force of the machine and the displacement of the actuator were recorded by the machine. It has to be stated here that the whole procedure was displacement controlled, meaning that a constant displacement rate of the head of the machine was applied equal to $1\,{}^{mm}/_{min}$. In addition, the circumferential strain was also measured with stain gauges. A single stain gauge of $5\,mm$ was fitted in each specimen at 45° angle relative to the axis of the applied tensile force. It is crucial that the position of the strain gauge is not on the angle 90° where the openings in between the disks are (Figure 3.7).

This is due to the local bending of the specimen there, as this area is unsupported and the strain results would not be representative of the surface strains produced in the specimen as proposed in Yoon et al (1997). The stress in the circumferential direction according to ASTM D2290 was calculated in eq. (3.17).

$$\sigma = \frac{P}{2A_m} \tag{3.17}$$

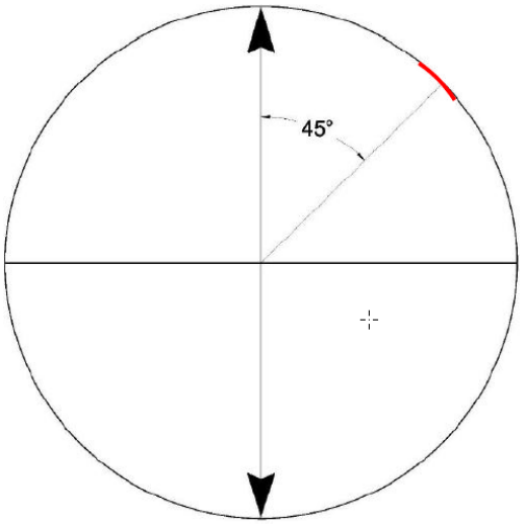

Figure 3.7 Scheme of the strain gauge position on the ring specimen

where P is the tensile force measured by the machine and A_m is the cross section of the ring specimen. All data of the above measured quantities were recorded and saved with Spider 8 DAQ of HBM which was available in the STL.

The seven specimens were named based only on their width as the other manufacturing parameters were the same (Figure 3.8). The standard name was CXX-Y, where XX was the width of each specimen and Y the serial number of the specimen. C20-2 & C20-3 were cut with the reciprocating saw and therefore they were rejected from the analysis of the results.

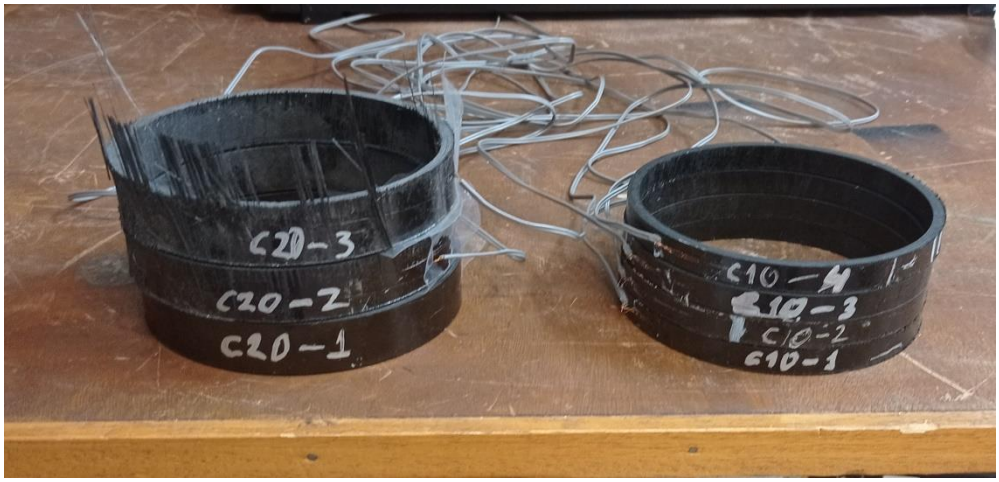

Figure 3.8 Nomenclature of the specimens

3.2.2 Results

The test results of the seven ring specimens are presented in the chart in Figure 3.9 where circumferential stress vs circumferential strain curves were plotted. Obviously, the results were

defective and not the ones expected. Further investigation was done though in order to reveal what went wrong.

Two major flaws were pinpointed: Firstly, the data exhibited abnormalities as the stresses seemed not to increase smoothly and linearly as the strain also increased. Sharply horizontal increases or decreases of the strain were visible giving a view of "steps" on the curves. These steps were more intense in low strain ranges and seemed to be mitigated at high strains but not completely disappear. The second issue which observed was the absence of repeatability in the results. Each specimen curve seemed to have its own unique behavior and the slope of the curves, even for specimens from batches with the same width, diverged from each other.

As already mentioned before, the stresses were calculated according eq. (3.17), while the strains data were obtained by the single strain gauge attached on the circumference of each specimen. In order to investigate which of the two measured quantities was problematic, the tensile force versus the displacement of the head of the machine for specimen C20-3 was plotted in Figure 3.10. This was done for each specimen. It is visible that the force applied by the machine has a smooth continuous increase as the machine head moves upward with a constant rate of $1\,{}^{mm}/_{min}$. As a consequence, the zigzags of the curves in $\sigma - \varepsilon$ charts owe to the strain gauge measurements.

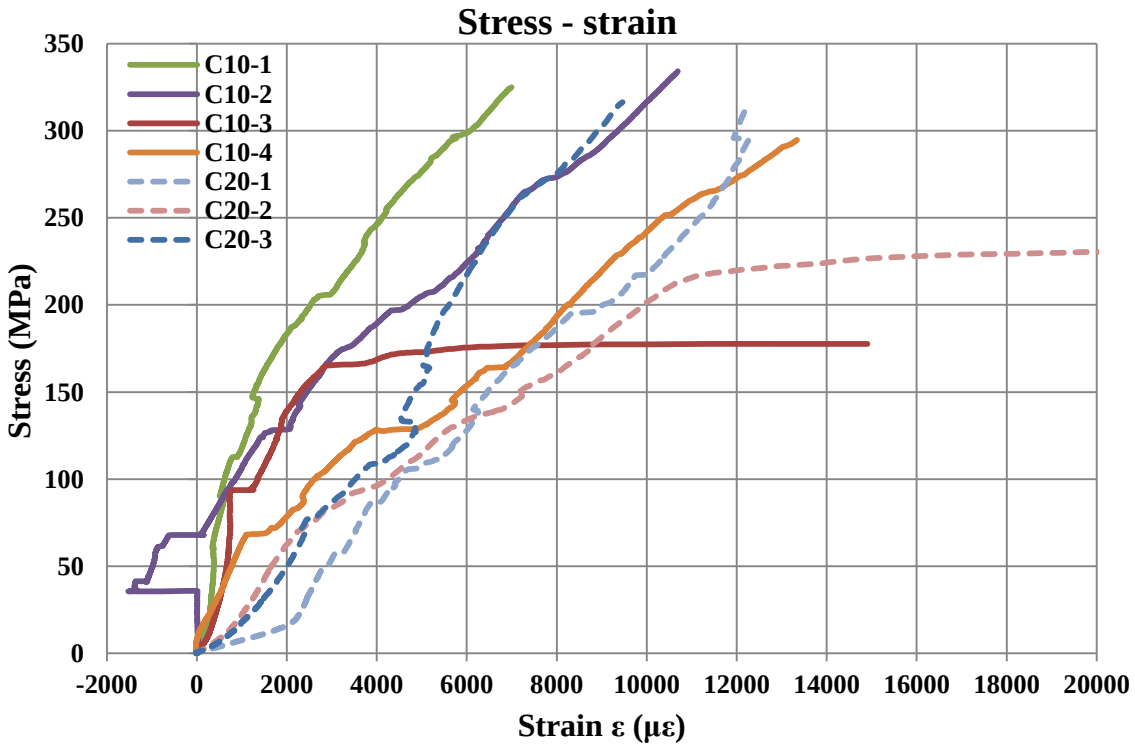

Figure 3.9 Stress - strain graphs for all specimens

Assumptions were made about the reasons of this behavior. The most predominant was probably the smaller diameter between the metal half disks (with the attached metal ring-shaped

chocks) and the ring specimen. Thus, as the load increased during the test procedure the disks touched the specimen at two single points (180° apart) on the specimen vertical axis and not to its whole periphery as it should be (except the unsupported length in between the disks, as it mentioned to be). The strain gauge positioned at 45° was basically at unsupported location vulnerable to small, local bending of the specimen. The steps of the curve which either increased or decreased the strain indicated that the specimen at this circumferential position was either under tensile or compression respectively due to the small local bending. Despite this though, the strains tended to increase as it is obvious by the curves. At high strain values the curves become smoother which comply with the aforementioned assumption as in high tensile strains small local bending became negligible.

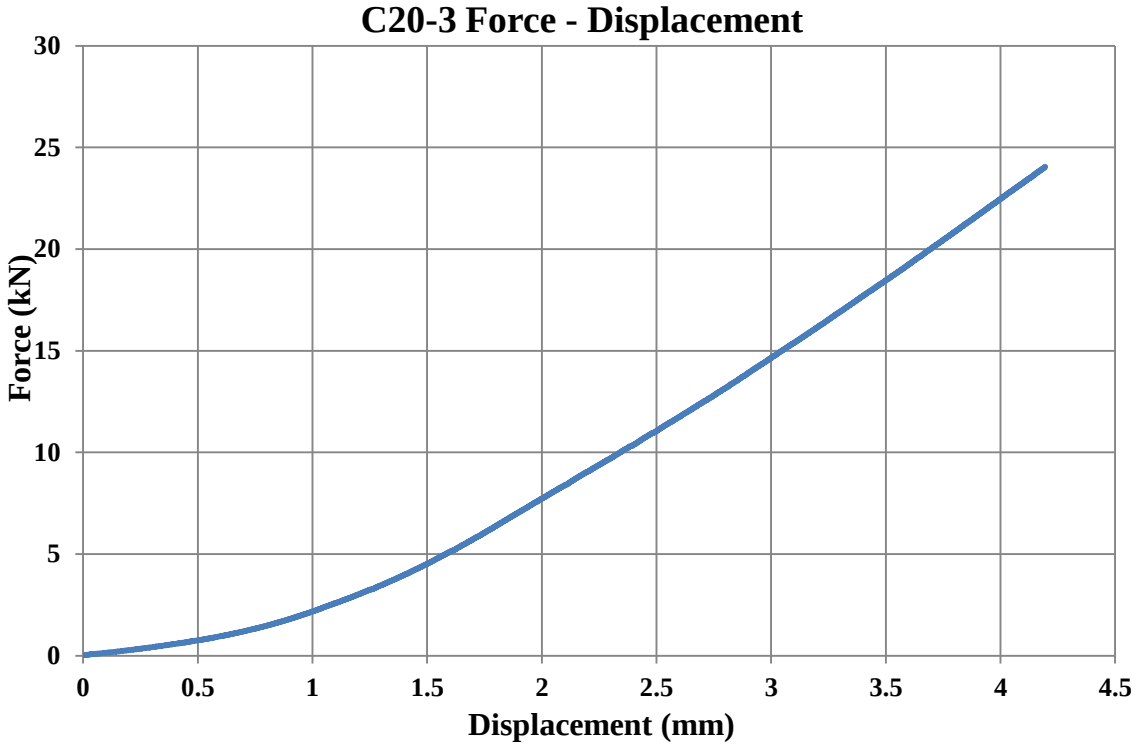

Figure 3.10 Force - displacement graph for C20-3 specimen

The disks and the metal chocks and their relative position to the inner surface of the specimen that were in contact are also linked with the previous assumption. This fixture should be ensured to be completely horizontal. This may not have been met in our case. The relative position of the fixture could have affected the local bending of the specimen at the strain gauge's area and thus the results of the strain data.

Taking these into account, some of the specimens were excluded from the processing of their results. The C10-1 specimen was excluded because it had a very lower failure strain relative to the other specimens. In addition, when C10-3 specimen was examined, the bonding between strain gauge and the specimen surface failed way before the specimen broke. Thus no reliable

results could be obtained. The C20-2 and C20-3 specimens were cut with the reciprocating saw and therefore their results were not reliable. As the plot in Figure 3.9 shows, C20-2 failed at very high strain level compared to the others while the C20-3 failed at stain lower even from the batches of specimen with width 10 mm.

From the last 3 remaining specimens an attempt was made to extract information about the Young's modulus. First of all, a loading up to a certain strain level and an unloading was necessary according to Yoon et al. (1997) in order to accurately estimate the Young's modulus as the mean value of the slopes of the loading-unloading curves which form a hysteresis loop due to friction. This was not done in our case as it mentioned before. Previous studies though (Papadakis et al. 2017) concluded that percentage divergence of the slopes between the loading curve only estimation and the loading-unloading curves estimation varied approximately in the range of $3\% - 6\%$. Thus difference is not negligible, albeit not crucial and thus, the estimated values in our case were reduced by an average factor of 4.5%.

According to standard ASTM D3039 which refers to flat composite material specimens under tensile, the Young's modulus is proposed to be calculated as the chord modulus meaning the slope of the line that connects two points of the curve which have 1000 με and 3000 με strain values respectively, only if the material fails at strains above 6000 με. In our case though, the curves exhibited abnormalities in low strain ranges, as elaborated before, with a tendency to increase smoother at higher strain ranges. Having that in mind, plus the fact that composite materials do not have a proportional limit and thus the stress-strain curves increase almost linearly in the whole strain range, a different calculation of the Young's modulus was tried.

For each of the three remained specimens, linear regression was applied in order to have an estimation of their slopes (Figure 3.11 - Figure 3.13). Three different strain ranges were examined: $3000\ \mu e - 10000\ \mu e$, $5000\ \mu e - 10000\ \mu e$ and $7000\ \mu e - 10000\ \mu e$. in order to find the one in which corresponding liner approaches fit better to the initial curves and their slopes have the minimum deviance among the tested specimens. In all of the three ranges the fit of the linear regression to the data is satisfying, as the R-squared value (coefficient of determination) is quite high ranging from 96.9% to 99.8%. In order to select the most suitable strain range the convergence of the estimated values of Young's modulus for each ring specimen in each range was examined. The Coefficient of Variation (CV) was used for that purpose. The differences from the theoretical values $E_{2,theoritical} = 21.80\ GPa$ (from Table 3.7) were also calculated. All these are presented in Table 3.8.

Table 3.8 Calculation of E_Y in three different strain ranges

E_2 (GPa)	C10-2	C10-4	C20-1	Average	CV	Average difference from theoretical value
~3000με - ~10000με	21.30	19.00	24.30	21.53	10.08%	-1.2%
~5000με - ~10000μεμε	22.20	22.60	23.40	**22.73**	2.19%	4.3%
~7000με - ~10000με	18.50	25.60	16.90	20.33	18.59%	-6.7%

The CV value of the tested specimens in the range of $5000\ \mu e - 10000\ \mu e$ was the lower which indicates similarity among the values of the the specimens in this strain range. The difference from the theoretical value ($E_{Y\_THEORETICAL} = 21.80\ GPa$) was 4.3% which was not the smaller among the three ranges tested.

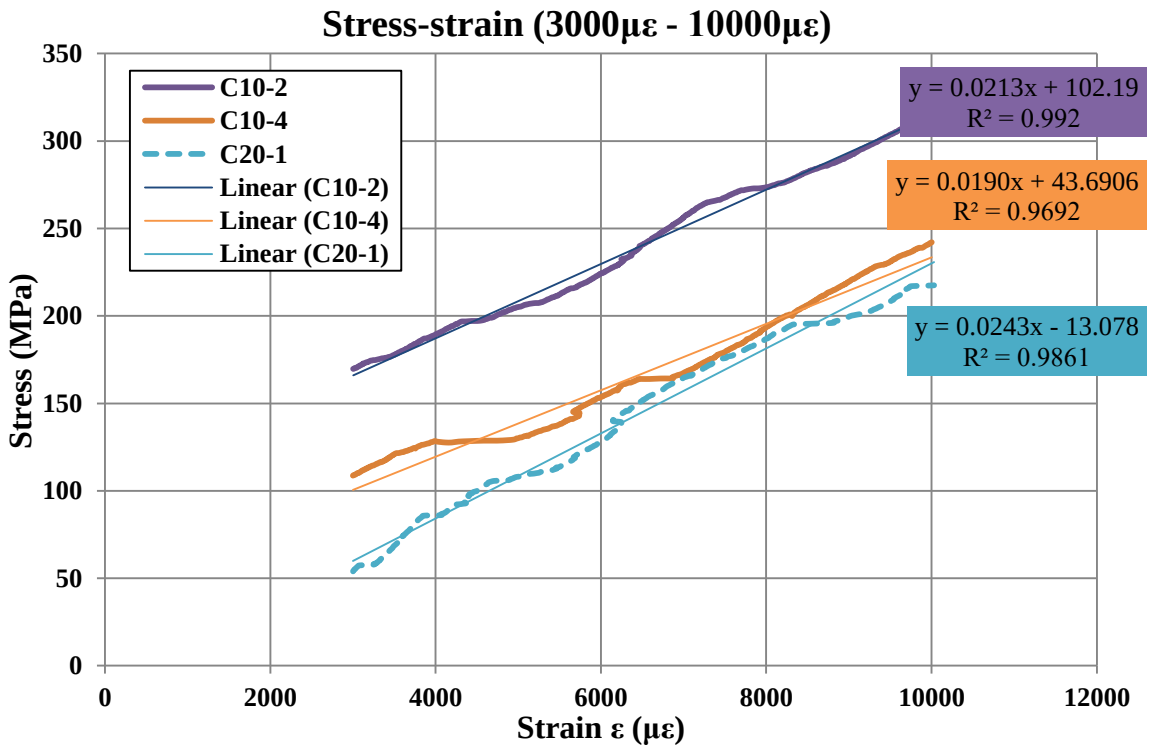

Figure 3.11 Stress-strain graph in range 300με - 10000με

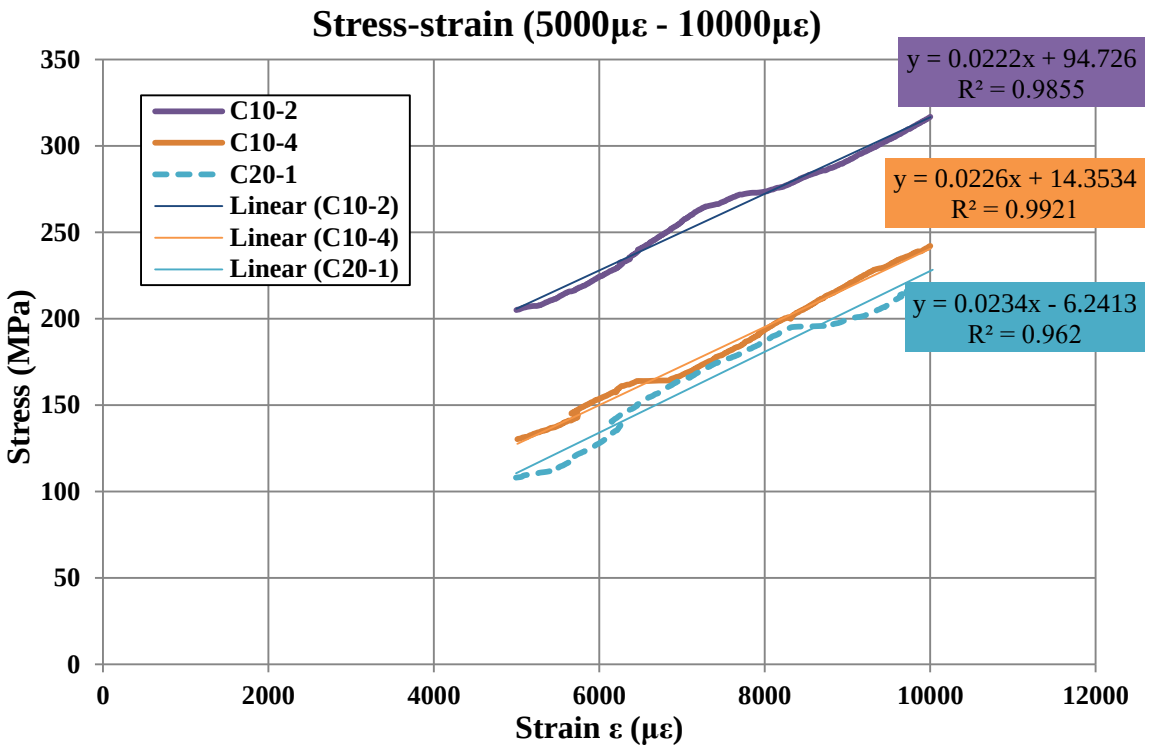

Figure 3.12 Stress-strain graph in range 5000με - 10000με

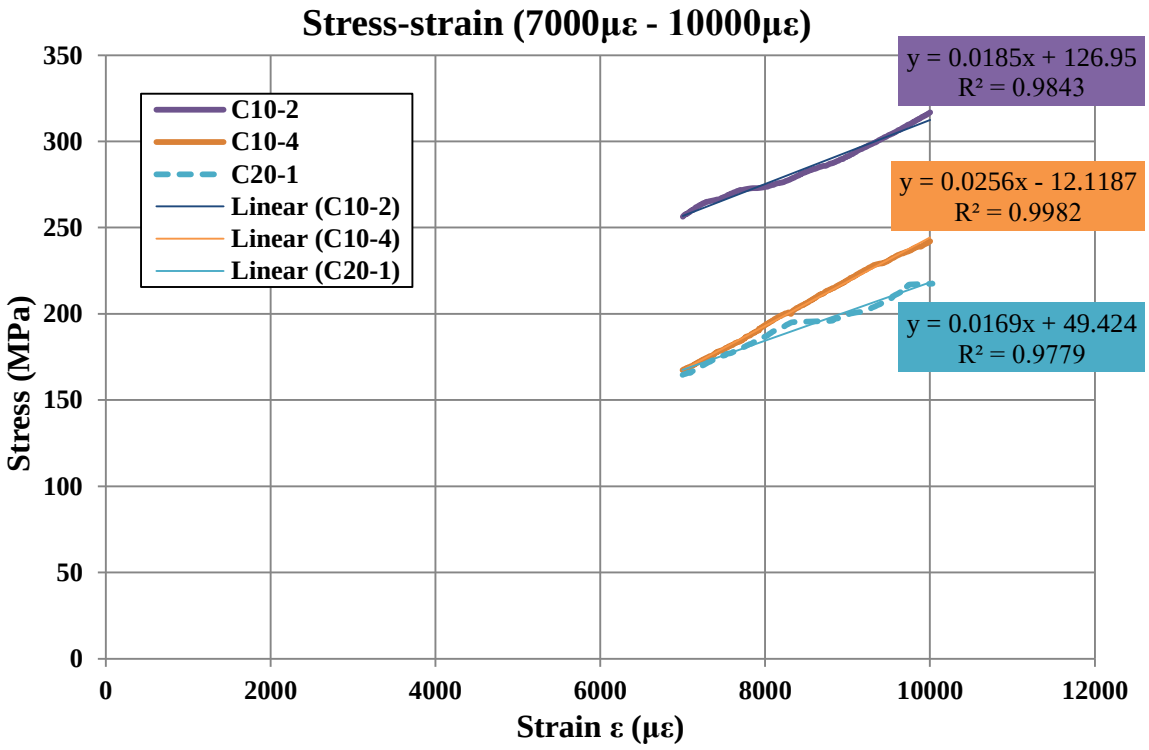

Figure 3.13 Stress-strain graph in range 7000με - 10000με

Considering now an approximately 4.5% reduction on the average value of E_Y due to the omission of the unloading phase of the test as proposed in Yoon et al. (1997), the final average value becomes:

$$E_{Y,experimental} = 21.71\ GPa$$

The difference from the theoretical value was then -0.41 %.

Lastly, it should be mentioned that the apparent hoop strength was not concerned in the thesis and therefore no corresponding calculations were made. However, the results seemed to comply with the observation stated in Papadakis et al. (2017) that by increasing the width, a small decrease in the apparent hoop strength is made.

3.2.3 Conclusions

Despite this satisfying approximation with the theoretical estimation, an unambiguous conclusion cannot be made. Hesitations arise due to the small number of samples that were tested (only three) along with the absence of repeatability of the data due to the previous mentioned reasons. The inappropriate fit of specimens on the fixture due to the half disks smaller diameter led to an increased uncertainty on the results. Raw data of stress-strain curves were impossible to analyze, thus, linear regressions for each curve was drawn in order to extract information about the Young's modulus. Therefore, future works should pay high attention at these factors along with the proper implementation of the procedure described in the standard.

Lastly, it has to be mentioned that the predominant failure mode of the non-defective specimens for the ± 12° plies, which mainly resist in the applied tensile load, was fibers fracture perpendicular to their orientation due to tension, while for the ± 80° plies located in the middle plane small signs of delamination were also visible (Figure 3.14a-c). According to Themelakis (2017) and Papadakis et al. (2017) these failure modes are normal. This indicates that probably no initial imperfections to the material of the intact specimens existed, which would affect the failure mode and the behavior of the specimens during the test, and thus the abnormal behavior of the $\sigma - \varepsilon$ curves indeed is owed to the faulty measurements of the strain gauges due to the reasons mentioned before and not the material of specimens.

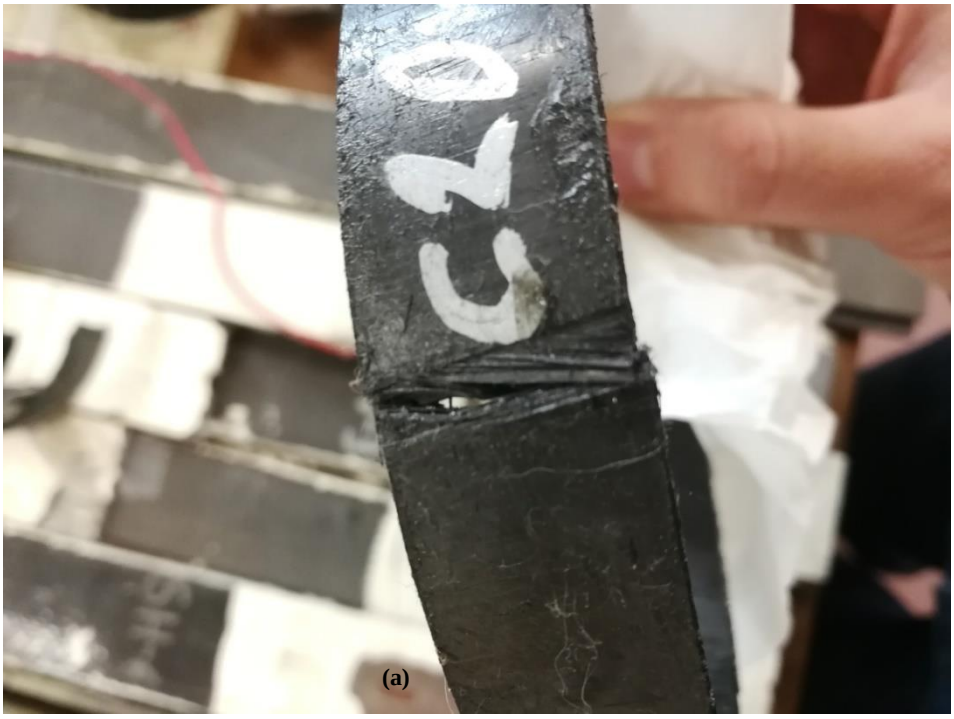

(a)

(b)

(c)

Figure 3.14 (a) outer surface of broken specimen where ± 80° plies are visible
(b) inner surface of specimen where fractured ± 12° plies are also visible
(c) signs of delamination in the middle plane through thickness of the specimen

CHAPTER 4 TORSIONAL TEST OF CFRP SHAFT

In this chapter, static torsional tests, conducted on the CFRP shaft described previously in Chapter 3, are presented. These tests took place in the facilities of LTM of the School of Applied Mathematics and Physical Sciences where the torsion machine is located. The main aim of these tests was to examine the applicability of the TT 10k system on CFRP shafts under static torsion which was done for the first time in author's knowledge. In addition, the results of the test were studied in order to calculate the torsional stiffness of the shaft, compare it to analytical and numerical results and estimate the buckling modeshape of the shaft.

4.1 Preparation of equipment

4.1.1 CFRP Shaft and Torsion Machine

The lay-up and principal dimensions of CFRP shaft were already presented in Section CHAPTER 3. The shaft was initially delivered by the manufacturer as shown in Figure 4.1. Flanges had been added at its edges in order to appropriately attach the shaft to the torsion machine. The connection between the flange and the shaft was made with adhesive in the internal surface of the shaft. In previous tests though, this bonding failed prior to the shaft. In order to enhance this bonding so that the shaft achieves a greater torque and thus the mechanical behavior of the shaft is better examined, through thickness bolts were placed in the region of the bonding at both ends of the shaft.

Figure 4.1 CFRP shaft when delivered from manufacturer

Two metal rings were placed circumferentially on the external surface of the shaft at its edges. These rings were cut from a metal elongated plate which was previously bended to get the appropriate ring shape. Then they were glued on the edges of the shaft, where the shaft and flange were internally bonded. Then holes were drilled alternately per 45 degrees and at different longitudinal positions and the bolts were placed. Figure 4.2(a) shows the final external view of the edges of the shaft where the metal ring, the bolts and the flange are visible. Figure 4.2(b) shows the interior area where the bolts penetrated the shaft-flange bond. Experience gained from previous tests (Vavatsikos 2020) led to the implementation of the above method, mainly for two reasons: firstly, to avoid failure of the bonding between the flange and the shaft in the internal surface of the shaft and secondly, to prevent the local wakening of the shaft and the possible penetration of the bolts inside the composite material layers as the torsional test evolved.

Figure 4.2 (a) External view of the edges of the shaft where attached metal ring-shaped piece and the bolts are visible (b) Internal view of bolts penetration in the shaft-flange connection

The torsional test machine of the LTM was used for the torsional tests (Figure 4.3). It consists of the following parts: one fixed, where the control panel (Figure 4.6 a) is located, and one movable which can move on rails in order to fit to the desired shaft length. Each part has the same plateau where the appropriate flanges for each test can be mounted. The plateau of the movable end, through which the torque is applied, along with the flange used in our torsional test is shown in Figure 4.4 (a).

On the control panel there are the necessary buttons for the operation of the machine such as for the selection of the angle speed imposed to the shaft. The machine load is displacement controlled having three standard rotational speeds

- High: 2.05 deg/s
- Mid: 1.00 deg/s
- Low: 0.52 deg/s

The angle is measured by a digital angle measurement system (clinometer) situated on the movable part and was supplementary installed on the machine in the past (Figure 4.4 (b)). The machine has a maximum torque capability of $600\ kgm\ =\ 5884\ Nm$. The special designed adapter is depicted in Figure 4.5 (a). In Figure 4.5 (b) a draft of the adapter along with its dimensions is shown.

Figure 4.3 Torsional test machine of the LTM (Vavatsikos 2020)

Figure 4.4 (a) Movable end plateau with the adapter mounted
(b)Angle measurement system (digital clinometer

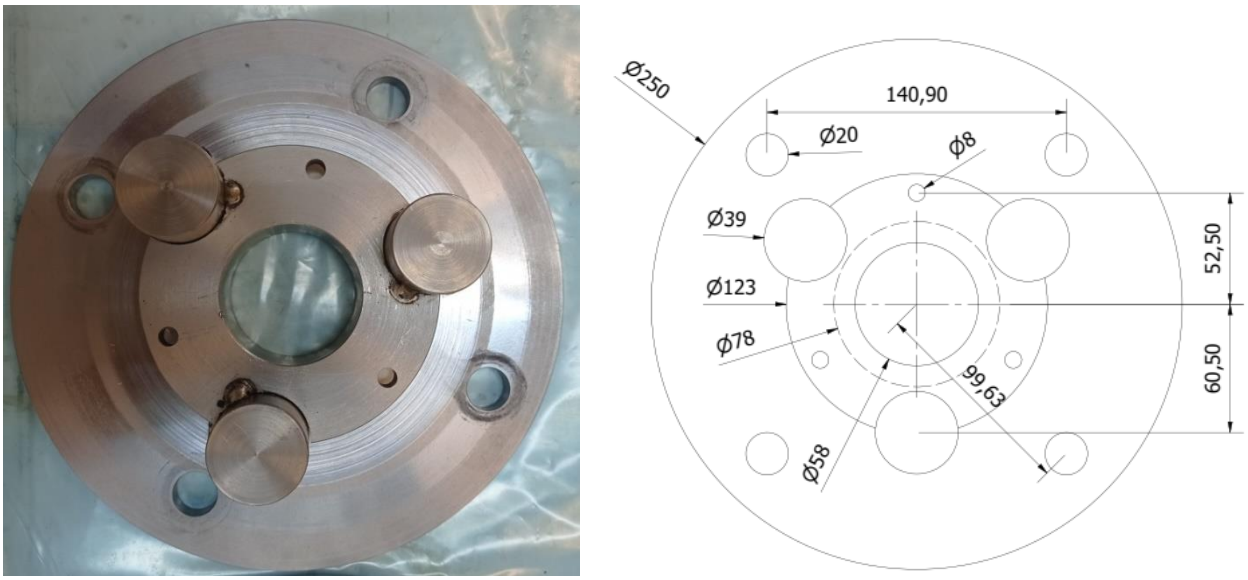

Figure 4.5 (a) Special designed adapter
(b) Adapter schematically depicted

Lastly, apart from the analog torque measuring system located on the control panel (Figure 4.6 b) a Programmable Logic Controller (PLC) (Vision 290 by Unitronics) was attached on the machine in the past in order to get real time, digitalized data of torque and rotation angle. An

extra socket was added on the PLC in order to be able to connect to the Spider DAQ and sample with 25 Hz sample frequency without interacting with the PLC. In that way, data of torque and angle was saved as a voltage signal in a range of 0-10 V wich corresponds at 0-600 kgm and 0-360 deg respectively.

Figure 4.6(a) Control panel of machine (Vavatsikos)
(b) Analog torque measuring system (Vavatsikos)

4.1.2 Shaft preparation - Strain gauges and TorqueTrak 10K placement

First of all, the adapters were mounted on the plateaus of the machine fastened by appropriate bolts (UNC 8 G 3/4×3 with Allen head). Each flange of the shaft (Figure 4.1 and Figure 4.2(a)) had a special designed end so that it fit to the adapter even without the need of bolts. The adapters had three protruded pins (Figure 4.5 (a)). Correspondingly, the end of the flanges had three half-disk-shaped notches on their periphery in order to fit to the protruded pins of the adapters. In this way, although no bolts were used to fasten the shaft, it was still supported and the torque was transferred.

Prior to the installation of the shaft on the machine, strain gauges were attached on the external surface of the shaft and on specific positions circumferentially, longitudinally or even in both directions, in order to get information about the developed strains. In that way, estimation of the torsional buckling modeshape of the shaft could be done in Section 4.5. In Figure 4.7 a scheme of the positions of the attached strain gauges is shown.

Two groups of strain gauges were glued on the shaft. The first one had six single strain gauges with 5 mm gauge length and 120 Ohm gauge resistance, manufactured by Tokyo Measuring Instrument Lab as general purpose strain gauges for metal, ceramics and composite materials (type FLAB-5-11-1LJC-F) which has two 1 m long, vinyl lead wires pre-integrated on the strain

gauges. These cables are appropriate for general use when no temperature changes occur (https://tml.jp/e/product/strain_gauge/leadwire_integrated_straingauge.html). This group used to measure only circumferential strains at specific circumferential points shown in Figure 4.7. The second group had six strain gauges consisted of biaxial, 0°/90° stacked rosette with 120 Ohm gauge resistance and 5 mm gauge length. They were manufactured by Kyowa (type KFG-5-120-D16-11L1M2S) and they also had integrated two 1 m long, vinyl-coated lead wires. These strain gauges were used to measure both circumferential and longitudinal strains at specific circumferential points and at L/2 and 3L/4 longitudinal positions (Figure 4.7).

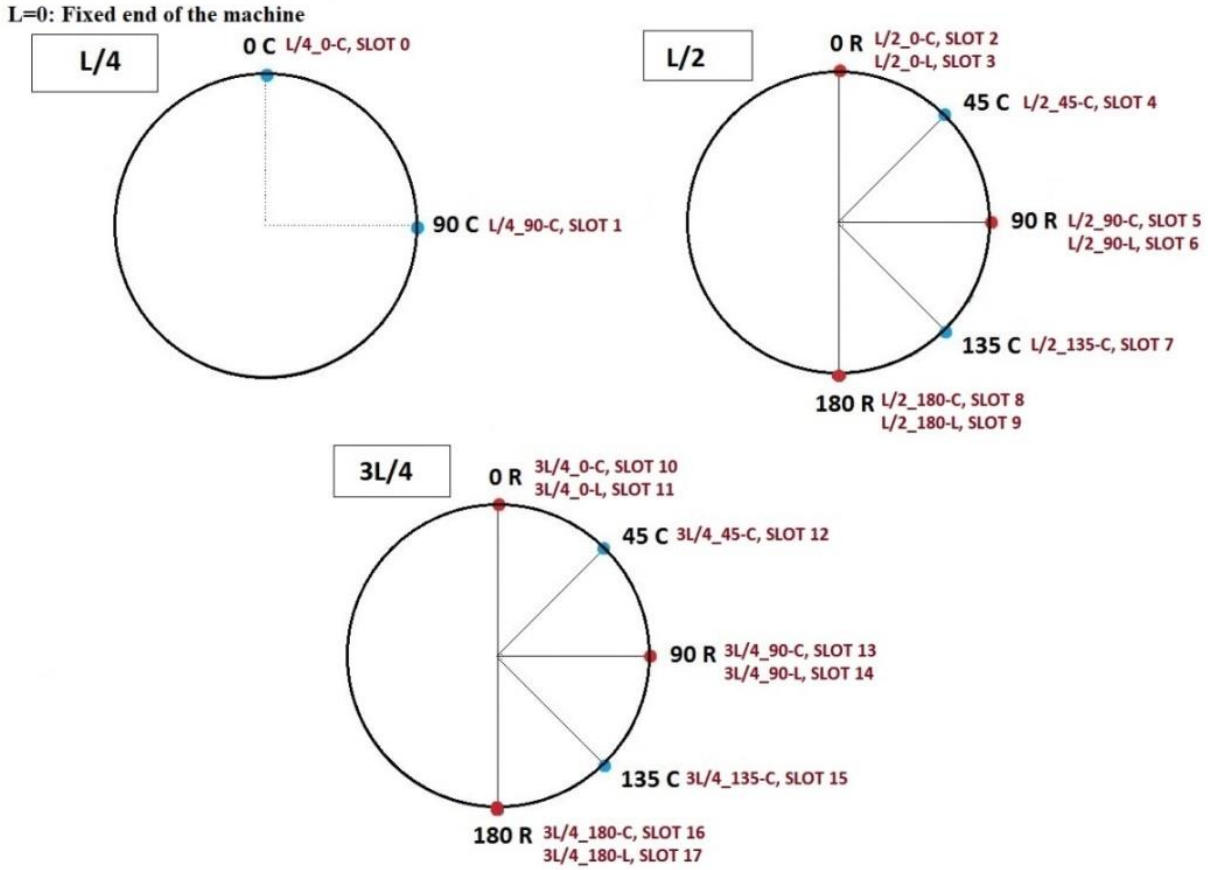

Figure 4.7 Schematic representation of the positions of the attached strain gauges

In all gauges M-Bond 200 adhesive by Micro-Measurements was used which is a cyanoacrylate suitable for routine applications under room temperature. In order to avoid stress concentration on the exposed part of the pre-integrated wires and thus imminent faulty strain measurements, these wires of each strain gauge were slightly loosened after the bonding. Lastly, all the above strain gauges as well as the different grids of the biaxial gauges where connected to the Spider DAQ, each at separate socket.

The last part of the test preparation was the installation of the TorqueTrak 10K on the shaft. The CEA-06-250USA-350 strain gauge by Micro-Measurements was used which has a four-

element full-bridge pattern for shear-strain measurements with grids being 90° apart and 45° relative to the shaft axis. It is a universal general purpose strain gauge appropriate for composite materials with 0.250 in gauge length (6.35 mm) and 350 Ohm gauge resistance. The strain gauge was placed in L/2 longitudinal position and at approximately 112.5° angle in circumference, in between the biaxal rosette gauge at 90° and the single gauge at 135°. A close look at this area is shown in Figure 4.8.

Figure 4.8 L/2 longitudinal position of shaft where the following sensors are visible: single, four-element shear strain (TorqueTrak 10K) and biaxial strain gauges

The transmitter of the TorqueTrak 10K was placed above the battery and connected via a 2-conductor power cable (Figure 4.9). This was nearby to the shear strain gauge. Then they were wrapped around the shaft with tape in order to be secured. A 4-conductor ribbon cable with equal number of different colors was used to connect the strain gauge to the transmitter, as in the appropriate pattern which has already been analyzed in Section 2.1.3.2. The Receiver was placed within the recommended maximum distance of 3 m away from the transmitter. Via the Com (digital output) the Receiver was connected to a discrete socket of the Spider DAQ and the real time data were displayed and saved in a computer.

Figure 4.9 Transmitter, battery and SG of TorqueTrak 10K placed on the shaft

4.2 Test conduction

In Figure 4.10 the final arrangement of the shaft which is mounted on the torsional test machine is shown minutes before the first test starts. In total, twenty one different sockets of the Spider DAQ were used and specifically: eighteen for the strain gauges (single and biaxial), one for the TT 10K, one for the angle signal and one for the torque signal from the machine. The sampling frequency of all the above channels that the Spider DAQ recorded the data was 25 Hz i.e. one sample per 40ms. In addition, data of torque and angle recorded directly from the PLC of machine with a sampling frequency of 1Hz were also obtained. The gauge factors for the single and biaxial strain gauges were confirmed to be 2.079 while the gauge factor for the 4-element full-bridge gauge was 2.035 as it is written on their packages.

A determinant issue was the selection of the settings to the TT 10K in order to successfully measure the torsion torque applied to the shaft. As it will be clear later in the results processing, the initial applied settings were incorrect leading to erroneous results. These errors were realized and was tried to be corrected afterwards in order to conclude whether this torque meter could be used on composite shaft when the correct procedure is followed.

Figure 4.10 The final arrangement of the shaft minutes before the torsional tests

After the settings of the TT10k were applied, one trial and two main static torsional tests were conducted. The two tests were conducted reaching a maximum value of torque close to the maximum capacity of the torsion machine. In the second test this peak in the torque was held steady for almost 20 sec before unloading. An interesting observation during the torsional tests was that the fixed end of the torsion machine seemed to be slightly loose and rotate in the same direction with the movable end while the rotational displacement was applied. Therefore, the recorded rotational angle is expected to be slightly bigger than the actual one applied.

Apart from the experimental tests, static torsional buckling analysis of the shaft was made with Finite Element Method (FEM) in ANSYS which included modeling and meshing of the shaft, boundary conditions, solution and post-processing (Hu et al. 2016). The creation of the model and the analytical script written in ANSYS Parametric Design Language (APDL) that was used, were received from Bilalis (2016) and the interested reader should refer to it for more detailed information. Briefly, the composite shaft was modeled as a layered structure using SHELL 281 structural shell element and the mechanical properties for each layer according to manufacturer. Then, eigenvalue buckling analysis was conducted were the possible buckling modeshapes and buckling load were obtained. Afterwards, non-linear buckling analysis was made in order to obtain the actual displacements, strains and stresses. The numerical results are

presented in the next sections and were used for comparison and evaluation of the experimental results.

4.3 Results processing

The torque versus time curves after the removal of the initial offset is depicted in Figure 4.11. It can be seen that for each test and for the loading and unloading stage of the curves, the data recorded from the Spider DAQ and the PLC of the machine exhibit almost the same behavior. For test 1, the unloading phase followed immediately after the peak value was reached. In test 2 the peak value of torque held steady for about 20 sec as depicted in the curve of the data obtained through Spider DAQ. The data provided from the PLC of the machine on the other hand, showed that unloading came almost instantly after the peak torque reached, just like in test 1. This discrepancy is obvious problematic and the two methods of recording the torque vs time data should be thoroughly examined in the future.

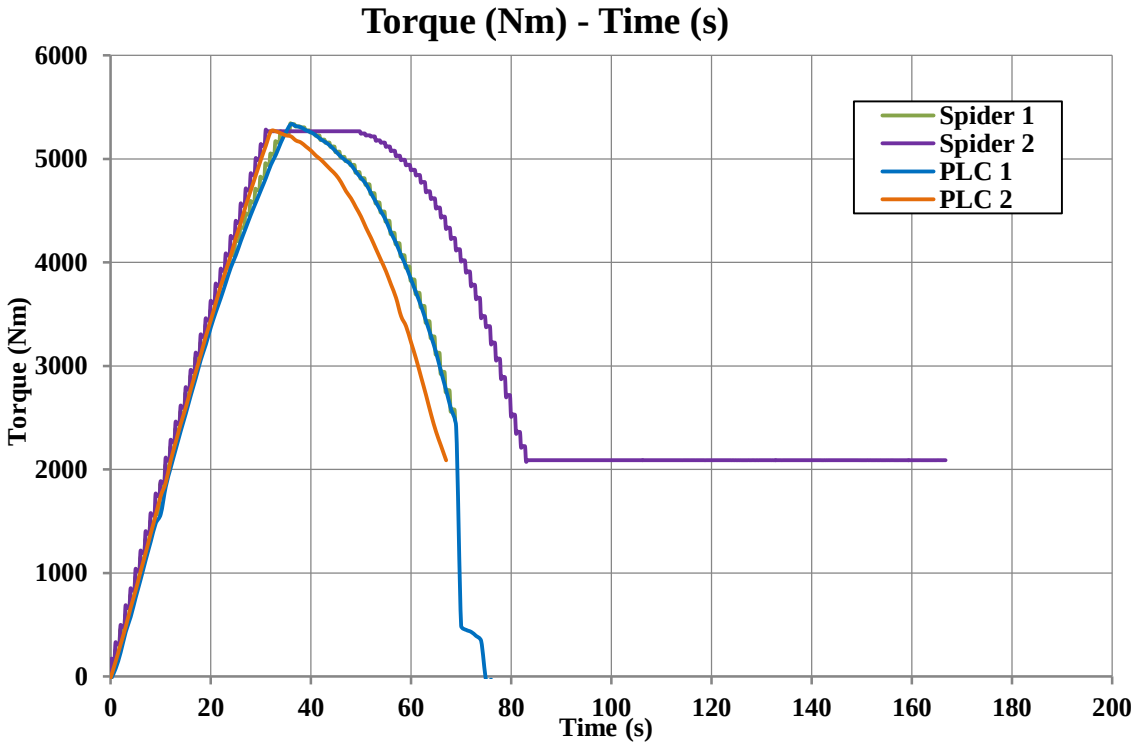

Figure 4.11 Torque (after offset) vs time

Data obtained from the Spider DAQ had a major flaw which was the appearance of "steps", meaning that the curves did not load and unload smoothly, but small repetitive risings and failings occurred. On the other hand, data obtained directly from the PLC did not exhibit such behavior. It is apparent that the sampling frequency of 25 Hz of the Spider DAQ is considerably higher than the 1 Hz sampling frequency of the PLC of the machine, leading to the appearance of "steps".

The same applies for the rotational angle versus time curves (Figure 4.12) where the formation of “steps” is also observed in the curves of the data obtained from PLC. The first assumption that can be made is that the 1 Hz sampling frequency is also relatively high for the specific angle speed that was applied. For that reason, a closer examination of the plotted data recorded from the PLC for the first test was made (Figure 4.13). It can be seen that at some angle values the machine seemed to be stuck for 2 or 3 consecutive seconds, which is not possible considering the three available angle speeds. Therefore, it was concluded that either the displacement controlled system of the machine was defective, leading to not smooth application of the angle speed, or the clinometer was not firmly fixed at its position and could not measure correctly the angle at each interval. Unfortunately these were not a priori known. Thus, the two torsional tests took place in that way bearing in mind the potential detrimental effects these factors may have on the test results.

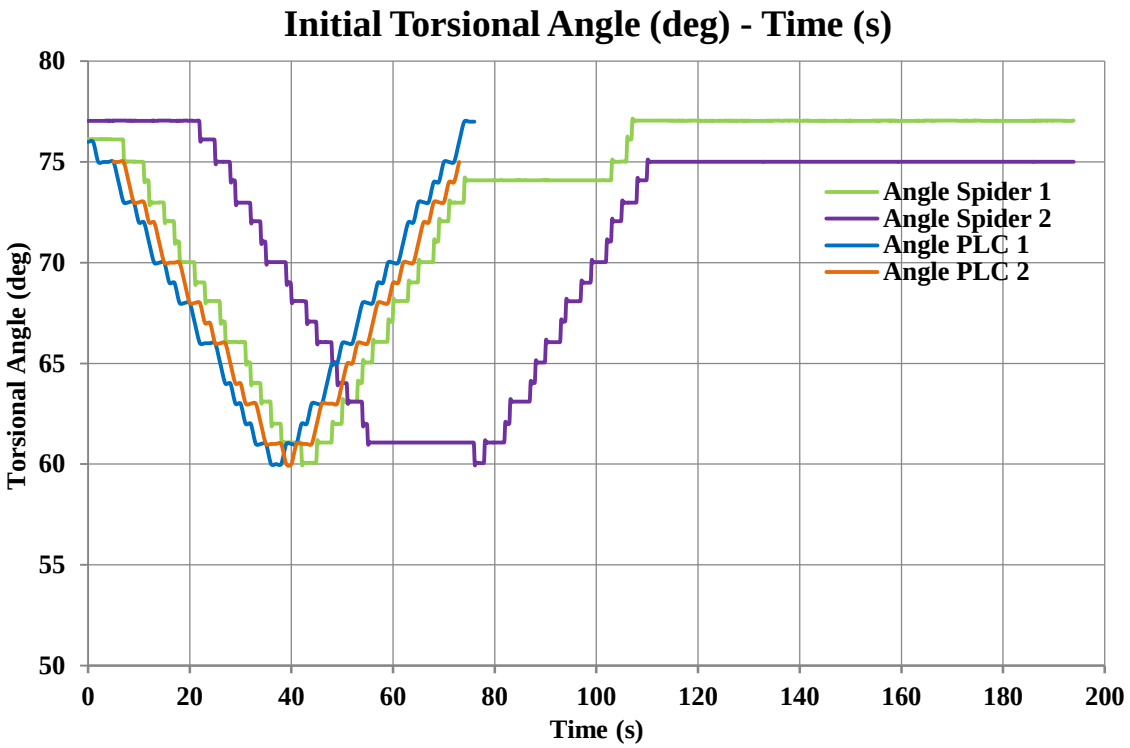

Figure 4.12 Initial torsional angle vs time

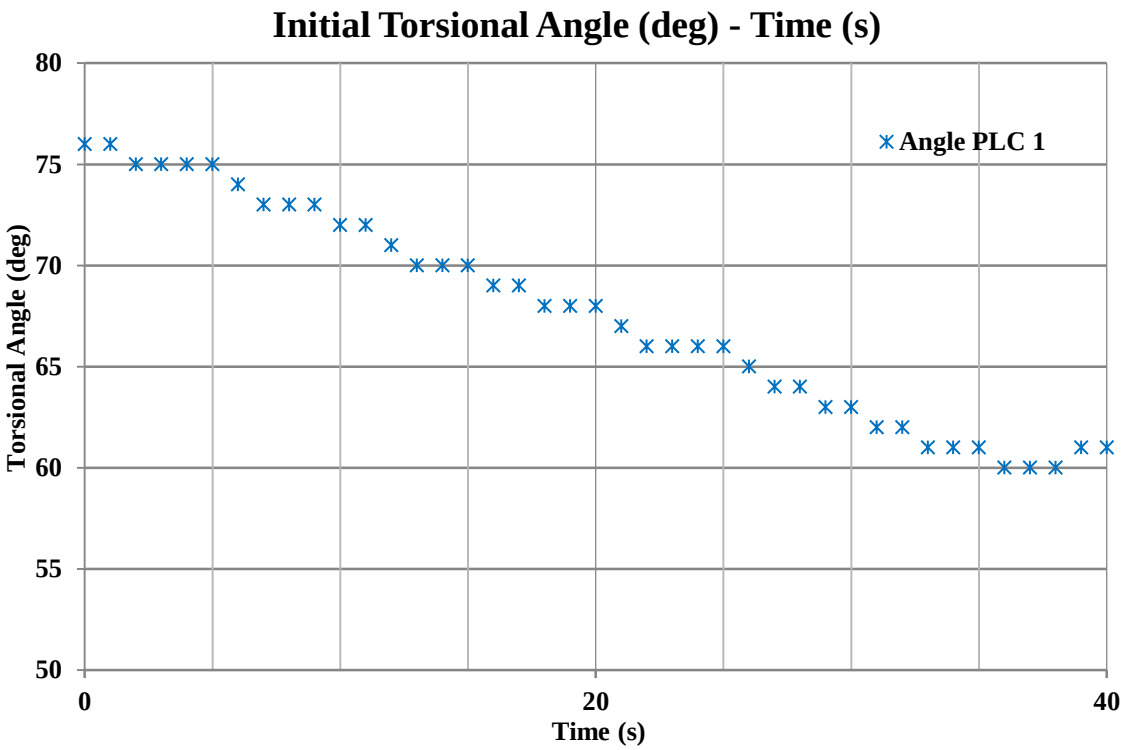

Figure 4.13 Close look at the angle vs time curve from PLC data

The initial torque - rotational angle graph for the loading part is shown in Figure 4.14. The "steps' on the torque - angle curves are an interference of the "steps" that appear in the curved of both torque and angle data, due to the reasons mentioned before. The initial angle recorded by the clinometer at t=0 sec for each test, was set as the zero angle and the remaining rotational angles (which were diminishing as shown in Figure 4.12) were subtracted from this initial value.

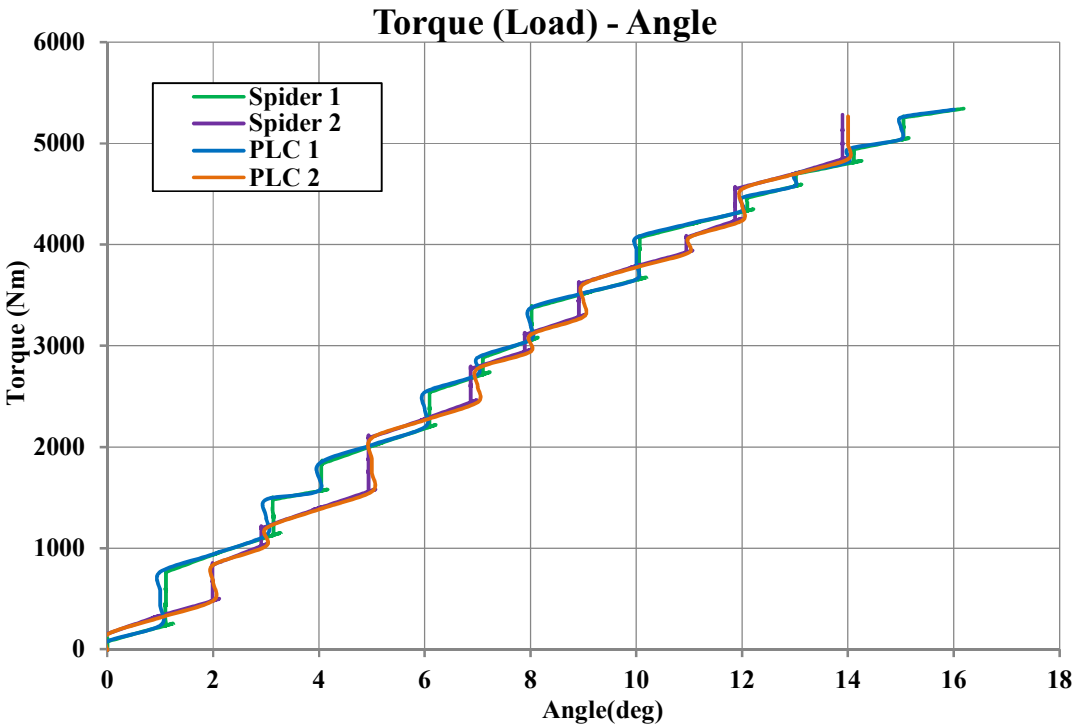

Figure 4.14 Torque vs Angle (loading part)

In order to able to process the Spider DAQ and PLC data and have a better visual representation, polynomial interpolation was done for the loading part of their curves (Figure 4.15). These polynomial curves were selected to be of 2nd order which exhibited high R-squared values (ranging from 0.991 to 0.994) and seemed to visually fit well on the data.

As known from classical mechanics the torque versus rotation angle correlation should be linear. But due to the flaws of the data mentioned previously the linear interpolation seemed not to fit well and the R-squared values were rather smaller. For that reason, 2nd order polynomials were chosen. The curves from the two different recording methods (Spider DAQ and PLC of the machine) of the same test seemed visually to coincide. In order to further evaluate whether the results between the two different tests actually agree with each other, estimation about the torsional strength for each polynomial curve was made. For this reason, the respective coefficients of the polynomial curves were calculated (Table 4.1). It can be seen there that the coefficient of the highest order factor for each group of data is negative, which means that their slopes diminish as the angle increases.

Table 4.1 Coefficients of polynomial interpolation curves

	x^2	x	constant
Spider DAQ 2	-6.977300897	448.8077977	0
Spider DAQ 3	-1.689823824	386.0236576	19.07
PLC 2	-7.678760205	458.3790761	0
PLC 3	-1.895842526	386.5327356	0

In the same graph the torque versus rotation angle curves from previous static torsional tests conducted in Vavatsikos (2020) are also depicted for comparison. These tests were performed on an identical shaft as already mentioned before, with no bolts placed on its edge though and in different torsion device located in the facilities of B&T Composite in Florina, Greece (Vavatsikos 2020). The torsional stiffness estimations from the experimental data in conjunction with the results obtained from TT 10K of Binsfeld, theoretical and numerical analysis are presented in Section 4.4.

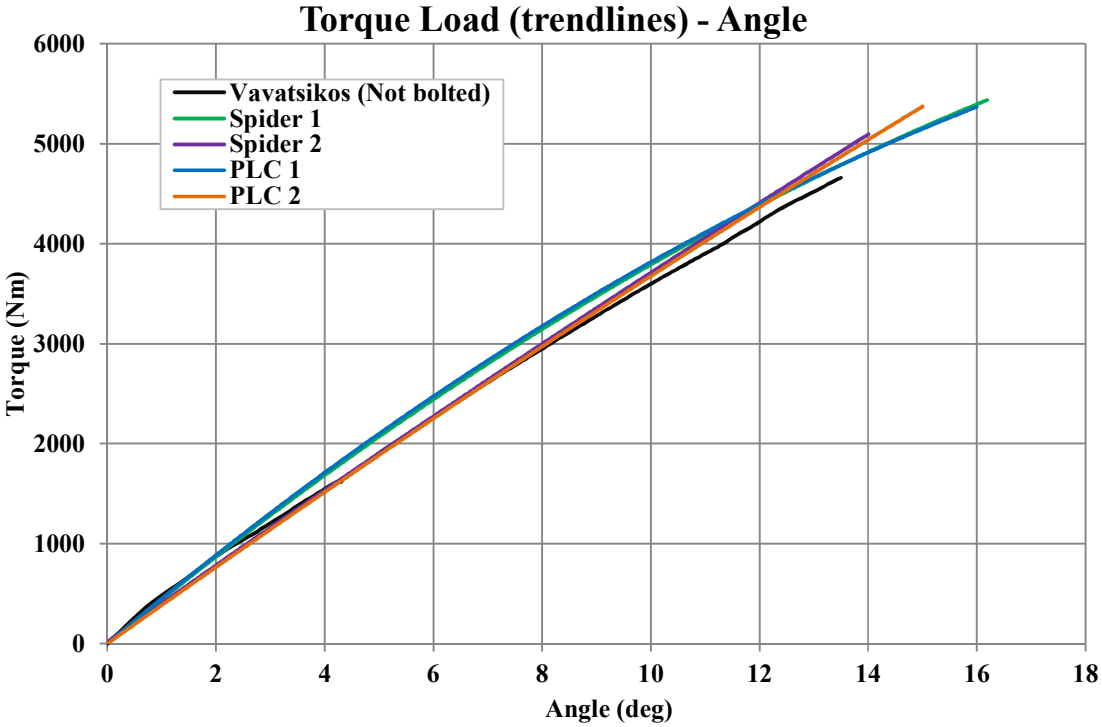

Figure 4.15 Torque vs Torsional Angle (Loading part)

Lastly, in Table 4.2 the maximum torque and rotational angle of the non-bolted shafts in Vavatsikos (2020) is given, along with the maximum torque and angle achieved in the two tests in this thesis. It is evident that the method used to attach the flange on the shaft, described in Section CHAPTER 4 and depicted in Figure 4.2, contributed to the increase in the torsional strength and eliminated the possibility of premature failure in the flange-shaft connection area as happened in the shafts in Vavatsikos (2020).

Table 4.2 Maximum torque and torsional angle values

	$T_{MAX}\ (Nm)$	$R_{MAX}\ (deg)$
Non-bolted shaft (Vavatsikos)	**4659 (Failure)**	**13.50**
Test 1	**5344**	**16.19**
Test 2	**5283**	**15.03**

4.4 Results from TorqueTrak 10K

The main aim of the tests conducted in this thesis was to investigate the feasibility of using the TT 10K on a rotating shaft made from composite material. Due to lack of availability of a relative test rig with rotating engine on which the shaft could be mounted, this could not be examined in this thesis. Thus, this Section is only involved in the attachment of the TT 10K on the carbon shaft under static torsion and studies the potential issues arise and the differences compared to the case when it is attached on a metal shaft.

Mainly due to the fact that the calibration procedure (described in Section 2.1.3.2) prior to the conduction of the tests was not followed exactly as described in the manual, the initial voltage results of the TT 10K were faulty. As there was no possibility to carry out the torsional test again, efforts were made to fix and edit the results post hoc. Comparison with the results of Spider DAQ and the PLC of the machine was made. Finally, useful conclusion where drawn and clarifications were given on what should be done in order to avoid repeat these errors in future implementation of the TT 10K

The initial selected settings are briefly stated below. Firstly, Channel 1 was selected as this had the better signal strength. The Input parameter was selected to have the Transmitter value. The Filter parameter had its default value of 500 Hz. The Input AutoZero parameter was only applied prior to the first trial test and was omitted before the other two main tests. By that, every previous test led to the appearance of an initial offset to the next test. This can be seen at the voltage values at the beginning of each test ($t = 0\ sec$) below. During the process of the results these offsets were manually erased.

$$V_{t=0,Trial\ Test} = 0.0008\ V$$
$$V_{t=0,Test\ 1} = 0.0588\ V$$
$$V_{t=0,Test\ 2} = 0.5948\ V$$

The foremost parameter chosen was the Gain parameter. A value of 500 was set for the Transmitter Gain, which corresponds at ±4000 με full scale strain range in the case of a full bridge pattern with 4 active arms. This was calculated with the aim of an online calculator provided by Binsfeld, a screen shot of which is presented in Figure 4.16.

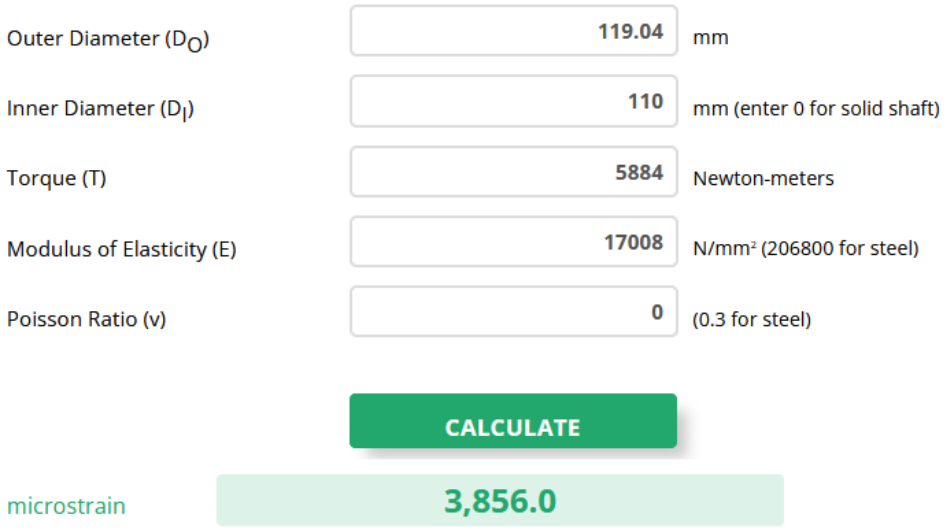

Figure 4.16 Full scale strain calculation (Binsfeld site)

The calculations are based on eq. (2.9), which is presented again here along with eq. (2.6) and (2.8). The Torque (T) value was equal to the maximum capability of the torsion machine. For orthotropic materials eq. (2.8) cannot be applied in general and therefore eq. (2.6) was used instead. Thus, in the online calculator (Figure 4.16) field of Modulus of Elasticity (E) was chosen equal to $2 \cdot G$ while the Poisson's ratio $\nu = 0$.

$$\varepsilon = \frac{T \cdot \frac{D_0}{2}}{2G \cdot I_P} \tag{2.6}$$

$$G = \frac{E}{2(1+\nu)} \tag{2.8}$$

$$\varepsilon = \frac{T \cdot \frac{D_0}{2} \cdot (1+\nu)}{E \cdot I_P} \tag{2.9}$$

As the full scale strain was 3856 με the Transmitter Gain was selected equal to 500 (see Table 2.2). The main fault was that the System Gain was selected to have its default value, i.e. the same with the Transmitter Gain, thus equal to 500. This was wrong as the calibration procedure should have conducted prior to this selection which would have defined the correct System Gain value. This had detrimental effects on the test measurements.

In Figure 4.17 the initial voltage data from TT 10K as recorded from Spider DAQ are depicted versus time. First of all, it is noticed that the maximum voltage value achieved in both tests exceeds the full scale voltage of 10V and entered the overflow, safety range of ± 2 V above the nominal range ± 10 V (which can be reduced depending on the application of the Output Offset parameter). Considering that the full scale of 10 V of the TT 10K should normally correspond to

the ($T_{MACHINE} = 600\ \text{kg} \cdot \text{m} = 5884\ Nm$) it would be expected that the real applied torque was greater than $T_{MACHINE}$. As can be seen from the torque data obtained though the torsion machine recording though, this was not true and the maximum torque achieved in both tests was lower than the maximum capability of the torsion machine $T_{MACHINE}$. This is attributed to the faulty calibration as already stated before. This evidence is strongly supported by the fact that the slope of the curves in the loading phase between the data obtained though TT 10K and the torsion machine recording (Spider DAQ) diverge from each other as depicted in Figure 4.17. This is not expected to happen as the torsional voltage signal of the machine recording has also a range of 0-10 V and thus should coincide.

Furthermore, the maximum reached voltage value in both tests was exactly the same and equal to 10.637 V. This was not expected to happen as the maximum reached torque values in each of the two tests were not equal ($T_{SPIDER\ 2,MAX} = 5328.7\ Nm$ and $T_{SPIDER\ 3,MAX} = 5266.2 Nm$) although the difference was small. The maximum voltage values given from the TT 10K should accordingly have a respective difference. In addition, it can be seen that these peak values stay constant for a period of time (around 13 sec in test No. 1 and around 28 sec and No. 2 respectively). In reality, this was only true for test N$^{\underline{o}}$ 2 (see curve from the recordings Spider DAQ 2 in Figure 4.17) and for a smaller time period though (~20 sec). In test No.1 the unloading phase directly followed the peak value.

The following conclusions were drawn: Firstly, the TT 10K signals in both cases have reached their maximum overflow values and could not increase further, leading to this stagnation at their peak values. This happened as the calibration procedure was not precisely followed which means that neither was the scale factor correctly calculated, nor was the deadweight or shunt calibration applied. This caused this overcome in the nominal voltage signal range. As a result of that the maximum nominal limit of +10 V did not correspond to the maximum torque capability of the machine and although this torque was never reached, the output voltage of the TT 10K exceeded this +10 V limit.

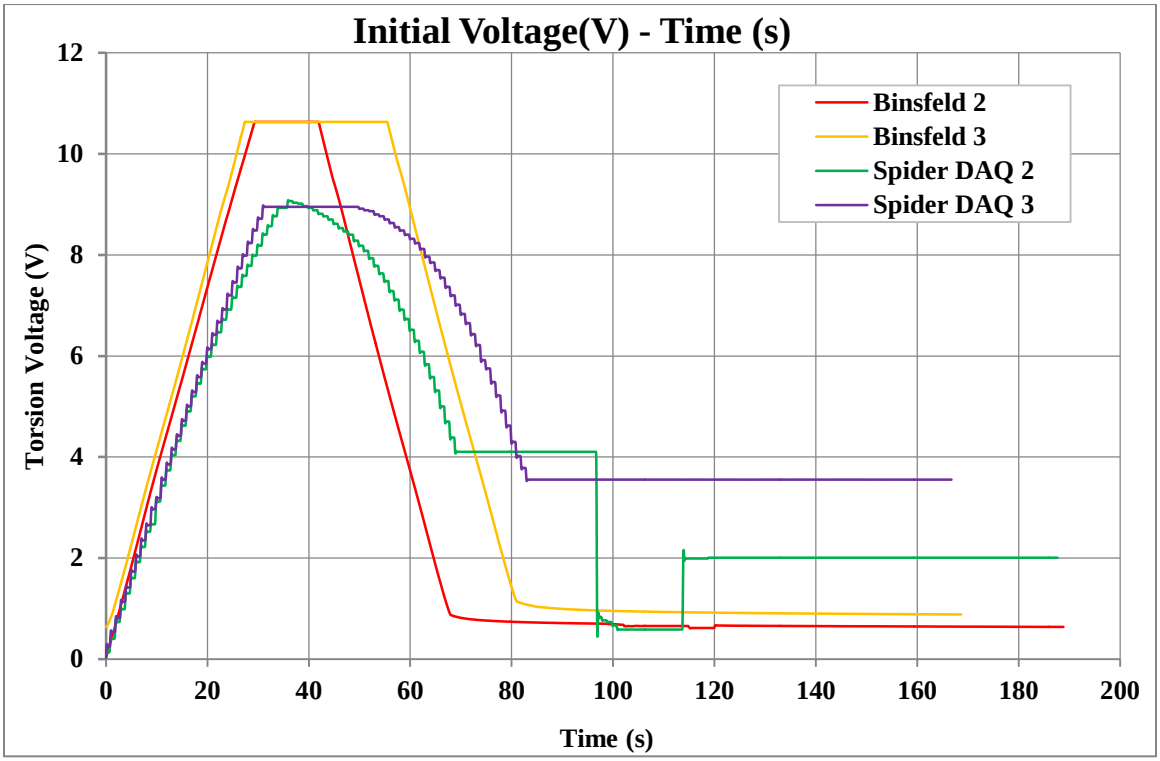

Figure 4.17 Initial Binsfeld voltage data vs time

As already described in Section 2.1.3.2, in order to estimate the System Gain value, two steps are required: calculate the scale factor, which practically modifies the full scale torque output so that it corresponds to a convenient voltage value, and the calibration-dependent adjustment of the voltage output which relates the actual applied torque with the TT 10K torque output. Despite the fact that these steps were not precisely followed and the System Gain was incorrectly selected to its default value, this was tried to be fixed technically afterwards.

Firstly, the appropriate scale factor was calculated and then applied on the torque data. The full scale torque was then calculated from eq. (2.6). The necessary quantities and their values are given in Table 4.3.

Table 4.3 Quantities for the full scale torque calculation

Quantities	Values
$V_{FS}\ (V)$	10
π	3.141593
$E_X\ (\frac{N}{mm^2})$	110810.7
$G_{XY}(\frac{N}{mm^2})$	8503.9
$D_0(mm)$	119.04
$D_i\ (mm)$	110.00
$V_{EXC}\ (V)$	2.5
GF	2.035
N	4
ν_{XY}	0.36
G_{XMT}	500

The full scale torque value is then:

$$T_{FS\_G_{12}} = 5997.7\ Nm$$

In order to scale the torque output so that the full scale voltage output (10 V) corresponds to the maximum (reference) torque capability of the machine ($T_{MACHINE}$ or $T_{REF} = 5884$ N · m) and not the above full scale value, the scale factor Z was calculated:

$$Z_{G_{12}} = \frac{T_{FS}}{T_{REF}} = \frac{5997.7}{5884} = 1.019335$$

The initial torque results were divided with the scale factor. In that way the torque output was adjusted to the new full scale voltage output. The initial value of the System Gain was then calculated. The final step is the deadweight calibration in which the System Gain is readjusted so that the output torque value corresponds to the known applied torque from the torsion machine. This is achieved by adjusting the TT 10K voltage output so that it corresponds to the known applied torque from the machine. This readjustment was made based on the reliable data given by machine recording for test No 1. The time when the TT 10K voltage output gets its maximum value for the first time was selected for the calibration (t≈34 sec in Figure 4.17). The fraction at that time of the voltage value given by the machine recording (which is directly proportional to the applied torque) to the voltage value of the TT 10K was calculated. Of course, in the real implementation of the calibration, any smaller value of torque can be applied (at least in the 10% range of the expected maximum torque).

$$Calibration\ factor = \frac{V_{MACHINE,\ t\approx 34sec}}{V_{TT10K,\ t\approx 34sec}} = \frac{7.785}{10.578} = 0.735980337$$

The voltage data of the TT 10K was multiplied with that value. This corresponds to the readjustment of the System Gain, which should have been done, until the output of the TT 10K is the same as the known applied torque. In Figure 4.18 the final voltage versus time results are plotted after the scaling and calibration have been done and after the offset on time has been erased. The data from the machine recordings are also depicted for comparison. As can be seen, the loading parts of all the curves seem to coincide. Furthermore, due to the reason mentioned previously, the curves corresponding to the TT 10k data could not record the full range of the voltage that corresponded to the applied range of torque and therefore, did not catch up with the maximum applied torque.

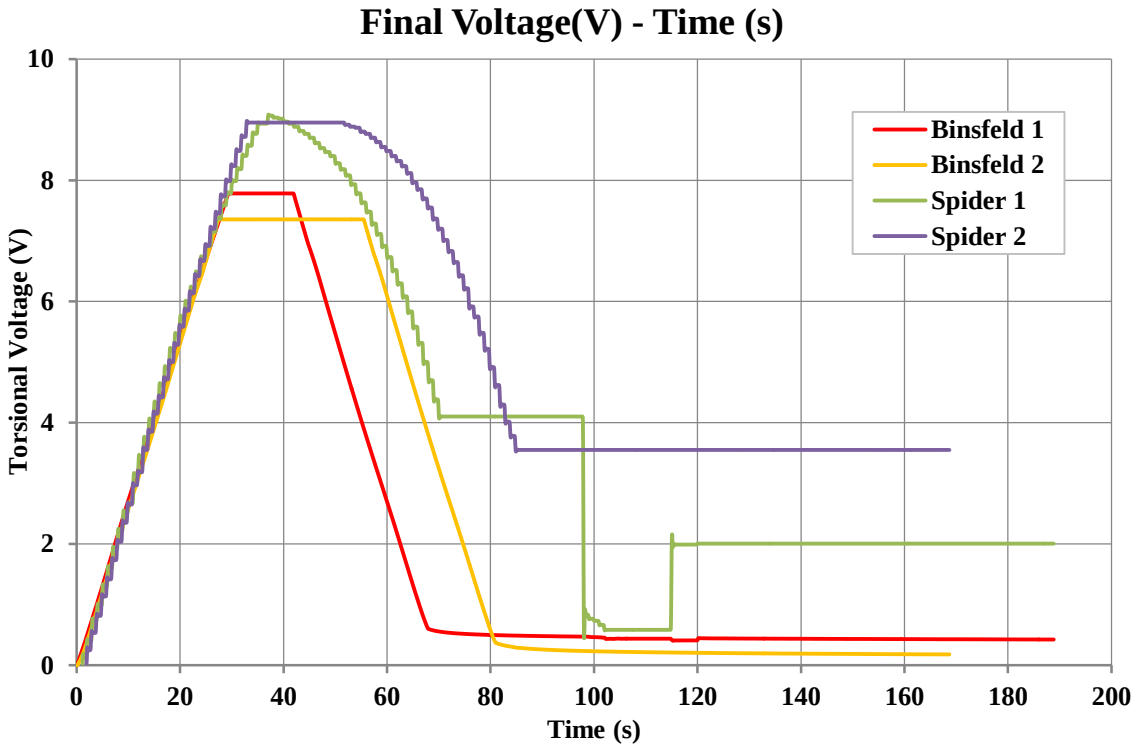

Figure 4.18 Final Binsfeld voltage data vs time

The torque versus time graph has exactly the same shape as the voltage versus time graph, thus it is not presented here. In the torque versus angle graph, "steps" are also present in the curves from the data obtained through TT 10k as expected due to the defective angle data. Therefore, trendlines were drawn in order to get a better visual representation. 2nd order polynomials were again chosen. The final torque versus angle graph is given in Figure 4.19. Curves of the data obtained from Spider DAQ, PLC and TT 10k were drawn, along with the

curve of the test conducted in Vavatsikos (2020) and the curve from the numerical solution in ANSYS. Then, torsional stiffness estimations were conducted.

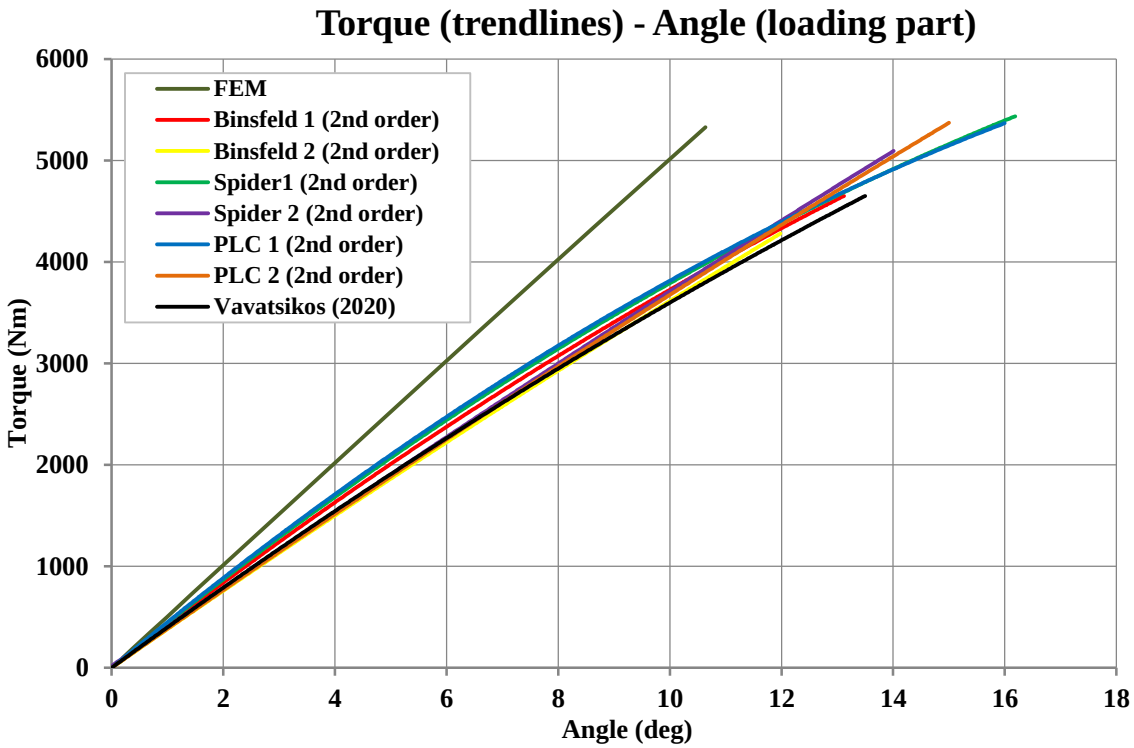

Figure 4.19 Loading part of torque vs angle (trendlines)

Theoretical estimations of the torsional stiffness were initially conducted with two different analytical methods: Classical Lamination Theory (CLT) and Mechanical Analytical Solution (MAS). With CLT torsional stiffness can be calculated from the torsional equation (eq. (4.1)).

$$K_{CLT} = \frac{G_{xy} I_p}{L} \tag{4.1}$$

where G_{xy} is the equivalent shear of modulus which was calculated in Section CHAPTER 3, I_p is the polar moment of inertia of the cross section of the shaft, which is given form eq. (4.2), and L is the length of the shaft.

Table 4.4 gives the calculated values of these quantities.

$$I_P = \frac{\pi}{32}({D_i}^4 - D_0^4) \tag{4.2}$$

Table 4.4 Calculated values of quantities in eq. (4.1)

Quantities	Calculate values
G_{xy} (GPa)	8.502
I_P (mm^2)	5340087.3
L (m)	1.255

The torsional stiffness value through CLT method was then equal to:

$$K_{CLT} = 631.436 \ {}^{Nm}/_{deg}$$

CLT method does not take into account the position of each lamina (stacking sequence) in the laminated composite but only the orientation and the percentage of each lamina (Hu et al. 2016). On the other hand, in MAS method the stacking sequence affects the final estimation. In this method, the torsional stiffness is calculated through eq. (4.3):

$$K_{MAS} = \frac{G_{xy} I_P}{L} = \frac{1}{L} \cdot \sum_{k=1}^{n} ({G_{xy}}^k \cdot {I_P}^k) \tag{4.3}$$

where ${G_{xy}}^k$ is the shear of modulus of lamina k in xy direction which is equal to ${G_{xy}}^k = (\overline{Q_{66}})_k$, ${I_P}^k$ is polar moment of inertia of the cross section of lamina k and n is the total number of laminas. Table 4.5 gives the calculated values of each quantity presented in eq. (4.3) for each lamina and the final value of the torsional stiffness.

Table 4.5 Torsional stiffness calculation results through MAS method

Fiber type	k (number of layer)	Fiber Angle	Thickness (mm)	${G_{xy}}^k$ (GPa)	${I_P}^k$ (mm^4)	${G_{xy}}^k \cdot {I_P}^k$ $(N \cdot m^2)$	K_{MAS} $({}^{Nm}/_{deg})$
24k	1	12	0.56	8.615	592250.8	5102.04	$\frac{1}{L} \cdot \sum_{k=1}^{n} ({G_{xy}}^k \cdot {I_P}^k)$
	2	-12	0.56	8.615	610367.1	5258.11	
	3	12	0.56	8.615	628849.2	5417.32	
	4	-12	0.56	8.615	647700.6	5579.72	
	5	80	0.24	7.087	288050.0	2041.48	
	6	-80	0.24	7.087	291726.8	2067.54	
	7	12	0.56	8.615	683975.8	5892.22	
	8	-12	0.56	8.615	703908.0	6063.93	
12k	9	12	0.34	8.958	442746.5	3966.06	
	10	-12	0.34	8.958	450512.5	4035.63	
						45424.06	631.713

For the experimental data, the torsional stiffness was calculated as the mean value of the slope in 7 different points along the curves, one per degree in the range of 0 - 8 degrees, which

approximately corresponds at a range of 0 - 3000 Nm in torque. This range was considered as adequately representative of the torsional behavior of the shaft, as no failures on the shaft would have yet occurred which would potentially affect the torsional stiffness. Torsional stiffness for the test conducted in Vavatsikos (2020) was also calculated in similar way. In Table 4.6 the stiffness values, obtained from all these data, are given.

Table 4.6 Torsional Stiffness estimations

Torsional Stiffness (Nm/deg)			
		Test No. 1	**Test No. 2**
Experimental	**Spider DAQ**	**386.710**	**370.984**
	PLC	**390.038**	**369.660**
	TT 10k	**379.048**	**364.009**
	Average	**385.265**	**368.218**
TS_{VAV} (Vavatsikos 2020)		**364.691**	
Theoretical	**CLT**	**631.436**	
	MAS	**631.713**	
Numerical	**FEM**	**630.707**	

In both tests, the TT 10K recorded the lowest values of torsional stiffness between the three ways that the experimental data were obtained (Spider DAQ, PLC and TT 10k) for each test but still very close (2.90% for test No. 1 and 1.92% for test No.2). The torsional stiffness estimations from the experimental data in test No.2 were in general smaller than in test No.1 (around 4.4% for the average values of the three ways. This may be attributed to the potential development of defects, like fiber breakages in the shaft which may had occurred and which consequently affected the torsional stiffness of the shaft.

On the other hand, the difference between the average torsional stiffness of test No.1 and TS_{VAV} was 5.64% and between the average torsional stiffness of test No.2 and TS_{VAV} was 0.97%. The quality of the connection between composite shaft and metal flange with adhesive at the end fittings areas in Vavatsikos (2020) should be mainly taken into account for these deviations. The impact of this connection on the mechanical properties and the torsional stiffness of the shaft was not completely clear and more work is proposed to be done in that field. It needs to be reminded here that the shaft in Vavatsikos (2020) failed at this connection area due to debonding of the metal flange. It should be also noted that the active length of the non-bolted shafts in Vavatsikos (2020), schematically defined in Figure 4.20, and the active length of our shaft (the closest distance between the edges of the metal rings of the flanges, see Figure 4.2) is equal and thus the deviations in the torsional stiffness between these estimations cannot be attributed to this reason.

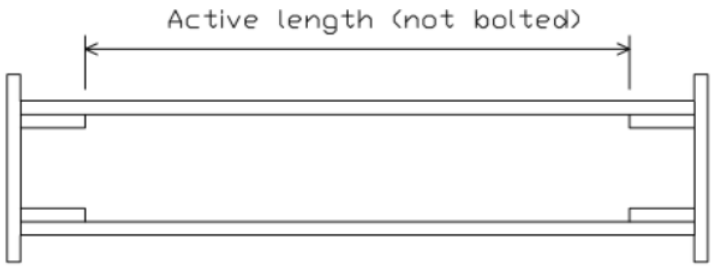

Figure 4.20 Active length of the shaft used in Vavatsikos (2020)

What puzzled though were the theoretical and numerical results. As expected, their relative estimations were very close with the numerical being only -0.14% smaller than the theoretical ones. However, their respective deviations from the average value of the experimental results for test No.1 was 63.93% and 63.71% respectively and from the experimental results of test No.2 was 71.52% and 71.29% respectively. In Bilalis (2016) similar deviation between the experimental and the numerical results was derived. One possible explanation for these enormous deviations, and probably the main one, is the questionable reliability and the uncertainty of the results of the tests, for example due to the defective displacement control system of the torsion machine as already stated before. Another potential reason could be the fact that the exact geometrical parameters of the real shaft (e.g. achieved orientation of each layer, actual thickness and internal diameters) were not precisely known. This would affect the theoretical and analytical estimations of the torsional stiffness as well as equivalent mechanical properties of the shaft that were calculated and used in the formula of torque in TT 10k. It should be noted here that ultrasonic thickness measurement (see Section CHAPTER 3), which gave a quite different thickness than the one proposed by the manufacturer, was conducted on the identical shaft used by Vavatsikos (2020). This measured value was considered as the thickness of our shaft but the actual thickness of the shaft that was used in the torsional test was not exactly known. Lastly, the fact that the fixed end of the torsion machine seemed rather loose (which has already mentioned before) surely resulted to slightly greater rotational angle values recorded than the actual ones applied and thus to a smaller torsional stiffness estimated value.

Evaluation of the results of TT 10K was also done by comparing the strains at the surface of the shaft that were experimentally measures, with the ones theoretically calculated. In addition investigation was whether the equivalent elastic modulus at the longitudinal (E_1) and hoop (E_2) direction along with the equivalent Poisson ratios could be used (ν_{12} and ν_{21} respectively) could be applied instead of G_{12}, although it is known that eq. (2.8) is not applicable in composite materials. The respective full scale strain and Transmitter Gain values for the each occasion were also calculated. The main aim of this evaluation was to conclude which pair of equivalent material properties (G_{12}, E_1 and ν_{12} , E_2 and ν_{21}), when used in eq. (2.2) and (2.9), give the most reliable results. The strains were calculated based on the eq. (2.7), given in TT 10K User's Guide, which is presented again below. Just like in the torque data, the strains data were then scaled

(System Gain adjustment) with the respective scale factor of each pair of modulus and Poisson's ratios.

$$\varepsilon_{FS} = \frac{V_{FS} \cdot 4}{N \cdot V_{EXC} \cdot GF \cdot G_{XMT}} \tag{2.7}$$

where $N = 4$ for the case of a full bridge pattern with 4 active arms.

The theoretical strains were obtained from Zhao & Pang (1995) which has been previously presented in Section. The theoretical relationship between the applied torque and the strains on the external surface of a thin-walled shaft made from composite materials is given, for the case where its one end is fixed and on the other a static torque is applied. The coordinate system of the shaft along with the positive stresses is depicted in Figure 4.21. The relative shear angle $\gamma_{z\varphi}$ is given in eq. (4.4).

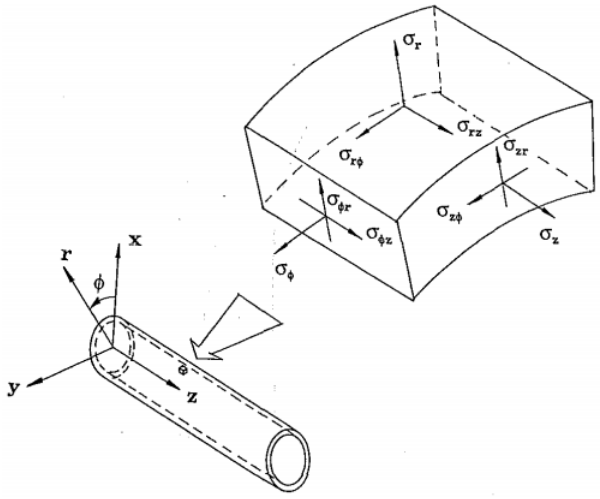

Figure 4.21 Cylindrical coordinate system of the shaft and positive stresses

$$\gamma_{z\varphi} = \frac{Tr}{2\pi \sum_{k=1}^{n} (\bar{Q}_{66})(R_i + \sum_{l=1}^{k} t_k)^3 t_k} \tag{4.4}$$

where $\bar{Q}_{66}$ is the element of matrix $[\bar{Q}]$ which is given in eq. (3.16), $R_i = 55mm$ the internal radius, $n = 10$ the total number of plies of the shaft, t_k is the thickness of each ply (Table 3.1), l indicates all the plies before the k-ply and r is the radius on which the relative angle is calculated (here the external radius $r_0 = 59.5mm$). For each torque value obtained the shear strain $\varepsilon_{z\varphi}$ was calculated, which is given by eq. (4.5).

$$\varepsilon_{z\varphi} = \frac{\gamma_{z\varphi}}{2} \tag{4.5}$$

In Figure 4.22 and Figure 4.23 the strain versus torque chart is presented, for both the theoretically obtained strain data from eq. (4.1) and (4.3) and the experimental ones from TT 10K, for tests No. 1 and No. 2 respectively. For the theoretical strains, the torque data was obtained from Spider DAQ, while for the experimental strains the torque data were obtained from TT 10K data. It can be seen that the curve for the case where the G_{12} is used, instead of the other pairs of elastic modulus and the Poisson's ratios, almost coincide with the curves of the theoretical strains. On the other hand, the rest curves exhibit a significant deviation from the theoretical one.

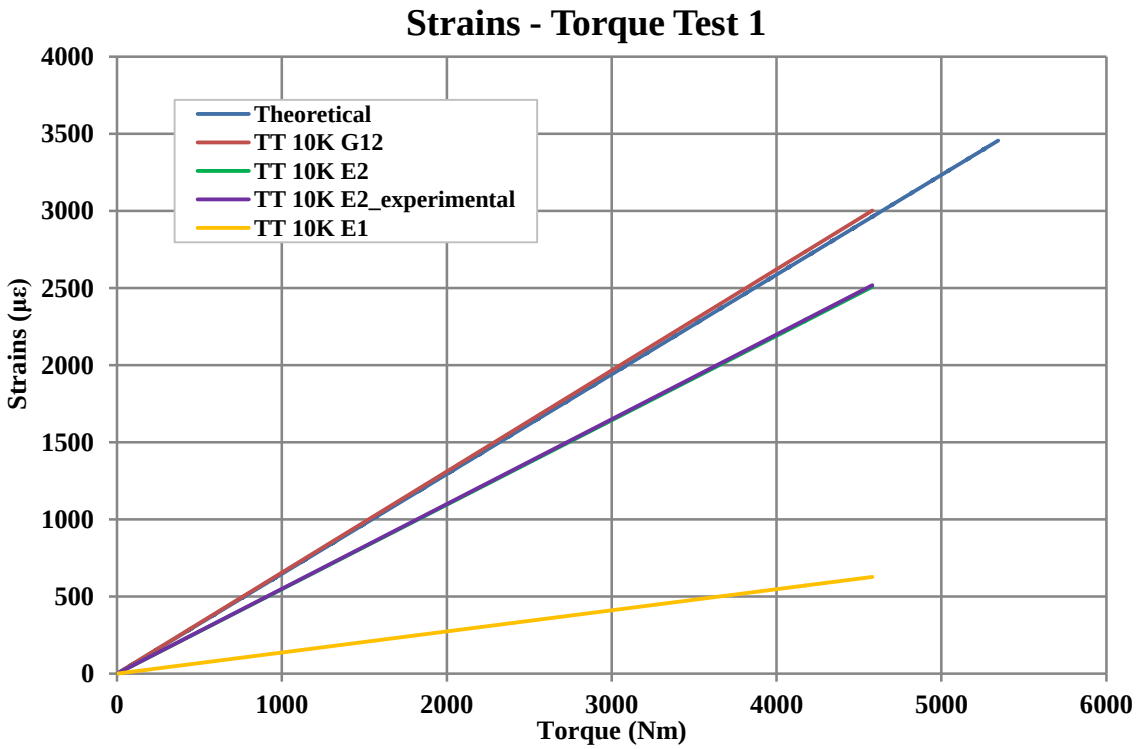

Figure 4.22 Strain vs torque graph for test No. 1

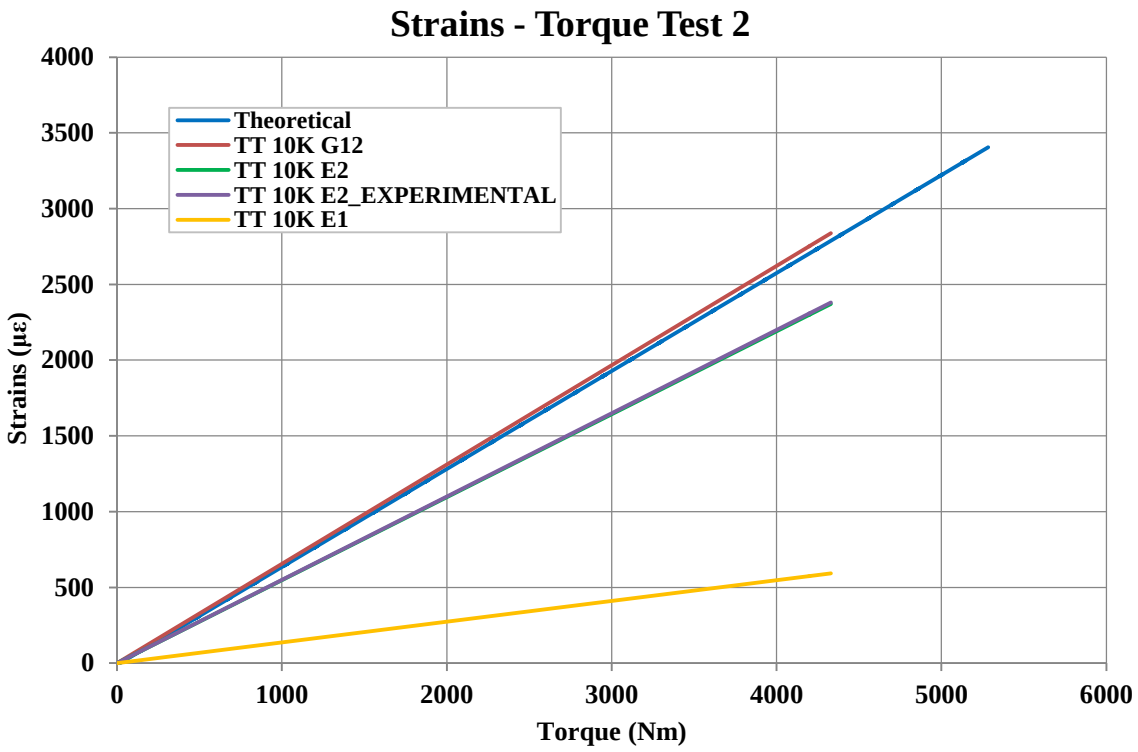

Figure 4.23 Strain vs torque graph for test No. 2

In conclusion, the TT 10K could record torque and strain data with excellent compliance with the theoretical estimations. In order to achieve this, it is vital to make the proper calibration on time. In addition, the material of the shaft should be taken into account prior to the calibration so that the right adjustment of the torque versus voltage output equation is done. The results presented in Figure 4.22 and Figure 4.23 confirm that in the case of a shaft made of composite materials, calculation of the torque in TT 10k should be made with eq. (2.9) instead of eq. (2.2), where shear modulus G is not substituted by its equivalent relationship given in eq. (2.8) ($G = \frac{E}{2(1+\nu)}$).

4.5 Torsional buckling modeshape estimation

When a hollow shaft is under torsion, instability can occur when the torque reaches a certain value. This is called torsional buckling and this load is important in the design of drive shafts. In this section the strains recorded from the single and biaxial strain gauges and obtained through the Spider DAQ were plotted in Strain versus Time and Strain versus Torque diagrams. Examination of these diagrams was made in order to get an indication about the torsional buckling modeshape that was being developed on the shaft.

For that reason, theoretical estimations, available in the literature, of the critical buckling torque of CFRP shafts were obtained. In Stedile Filho et al. (2018), analytical approaches were used to determine eq. (4.6).

$$T_{cr,1} = (2\pi r^2 t) \cdot (0.272) \cdot (E_X \cdot E_Y^3)^{\frac{1}{4}} \left(\frac{t}{r}\right)^{\frac{3}{2}} \quad (4.6)$$

where r is the mean radius in mm, t is the thickness in mm and E_X and E_Y are the elastic modulus in GPa in the longitudinal and hoop direction respectively. In Vinson & Sierakowski (2008) one more solution for the buckling torque is given in eq. (4.7). This equation is only valid if the condition in eq. (4.9) is fulfilled.

$$T_{cr,2} = 21.75 \cdot (D_{22})^{\frac{5}{8}} \cdot (E_X t)^{\frac{3}{8}} \cdot \left(\frac{R^{5/4}}{L^{1/2}}\right) \quad (4.7)$$

where:

$$D_{ij} = \sum_{k=1}^{n} (\bar{Q}_{ij})_k t_k [\bar{z}_k^2 + \frac{t_k^2}{12}] \quad (4.8)$$

t_k is the thickness of each layer and z_k is the distance of each layer from the mid-layer.

$$\left(\frac{D_{22}}{D_{11}}\right)^{5/6} \cdot \left(\frac{E_X t}{12 D_{11}}\right)^{\frac{1}{2}} \cdot \left(\frac{L^2}{R}\right) \geq 500 \quad (4.9)$$

In Table 4.7 the results of the calculations of the critical buckling torque from eq. (4.6) - (4.7) are given. It can be seen the maximum achieved torque in the tests (~5.3 kNm) conducted in this thesis were three to four times under the theoretical estimations of the buckling torque. Buckling torque from the results of the numerical solution was also acquired. The eigenvalue buckling analysis gave a critical buckling torque equal to $T_{cr,FEM} = 13239.2$ Nm which is lower than the analytical estimations and confirms that the analytical estimations are in general conservatives as stated in Stedile Filho et al. (2018). The buckling modeshape at this critical buckling torque was type 2, meaning that two crests and two troughs were developed when the shaft deformed, with each crest being 90° circumferentially apart from each trough (Figure 4.24). Other buckling loads obtained from the eigenvalue buckling analysis are given in Table 4.8 along with their corresponding buckling modeshapes.

Table 4.7 Theoretical estimation of buckling torque in Nm

$T_{cr,1}$	**18386.11**
$T_{cr,2}$	**16429.58**

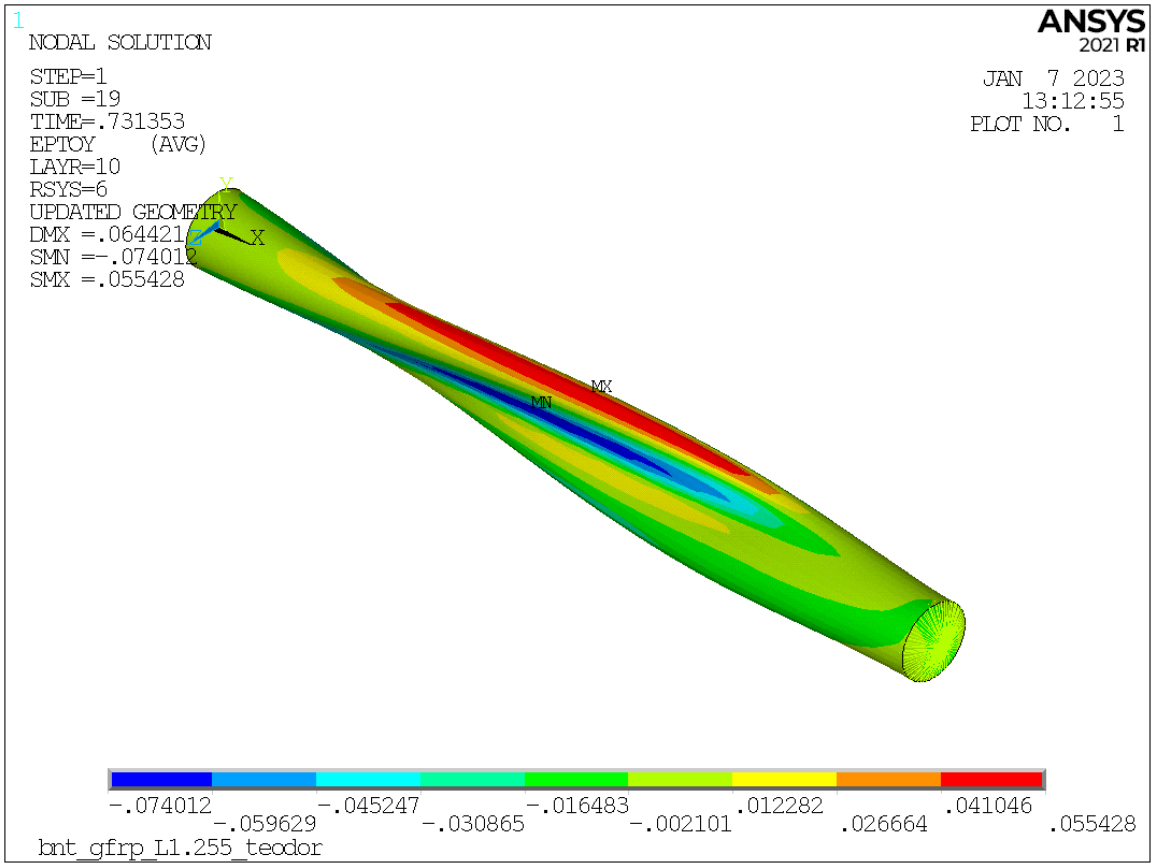

Figure 4.24 Contour plot of circumferential strains in buckling deformed shape of the shaft

Table 4.8 Eigenvalue buckling analysis results: Torque and modeshape

Buckling Torque (Nm)	Buckling modeshape
-15390.4	3
-15390.4	3
-13460.8	2
-13460.8	2
13239.2	**2**
13239.2	2
15184.6	3
15184.6	3
17651.4	3
17651.4	3

The experimental strains results of the various strain gauges used, exhibited the same behavior between the two tests conducted, meaning that whenever a strain gauge in test No.1 recorded tensile or compressive strains, the same happened for the same SG in test No.2 and these strains had the same pattern. Therefore, the results of test No.1 were only assessed.

In Figure 4.25 and Figure 4.26 the circumferential and longitudinal strains versus time have been plotted respectively from the corresponding strain gauges of Figure 4.7. The torque data are also plotted on the secondary vertical axes. All the curves (strains and torque) exhibit the same behavior in the loading phase with respect to the time. In the unloading phase the torque curve d not follow the exact same path as the strain curves but this is not crucial for the processing of the results as only the loading part is important.

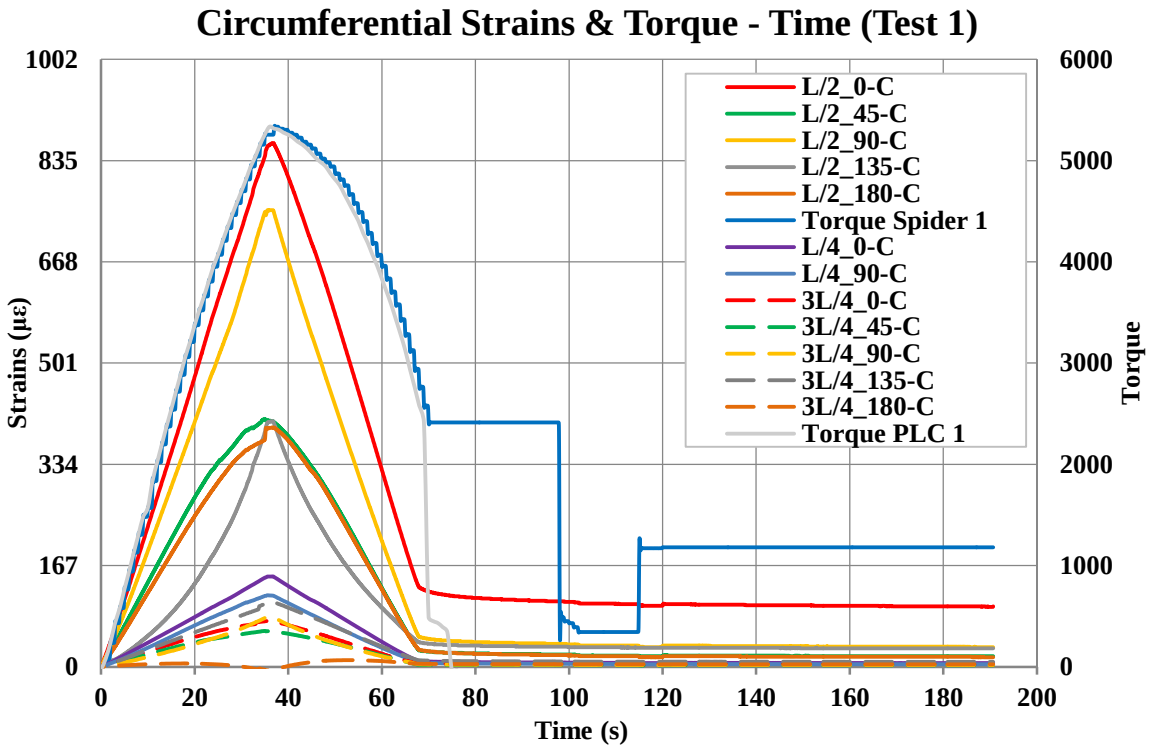

Figure 4.25 Circumferential strains and torque vs time (Test 1)

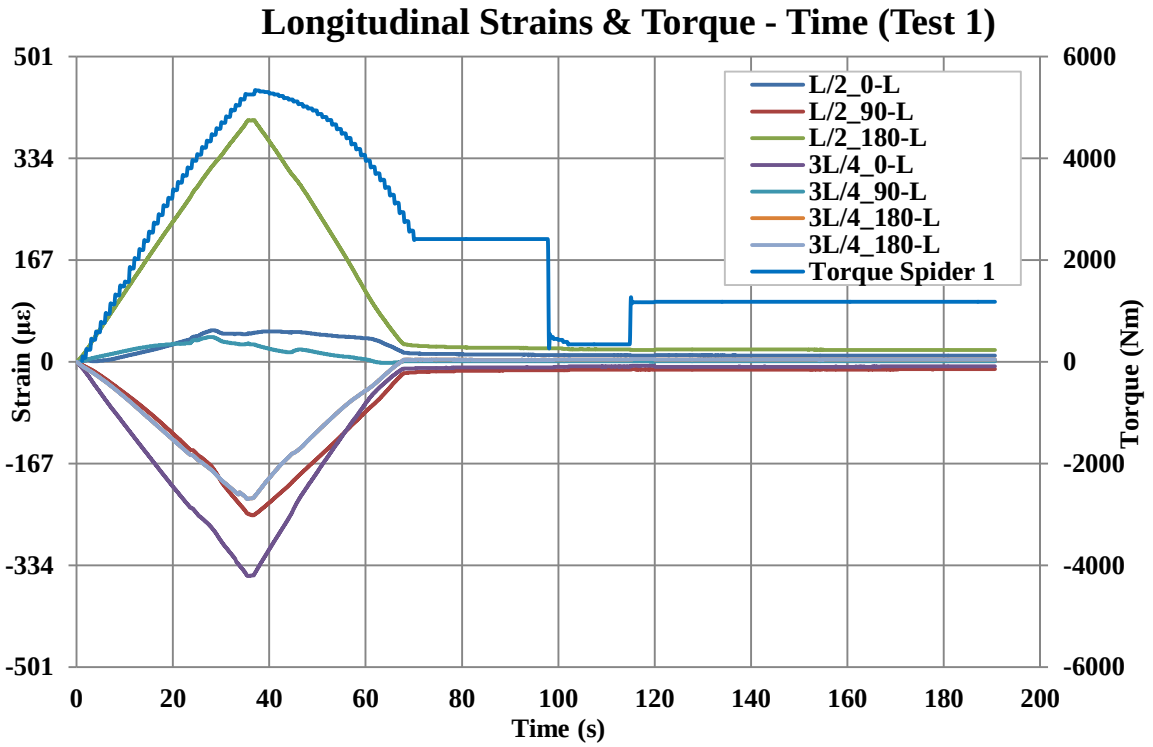

Figure 4.26 Longitudinal strains and torque vs time (Test 1)

In Figure 4.28 to Figure 4.32 the circumferential and longitudinal strains versus torque are demonstrated separately at each of the three cross sections (L/4, L/2, 3L/4). 2nd order polynomial approaches were used in order to get an improved representation of the strain versus torque curves. In some few cases (L/2_135-C, 3L/4_90-C, 3L/4_135-C) 3rd order approaches were used as the conformed better with the initial data. The visual fit between the initial curves and the polynomials seemed accurate and in almost all cases the R-squared value tended to (or even exceeded) 0.999. This implies that these polynomials approaches were reliable. In that way, conclusions about the tendency of strains at each position could be drawn and comparison between the different curves could be made.

Furthermore, the circumferential strain results from the numerical approach were also plotted in the same graphs. After trials, the $0.8\%D_i$ initial imperfections size was selected for the non-linear buckling analysis as the most representative of the actual imperfection of the experimental shaft. This was done by selecting two nodes in the mid-length section of the shaft model where the maximum and the minimum circumferential strains occurred (90 degrees apart). These nodes were obvious on a crest and a trough respectively in the deformed shape of the shaft model. These strains were plotted in a circumferential strain-torque diagram along with the experimental strains recorded from the SG in the mid-length section (Figure 4.27). The experimental strain-torque curves should lie in-between the strain-torque curves of the numerical solution meaning that the maximum and minimum numerical strains should be an upper and lower limit of the experimental curves. Having that in mind, 3 cases of initial imperfection sizes of the shaft model

were tested ($1\%D_i$, $0.75\%D_i$ and finally $0.8\%D_i$). The last value ($0.8\%D_i$) was selected as in that case the curve of the SG which recorded the maximum strains in L/2 (in that case the SG at 0°) was very close to the numerical strain-torque curve with the maximum strains. Then for mid-length section the node in the model with the higher circumferential strain (top of crest) was assigned to be in the same position with the SG at 0 degree which recorded the highest experimental circumferential strains. The rest of the nodes then were automatically assigned to the corresponding SG positions.

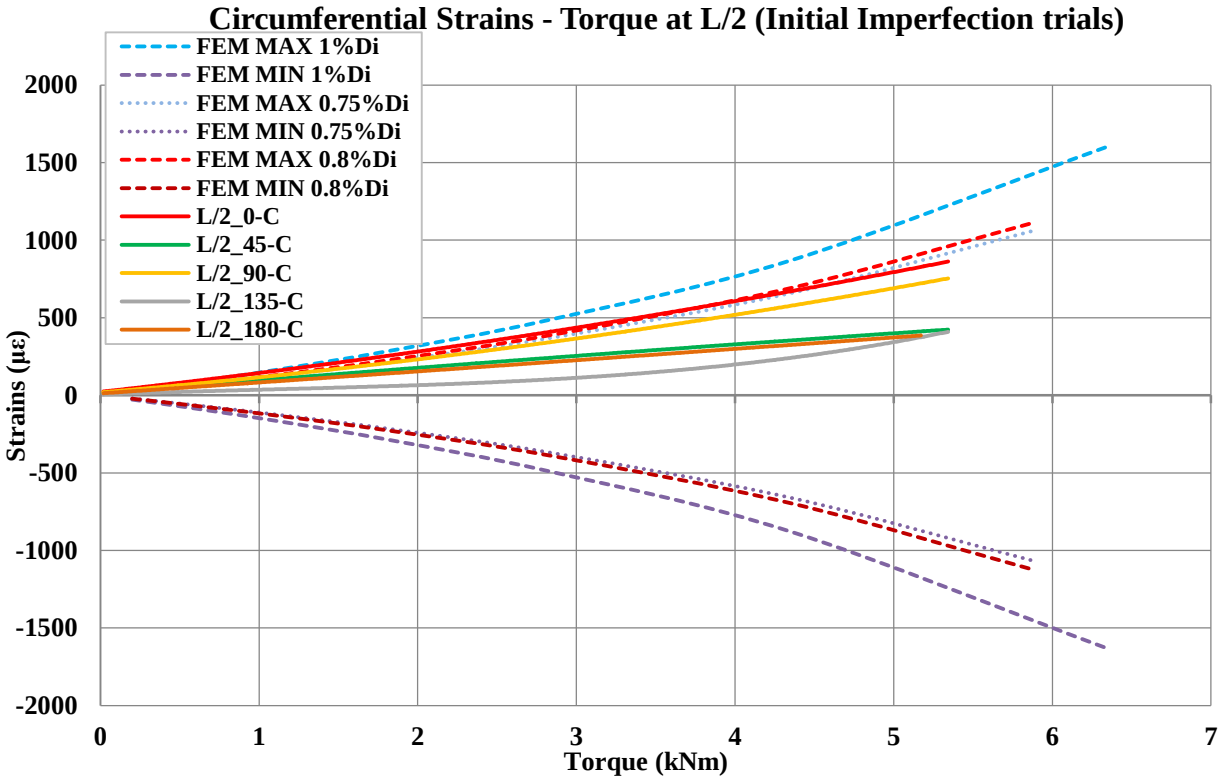

Figure 4.27 Experiment and numerical circumferential strains with 3 initial imperfections sizes trials for the shaft model

At cross section L/4 circumferential strains were measured from SG No. 0 and No. 1 at 0 degrees and 90 degrees respectively. In all the torque range, strains at 0 degrees were higher than strains at 90 degrees and reached a maximum value of 892 με. The slopes of both curves had a slight tendency to increase while the torque was increasing, which indicated that they were probably near a forming crest.

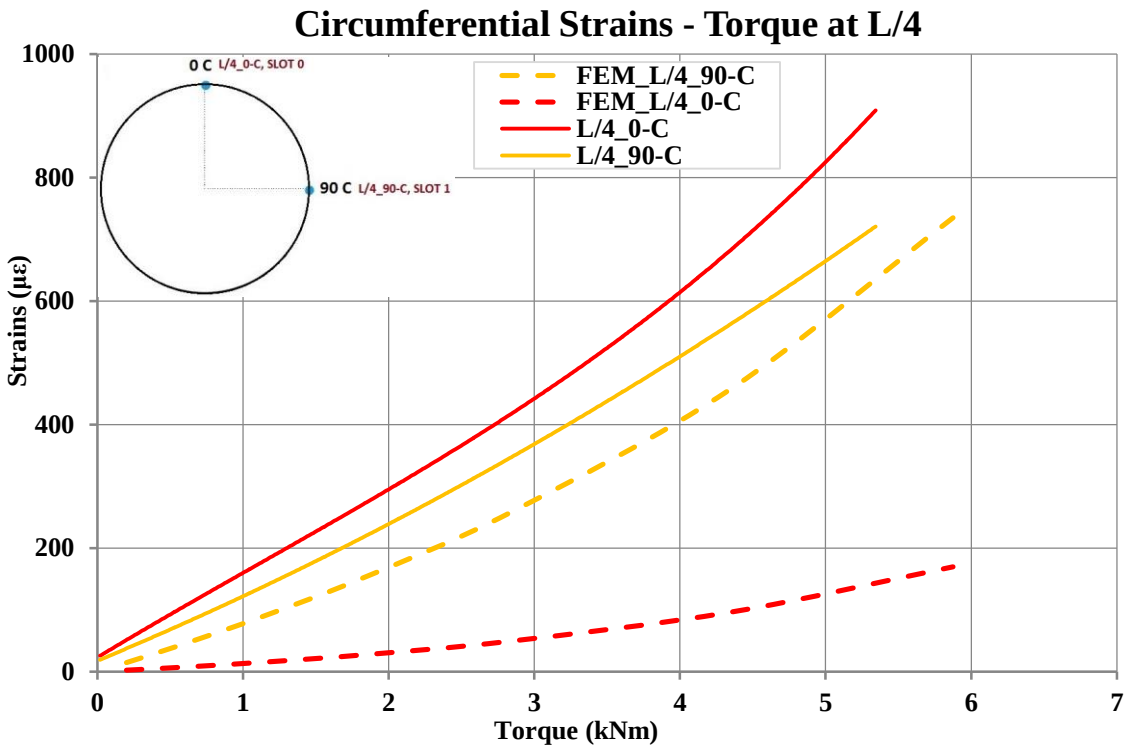

Figure 4.28 Circumferential strains vs torque at L/4

At cross section L/2 (Figure 4.29) all the circumferential strain gauges measured tensile strains. Just like at L/4 (Figure 4.28), the strain gauge at 0 degrees measured the higher circumferential strains at the whole torque range compared to the other strain gauges and reached the maximum value of 864 με. The curve of strain gauge No. 7, which measured circumferential strains at 135 degrees, had a strong tensile tendency, as can be seen by its increasing slope, and indicates that was probably positioned on a crest. The curves of 0 degrees (strain gauge No. 2) and 90 degrees (SG No. 5) showed a milder tensile tendency. The curves which correspond to SG No. 4 (45 degrees) and SG No. 8 (180 degrees) had an almost constant positive slope with a barely noticeable compressive tendency at higher loads.

Figure 4.30 shows the longitudinal strain at L/2 cross section. SG No. 3 at 0 degrees recorded low tensile strains with a small increasing tendency aligned to the corresponding circumferential SG No. 2 at the same position. SG No. 6 at 90 degrees measured compressive strains with a mild compressive tendency. In contrast, the circumferential SG No. 5 at the same position exhibited increasing tensile tendency with tensile strains. The lower strain value recorded was -252 με. Lastly, SG No. 9 measured tensile strain, with a mild tensile tendency, similarly to the circumferential strain gauge 8 at the same position. The maximum strain value recorder was 396.9 με.

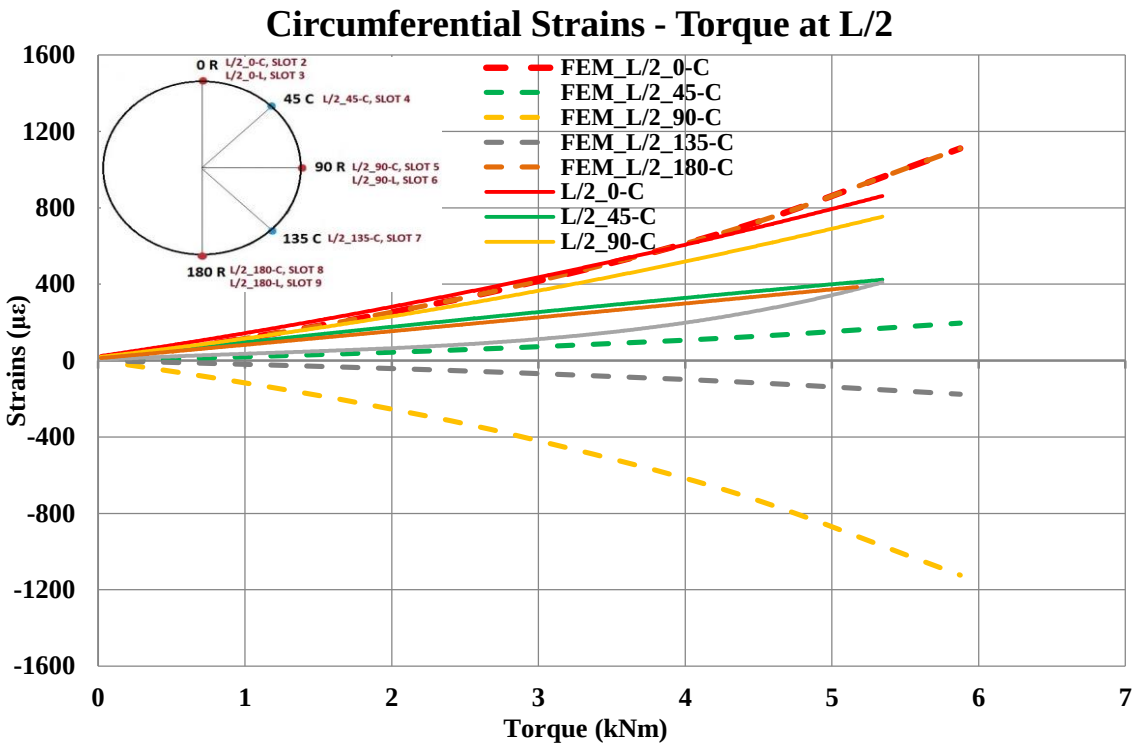

Figure 4.29 Circumferential strains vs torque at L/2

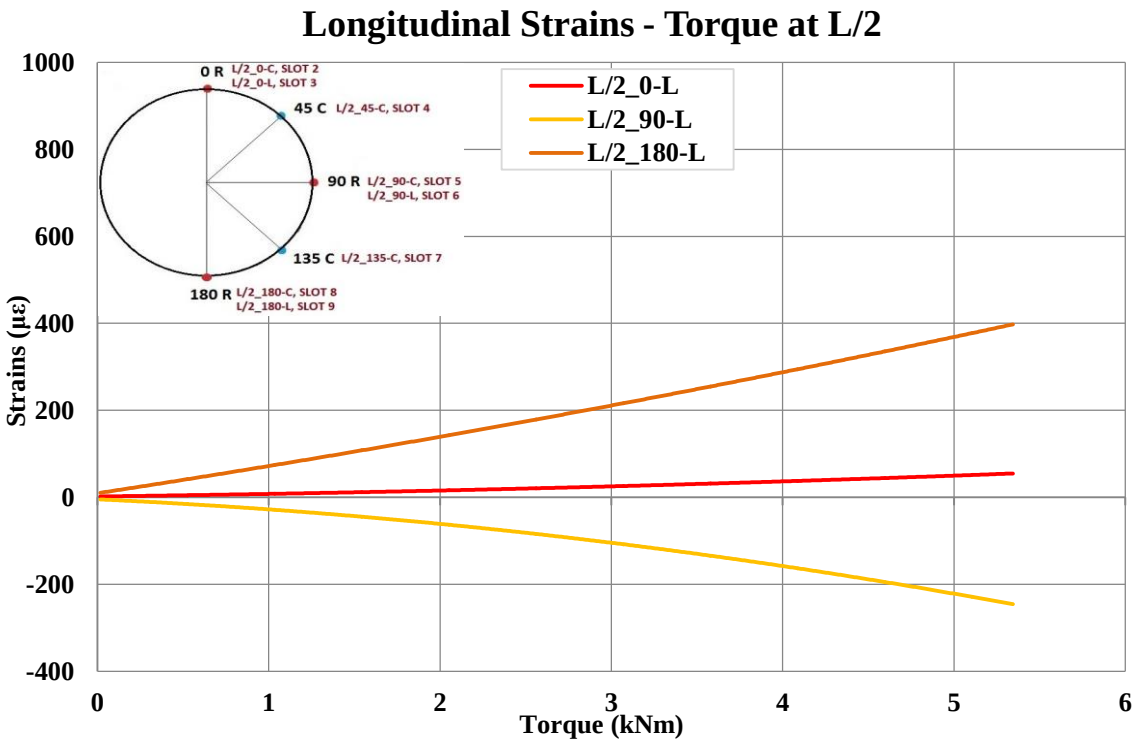

Figure 4.30 Longitudinal strains vs torque at L/2

A rather different image of the circumferential strains at cross section 3L/4 is given in Figure 4.31. Firstly, the SG No. 10 and 13, measured tensile circumferential strains at 0 degrees and 90 degrees. Their behavior was similar to the corresponding SG No. 2 and 5 at cross sections L/4 and L/2 with the difference that the curve of SG No. 13 had a more steep slope and thus a stronger tensile tendency. SG No. 12 at 45 degrees measured tensile circumferential strains and its curve had an almost constant tensile tendency with a barely noticeable compressive tendency at higher loads just like in the case of SG No. 4 at the same position in cross section L/2. SG No. 15 at 125 degrees still recorded tensile strains with a strong tensile tendency. This SG measured the higher strains among the other, with the maximum strain value at this cross section being 639 με. The last circumferential SG, placed at 180 degrees, measured low values of tensile strains which turned into compressive strains at high torque. The curve of this strain gauge had an obvious compressive tendency which is interesting when combine with the results of SG No. 8 at L/2.

Longitudinal strains at cross section 3L/4 (Figure 4.32) exhibit significant deviations from the longitudinal strain gauges at L/2 (Figure 4.30). It is interesting that no similarities occurred between them. SG No. 11 at 0 degrees recorded compressive strains and its curve had a strong compressive tendency. It measured the maximum compressive strain at -351 με. Identical behavior exhibited SG No. 17, at 180 degrees, which though measured rather lower strains. SG No. 14, at 180, degrees measured tensile strains with almost zero values.

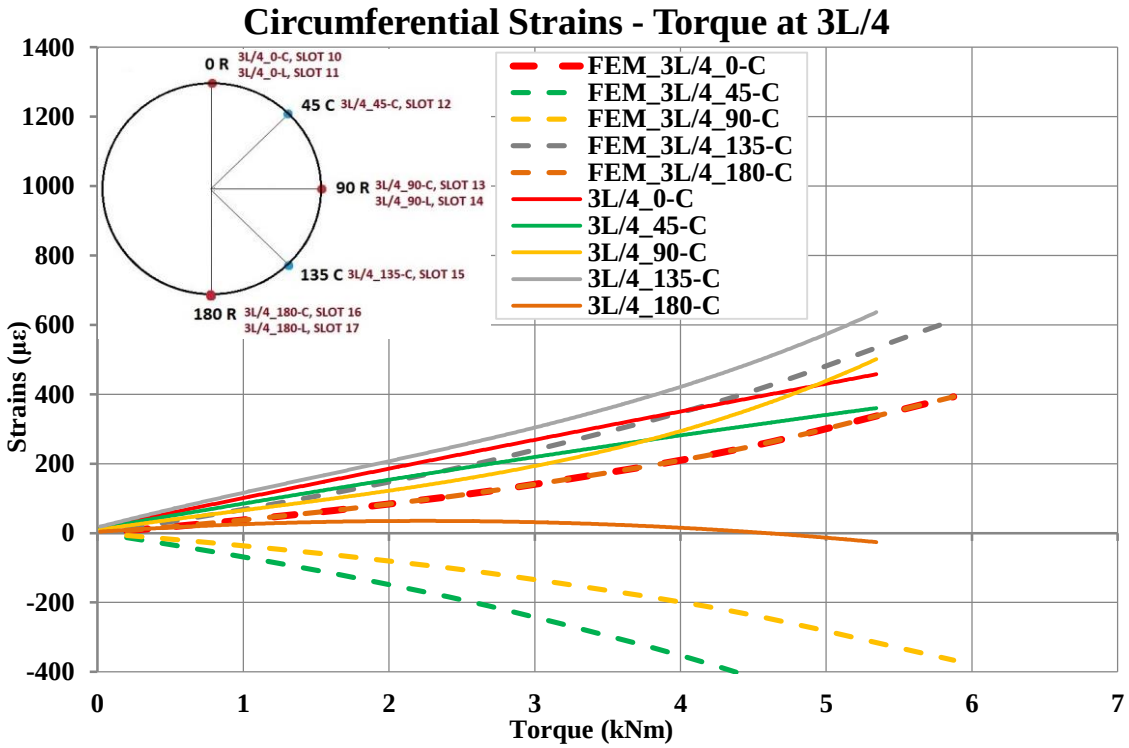

Figure 4.31 Circumferential strains vs torque at 3L/4

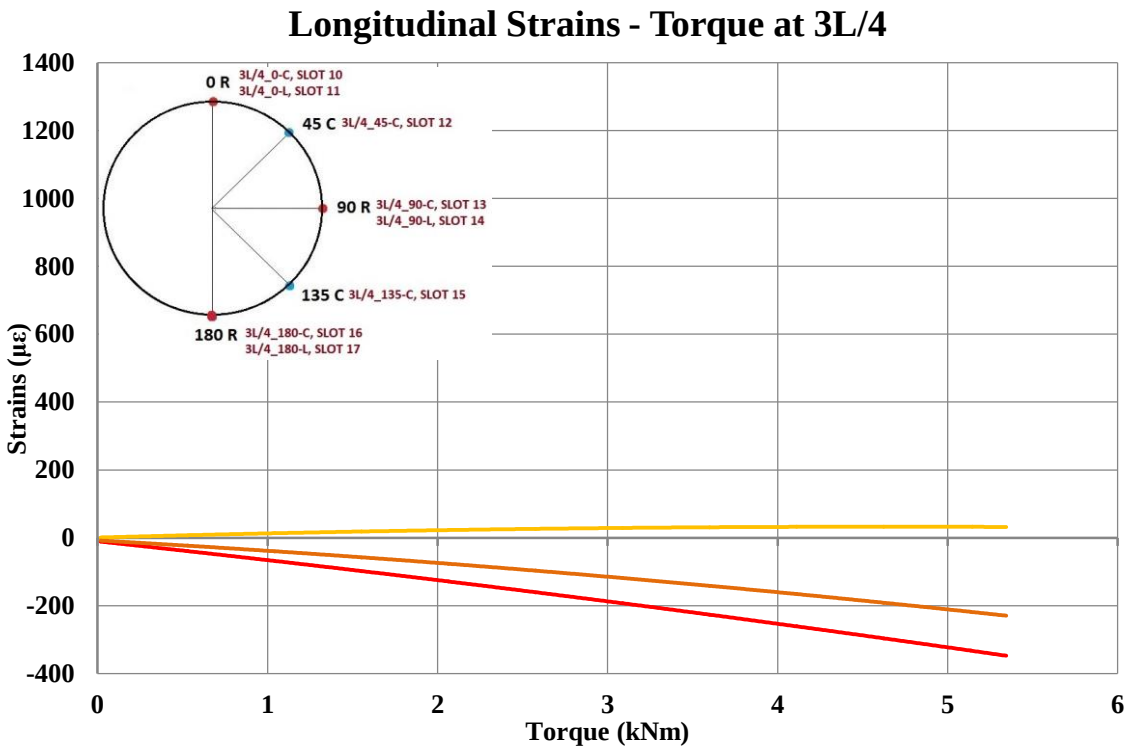

Figure 4.32 Longitudinal strains vs torque at 3L/4

In order to estimate the imminent torsional buckling modeshape, the circumferential strains obtained from the three cross sections were evaluated. The first observation is that all experimental circumferential strains were tensile except at of SG No. 16 at 180 degrees at 3L/4 which was compressive in high torque values. This was not expected as the strain gauges were placed in a range of 0-180 degrees and therefore even for the minimum type-2 modeshape, where 2 crests and 2 troughs are formed on the shaft, the points on the forming troughs should have compressive strains. Probably the imminent modeshape was not yet totally formed. From the results from eq. (4.6) and (4.7) and the numerical results from FEM it can be stated that the maximum achieved torque probably fell short of the critical buckling torque.

Despite this uncertainty of the results, some extra observations could also be made. Firstly, circumferential strains at 0 and 90 degrees had a steady behavior in all of the three cross sections. They had an obvious tensile tendency with the strains at 0 degrees being constantly greater than that at 90 degrees except at high torques at cross section 3L/4. It can be stated then the corresponding strain gauges were placed on (or at least near) the areas of crests. Curves corresponding to strains at 45 degrees seemed to had a subtle compressive tendency or at least an almost constant linear increasing slope. The same applied for the strains at 180 degrees which though at cross section 3L/4 had a more obvious increasing compressive tendency. Thus, these points could be on the areas of forming troughs. Lastly, strains at 135 degrees exhibited the strongest tensile tendency, although in cross section L/2 the corresponding SG No. 7 measured relative low strain values. This point was certainly on the area of a forming crest.

The numerical results on the other hand, in general did not entirely comply with the experimental ones at every circumferential position. The main problem was that all of the experimental strains were tensile in contrast to the numerical results where highly compressive strains also occurred. For example, in L/2 the numerical strains at 90 degrees were compressive which was expected as the node with the highest strains (top of a crest) in the shaft model was assigned to be in the 0 degrees and therefore, due to the type-2 buckling modeshape, at 90 degrees the center of trough will occur. The experimental results in the same position were tensile as it has been mentioned previously. Same observations can be made for other SG positions too. These deviations could be attributed to two potential reasons. Firstly, the circumferential position with the maximum experimental strains (0 degree in L/2) may not be the actual position where the crest would occur, due to the fact the applied torque was much lower than the buckling torque. Thus, non-proper match of the SG nodes in the shaft model with the SG positions may have made. Secondly, type-3 buckling modeshape may have occurred, although the FEM analysis gave a type-2 critical buckling modeshape. This deviation may be due to the uncertainty of the exact geometrical parameters of the shaft (layers orientation and thickness) which would affect the shaft model and the numerical results.

In Figure 4.33 the maximum values of strains measured at each cross section are vividly depicted in a radar diagram. The vertical axis corresponds to the circumferential strains (με), while the circumferential angles of the shaft are also observed. The corresponding results from Vavatsikos (2020) are also plotted for comparison, which indicate a type-2 torsional buckling modeshape. On the other hand, the experimental results do not clearly indicate which modeshape was forming. Type-2 and type-3 modeshape are the equally possible. The high strain values at 90 and 135 degrees, along with the previous analyzed tensile tendency of the strains at these points, indicate a forming crest at this area. Another crest could have been near 0 degrees, but it is not clear if this crest was exactly on this point. If this is true, then a type-3 modeshape could be more possible as the interval between two crests in that case is 120 degrees. However, type-2 modeshape should not be rejected as the forming crest could have been at the left of 0 degree point (near 315 degrees), where no strain data are available though. In that case, interval of the crests would be 180 degrees which indicates type-2 modeshape. Furthermore, as can be seen, points at 45 and 180 degrees are probably on forming trough which confirms the previous analysis based on the tendency of the corresponding strain versus torque curves.

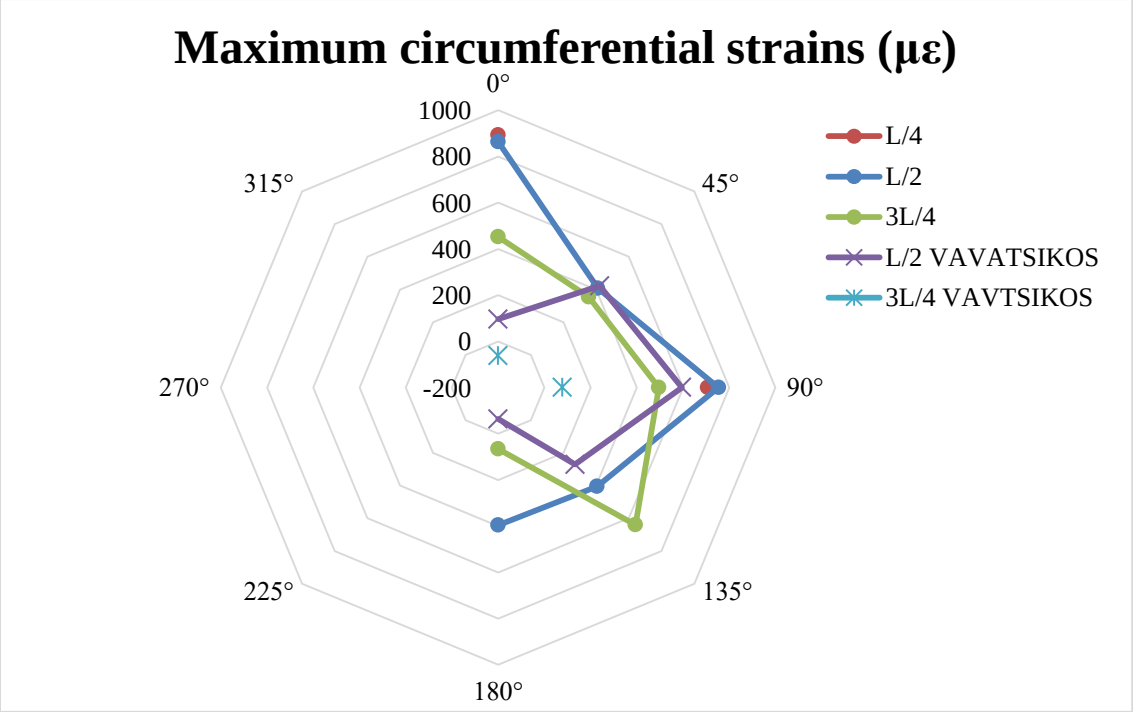

Figure 4.33 Maximum circumferential strains in radar graph

Lastly, the longitudinal strains seemed not to comply with the circumferential strains at the same point. In most casew when the circumferential strain was tensile, the corresponding longitudinal was compressive and vice versa, which was not expected to occur. As the shaft was mainly under tension in the circumferential direction, the same was also expected for the longitudinal direction. Thus, for loads much lower than the buckling load other phenomena affect the response of the shaft under torsion and therefore, no safe conclusions can be drawn.

CHAPTER 5 CONCLUSIONS - RECOMMENDATIONS FOR FUTURE WORK

From the research in the literature and the presentation of methods for strain and torque measurement on shafts, with emphasis on the ones made of composite materials, as well as from the experimental static torsional tests conducted on a CFRP shaft, the following useful conclusions can be drawn:

- Strain measurement on shaft is mainly done for two reasons: stress analysis which is related to SHM and torque measurement. Commonly used strain sensors are electrical resistance SGs and FOS which also have embedding capabilities in composite structures. These two types of strain sensors are also the only which the Classification Societies are referred to. Conventionally, SGs are the widely used strain sensors in both metal and composite structures as they are easy to use and offer accurate results. On the other hand, they are aimed for short term use, especially when exposed to harsh environments, are prone to E/M interference and extensive wiring may be required. FOS do not have such drawbacks. They offer distributing strain measurement capabilities and can be more easily embedded.
- SGs are the predominant strain sensors used in torque transducers and many companies offer compact solution for driveshafts which are based on SG. For non-contact joint between the stationary and the rotating part, inductive power supply and/or signal transmission or wireless RF telemetry are the methods that are mainly used. On composite shafts, SGs measurement is more difficult due to the orthotropic behavior and more aspects have to be taken into consideration, such as alignment of SGs, in order to work properly. Other solutions can be used, such as strains measurement on a metal part of the shaft or compact torque transducers with integrating SG.
- FOS on shafts have been examined for torsion measurement on metal shaft and for SHM on composite shafts, but such applications have not yet used in operating shaft and no complete systems based on FOS are commercially available. Fiber optic rotary joints and other systems for non-contact signal transmission through lenses were also presented. The ingress/egress point of such systems on rotating driveshaft is a problem that remains to be tackled. Hollow FORJ have been used in medical application and can offer the basis for the solution of this issue.
- Twist angle measurement is another method specifically aimed for torque measurement of rotating shaft and many torque meters are commercially available which are based on this technique. Placement on already existing shafts without disassembly can be achieved and rotating speed can also be measured simultaneously. Novel systems are also under development.
- Other methods are based on SAW, with some manufactures offering torque transducers based on this technique, DIC and other systems with novel working principles.

- To sum up, conventional methods (SG, twist angle) are still the predominant way in the market to measure torque on shafts and novel techniques arise but are still more or less in preliminary stage.
- Equivalent mechanical properties of a CFRP were calculated and the split-disk experiment on ring-shaped specimens was conducted in order to calculate the equivalent Young's modulus in the hoop direction. Although problems occurred in the experimental procedure and the results had low repeatability, probably due to the larger diameter of the specimen with respect to the metal half disks, the final value obtained was close to the theoretical estimation.
- Static torsional tests on a CFRP shaft exhibited problems due to the defective torsion machine and specifically due to the angle measurement system or the displacement control system. In addition, the TT 10K torque meter, which is based on RF telemetry signal transmission was also attached on the shaft but was not correctly used as not proper calibration was made prior to the conduction of the test. Despite that, processing of the results afterwards confirmed the applicability of TT 10K on composite shafts. An interesting observation is that eq. (3.8) cannot be used on composite materials and this must be taken into account when using this device on composite shafts.
- As the maximum achieved torque was lower than the critical buckling torque obtained from FEM and analytical solutions, the experimental results from 18 single SG attached on the circumference of the shaft did not give clear indications about the imminent buckling modeshape.

Lastly, as future recommendations are proposed that:

- Implementation of FBG on a composite shaft along with FORJ for non-contact coupling under laboratory conditions.
- Static torsional test of the CFRP at a properly working torsion machine until failure of the shaft, in order to compare the results of the single SG and the FEM.
- Correct application of the TT 10K on the CFRP shaft under static torsional test. Calibration procedure should be followed precisely as proposed by the manufacturer. Trials on a rotating shaft should then follow.

CHAPTER 6 LITERATURE

Ajovalasit, A. (2005). Embedded Strain Gauges: Effect of the Stress Normal to the Grid. Strain, 41(3), 95-103.

Ajovalasit, A. (2011). Advances in strain gauge measurement on composite materials. Strain, 47(4), 313–325.

Aloisi, S., Galietti, U., & Pappalettere, C. (1998). Strain Measurement in Composite Materials Using Embedded Strain Gauges. Key Engineering Materials, 144, 251–260.

Arena, M., & Viscardi, M. (2020). Strain state detection in composite structures: Review and new challenges. Journal of Composites Science, 4(2).

Balageas, D., Fritzen, C.-P., & Güemes, A. (2006). Structural Health Monitoring. 1st ed. ISTE Ltd

Belhouideg, S., & Lagache, M. (2017). Effect of Embedded Strain Gage on the Mechanical Behavior of Composite Structures. Journal of Modern Materials, 5(1), 1–7.

Bilalis, E. (2016). "Experimental and Numerical Study of Composite Shafts". Diploma Thesis, School of Naval Architecture and Marine Engineering, Shipbuilding Technology Laboratory, National Technical University of Athens

Bonisławski, M., Hołub, M., Borkowski, T., & Kowalak, P. (2019). A novel telemetry system for real time, ship main propulsion power measurement. Sensors, 19(21).

Cai, J., Qiu, L., Yuan, S., Shi, L., Liu, P., & Liang, D. (2012). Structural Health Monitoring for Composite Materials. Composites and Their Applications. https://doi.org/10.5772/48215

Chatzinas, P. (2021). "Πειραματική παραμετρική μελέτη μέτρησης μηχανικών ιδιοτήτων σύνθετων υλικών από περιέλιξη ινών και εφαρμογή στατιστικής ανάλυσης" (In Greek). Diploma Thesis, School of Naval Architecture and Marine Engineering Shipbuilding Technology Laboratory, National Technical University of Athens.

Chen, C., Ma, T., Jin, H., Wu, Y., Hou, Z., & Li, F. (2020). Torque and rotational speed sensor based on resistance and capacitive grating for rotational shaft of mechanical systems. Mechanical Systems and Signal Processing, 142.

Cheng, B., Zhu, W., Hua, L., Liu, J., Li, Y., Nygaard, R., & Xiao, H. (2016). Distributed torsion sensor based on cascaded coaxial cable Fabry-Perot interferometers. Measurement Science and Technology, 27(7).

de Silva, C. W. (2016). Sensors and Actuators.

Donohoe, B., Geraghty, D., & O'Donnell, G. E. (2011). Wireless calibration of a surface acoustic wave resonator as a strain sensor. IEEE Sensors Journal, 11(4), 1026–1032.

Dorsey, Glenn; O'Brien, M. Fiber Optic Rotary Joints (FORJ) - Performance and Application Highlights. White Paper.

Elforjani, M. A. (2010). Condition Monitoring of Slow Speed Rotating Machinery Using Acoustic Emission Technology. School Of Engineering, Cranfield University

Elmahdy, A., Verleysen P. (2018). The Use of 2D and 3D High-Speed Digital Image Correlation in Full Field Strain Measurements of Composite Materials Subjected to High Strain Rates. Proceedings of The 18th International Conference on Experimental Mechanics, 2(8).

Farrar, C. R., & Worden, K. (2013). Structural Health Monitoring: A Machine Learning Perspective. John Wiley & Sons, Ltd.

Fu, D., Zhang, Y. nan, Zhang, A., Han, B., Wu, Q., & Zhao, Y. (2019). Novel Fiber Grating for Sensing Applications. Physica Status Solidi (A) Applications and Materials Science, 216(6), 1–20.

Garinei, A., & Marsili, R. (2017). Development of a non-contact torque transducer based on the laser speckle contrast method. Journal of Sensors and Sensor Systems, 6(2), 253–258.

Geng P., Xing, J., Wang, Q. (2021). Analytical model for stress and deformation of multiple-winding-angle filament-wound composite pipes/vessels under multiple combined loads. Applied Mathematical Modelling, 94, 576-596.

Glišić, B., & Inaudi, D. (2007). Fibre Optic Methods for Structural Health Monitoring. John Wiley & Sons Ltd.

Goyal, D., Chaudhary, A., Dang, R. K., Pabla, B. S., & Dhami, S. S. (2018). Condition monitoring of rotating machines: A Review. World Scientific News, 113, 98–108.

Graham-Jones, J., & Summerscales, J. (2016). Marine Applications of Advanced Fibre-Reinforced Composites.

Green, E. (1998). Marine Composites. 2nd ed. Eric Greene Associates

Grzybek, D., & Micek, P. (2019). Piezoelectric energy harvesting based on macro fiber composite from a rotating shaft. Physica Scripta, 94(9).

Guijs, R. P. (2018). Power Measurements and Noise & Vibration Levels in Composite Shafts in the Maritime Industry. Engineering Technology, University of Twente.

Hoffmann, K. (1989). An Introduction to Stress Analysis and Transducer Design using Strain Gauges. HBM.

Hoffmann, K. (2001). Applying the wheatstone bridge circuit. HBM.

Horoschenkoff, A., Klein, S., & Haase, K.-H. (2006). Structural integration of strain gages. Strain, 1–56.

Hu, Y., Yang, M., Zhang, J., Song, C., & Hong, T. (2016). Effect of stacking sequence on the torsional stiffness of the composite drive shaft. Advanced Composite Materials, 26(6), 537–552.

Installation Case Study Hull Stress Monitoring System, HULLFIB.

Ibrahim, R. A. (2017). Structural Health Monitoring Basic Ingredients and Sensors. Handbook of Structural Life Assessment, 211–261.

Ivče, R., Jurdana, I., & Kos, S. (2014). Ship's cargo handling system with the optical fiber sensor technology application. Scientific Journal of Maritime Research, 28(2), 118–127.

Janeliukstis, R., & Chen, X. (2021). Review of digital image correlation application to large-scale composite structure testing. Composite Structures, 271.

Jensen, A. E., Taby, J., Pran, K., Sagvolden, G., & Wang, G. (2001). Measurement of Global Loads on a Full-Scale SES Vessel Using Networks of Fiber Optic Sensors. Journal of Ship Research, 45(3), 205–215.

Jing, W., Jia, D., Tang, F., Zhang, H., Zhang, Y., Zhou, G., Yu, J., Kong, F., & Liu, K. (2004). Design and implementation of a broadband optical rotary joint using C-lenses. Optics Express, 12(17).

Kang, H. K., Park, J. W., Ryu, C. Y., Hong, C. S., & Kim, C. G. (2000). Development of fibre optic ingress/egress methods for smart composite structures. Smart Materials and Structures, 9(2), 149–156.

Keramidis, M. (2020). Μελέτη αντικατάστασης άξονα του Εργαστηρίου Ναυτικής Μηχανολογίας από νέο από Σύνθετα Υλικά (In Greek). School of Naval Architecture and Marine Engineering Shipbuilding Technology Laboratory, National Technical University of Athens.

Kersey, A. D., Davis, M. A., Berkoff, T. A., Dandridge, A. D., Jones, R. T., Tsai, T.-E., Cogdell, G. B., Wang, G., Havsgaard, G. B., Pran, K., & Knudsen, S. (1997). Transient load monitoring on a composite hull ship using distributed fiber optic Bragg grating sensors Article. Smart Structures and Materials 1997: Smart Sensing, Processing, and Instrumentation, 3042, 421–430.

Kim, K. S., Breslauer, M., & Springer, G. S. (1992). The Effect of Embedded Sensors on the Strength of Composite Laminates. Journal of Reinforced Plastics and Composites, 11(8), 949–958.

Kinet, D., Mégret, P., Goossen, K. W., Qiu, L., Heider, D., & Caucheteur, C. (2014). Fiber Bragg grating sensors toward structural health monitoring in composite materials: Challenges and solutions. Sensors (Switzerland), 14(4), 7394–7419.

Konstantaki, M., Violakis, G., Pappas, G. A., Geernaert, T., Korakas, N., Tiriakidis, N., Tiriakidi, T., Tiriakidis, K., Thienpont, H., Berghmans, F., Botsis, J., & Pissadakis, S. (2021). Monitoring of torque induced strain in composite shafts with embedded and surface-mounted optical fiber bragg gratings. Sensors, 21(7).

Kopecki, H., Święch, Ł., & Kołodziejczyk, R. (2020). On the Identification of Local Structural Defects in Composite Thin-Walled Structures. Advances in Science and Technology Research Journal, 14(1), 154–166.

Kotsidis, E. (2012). "ΧΡΗΣΗ ΑΙΣΘΗΤΗΡΩΝ ΟΠΤΙΚΩΝ ΙΝΩΝ ΓΙΑ ΤΗΝ ΜΕΤΡΗΣΗ ΠΑΡΑΜΟΡΦΩΣΕΩΝ ΣΕ ΣΥΝΘΕΤΑ ΥΛΙΚΑ ΚΑΙ ΣΥΝΔΕΣΜΟΥΣ ΜΕ ΚΟΛΛΗΤΙΚΑ ΜΕΣΑ" (In Greek). Postgraduate Diploma Thesis, School of Naval Architecture and Marine Engineering Shipbuilding Technology Laboratory, National Technical University of Athens.

Krimmel, W. (2006). Evolution and Future of Torque Measurement Technology. Sensors & Transducers, 65(3), 500–508.

Kruger, L., Swart, P. L., Chtcherbakov, A. A., & van Wyk, A. J. (2004). Non-contact torsion sensor using fibre Bragg gratings. Measurement Science and Technology, 15(8), 1448–1452.

Kuang, K. S. C., Kenny, R., Whelan, M. P., Cantwell, W. J., & Chalker, P. R. (2001). Embedded fibre Bragg grating sensors in advanced composite materials. Composites Science and Technology, 61(10), 1379–1387.

Kuschmierz, R., Filippatos, A., Günther, P., Langkamp, A., Hufenbach, W., Czarske, J., & Fischer, A. (2015). In-process, non-destructive, dynamic testing of high-speed polymer composite rotors. Mechanical Systems and Signal Processing, 54–55, 325–335.

Lee, D. C., Lee, J. J., & Yun, S. J. (1995). The mechanical characteristics of smart composite structures with embedded optical fiber sensors. Composite Structures, 32(1–4), 39–50.

Lee, J. M., & Hwang, Y. (2008). A novel online rotor condition monitoring system using fiber Bragg grating (FBG) sensors and a rotary optical coupler. Measurement Science and Technology, 19(6).

Li, G., Bao, M., Ding, S., Li, Y. (2017). A system for accurate measuring of thermal-structure displacement on a high speed rotating turbine disk by using digital image correlation technology. Aplied Thermal Engineering, 113, 36-46

Lich, J., Wollmann, T., Filippatos, A., Gude, M., Czarske, J., & Kuschmierz, R. (2019). Diffraction-grating-based insitu displacement, tilt, and strain measurements on high-speed composite rotors. Applied Optics, 58(29), 8021–8030.

Luyckx, G., Voet, E., Lammens, N., & Degrieck, J. (2011). Strain measurements of composite laminates with embedded fibre bragg gratings: Criticism and opportunities for research. Sensors, 11(1), 384–408.

Ma, Z., & Chen, X. (2018). Fiber bragg gratings sensors for aircraft wing shape measurement: Recent applications and technical analysis. Sensors (Switzerland), 19(1).

Mandal, D., & Banerjee, S. (2022). Surface Acoustic Wave (SAW) Sensors: Physics, Materials, and Applications. Sensors, 22(3).

Matveenko, V. P., Shardakov, I. N., Voronkov, A. A., Kosheleva, N. A., Lobanov, D. S., Serovaev, G. S., Spaskova, E. M., & Shipunov, G. S. (2017). Measurement of strains by optical fiber Bragg grating sensors embedded into polymer composite material. Structural Control and Health Monitoring, 25(3), 1–11.

Mavrakis, G. (2015). "Ανάπτυξη Διάταξης Μέτρησης Ροπής σε Στρεφόμενες Ηλεκτρικές Μηχανές" (In Greek). Diploma Thesis, School of Naval Architecture and Marine Engineering Shipbuilding Technology Laboratory, National Technical University of Athens.

McCormick, N., & Lord, J. (2010). Digital image correlation. Materials Today, 13(12), 52–54.

Micek, P., & Grzybek, D. (2020). Wireless stress sensor based on piezoelectric energy harvesting for a rotating shaft. Sensors and Actuators, A: Physical, 301, 111744.

Mouritz, A. P., Gellert, E., Burchill, P., & Challis, K. (2001). Review of advanced composite structures for naval ships and submarines. Composite Structures, 53, 21–41.

Nicolas, M. J., Sullivan, R. W., & Richards, W. L. (2016). Large scale applications using FBG sensors: Determination of in-flight loads and shape of a composite aircraft wing. Aerospace, 3(3).

Pantaleo, A., Pellerano, A., & Pellerano, S. (2006). An optical torque transducer for high-speed cutting. Measurement Science and Technology, 17(2), 331–339.

Papadakis, A. Z., Themelakis, J. G., & Tsouvalis, N. G. (2018). The effect of geometric and manufacturing parameters on filament wound composites split disk test results. 17th International Congress of the International Maritime Association of the Mediterranean (IMAM 2017) , 2, 713–721.

Phelps, B., & Morris, B. (2013). Review of Hull Structural Monitoring Systems for Navy Ships. Maritime Platforms Division, Defence Science and Technology Organisation.

Philipp, K., Filippatos, A., Kuschmierz, R., Langkamp, A., Gude, M., Fischer, A., & Czarske, J. (2016). Multi-sensor system for in situ shape monitoring and damage identification of high-speed composite rotors. Mechanical Systems and Signal Processing, 76–77, 187–200.

Qiu, L., Teitelbaum, M. E., Goossen, K. W., Heider, D., O'Brien, D. J., & Wetzel, E. D. (2009). Normal free space coupling to fiber Bragg grating sensors. Sensors and Smart Structures Technologies for Civil, Mechanical, and Aerospace Systems, Proc. of SPIE, 7292.

Qiu, Y., Wang, Q. B., Zhao, H. T., Chen, J. A., & Wang, Y. Y. (2013). Review on composite structural health monitoring based on fiber Bragg grating sensing principle. Journal of Shanghai Jiaotong University (Science), 18(2), 129–139.

Ramakrishnan, M., Rajan, G., Semenova, Y., & Farrell, G. (2016). Overview of fiber optic sensor technologies for strain/temperature sensing applications in composite materials. Sensors (Switzerland), 16(1).

Rangaswamy, T., & Vijayarangan, S. (2005). Optimal sizing and stacking sequence of composite drive shafts. Materials Science, 11(2), 133–139.

Shamsuddoha, Md., David, M., Oromiehie, E., Prusty, B. G. (2021). Distributed optical fibre sensor based monitoring of thermoplastic carbon composite cylinders under biaxial loading: Experimental and numerical investigations. Composite Structures, 261.

Schicker, R., & Wegener, G. Measuring torque correctly. HBM. www.hbm.com/torque

Schnack, E., Prinz, B., & Dimitrov, S. (2004). Interlaminar stress determination in carbon fibre epoxy composites with the embedded strain gauge technique. Strain, 40(3), 113–118.

Shadmehri, F., & Van Hoa, S. (2019). Digital image correlation applications in composite automated manufacturing, inspection, and testing. Applied Sciences (Switzerland), 9(13).

Silva-Muñoz, R. A., & Lopez-Anido, R. A. (2008). Structural health monitoring of marine composite structural joints using embedded fiber Bragg grating strain sensors. Composite Structures, 89(2), 224–234. https://doi.org/10.1016/j.compstruct.2008.07.027

Singh, T., & Sehgal, S. (2022). Structural Health Monitoring of Composite Materials. Archives of Computational Methods in Engineering, 29(4), 1997–2017.

Snow, J. W. (1998). An Overview of Fibre Optic Rotary Joint Technology and Recent Advances. IFAC Proceedings Volumes, 31(33), 77–81. https://doi.org/10.1016/s1474-6670(17)38390-8

Staszewski, W. J., Boller, C., & Tomlinson, G. R. (2004). Health Monitoring of Aerospace Structures. John Wiley & Sons Ltd.

Stedile Filho, P., Almeida, J. H. S., & Amico, S. C. (2018). Carbon/epoxy filament wound composite drive shafts under torsion and compression. Journal of Composite Materials, 52(8), 1103–1111.

Swart, P. L., Chtcherbakov, A. A., & Van Wyk, A. J. (2006). Dual Bragg grating sensor for concurrent torsion and temperature measurement. Measurement Science and Technology, 17(5), 1057–1064.

Themelakis, I. G. (2017). "ΠΕΙΡΑΜΑΤΙΚΗ ΠΑΡΑΜΕΤΡΙΚΗ ΜΕΛΕΤΗ ΤΩΝ ΜΗΧΑΝΙΚΩΝ ΙΔΙΟΤΗΤΩΝ ΔΑΚΤΥΛΙΟΕΙΔΩΝ ΔΟΚΙΜΙΩΝ ΑΠΟ ΣΥΝΘΕΤΑ ΥΛΙΚΑ" (In Greek). Diploma Thesis, School of Naval Architecture and Marine Engineering Shipbuilding Technology Laboratory, National Technical University of Athens.

Tian, X. G., & Tao, X. M. (2001). Torsion measurement using fiber bragg grating sensors. Experimental Mechanics, 41(3), 248–253.

Tsouvalis, N. (1998). "ΑΝΑΛΥΣΗ ΚΑΙ ΣΧΕΔΙΑΣΗ ΣΚΑΦΩΝ ΑΠΟ ΣΥΝΘΕΤΑ ΥΛΙΚΑ" (In Greek). School of Naval Architecture and Marine Engineering Shipbuilding Technology Laboratory, National Technical University of Athens.

Tuttle, M. E., & Brinson, H. F. (1985). Resistance-foil strain-gage technology as applied to composite materials. Experimental Mechanics, 26(2).

Vanlanduit, S., Sorgente, M., Zadeh, A. R., Güemes, A., & Faisal, N. (2021). Strain Monitoring. Springer Aerospace Technology, 219–241.

Vavatsikos, D. (2020). "Static Torsional Tests of Composite Driveshafts". Diploma Thesis, School of Naval Architecture and Marine Engineering Shipbuilding Technology Laboratory, National Technical University of Athens.

Vinson, J. R., & Sierakowski, R. L. (2008). The Behavior of Structures Composed of Composite Materials. Springer.

Vishay Precision Group, Micro-measurements Application Note VMM-1 (2010). Strain Gage Measurements on Plastics and Composites.

Yoon, S. H. O., Kim, C. G., & Cho, W. M. (1997). Measurement of tensile properties using filament wound ring specimens. Journal of Reinforced Plastics and Composites, 16(9), 810–824.

Yoon, S.-H., Cho, W.-M., & Kim, C.-G. (1997). Measurement of Modulus in Filament Wound Ring. 25–28.

Zappa, E., Mazzoleni, P., & Matinmanesh, A. (2014). Uncertainty assessment of digital image correlation method in dynamic applications. Optics and Lasers in Engineering, 56, 140–151.

Zappalá, D., Bezziccheri, M., Crabtree, C. J., & Paone, N. (2018). Non-intrusive torque measurement for rotating shafts using optical sensing of zebra-tapes. Measurement Science and Technology, 29(6).

Zhao, Y., & Pang, S. S. (1995). Stress-strain and failure analyses of composite pipe under torsion. Journal of Pressure Vessel Technology, Transactions of the ASME, 117(3), 273–278.